

**ENGINEERING BEHAVIOR AND CHARACTERIZATION OF
PHYSICAL-CHEMICAL PARTICULATE MIXTURES USING
GEOPHYSICAL MEASUREMENT TECHNIQUES**

A thesis

Presented to

The Academic Faculty

by

Hyunwook Choo

In Partial Fulfillment

of the Requirements for the Degree

Doctor of Philosophy in the School of Civil and Environmental Engineering

Georgia Institute of Technology

August 2013

Copyright © 2013 by Hyunwook Choo

**ENGINEERING BEHAVIOR AND CHARACTERIZATION OF
PHYSICAL-CHEMICAL PARTICULATE MIXTURES USING
GEOPHYSICAL MEASUREMENT TECHNIQUES**

Approved by:

Dr. Susan E. Burns, Advisor
School of Civil and Environmental
Engineering
Georgia Institute of Technology

Dr. J. Carlos Santamarina
School of Civil and Environmental
Engineering
Georgia Institute of Technology

Dr. J. David Frost
School of Civil and Environmental
Engineering
Georgia Institute of Technology

Dr. Paul W. Mayne
School of Civil and Environmental
Engineering
Georgia Institute of Technology

Dr. Christian Huber
School of Earth and Atmospheric
Sciences
Georgia Institute of Technology

Date Approved: May 9, 2013

To my family, Jungmo Choo, Sunhee Park, Eunjoo Choo, and Youngjoon Choo

ACKNOWLEDGEMENTS

First of all, I would like to show my gratitude to my advisor, Dr. Susan Burns for her guidance, invaluable support, encouragement, and generosity not only as an advisor, but also as a sincere friend. It has been a great pleasure to be one of her graduate students. Through the work with her at Georgia Tech, I could grow up not only professionally but also personally.

I wish to acknowledge my thesis committee for their useful comments and suggestions: Dr. Carlos Santamarina, Dr. David Frost, Dr. Paul Mayne, and Dr. Christian Huber. I also wish to express my gratitude to my former advisor in Korea, Dr. Woojin Lee for his great advices and support.

I also would like to thank the past and current members of the Geoenvironmental Laboratory for their help and encouragement: Bate B., Joan Larrahondo, Aditya Bhatt, Qian Zhao, Nortey Yeboah, Kip gray, and Cameron Troxel. I owe my sincere gratitude to my good friends at Georgia Tech, especially to Hosung Shin, Jongwon Jung, Taeseo Ku, Sihyun Kim, Chiwon In, Minsu Cha, Eunhyea Chung, Junbong Jang, Hyungkoo Yoon, Sunghun Hwang, Seokho Jeong, Sunghun Jung, and Seunghee Kim.

Last but not the least, I would like to thank my parents, sister, brother, and brother-in-law for their confidence in me and dedicated support. None of this would have been possible without their love.

TABLE OF CONTENTS

	Page
ACKNOWLEDGEMENTS.....	IV
LIST OF TABLES.....	VIII
LIST OF FIGURES.....	X
LIST OF SYMBOLS.....	XVI
LIST OF ABBREVIATIONS.....	XX
SUMMARY.....	XXI
CHAPTER 1 INTRODUCTION.....	1
1.1 Thesis Organization.....	2
CHAPTER 2 SHEAR WAVE VELOCITY OF BINARY MIXTURES OF SILICA PARTICLES AS A FUNCTION OF FINES FRACTION, SIZE RATIOS AND RELATIVE DENSITIES.....	7
2.1 Introduction.....	7
2.2 Theoretical Aspects of Binary Mixture.....	9
2.2.1 Pore Size.....	9
2.2.2 Critical Fines (Small Particles) Content.....	10
2.2.3 Intergranular Void Ratio.....	12
2.3 Experimental Program.....	14
2.3.1 Materials.....	14
2.3.2 Shear Wave Velocity Measurements.....	15
2.3.3 Sample Preparation and Testing Program.....	17
2.4 Results and Analysis.....	18
2.4.1 The Variation of Extreme Void Ratio.....	19
2.4.2 Shear Wave Velocity.....	22
2.4.3 The Variations of α -factors and β -exponents.....	33
2.5 Discussion.....	38
2.5.1 Effect of Packing Density.....	38
2.5.2 Effects of Fines Content and Size Ratio.....	40
2.5.3 Intergranular Void Ratio.....	41
2.5.4 Critical Fines Content.....	45
2.6 SUMMARY.....	46
CHAPTER 3 EFFECT OF OVERCONSOLIDATION RATIO ON DYNAMIC PROPERTIES OF BINARY MIXTURES OF SILICA PARTICLES.....	48
3.1 Introduction.....	48

3.2 Theoretical Framework.....	49
3.2.1 Critical Fines (Small Particles) Content.....	49
3.2.2 Overconsolidation Ratio Exponent in Maximum Shear Modulus Relationship.....	51
3.2.3 Stress History and Stress Exponents during Loading and Unloading.....	53
3.3 Experimental Program.....	55
3.3.1 Materials.....	55
3.3.2 Test Equipment and Shear Wave Velocity Measurements.....	57
3.3.3 Sample Preparation and Testing Program.....	58
3.4 Results and Discussion.....	59
3.4.1 Small Strain Stiffness during Loading and Unloading.....	59
3.4.2 Effect of Size Ratio.....	62
3.4.3 Effect of Fines (Small Particles) Content.....	64
3.5 Summary.....	68
 CHAPTER 4 SMALL TO INTERMEDIATE STRAIN PROPERTIES OF FLY ASH WITH VARIOUS CARBON AND BIOMASS CONTENTS.....	 70
4.1 Introduction.....	70
4.2 Theoretical Aspects.....	71
4.2.1 Critical Fines Content / Critical Carbon Content.....	72
4.2.2 Interfine Void Ratio.....	74
4.3 Experimental Program.....	76
4.3.1 Materials.....	76
4.3.2 Test Equipment and Shear Wave Velocity Measurement.....	78
4.3.3 Sample Preparation.....	81
4.4 Test Results and Analysis.....	82
4.4.1 Effect of Carbon Content on G_{max}	82
4.4.2 Effect of Biomass Content on G_{max}	83
4.4.3 G_{max} in Terms of Interfine Void Ratio.....	86
4.4.4 Intermediate Strain Properties: Constrained Modulus or Compressibility.....	87
4.4.5 Stiffness Anisotropy of Fly Ash.....	89
4.5 Summary.....	92
 CHAPTER 5 IMPACT OF UNBURNED CARBON PARTICLES ON THE ELECTRICAL CONDUCTIVITY OF FLY ASH SLURRY.....	 94
5.1 Introduction.....	94
5.2 Theoretical Aspects.....	96
5.2.1 Electrical Conductivity.....	96
5.2.2 Stress Dependency of Conductive Particles.....	98

5.3 Experimental Program.....	101
5.3.1 Materials.....	101
5.3.2 Test Equipment.....	102
5.3.3 Sample Preparation and Electrical Conductivity/Resistivity Measurements.....	104
5.4 Test Results and Analysis.....	105
5.4.1 Electrical Conductivity as a Function of Void Ratio.....	105
5.4.2 Carbon Particle Conduction.....	108
5.5 Discussion.....	110
5.5.1 Dependency of Carbon Particle Conduction on Stress.....	110
5.5.2 Dependency of Carbon Particle Conduction on Pore Water Conductivity.....	113
5.5.3 Estimation of Carbon Particle Conduction by Regression Analysis	116
5.6 Summary.....	118
 CHAPTER 6 THERMAL CONDUCTIVITY OF DRY FLY ASHES WITH VARIOUS CARBON AND BIOMASS CONTENTS	 120
6.1 Introduction.....	120
6.1.1 Thermal Conductivity.....	121
6.1.2 Thermal Conductivity Governing Factors.....	121
6.2 Experimental Program.....	122
6.2.1 Materials.....	122
6.2.2 Thermal Conductivity Measurement.....	124
6.3 Results and Discussion.....	126
6.3.1 Effect of Carbon Content.....	126
6.3.2 Effect of Biomass Content.....	128
6.3.3 Comparison with Thermal Conductivity of Dry Natural Soils.....	130
6.4 Summary.....	134
 CHAPTER 7 EFFECT OF COATING OF NANO-SIZED PARTICLES ONTO SAND SURFACE: SMALL STRAIN STIFFNESS OF IRON OXIDE COATED SANDS ACCORDING TO IRON COATING DENSITY AND SAND PARTICLE SIZE.....	 136
7.1 Introduction.....	136
7.2 Review of Theoretically Derived Small Strain Stiffness.....	138
7.2.1 Normal Stiffness.....	138
7.2.2 Tangential Stiffness.....	141
7.2.3 Theoretical Expression of Maximum Shear Modulus for Random Packing of Spheres.....	144
7.3 Experimental Program.....	147
7.3.1 Materials	147

7.3.2 Test Equipment and Program.....	149
7.4 Results.....	150
7.5 Analysis and Discussion.....	153
7.5.1 Effect of Applied Stress and Packing Density on Contact Mode....	153
7.5.2 Effects of Coating Density of Nano-sized Particles and Sand Particle Size on Contact Mode.....	156
7.5.3 Comparison of Test Results with Theoretical G_{max}	162
7.6 Summary.....	163
 CHAPTER 8 REVIEW OF ARCHIE'S EQUATION THROUGH THEORETICAL DERIVATION AND EXPERIMENTAL STUDY ON UNCOATED AND HEMATITE COATED SOILS.....	 166
8.1 Introduction.....	166
8.1.1 Chemical Weathering and Iron Oxide.....	167
8.2 Theoretical Framework.....	168
8.2.1 Electrical Resistivity/Conductivity.....	168
8.2.2 Surface Conductivity.....	173
8.3 Experimental Program.....	175
8.3.1 Materials.....	175
8.3.2 Test Equipment and Electrical Resistivity Measurements.....	176
8.3.3 Sample Preparation and Testing Program.....	180
8.4 Test Results and Analysis.....	181
8.4.1 Uncoated and Hematite Coated Ottawa Sands.....	181
8.4.2 Uncoated and Iron Oxide Coated Kaolinites.....	184
8.5 Discussion.....	188
8.5.1 Contribution of Surface Conduction to Conductivity of a Porous Media.....	188
8.5.2 Effect of Iron Oxide Coating on Electrical Conductivity of Soils...	193
8.6 Summary.....	196
 CHAPTER 9 CONCLUSIONS AND RECOMMENDATIONS.....	 198
REFERENCES.....	205
VITA.....	216

LIST OF TABLES

	page
Table 2-1. Material Properties of Binary Soil Mixtures.....	15
Table 2-2. Experimental Matrix for Bender Element Testing.....	18
Table 2-3. Calculated Critical Fines Content	45
Table 3-1. Material Properties of Binary Mixtures.....	56
Table 3-2. Test Matrix for Binary Mixtures	59
Table 3-3. Calculated Critical Fines (Small Particles) Content.....	67
Table 4-1. Calculated Critical Fines Content and Critical Carbon Content.....	74
Table 4-2. Material Properties	77
Table 5-1. Material Properties	101
Table 6-1. Material Properties	123
Table 6-2. Test Matrix.....	125
Table 6-3. Empirical (Semi-empirical) Models for Thermal Conductivity of Dry Soils	131
Table 7-1. Material Properties	149
Table 7-2. Theoretical Spacing between Hematite Nanoparticles.....	157
Table 8-1. Material Properties	176
Table 8-2. Test Matrix.....	181

LIST OF FIGURES

	page
Figure 2.1. Illustration of simple cubic and cubic tetrahedral soil particle packings: the maximum size of small particles (d_s), which could be retained in the pore space between large particles with a median grain size of D , was $0.414 \cdot D$ for loose packing and $0.155 \cdot D$ for dense packing.....	10
Figure 2.2. Gravimetric-volumetric analyses of large and small materials: W = weight; V = volume; L = large particle; S = small particle; a = volume of large particles; b = volume of small particles. Note that $a \cdot e_L = b + b \cdot e_s$ at critical fines content, and the volume of small particles are considered as voids in the concept of intergranular void ratio.	12
Figure 2.3. Grain size distributions of the tested soils.	15
Figure 2.4. Setup for shear wave measurement after the method of Lee and Santamarina (2005).....	17
Figure 2.5. The variation of extreme void ratios for tested binary mixtures: (a) variation of e_{max} ; (b) variation of e_{min} ; size ratio for ASTM 20/30 with GS22 30/40 = 0.699; size ratio for ASTM 20/30 with ASTM 60/80 = 0.282; size ratio for ASTM 20/30 with ASTM 100/200 = 0.157; size ratio for ASTM 20/30 with SCS R40 = 0.014...	21
Figure 2.6. Shear wave velocity of ASTM 20/30 with GS22 30/40 according to D_r : size ratio = 0.699; applied vertical effective stress = 98.2 kPa.....	23
Figure 2.7. Shear wave velocity of ASTM 20/30 and GS22 30/40 mixture as a function of the global void ratio: (a) = vertical effective stress of 98.2 kPa; (b) = vertical effective stress of 195 kPa.	24
Figure 2.8. Shear wave velocity of ASTM 20/30 with ASTM 60/80 according to D_r : size ratio = 0.282; applied vertical effective stress = 98.2 kPa.....	26
Figure 2.9. Shear wave velocity of ASTM 20/30 with ASTM 100/200 according to D_r : size ratio = 0.157; applied vertical effective stress = 195 kPa.....	27
Figure 2.10. Shear wave velocity of ASTM 20/30 with ASTM 60/80 according to intergranular void ratio: (a) applied vertical effective stress = 98.2 kPa; (b) applied vertical effective stress = 195 kPa.....	29
Figure 2.11. Shear wave velocity of ASTM 20/30 with ASTM 100/200 according to intergranular void ratio: (a) applied vertical effective stress = 98.2 kPa; (b) applied vertical effective stress = 195 kPa.....	30

Figure 2.12. Shear wave velocity of ASTM 20/30 with Sil-Co-Sil R40 according to D_r : size ratio = 0.014; applied vertical effective stress = 98.2 kPa.	32
Figure 2.13. Shear wave velocity of ASTM 20/30 with Sil-Co-Sil R40 according to intergranular void ratio: applied vertical effective stress = 98.2 kPa.	33
Figure 2.14. α - β variations according to size ratios and fines content: (a) ASTM 20/30 with GS22 30/40 (sr = 0.699); (b) ASTM 20/30 with ASTM 60/80 (sr = 0.282); (c) ASTM 20/30 with ASTM 100/200 (sr = 0.157); (d) ASTM 20/30 with SCS R40 (sr = 0.014).	35
Figure 2.15. The relation of α - β for the tested binary mixtures (fines content < critical fines content): with increasing the fines content, the measured α -factor increased while the β -exponent decreased, indicating that the stiffness of the soil mixture decreased with the addition of fine particles.	38
Figure 2.16. Retention of small particles according to packing (sr=0.2): small particles with the size of $0.155 D_{50} < d_s < 0.414 D_{50}$ can be retained into the pore space between large particles in the case of loose packing; however, they cannot be retained in the case of dense packing leading to greater interruption of direct contacts between large particles.	40
Figure 2.17. Comparison between the stiffness of unmixed soils with global void ratio and the stiffness of binary mixtures with intergranular void ratio at $\sigma'_v = 98.3$ kPa: for comparison, the result of Robertson et al. (1996) for Ottawa sand was also plotted above; closed figures = shear wave velocity of pure materials in terms of global void ratio; open figures = shear wave velocity of mixtures in terms of intergranular void ratio.	43
Figure 2.18. Effects of size ratio and fines content on shear wave velocity at $\sigma'_v = 195$ kPa: as the fines content increased, there was an increase in the intergranular void ratio, and as the size ratio decreased, the relationship between the normalized shear wave velocity and intergranular void ratio shifted to the left.	44
Figure 3.1. Typical variation of G_{max} during loading and unloading for the model of OCR exponent estimation: σ'_i = initial effective vertical stress; σ'_{max} = maximum effective vertical stress; n_u = stress exponent during unloading; n_l = stress exponent during loading.	53
Figure 3.2. Grain size distribution of tested materials.	57
Figure 3.3. A-n variations as size ratios and fines contents during loading and unloading: (a) ASTM 20/30 with ASTM 100/200 (size ratio: 0.157); (b) ASTM 60/80 with SCS R40 (size ratio: 0.051); (c) ASTM 20/30 with SCS R40 (size ratio: 0.014).	61
Figure 3.4. Normalized G_{max} ratio as a function of size ratio: normalized G_{max} ratio = Equation (3-15); d_s/D for ASTM 20/30 with ASTM 100/200 = 0.157; d_s/D for ASTM 60/80 with SCS R40 = 0.049; d_s/D for ASTM 20/30 with SCS R40 = 0.014.	

(For comparison, data from related investigation with tests on d_s/D for ASTM 20/30 with ASTM 60/80 = 0.282 are included above.).....	64
Figure 3.5. The variation of “ n_l-n_u ” according to fines content: the mixture of ASTM 20/30 with SCS R40.	65
Figure 3.6. The variations of G_{max} ratio according to fines content: the mixture of ASTM 20/30 with SCS R40; G_{max} ratio = Equation (3-16).....	66
Figure 4.1. Typical SEM image for fly ash with unburned carbon.	72
Figure 4.2. Phase diagram for fly ash with unburned carbon particles: large particles = unburned carbon particles; small particles = aluminosilicate microspheres.....	76
Figure 4.3. Liquid limit variation with biomass content, indicating the presence of hydrophilic functional group.....	78
Figure 4.4. Setup for shear wave measurement, after the method of Lee and Santamarina (2005).....	80
Figure 4.5. G_{max} dependency on carbon content for 100 % coal fired fly ashes: unburned carbon contents (TOC) = 1.1 ~ 9.6 %	83
Figure 4.6. G_{max} dependency on biomass content: (a) CP3 samples with biomass contents ranging from 0 to 8.2 %; (b) CP4 samples with biomass contents ranging from 0 to 5.5 %; BC = biomass content; TOC = unburned carbon content. Note that CP3 samples (CP3-1, 2 and 3) were produced in the same power plant, and CP4 samples (CP4-1 and 2) were produced in the same power plant.	85
Figure 4.7. G_{max} variation as a function of effective vertical stress and interfine void ratio: G_{max} of different fly ashes can be expressed in terms of interfine void ratio regardless of fly ash fuel source.	87
Figure 4.8. Variation of volumetric strain according to vertical stress: the variation of maximum vertical strain varied with fly ash type.	88
Figure 4.9. Variation of constrained modulus with initial water content: constrained modulus decreased with increasing initial mixing water content and applied stress reflecting an increase in mass density and frictional resistance.....	89
Figure 4.10. Stress-induced small strain stiffness anisotropy during loading: variation of $G_{max}(HH) / G_{max}(VH)$ as a function of vertical stress. Note: $G_{max}(HH)$ (Equation (4-12)); $G_{max}(VH)$ (Equation (4-11)).	90
Figure 4.11. Inherent stiffness anisotropy at small strains obtained by plotting the variation of A_F and K_0 -coefficient according to unloading vertical stress: A_F (fabric anisotropy factor) = Equation (4-13); K_0 coefficient = Equation (4-14).	92

Figure 5.1. Phase diagram for fly ash with unburned carbon content.....	97
Figure 5.2. Schematic diagram of two electrically conductive spheres in contact: a = contact radius; E_g and ν_g = elastic properties of grains; R = radius of sphere; ρ = resistivity of sphere.....	99
Figure 5.3. Setup for electrical resistivity/conductivity measurement after the method of Kim et al. (2011a).....	104
Figure 5.4. Electrical conductivity of tested fly ashes according to void ratio and applied stress: (a) $\sigma_w = 0.227$ S/m; (b) $\sigma_w = 0.970$ S/m; (c) $\sigma_w = 4.295$ S/m. Note that Archie's equation ($\sigma_{mix} = n^m \cdot \sigma_w$, m was assumed as 2) was plotted under the assumption of fully-saturated condition.	107
Figure 5.5. Carbon particle conduction according to carbon content: (a) $\sigma_w = 0.970$ S/m; (b) $\sigma_w = 4.295$ S/m; applied vertical effective stress: 28 kPa; carbon particle conduction = Equation (5-15).	109
Figure 5.6. Dependency of carbon particle conduction on applied vertical stress: (a) $\sigma_w = 0.970$ S/m; (b) $\sigma_w = 4.295$ S/m.....	111
Figure 5.7. Stress dependency of different fly ashes according to carbon content: stress exponent reflects the dependency of carbon particle conduction on applied stress (Equation (5-17))......	113
Figure 5.8. Three resistances in parallel: (a) general model; (b) modified model for carbon particles; r_w = pore water resistance; r_p = particle resistance; r_s = surface resistance.....	114
Figure 5.9. Dependency of carbon particle conduction on pore water conductivity: carbon particle conduction = Equation (5-15); applied vertical effective stress = 28 kPa.	116
Figure 6.1 Setup for thermal conductivity measurement: thermal needle probe = 60 mm (height) and 1.27 mm (diameter); steel cell = 100 mm (height) and 73 mm (diameter).	125
Figure 6.2. Effect of carbon content on thermal conductivity: (a) variation according to porosity; (b) variation according to dry density; TOC = unburned carbon content; thermal conductivity = Equation (6-1).	127
Figure 6.3. Effect of biomass content on thermal conductivity: (a) variation according to porosity; (b) variation according to dry density; BC = biomass content.	129
Figure 6.4. Comparison with previous data (pure sand = Yun and Santamarina (2008); natural soil = Johansen (1975) & Smith and Byers (1938); peat = Smith and Byers (1938) & Gavriliev (2004); fly ash = Rao and Singh (1999); trend line = Johansen	

(1975)): (a) variation according to porosity; (b) variation according to dry density.	133
Figure 7.1. Two elastically dissimilar spheres in contact (Hertz contact).	139
Figure 7.2. Profile of two spheres in contact under partial slip.	143
Figure 7.3. Theoretical G_{max} estimation according to contact mode (contact model not to scale): (1) prevalent nano particle-to-nano particle contacts; (2) prevalent sand particle-to-nano particle contacts; (3) prevalent sand particle-to-sand particle contacts; G_{max} = Equation (7-30).....	147
Figure 7.4. Variation of shear wave velocity according to applied vertical stress: iron contents (mg_Fe / g_sand) for hematite coated 20/30 = 0.43; for goethite coated 20/30 = 0.13; hematite coated graded = 1.22; hematite coated 100/200 = 6.35; goethite coated 100/200 = 0.62.	152
Figure 7.5. Variation of shear wave velocity ratio according to applied vertical stress: initial D_r of loose packing = 30~ 35 %; initial D_r of dense packing = 70~80 %; closed figures = loose packing; open figures = dense packing.	154
Figure 7.6. Hertzian contact area of ASTM 100/200: SEM = hematite coated 100/200 (size of hematite particle \approx 140 nm); Hertz contact radius = Equation (7-29) at P (isotropic confining pressure) = 12 kPa (low confinement) and 400 kPa (high confinement) and e (void ratio) = 0.6 (dense packing) and 0.8 (loose packing). ...	156
Figure 7.7. Hertzian contact area of ASTM 20/30: SEM = hematite coated 20/30 (size of hematite particle \approx 140 nm); Hertz contact radius = Equation (29) at P (isotropic confining pressure) = 12 kPa (low confinement) and e (void ratio) = 0.6 (dense packing).	159
Figure 7.8. Variation of shear wave velocity ratio according to relative roughness: relative roughness = d/D ; d = diameter of hematite particles; D = diameter of substrate sand particles; initial relative density = 30 ~ 80 %; applied vertical stress = 25.6 ~ 388.6 kPa.	161
Figure 7.9. Comparison of measured G_{max} ratio with theoretical G_{max} ratio according to contact mode: G_{max} ratio = the ratio of G_{max} of hematite coated soil to G_{max} of uncoated soil; theoretical G_{max} ratio = Figure 7.3; closed figures = loose packing; open figures = dense packing.	163
Figure 8.1. Model for electronic transport phenomena in a porous media: A = total area; A_w = area of water; L = total length; L_e = length of flow path for water.	169
Figure 8.2. Simple conductivity model for a porous media: t_p = thickness of particle; t_w = thickness of water.	173

Figure 8.3. Setup for electrical conductivity/resistivity measurement after the method of Kim et al. (2011a).....	177
Figure 8.4. Typical arrangement of 4 electrodes: A and M = current electrodes; M and N = potential electrodes.	178
Figure 8.5. Calibration of resistivity probe with electrolytes: the slope K indicates the geometrical factor in Equation (8-24); resistance was measured by LCR meter; resistivity was measured by conductivity meter.	179
Figure 8.6. Electrical conductivity/resistivity variation of hematite coated and uncoated ASTM 60/80 sands according to porosity: pore water conductivity = 0.226 S/m; initial relative density = 30 ~ 70 %.	182
Figure 8.7. Conductivity of porous media according to pore water conductivity (hematite coated and uncoated ASTM 20/30 sands).	184
Figure 8.8. Zeta potential of hematite coated and uncoated kaolinite as a function of pH.	186
Figure 8.9. Electrical conductivity/resistivity variation of hematite coated and uncoated Kaolinites according to porosity: (a) pore water conductivity = $3.64 \cdot 10^{-2}$ S/m; (b) pore water conductivity = 1.026 S/m.	187
Figure 8.10. Estimated specific surface based on median grain size and uniformity coefficient: specific surface = Equation (8-27).	189
Figure 8.11. Comparison of mixed conductivity with pore water conduction under the various pore water conductivity and specific surface: (a) $\sigma_w = 1 \cdot 10^{-3}$ S/m; (b) $\sigma_w = 5 \cdot 10^{-2}$ S/m; (c) $\sigma_w = 5 \cdot 10^{-1}$ S/m; (d) $\sigma_w = 5$ S/m; mixed conductivity (solid line) = Equation (8-13); pore water conduction (dotted line) = Equation (8-14).....	190
Figure 8.12. Back-calculation of surface conductivity from the relation between the mixed conductivity and pore water conductivity: surface conductivity = Equation (8-29) under the assumption of constant surface conductivity.....	193

LIST OF SYMBOLS

α	fitting parameter (initial value) for shear wave velocity and particle conduction
β	fitting parameter (stress dependency) for shear wave velocity and particle conduction
γ_d	dry density
δ	interference (or remote displacement)
μ	coefficient of friction
ν_g	grain Poisson's ratio
ρ	mass density or electrical resistivity
ρ_s	total net charge density
ρ_0	structural surface charge density
ρ_H	proton surface charge density
ρ_{IP}	surface charge density of inner part
ρ_{OP}	surface charge density of outer part
ρ_w	mass density of water
σ_0	peak normal stress
σ'_0	mean effective stress
σ'_h	horizontal effective stress
σ'_v	vertical effective stress
σ_{mix}	electrical conductivity of the media (or mixture)
σ_p	electrical conductivity of the particles
σ_{cp}	corrected particle conductivity

σ_w	electrical conductivity of the pore water
σ_s	surface conductivity
φ	friction angle
A	G_{\max} at 1 kPa
A_F	fabric (or inherent) anisotropy factor
a	radius of the circular contact area of two spheres
a	volume of large particles
b	volume of small particles
C & K	calibration factor
C_N	coordination number
C_u	uniformity coefficient
D_r	relative density
d_s	size of small particles
D	size of large particles
D_{50}	median grain size
E^*	equivalent elastic modulus
e	void ratio
e_f	interfine void ratio
e_g	intergranular void ratio
e_L	void ratio of large particles
e_S	void ratio of small particles
e_{\max}	maximum void ratio
e_{\min}	minimum void ratio

F_N	normal force
F_T	tangential force
G	electrical conductance
G_g	grain shear modulus
G_{max}	maximum shear modulus
G_s	specific gravity
G_{sL}	specific gravity of large particle
G_{sS}	specific gravity of fine particles
K_0	coefficient of earth pressure at rest
K_p	particle conduction
K_{cp}	corrected carbon particle conduction
K_s	surface conduction
K_w	pore water conduction
k_t	thermal conductivity
L	total length
L_e	length of flow path for water
L_p	length of flow path for particles
n	porosity or G_{max} formula stress exponent
n_l	stress exponent during loading
n_u	stress exponent during unloading
P	isotropic pressure
Q	power
R	radius of particles

R^*	equivalent radius
r	electrical resistance
S	slope obtained from regressing ΔT on $\ln(t)$
S_a	mass-based specific surface
S_p	pore volume-based specific surface
S_v	solid volume-based specific surface
S_N	normal stiffness
S_T	tangential stiffness
T	tortuosity
t_p	thickness of particle
t_w	thickness of water
u_{IP}	ion mobility in the inner part
u_{OP}	ion mobility in the diffuse part
u_z	normal displacement
W	weight or water content
W_s	weight of fine particles
W_L	weight of large particles
V_s	shear wave velocity
V_V	volume of voids
V_S	volume of small particles
V_L	volume of large particles
V_T	total volume

LIST OF ABBREVIATIONS

BC	biomass content
DCB technique	dithionite-citrate-bicarbonate technique
EC	electrical conductivity
EM	electrophoretic mobility
FC	finer (small particles) content
FC*	critical finer content
ICP-OES	inductively coupled plasma – optical emission spectrometry
IEP	isoelectric charge point
LL	liquid limit
LOI	loss on ignition
OCR	overconsolidation ratio
PZC	point of zero charge
sr	size ratio (d_s/D)
TOC	unburned organic carbon content
TOC*	critical carbon content
ZP	zeta potential

SUMMARY

Natural geomaterials exhibit a wide range in size, physical properties, chemical properties, and mechanical behaviors. Soils that are composed of mixtures of particles with different physical and chemical properties pose a challenge to characterization and quantification of the engineering properties. This study examined the behavior of particulate mixtures composed of differently sized silica particles, mixtures composed of aluminosilicate and organic carbon particles, and mixtures composed of particles with approximately three orders of magnitude difference in particle size. This experimental investigation used elastic, electromagnetic, and thermal waves to characterize and to quantify the small to intermediate strain behavior of the mixtures.

The mechanical property of stiffness of mixed materials (e.g. binary mixtures of silica particles and fly ashes with various carbon and biomass contents) was evaluated through the stiffness of active grain contacts, and the stiffness of particles which carry applied load, using the physical concepts of intergranular void ratio and interfine void ratio. Additionally, the change in both contact mode/stiffness and electrical property due to the presence of nano-sized particles (i.e., iron oxides) on the surface of soil grains was evaluated according to applied stress, packing density, iron coating density, and substrate sand particle size. Finally, the biomass fraction and total organic carbon content of mixtures was used to quantify the electrical and thermal conductivities when particulate organic was mixed with aluminosilicate particles.

CHAPTER 1 INTRODUCTION

Natural geomaterials exhibit a wide range in size, physical properties, chemical properties, and mechanical behaviors. Soils that are composed of mixtures of particles with different physical and chemical properties pose a challenge to characterization and quantification of their engineering properties. The engineering behaviors of original host soils can be significantly changed by the properties and content of added materials, while, in some conditions, the behaviors of mixed materials can be comparable to those of host materials. Thus, the identification of properties of mixed materials for the design and analysis of geotechnical structure and soil-structure interaction is one of the most important tasks in geotechnical engineering. However, studies on the behaviors of mixtures of soil particles with various properties remained relatively limited due to, at least in part, the complexity of the structure and interaction between different particles despite the fact that knowledge of those mixed materials is a necessary prerequisite for the fundamental understanding of the behavior of a large of soils.

Geophysical properties, especially elastic shear wave velocity, electrical conductivity/resistivity, and thermal conductivity, strongly reflect the physical and geotechnical properties of soils (McDowell et al. 2002). This study examined the behavior of particulate mixtures composed of differently sized silica particles, mixtures composed of aluminosilicate and organic carbon particles, and mixtures composed of particles with approximately three orders of magnitude difference in particle size through the use of three geophysical testing methods (i.e., elastic, electromagnetic, and thermal waves). The stiffness of the mixed materials (e.g., binary mixtures of silica particles and fly ashes with various carbon and biomass

contents) was evaluated by the stiffness of active grain contacts, indicating the stiffness of particles which carry applied load, through the physical concepts of intergranular void ratio and interfine void ratio. Additionally, the change in both contact mode/stiffness and electrical properties due to the presence of nano-sized particles (i.e. iron oxides) on the surface of soil grains was evaluated according to applied stress, packing density, iron coating density, and substrate sand particle size. Finally, the biomass fraction and total organic carbon content of mixtures was used to quantify the electrical and thermal conductivities when the particulate organic was mixed with aluminosilicate particles.

Elastic shear wave velocity measurements were conducted by employing bender element tests, electrical conductivity/resistivity measurements were conducted using electromagnetic waves and were measured by employing a four-electrode resistivity probe, and thermal conductivity measurements (one property of thermal waves) were measured by employing a thermal needle probe. The shear wave velocity measurements, electrical conductivity measurements, and thermal conductivity measurements were small-perturbation, non-destructive soil testing methods leading to the determination of reliable constant fabric properties of soils without disturbance (Benson 2000; Santamarina et al. 2001). In addition, the shear wave velocity (or small strain stiffness), electrical conductivity, and thermal conductivity strongly reflect the physicochemical properties of soils, leading to insight into the nature of soil mixtures. A summary of the research focus for each chapter is given below.

1.1 Thesis Organization

This study focuses on finding the physical and chemical mechanisms behind the behaviors of a variety of mixed materials, based on particulate level simplification

of complex structure or complex interaction between particles with a range of physical and chemical properties. This study combined a series of experimental investigations with a theoretical framework to examine the fundamental mechanisms governing the behavior of mixed materials. Consequently, the key variables determining the behaviors of mixed materials were carefully selected and controlled to see the change of geophysical properties of mixed materials according to the change of key variables.

Chapter 2 quantified the dynamic properties of binary mixtures, including sand-sand mixtures with different particle sizes, and silty sand mixtures with small quantities of fines (up to critical fines content). By performing bender element tests on those mixtures, the variation of shear wave velocity values according to fines content, size ratios, and relative densities were evaluated. The intergranular void ratio, e_g , was employed as an indicator of mechanical properties of binary mixtures, instead of the global void ratio. Most notably, shear wave velocity of binary mixtures can be expressed in terms of intergranular void ratio, regardless of fines content at low fines content ($FC < FC^*$).

Chapter 3 focused on the stress-history-based dynamic properties of binary mixtures such as sand-sand mixtures with different sizes, and silty sand with non-plastic fines up to critical fines content. By performing bender element tests on those mixtures as a function of fines content, size ratio, and overconsolidation ratio, the stress-history-based G_{max} of binary mixtures was evaluated. For the relevant data analysis, the OCR exponent in the G_{max} formulation was expressed in terms of stress exponents during loading and unloading in this study.

Chapter 4 investigated the small to intermediate strain properties of fly ash. Stricter regulation of air emissions from coal fired power plants, coupled with the

addition of biomass as a co-fired source of energy, have resulted in fly ashes with relatively high carbon content. High carbon content fly ashes are typically landfilled unless another beneficial application can be found. Consequently, this study evaluated the suitability of fly ashes with various carbon and biomass contents in terms of small to intermediate strain geotechnical properties. The interfine void ratio, e_f , was employed instead of global void ratio to capture the alteration of interparticle contact or interparticle coordination between microspheres due to the change in carbon and biomass contents.

Chapter 5 investigated the impact of unburned carbon particles on the electrical conductivity of fly ash slurries. Because ASTM C618 prohibits the use of fly ash with carbon content greater than 6 % in concrete or cement, estimation of the in-situ unburned carbon content of fly/pond ash poses an important challenge. Additionally, with the recent stability issues in ash ponds, estimation of in situ void ratio or water content of ash is also critical to field performance of these ponds. Therefore, in this study, the efforts were directed toward determining the in-situ carbon content and void ratio of fly ash using electrical conductivity/resistivity measurements. Because unburned carbon particles are electrically conductive, the resulting media conductivity will be a function of carbon content, and electrical conductivity methods allowed determination of the carbon content of fly ash, coupled with void ratio or water content of the soil matrix.

Chapter 6 quantified the thermal conductivity of dry fly ashes. The studies on recent fly ashes with high contents of carbon and biomass particles in terms of mechanical and chemical aspects were relatively well developed; however, the thermal characterization of those fly ashes was limited. Consequently, this study evaluated the thermal conductivities of fly ashes with various carbon and biomass

contents to quantify the effect of unburned carbon particles and biomass fired fly ash on the rate of heat transfer of fly ash. The thermal needle probe method was employed in this study.

Chapter 7 focused on the effect of nano-sized particles on the alteration of contacts and, correspondingly, stiffness between sand particles. The presence of nano-sized particles can dramatically alter the physical and chemical properties of natural soils due to their small particle diameter (typically smaller than 100 nm) and correspondingly high specific surface. In addition, the mechanical properties of soils may also be changed due to the presence of nano-sized particles due to their impact on the contacts between particles. Therefore, this study assessed the change in stiffness at very small strain due to the presence of iron oxides (i.e., hematite and goethite), particularly focusing on the change in contact mode between particles. The iron oxide coating density of coated sands was controlled by changing the substrate sand particle size ranging from 0.11 to 0.72 mm, with corresponding iron contents ranging from 0.13 mg iron oxide/g sand (goethite) to 6.4 mg iron oxide/g sand (hematite).

Chapter 8 verified Archie's equation and quantified the electrical conductivity of uncoated and hematite coated soils. Electrical conductivity/resistivity measurement is one of the most widely used testing methods for subsurface exploration, with analysis typically performed using the work of Archie. Archie's equation is attractive due to its simplicity; however, it is empirical, and may not be applicable for fine grained soils, even though most coarse grained geomaterials, such as sands, gravels, and marine sediments, obey Archie's equation. This work developed a clear theoretical background for Archie's equation, and defined a clear boundary for the applicability of Archie's equation for a variety of soil types of and water chemistries.

In addition, this study also performed an experimental investigation to examine the electrical properties of uncoated and laboratory-prepared iron oxide (hematite) coated sands and clay, in order to evaluate the role of hematite adsorbed onto soil surfaces on the measured electrical conductivity/resistivity of the particulate mixture.

CHAPTER 2 SHEAR WAVE VELOCITY OF BINARY MIXTURES OF SILICA PARTICLES AS A FUNCTION OF FINES FRACTION, SIZE RATIOS AND RELATIVE DENSITIES

2.1 Introduction

Most natural sand deposits are actually a mixture of sand particles and varying quantities of fine grained soil particles (Carraro et al. 2009; Georgiannou et al. 1990; Iwasaki and Tatsuoka 1977; Salgado et al. 2000; Thevanayagam et al. 2002; Yang et al. 2006). Traditionally, studies to investigate the mechanical behaviors of sand deposits have been performed using clean sands, with the impact of fine grained particles on the behavior of sand deposits being studied more recently. Among the engineering properties, the liquefaction potential of sands with fines content (e.g. silt) has been widely studied, with some investigations reporting that liquefaction potential increases with increasing fines content (Chien et al. 2002; Georgiannou et al. 1990; Lade and Yamamuro 1997), but the others showing that it decreases with increasing fines content (Robertson and Campanella 1985; Salgado et al. 2000; Seed et al. 1983). These debatable results, reflecting the difficulty in the interpretation of behaviors of mixtures in terms of fines content, may be attributed to the difference in sample preparation method, testing condition (density and stress), as well as type and content of fines (plasticity).

A new look to the interpretation of mechanical behaviors of sands with fines, focusing on the effect of intergranular void ratio instead of the effect of fines content, on the behaviors of mixtures, has been developed (Carraro et al. 2003; Polito and Martin 2001; Thevanayagam 1998; Thevanayagam et al. 2002; Yang et al. 2006). In

this concept of intergranular void ratio, it was assumed that, at low fines content (fines content, $FC < \text{critical fines content, } FC^*$), smaller particles were generally retained in the pores of large particles, and did not participate in the load-carrying chain. Because the applied stress will be transferred through the contacts of large particles, the influence of fines (small particles) on the mechanical behavior of binary mixtures will be negligible. Consequently, several researchers treated the fines as void space, despite the increase in mass density achieved by adding smaller particles to the host sand. As a result, those previous studies that quantify cyclic stress ratio (CSR) and undrained strength of binary mixtures (e.g., silty sand) frequently report the mechanical behavior of binary mixtures as a function of intergranular void ratio, rather than the fines content or global void ratio.

In terms of dynamic properties, the maximum shear modulus (G_{\max}) gives insight into the deformation characteristics of soils, controls the shear wave velocity (V_s) of soil deposits, and is often a required parameter in design and analysis of soils and soil-structure interactions (Tatsuoka and Shibuya 1991). At very small strains (i.e., less than 0.001 %), the shear modulus is independent of strain amplitude and exhibits its maximum magnitude. Additionally, shear wave velocity is frequently used to define the state of soils, since it can be easily measured in the field as well as in the laboratory (Robertson et al. 1995), and can be used to quantify the stiffness of soils. In terms of shear wave velocity or maximum shear modulus, it is generally accepted that shear wave velocity (or maximum shear modulus) decreases with increasing non-plastic fines content (Andrus and Stokoe 2000; Huang et al. 2004; Iwasaki and Tatsuoka 1977; Liu and Mitchell 2006; Randolph et al. 1994; Salgado et al. 2000); however, only limited studies have systematically characterized the effect of fines content and size ratios on the alteration of shear wave velocity or small strain stiffness

of binary mixtures.

The present investigation quantifies the effect of fines content, size ratios between small and large particles, and relative densities on the shear wave velocity values of binary mixtures of silica particles such as sand-sand mixtures of two different sizes or silty sands containing small quantities of fines (~15%). Theoretical analysis of the behavior of binary mixtures was performed using the soil parameters of critical fines content and intergranular void ratio, because the classical geotechnical parameter of global void ratio was not suitable to describe the behaviors of binary mixtures. The experimental investigation performed 112 bender element tests that were analyzed according to fines content, size ratio, and packing density; however, the effect of plasticity on the binary mixtures was not considered.

2.2 Theoretical Aspects of Binary Mixture

2.2.1 Pore Size

The propagation of waves through a particulate medium is dependent on packing arrangement and packing density. Consequently, a theoretical analysis of packing of binary mixtures of particles was performed.

Spherical particles can be uniformly packed in arrangements with void ratios that range from 0.35 – 0.91. Examination of the simple cubic packing (loose packing condition) and the cubic tetrahedral packing (dense packing condition) demonstrates that the maximum size of small particles (d_s), which could be retained in the pore space between larger particles with a median grain size of D , was $0.414 \cdot D$ for loose packing and $0.155 \cdot D$ for dense packing (Figure 2.1) (Jang 2011; Santamarina et al. 2001). Consequently, in order to ensure the case of fine particles retained within the

pore space of large particles, the size ratio of the fine grained particle to the coarse grained particle (d_s/D) should be less than 0.155.

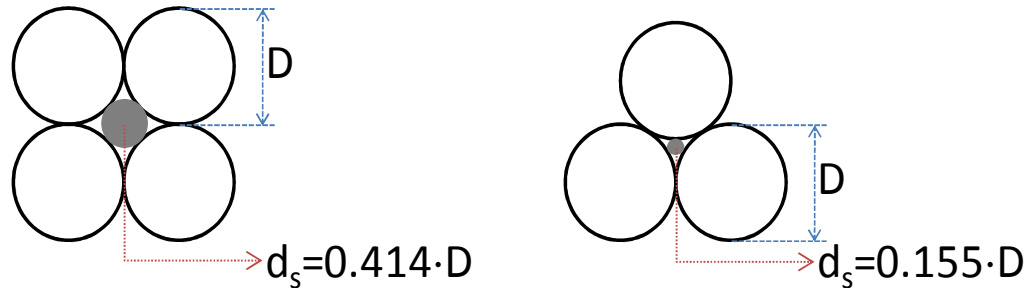


Figure 2.1. Illustration of simple cubic and cubic tetrahedral soil particle packings: the maximum size of small particles (d_s), which could be retained in the pore space between large particles with a median grain size of D , was $0.414 \cdot D$ for loose packing and $0.155 \cdot D$ for dense packing.

2.2.2 Critical Fines (Small Particles) Content

The critical fines (small particles) content is defined as the ratio of the weight of fine particles to the weight of the total mixture when the voids between large particles are fully filled with fine particles (Lade et al. 1998). Consequently, the following relation can be established for the condition of critical fines content (Figure 2.2):

$$a \cdot e_L = b \cdot (1 + e_s) \quad (2-1)$$

where, a is volume of large particles; b is volume of small particles, e_L is the void ratio of large particles, and e_s is the void ratio of small particles.

The fines content can be defined according to:

$$FC = \frac{w_S}{w_L + w_S} = \frac{b \cdot G_{sS} \cdot \gamma_w}{a \cdot G_{sL} \cdot \gamma_w + b \cdot G_{sS} \cdot \gamma_w} = \frac{b \cdot G_{sS}}{a \cdot G_{sL} + b \cdot G_{sS}} \quad (2-2)$$

where, W_S : weight of small particles; W_L : weight of large particles; G_{sL} : specific gravity of large particle; G_{sS} : specific gravity of small particles. By combining equations (2-1) and (2-2), results in the determination for the critical fines content of a binary mixture according to:

$$FC^* = \frac{G_{sS} \cdot e_L}{G_{sL}(1 + e_S) + G_{sS} \cdot e_L} \quad (2-3)$$

where, FC^* : critical fines (small particles) content.

Note that Equation (2-3) is the same relationship that Yang et al. (2006) suggested to determine the transitional fines content. Consequently, the critical fines content, transitional fines content, or limiting fines content (Polito and Martin 2001) describe essentially same conditions. Additionally, Thevanayagam et al. (2002) defined the critical fines content as the fines content when the interfine void ratio, e_f , decreased below the maximum void ratio of fines, with e_f defined as the ratio of global void ratio, e , to FC (Thevanayagam 1998).

Assuming the specific gravities of mixture particles are the same, (2-3) can be further simplified to:

$$FC^* \approx \frac{e_L}{1 + e_S + e_L} \quad (2-4)$$

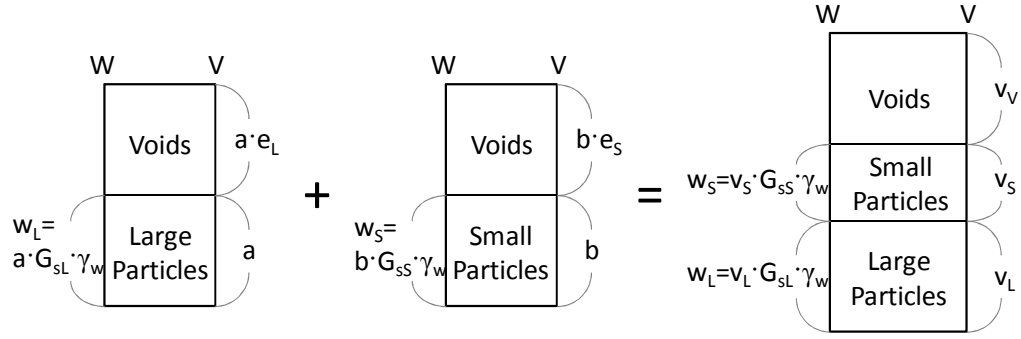


Figure 2.2. Gravimetric-volumetric analyses of large and small materials: W = weight; V = volume; L = large particle; S = small particle; a = volume of large particles; b = volume of small particles. Note that $a \cdot e_L = b + b \cdot e_s$ at critical fines content, and the volume of small particles are considered as voids in the concept of intergranular void ratio.

2.2.3 Intergranular Void Ratio

Application of a global void ratio to binary mixtures containing both large and small particles is limited because the global void ratio does not capture the mechanical behavior of coarse grained soils with smaller particles that are located in pore space between the larger particles. In this type of packing arrangement, it can be assumed that the fine-grained (small) particles do not participate in the load-carrying force chains. Consequently, a number of researchers introduced the concept of the intergranular void ratio, instead of global void ratio, to describe the behaviors of mixed materials such as silty sand (Georgiannou et al. 1990; Kuerbis and Vaid 1988; Thevanayagam 1998), where small particles are considered as voids when their content is low ($FC < FC^*$), resulting in (Figure 2.2):

$$e_g = \frac{v_V + v_S}{v_L} = \frac{v_T - v_L}{v_L} = \frac{v_T}{v_L} - 1 \quad (2-5)$$

where, V_V : volume of voids; V_S : volume of small particles; V_L : volume of large

particles; V_T : total volume

Additionally, the following equation can be made from Figure 2.2:

$$v_L = \frac{w_L}{G_{sL} \cdot \gamma_w} = \frac{w_T - w_S}{G_{sL} \cdot \gamma_w} \quad (2-6)$$

Combining (2-5) and (2-6) will yield:

$$e_g = \frac{G_{sL} \cdot \gamma_w \cdot v_T}{w_T - w_S} - 1 \quad (2-7)$$

Above Equation (2-7) is the same relation suggested by Kuerbis and Vaid (1988). And

total volume, V_T can be expressed as:

$$v_T = (1 + e) \cdot (v_L + v_S) \quad (2-8)$$

By substituting (2-2) and (2-8) into (2-7):

$$e_g = \frac{G_{sL} \cdot \gamma_w \cdot \frac{(1+e)(v_L + v_S)}{w_T} - 1 + FC}{1 - FC} = \frac{(1+e) \cdot \left(1 - FC + \frac{G_{sL}}{G_{sS}}\right) - 1 + FC}{1 - FC} \quad (2-9)$$

By simplification, (2-9) becomes:

$$e_g = \frac{e \cdot \left[FC \cdot \left(\frac{G_{sL}}{G_{sS}} - 1 \right) + 1 \right] + \frac{G_{sL}}{G_{sS}} \cdot FC}{1 - FC} \quad (2-10)$$

If the specific gravities of mixtures are the same, the equation can be further simplified to have the same form of Thevanayagam (1998):

$$e_g \approx \frac{e + FC}{1 - FC} \quad (2-11)$$

2.3 Experimental Program

2.3.1 Materials

ASTM 20/30 sand was chosen for use as the large particles for the binary mixtures and smaller particles were subsequently added to the ASTM 20/30 sand according to the selected size ratios ($\frac{d_s}{D_{50}}$) and fines (small particles) content. In all experiments performed in this study, the terminology large particles will be used to denote ASTM 20/30 sand, and the added materials will be denoted as small particles or fines, even though median grain sizes of the materials may be greater than 0.075 mm.

All soils were received from U.S. Silica Company, and were composed primarily of silicon dioxide (99.8%), with other trace materials, such as iron oxide or aluminum oxide composing approximately 0.2% of the mineralogy. The grain size distributions of the soil samples were obtained according to ASTM D422, and the limiting void ratios of the samples were determined according to ASTM D4253 and ASTM D4254. Measured properties of the soils used in the experimental investigation are given in Table 2-1 and Figure 2.3.

Table 2-1. Material Properties of Binary Soil Mixtures

Properties	ASTM 20/30	GS22 30/40	ASTM 60/80	ASTM 100/200	Sil-Co-Sil R40
D ₅₀ (mm)	0.72	0.503	0.203	0.113	0.010
Size Ratio (d _s / D)	-	0.699	0.282	0.157	0.014
G _s	2.65	2.65	2.65	2.65	2.65
e _{max}	0.742	0.949	0.912	0.879	1.81
e _{min}	0.502	0.689	0.584	0.560	0.64

Note: D₅₀ = median grain size; G_s = specific gravity

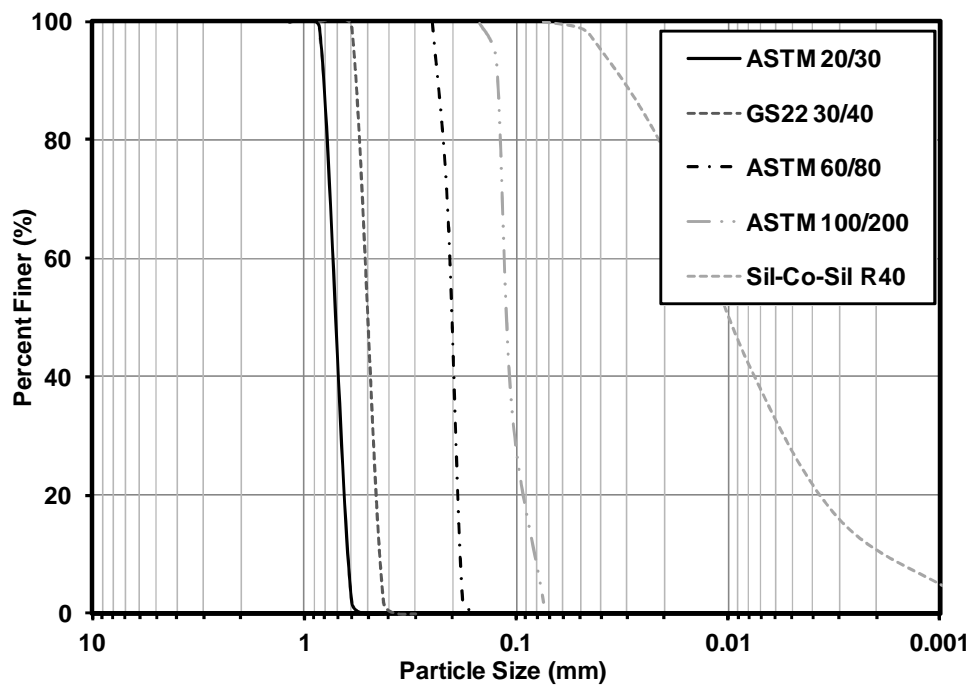


Figure 2.3. Grain size distributions of the tested soils.

2.3.2 Shear Wave Velocity Measurements

The shear wave velocity of each mixture was measured using bender elements fitted inside a modified oedometer cell, which allowed measurement of the shear

wave velocity as a function of increasing consolidation stress (after the method of Lee and Santamarina (2005)) (Figure 2.4). Prepared samples were tested in the K_0 condition under vertical stresses ranging from 13.5 kPa to 388.6 kPa, with shear wave velocity measured at the end of each load step. The shear wave, which traveled through the soil specimen, was generated by a function generator (33210A, Agilent), with a square wave of frequency = 20 Hz and amplitude =10 V, which was connected to the source bender element. The bender element that acted as the signal receiver was connected to a filter amplifier (3364, Krohn-Hite), which in turn was connected to a digital oscilloscope (DSO5014A, Agilent). A total of 1024 signals were stacked to reduce the influence of uncorrelated noise. Travel time of the shear wave was determined using the digitized signal, as recorded by the oscilloscope (Lee and Santamarina 2005), and the tip-to-tip distance (the distance from the tip of the source bender to the tip of the receiver bender element) was used as the travel distance (Fernandez 2000; Lee and Santamarina 2005).

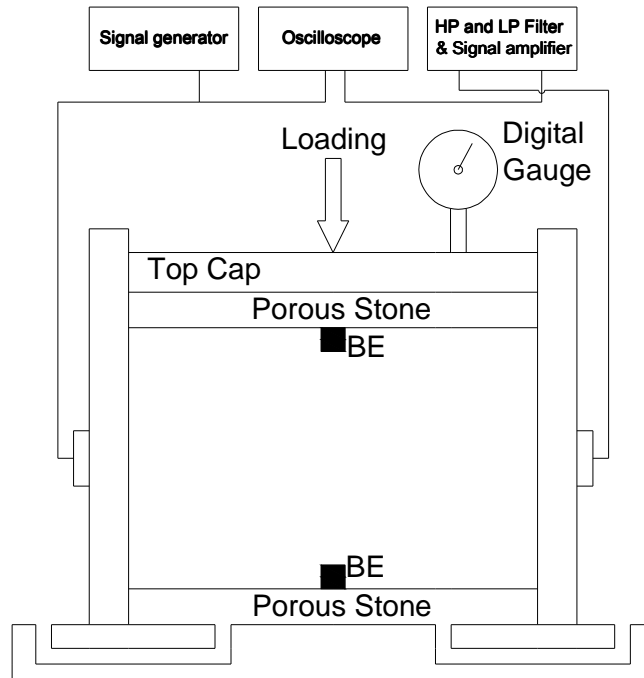


Figure 2.4. Setup for shear wave measurement after the method of Lee and Santamarina (2005).

2.3.3 Sample Preparation and Testing Program

Varying test results for binary mixtures, such as silty sand, have been obtained depending on the method of sample preparation employed, even when all other test conditions were held constant (Yamamuro and Wood 2004). Additionally, water sedimentation of particle mixtures has been shown to yield segregation between the large and small particles (Lade and Yamamuro 1997; Vaid et al. 1990). However, specimen preparation using dry funnel deposition with close to zero falling height has been widely used to produce relatively uniform specimens with good mixing of large and small particles (Ishihara 1993; Lade and Yamamuro 1997; Yamamuro and Lade 1997). Dry funnel deposition has the added advantage of producing a wide range of relative densities of the resulting mixtures.

ASTM 20/30 sand was used as the large particle host material, and smaller

particles (GS22 30/40, ASTM 60/80, ASTM 100/200, and Sil-Co-Sil R40) were added to ASTM 20/30 sand according to chosen size ratios and fines contents. Initial relative densities of the mixtures ranged from 20% to 80%, and the maximum fines contents were selected based on the critical fines content of each mixture. Tests were conducted in dry conditions. A total 112 bender element tests were performed to elucidate the effects of size ratio, relative density, and fines content on the shear wave velocity of the binary mixtures (Table 2-2).

Table 2-2. Experimental Matrix for Bender Element Testing

Type	Host material	Added Materials			
	ASTM 20/30	GS22 30/40	ASTM 60/80	ASTM 100/200	Sil-Co-Sil R40
Size Ratio (d_s/D)	-	0.699	0.282	0.157	0.014
Initial D_r	30, 50, 70 %	30, 50, 70 %	20 ~ 80 %	20 ~ 80 %	20 ~ 80 %
Fines Contents	-	20%	1%	1%	1%
	-	40%	5%	5%	5%
	-	60%	10%	10%	10%
	-	80%	20%	20%	15%
	-	100%	40%	40%	100%
	-	-	100%	100%	-

Note: size ratio = d_s (size of small particles) / D (size of large particles); D_r = relative density

2.4 Results and Analysis

ASTM 20/30 sand was mixed with four finer grained soils that were chosen to study three different mixing conditions: 1) GS22 30/40 mixture ($d_s > 0.414 \cdot D_{50}$ of

ASTM 20/30, small particles cannot be retained in the pores between larger particles); 2) ASTM 60/80 and ASTM 100/200 ($0.414 \cdot D_{50} > d_s > 0.155 \cdot D_{50}$ of ASTM 20/30, small particles retained in pore space between larger particles only in loose packing at low fines content, less than the critical fines content); and 3) Sil-Co-Sil R40 ($d_s \ll 0.155 \cdot D_{50}$, small particles retained in pore space between large grains, regardless of packing densities).

2.4.1 The Variation of Extreme Void Ratio

The limiting void ratios of the binary mixtures decreased with increasing fines (small particles) content until the pore space between the larger particles was completely filled with small particles. This condition coincided with the critical fines content. However, at fines contents larger than the critical fines content, larger particles were dispersed in a fines matrix and the void ratio increased as fines content increased. Further increases in the fines content approached the extreme void ratio of the added materials (Figure 2.5). The void ratio reduction observed below the critical fines content was impacted by multiple factors including size ratio, uniformity, surface roughness, and particle shape (Bowles 1979; Lade and Yamamuro 1997; Vallejo 2001). It is well known that uniformity, surface roughness, and particle shape determine the extreme void ratios of the host and added materials (Cho et al. 2006; Mitchell and Soga 2005; Youd 1973); consequently, the, size ratio and extreme void ratios of original soils will be the primary factors determining void ratio reduction of binary mixtures. The effect of these two factors on void ratio reduction was observed through the following: 1) the mixture with GS22 30/40 (size ratio ~ 0.7) resulted in void ratios that were linearly shifted from those of 20/30 sand to those of 30/40 sand, according to the mass content of small particles because small particles could not be

retained between large particles; 2) the extreme void ratios of ASTM 60/80 and ASTM 100/200 showed very similar numbers; consequently, the mixture with ASTM 100/200 showed greater void ratio (both e_{\max} and e_{\min}) reductions than those of the mixture with ASTM 60/80 due to the smaller size ratio (or greater size difference) because the fines could be more easily located in the voids of large particles, with an increase in size difference (Lade and Yamamuro 1997); and 3) the minimum void ratio of SCS R40 was comparable with those of other added materials, leading to the greatest void ratio (e_{\min}) reduction of the mixture with SCS R40 at a given fines content due to the much smaller size ratio; however, the maximum void ratio of SCS R40 was much greater than those of other added materials leading to limited void ratio (e_{\max}) reduction of the mixture with SCS R40 in spite of very small size ratio.

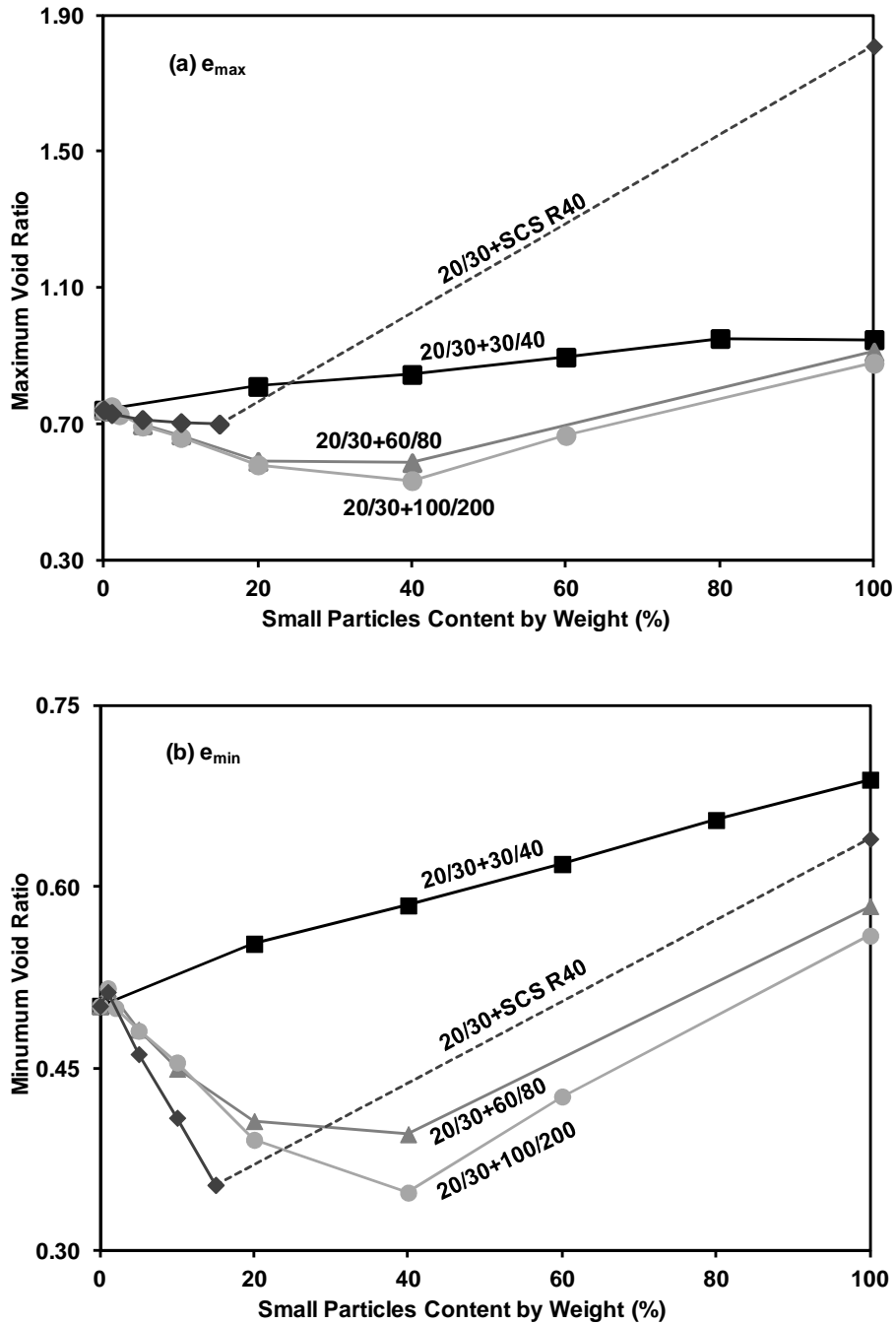


Figure 2.5. The variation of extreme void ratios for tested binary mixtures: (a) variation of e_{max} ; (b) variation of e_{min} ; size ratio for ASTM 20/30 with GS22 30/40 = 0.699; size ratio for ASTM 20/30 with ASTM 60/80 = 0.282; size ratio for ASTM 20/30 with ASTM 100/200 = 0.157; size ratio for ASTM 20/30 with SCS R40 = 0.014.

2.4.2 Shear Wave Velocity

A number of researcher expressed the G_{\max} or V_s estimating formulas including the function of void ratio to consider V_s or G_{\max} dependency on relative density (D_r) or void ratio (e) (DeAlba et al. 1984; Hardin and Richart 1963; Iwasaki and Tatsuoka 1977; Lo Presti et al. 1997), and following the expression of Hardin and Richart (1963) based on resonant column test results yield:

$$V_s = (m_1 - m_2 \cdot e) \cdot \left(\frac{\sigma'_0}{P_a} \right)^n \quad (2-12)$$

where, e = void ratio, m_1 and m_2 are material constants, P_a = atmospheric pressure (100 kPa), and $n \approx 0.25$, typically. Equation (2-12) clearly demonstrated that the shear wave velocity increases with a decrease in void ratio or with an increase in relative density due to the increase in interparticle coordination.

2.4.2.1 ASTM 20/30 with GS22 30/40

The mixture of ASTM 20/30 with GS22 30/40 was prepared to study the case of d_s greater than $0.414 \cdot D_{50}$ of ASTM 20/30, with no possibility of retaining of small particles to the pores between larger particles, as reflected in the variation of extreme void ratio (Figure 2.5). Comparison of the shear wave velocity of this mixture at fines content of 20%, 40%, 60%, and 80% indicated values of shear wave velocity increased relative to clean ASTM 20/30 or GS22 30/40 at fines content of 40 or 60 %, but were similar to the values for clean sands at fines contents of 20% and 80%. This increase is attributable to the increased coordination number that occurred as the soil matrix transitioned from large particle dominated to small particle dominated. Additionally, the shear wave velocity of all mixed materials increased with an increase in relative density reflecting an increase in interparticle coordination.

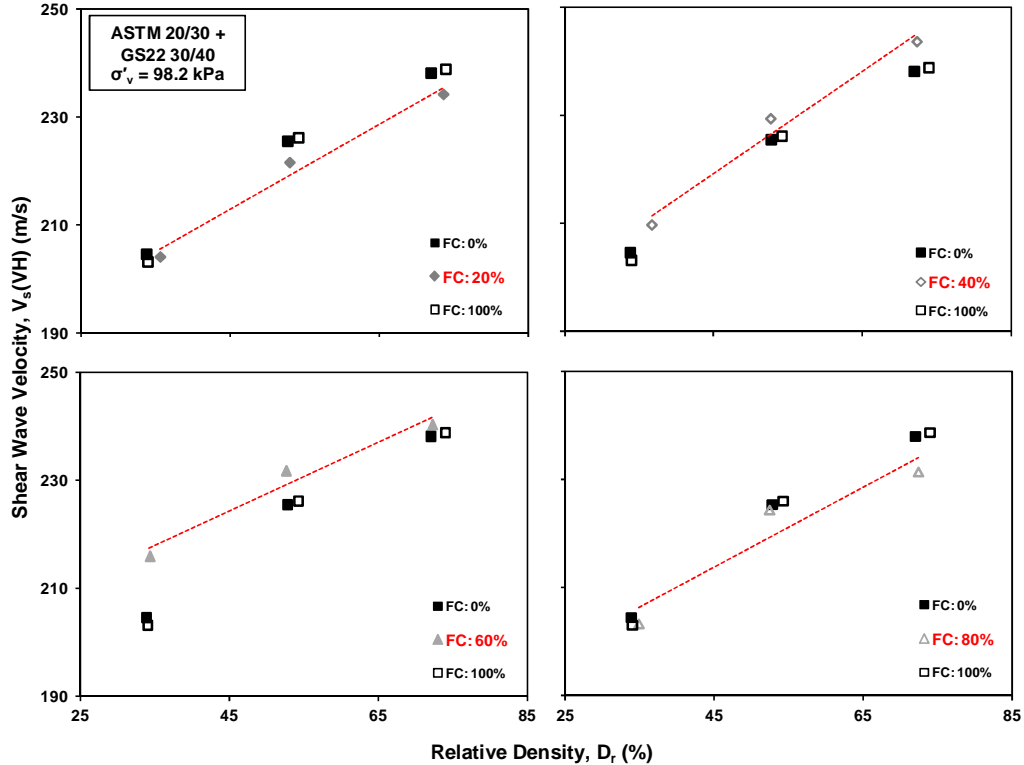


Figure 2.6. Shear wave velocity of ASTM 20/30 with GS22 30/40 according to D_r : size ratio = 0.699; applied vertical effective stress = 98.2 kPa.

Examination of the shear wave velocity measured for the mixture of ASTM 20/30 and GS22 30/40 as a function of the global void ratio demonstrated that with increasing content of smaller particles, the trend line shifted essentially proportionally as a function of the fines content (Figure 2.7). The data demonstrated that in cases where small particles could not be retained in the voids of large particles, the mechanical properties of mixtures changed from the properties of the large grain host material to those of the small grain mixture material, at a level that was almost proportional to the content of the fines. Note that the particle shapes differed between ASTM 20/30 sand and GS22 30/40 sand, which resulted in a significant difference in the tested void ratio ranges of the two unmixed sands (Youd 1973).

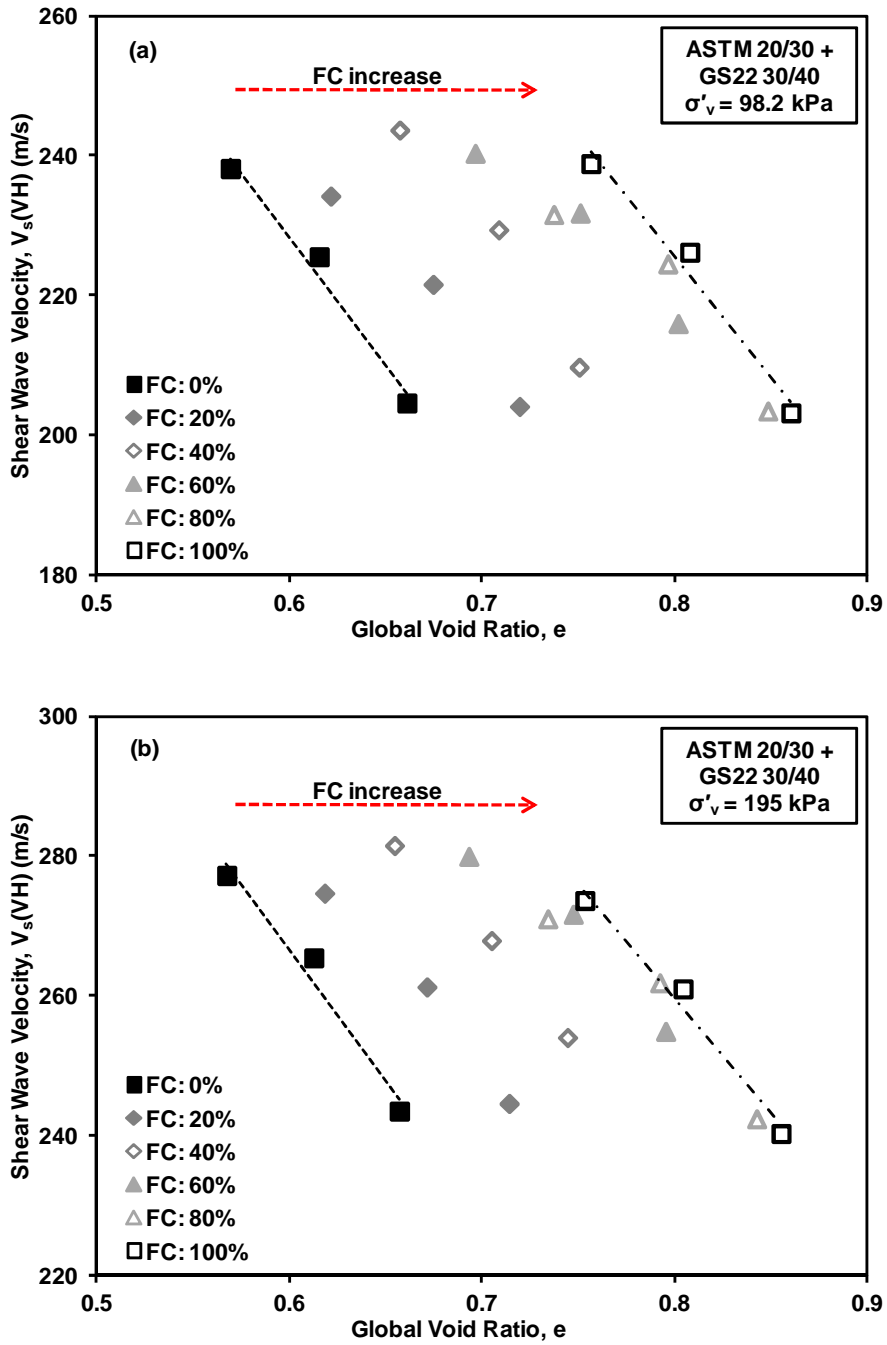


Figure 2.7. Shear wave velocity of ASTM 20/30 and GS22 30/40 mixture as a function of the global void ratio: (a) = vertical effective stress of 98.2 kPa; (b) = vertical effective stress of 195 kPa.

2.4.2.2 ASTM 20/30 with ASTM 60/80 and ASTM 100/200

The mixtures of ASTM 20/30 with ASTM 60/80 and ASTM 100/200 were prepared to study the case of $0.414 \cdot D_{50} > d_s > 0.155 \cdot D_{50}$. In loose packing of these mixtures, smaller particles were confined within the void space between large particles at low fines content ($FC < FC^*$); however, as packing density increased, the theoretical pore size between larger particles decreased from $0.414 \cdot D$ to $0.155 \cdot D$, resulting in exclusion of small particles from the large particle pore space. Ultimately, as the packing density of these mixtures increased, the direct contact between large particles was reduced by the presence of smaller particles. Comparison of the shear wave velocity as a function of relative density between the clean large matrix ($FC=0\%$) and the clean small matrix ($FC=100\%$) and mixtures with fines contents of 1%, 5%, 10%, 20%, and 40% demonstrated that the shear wave velocity was not dependent on the relative density up to the critical fines content ($\sim 20\%$) (Figure 2.8 and Figure 2.9). The mixture with 1% fines content did show comparable shear wave velocity to that of the original ASTM 20/30 sand, and correspondingly, a dependence on relative density reflecting less interruption of direct contacts between large particles with the condition of satisfying both very low fines content and great size ratio. At fines contents higher than critical (40%), in which case the smaller particles were the primary load-carrying skeleton, the shear wave velocity of the mixtures increased with increased relative density reflecting transition of structural skeleton from the contacts of large particles to the contacts of small particles.

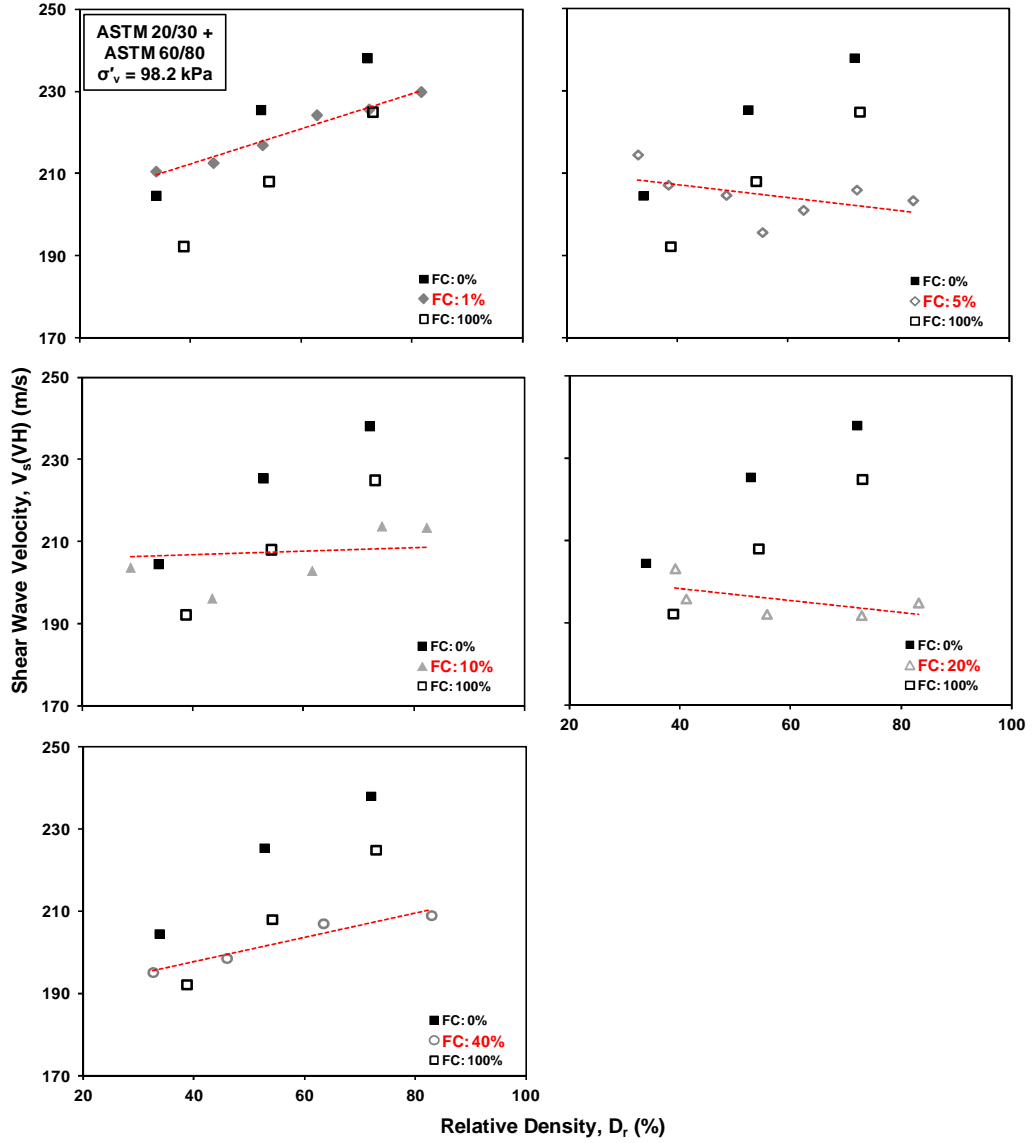


Figure 2.8. Shear wave velocity of ASTM 20/30 with ASTM 60/80 according to D_r :
size ratio = 0.282; applied vertical effective stress = 98.2 kPa.

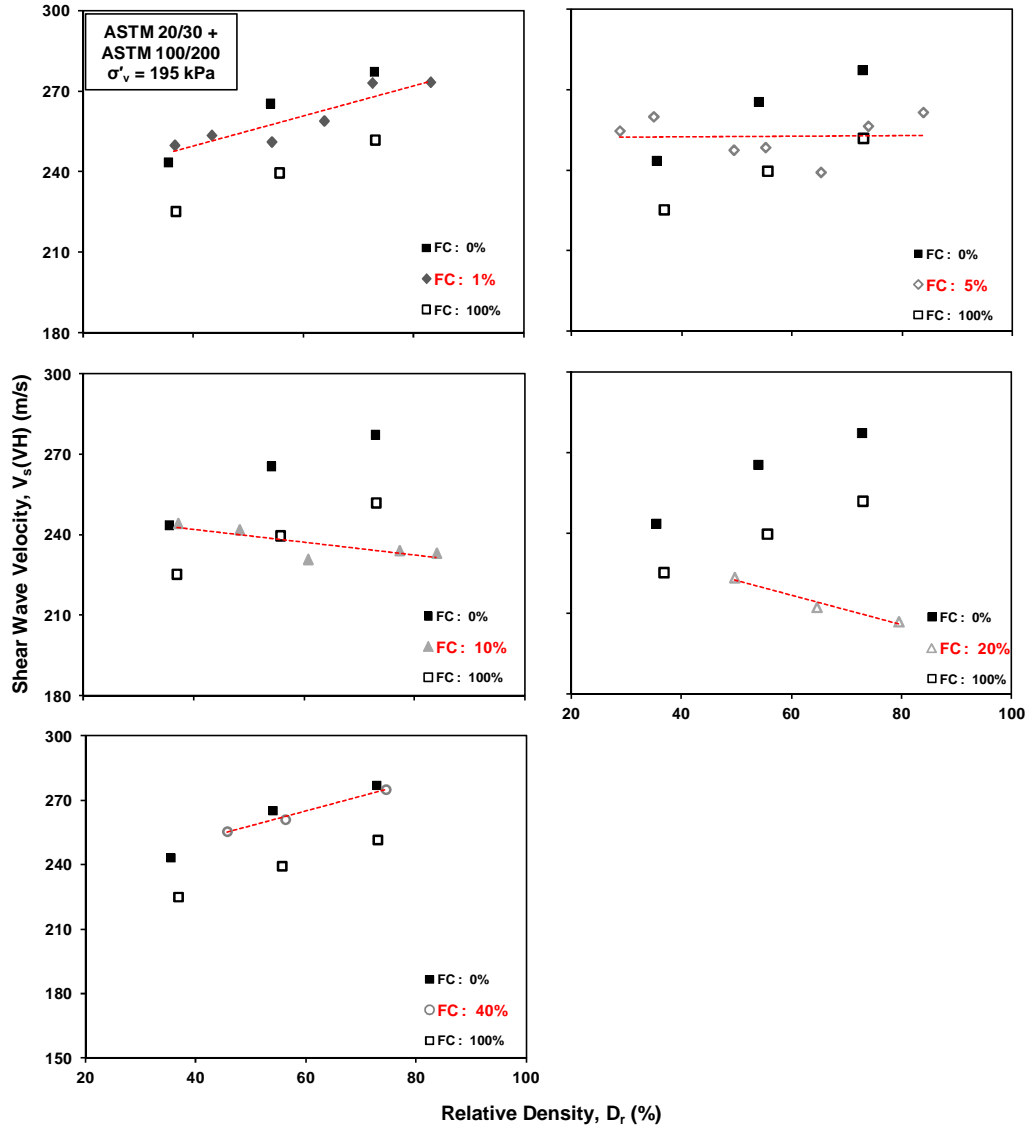


Figure 2.9. Shear wave velocity of ASTM 20/30 with ASTM 100/200 according to D_r : size ratio = 0.157; applied vertical effective stress = 195 kPa.

The shear wave velocity of the mixtures of ASTM 20/30 with ASTM 60/80 and ASTM 100/200 were analyzed in terms of intergranular void ratio (Figure 2.10 and Figure 2.11). At fines levels lower than critical ($FC < FC^*$), the shear wave velocity of the two mixtures can be expressed as a single function of intergranular void ratio, regardless of fines content. The velocity results at fines content 20 ~ 40 %

(~critical fines content) followed a separate trend, which indicated the stiffness of binary mixtures was governed by the stiffness of particles in the active force chain. At, or near, critical fines content, the active force chain was in a transitional zone that deviated from the behavior of either the large particles or the small particles.

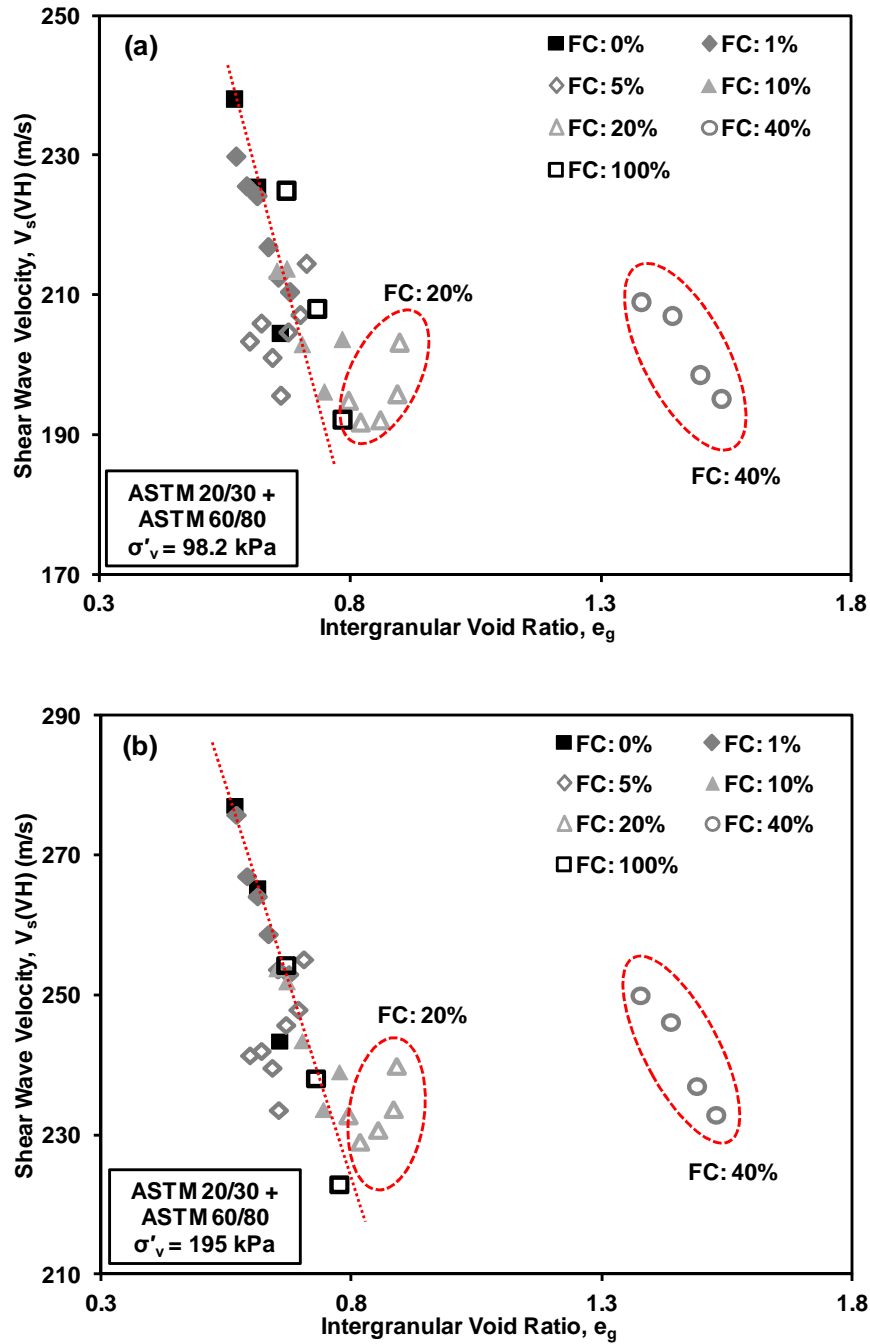


Figure 2.10. Shear wave velocity of ASTM 20/30 with ASTM 60/80 according to intergranular void ratio: (a) applied vertical effective stress = 98.2 kPa; (b) applied vertical effective stress = 195 kPa.

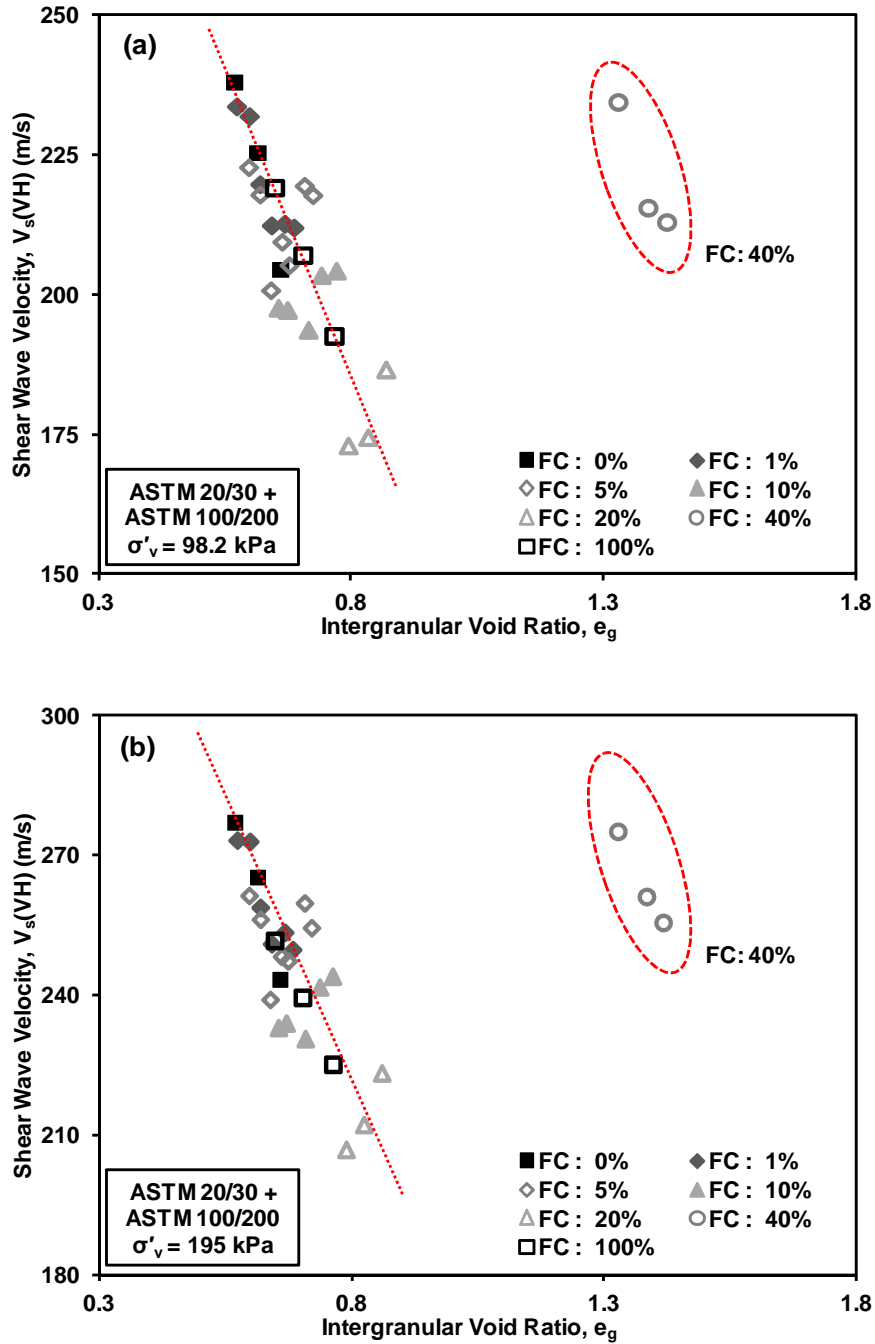


Figure 2.11. Shear wave velocity of ASTM 20/30 with ASTM 100/200 according to intergranular void ratio: (a) applied vertical effective stress = 98.2 kPa; (b) applied vertical effective stress = 195 kPa.

2.4.2.3 ASTM 2/30 with SCS R40

The mixture of ASTM 20/30 and Sil-Co-Sil R40 was prepared to study the case of $d_s \ll 0.155 \cdot D$, where smaller particles could be retained in the pore space between large grains, regardless of packing density. Consequently, the magnitude of interruption of direct contacts between large particles due to the presence of fine particles will be less affected by packing density leading to that shear wave velocities of this mixture increased with increasing packing densities at all tested levels of fines content (1%, 5%, 10%, 15%) (Figure 2.12). In addition, for this mixture, there was a dramatic decrease in stiffness of the soils with the addition of the fine particles (Figure 2.12). The maximum fines content tested in this study was 15 % due to consideration of both the critical fines content and the applicability of the ASTM standard for measuring extreme void ratios. Consistent with the mixtures that included the small particles from the 60/80 and 100/200 soils, the shear wave velocity of ASTM 20/30 with SCS R40 was expressed as a single function, that was independent of fines content at levels less than critical ($FC < FC^*$) (Figure 2.13).

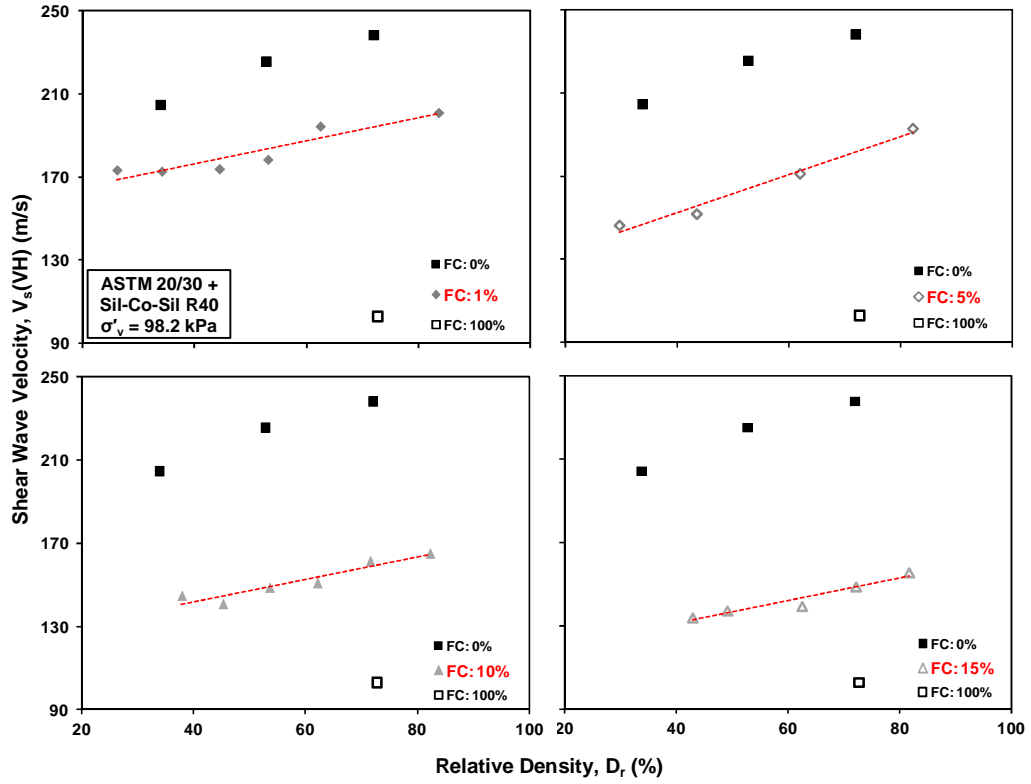


Figure 2.12. Shear wave velocity of ASTM 20/30 with Sil-Co-Sil R40 according to D_r : size ratio = 0.014; applied vertical effective stress = 98.2 kPa.

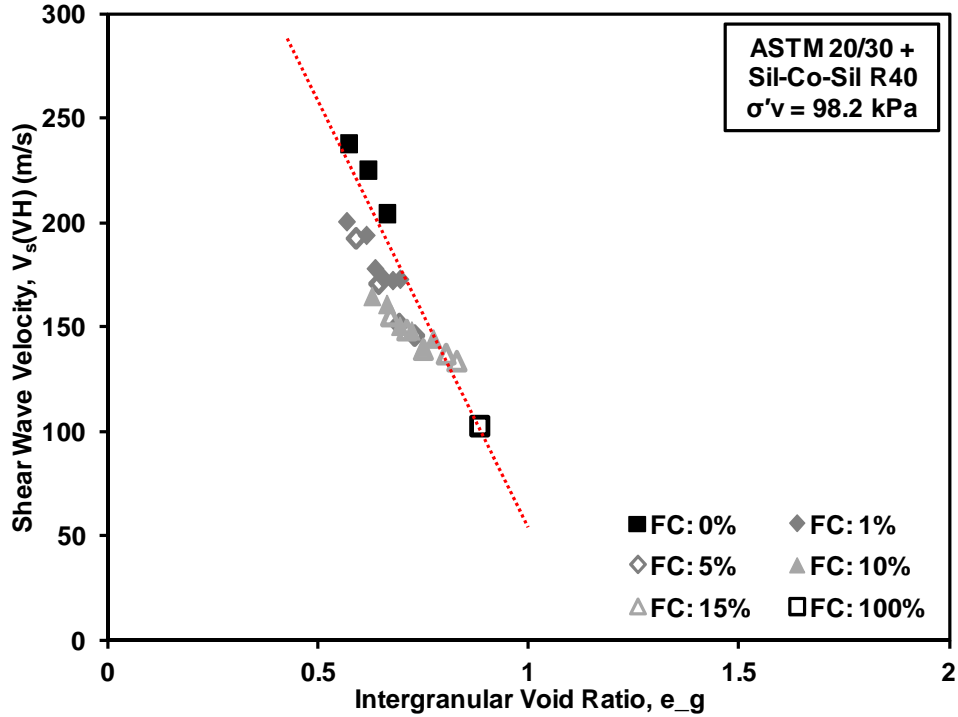


Figure 2.13. Shear wave velocity of ASTM 20/30 with Sil-Co-Sil R40 according to intergranular void ratio: applied vertical effective stress = 98.2 kPa.

2.4.3 The Variations of α -factors and β -exponents

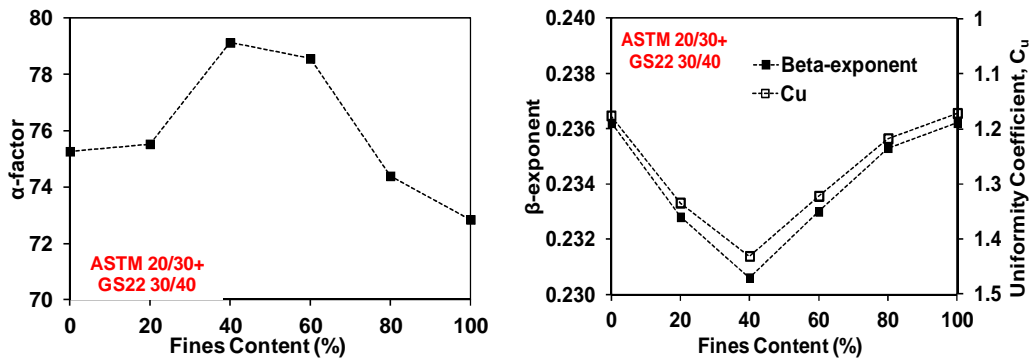
The shear wave velocity of the tested soils was analyzed according to (Roesler 1979; Santamarina et al. 2001):

$$V_s = \alpha \cdot \left(\frac{\sigma'_0}{1kPa} \right)^\beta \quad (2-13)$$

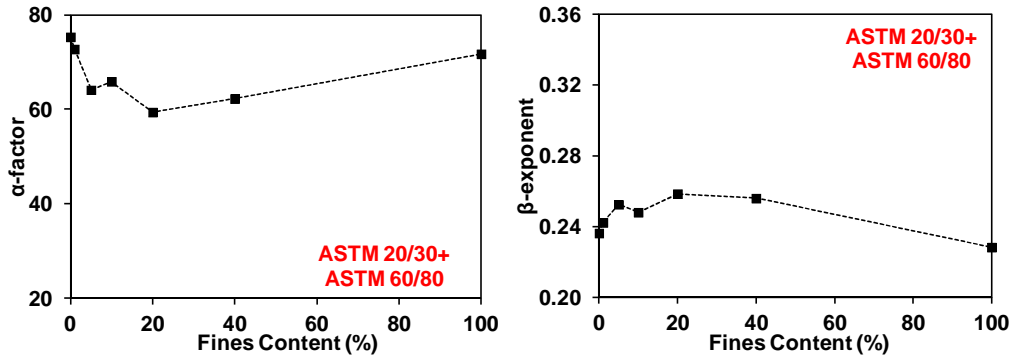
where, V_s is shear wave velocity in m/s, and σ'_0 is mean effective stress in kPa. The β -exponent reflects the stress-dependency of the material and is primarily affected by change in contact modes or coordination number between load-carrying particles during loading; therefore, stiffer materials, which will show smaller change in the coordination number as a function of loading will have smaller β . The α -factor corresponds to the wave velocity at 1 kPa, reflecting the initial stiffness of soils, and

varies with the initial state of the fabric and material properties. Stiffer materials will have greater α but smaller β , and the α -factor and β -exponent are inversely proportional (Santamarina et al. 2001).

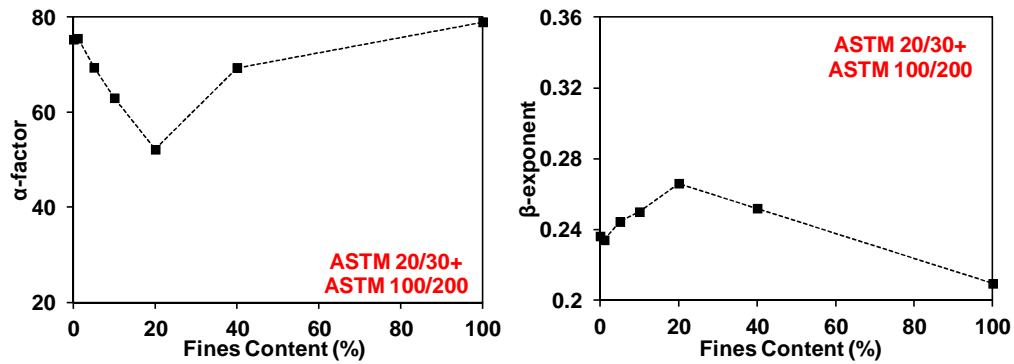
Analysis of the α -factors and β -exponents determined for the tested mixtures was performed as a function of size ratio and fines content (Figure 2.14). The mixture of ASTM 20/30 and GS22 30/40 (size ratio 0.699) exhibited the highest α -factor and lowest β -exponent at a fines content of approximately 40~60 %. The large size ratio for the mixture indicates that the smaller particles would not be retained in the pores between large particles. Thus, The increased stiffness at fines contents of 40~60 % can be explained in terms of increased coordination number due to the increased uniformity coefficient (Figure 2.14 a) (Shin and Santamarina 2013): a striking analogy between the variations of β -exponent according to fines content and the variations of uniformity coefficient in reverse order as fines content can be observed.



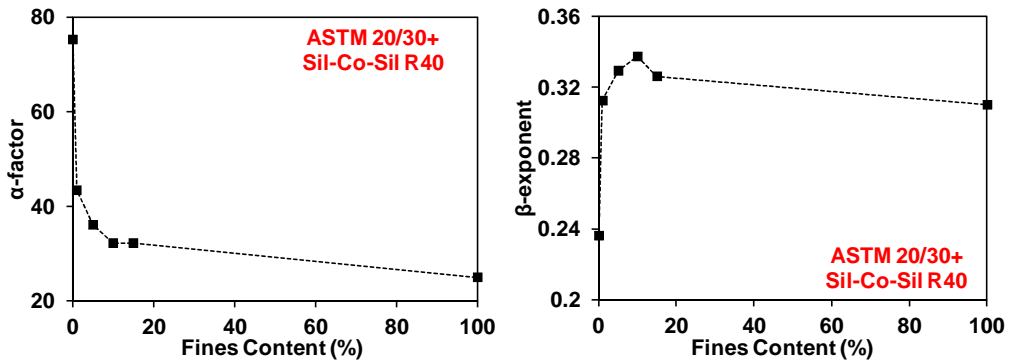
(a) The mixture with GS22 30/40



(b) The mixture with ASTM 60/80



(c) The mixture with ASTM 100/200



(d) The mixture with SCS R40

Figure 2.14. α - β variations according to size ratios and fines content: (a) ASTM 20/30 with GS22 30/40 ($sr = 0.699$); (b) ASTM 20/30 with ASTM 60/80 ($sr = 0.282$); (c) ASTM 20/30 with ASTM 100/200 ($sr = 0.157$); (d) ASTM 20/30 with SCS R40 ($sr = 0.014$).

For the mixtures of ASTM 20/30 with ASTM 60/80 and ASTM 100/200 (Figure 2.14 b and c), the α -factor decreased while the β -exponent increased until the critical fines content was reached. At fines (small particles) content below critical, the larger grains provided the active force chain, and increases in the fines content act to disrupt the direct contacts between large particles; the stiffness of soils is determined by the nature of both the interparticle contacts and the interparticle coordination number (Lee et al. 2007). Consequently, increasing the fines content will decrease the interparticle contacts and coordination number between large particles, resulting in a decreasing α -factor with increasing fines content (i.e., a decrease in the stiffness of the mixture). In the case when the fines content is larger than the critical fines content, the small particles act as the structural skeleton, and the α -factor will increase as the fines content is increased. This is attributable to the increase in direct contacts between smaller grains. The β -exponent, which reflects the stress dependency of the soil mixture, increased up to the critical fines content. Binary mixtures may experience a more pronounced increase in the coordination of large particles as the confining stress is increased because smaller particles, which do not participate in the load-carrying chain, may easily be displaced with an increase in confining stress. This will result in larger contacts between larger grains at high confining stresses, and correspondingly higher stiffness and higher β -exponent. Salgado et al. (2000) also reported that the stress exponent in their G_{\max} estimates for non-plastic silty sand increased with increasing fines content. In addition, previous studies for the mixture of sand and rubber also denote that V_s (or G_{\max}) is very sensitive to the change of stress near the transition sand fraction (Lee et al. 2010; Lee et al. 2007).

In the case of the mixture of ASTM 20/30 with Sil-Co-Sil R40 (Figure 2.14 d), which is non-plastic ground silica, there was a more pronounced decrease in the α -

factor and increase in the β -exponent, even at very low quantities of fines additions to the host sand, which is consistent with previous studies (Iwasaki and Tatsuoka 1977; Randolph et al. 1994; Salgado et al. 2000). Consistent with the previous two mixtures (20/30+60/80 and 20/30+100/200), the smallest α -factor and the highest β -exponent was observed at the approximate critical fines content.

Generally, as the stiffness of soils increases, α -factor increases but β -exponent decreases (Figure 2.15) (Santamarina et al. 2001). Consistent with the previous discussion, with increasing the fines content, the measured α -factor increased while the β -exponent decreased, indicating that the stiffness of the soil mixture decreased with the addition of fine particles. Notably, the mixture of ASTM 20/30 with SCS R40, which had the smallest size ratio, showed the greatest decrease in stiffness when compared to other mixtures with similar fines contents.

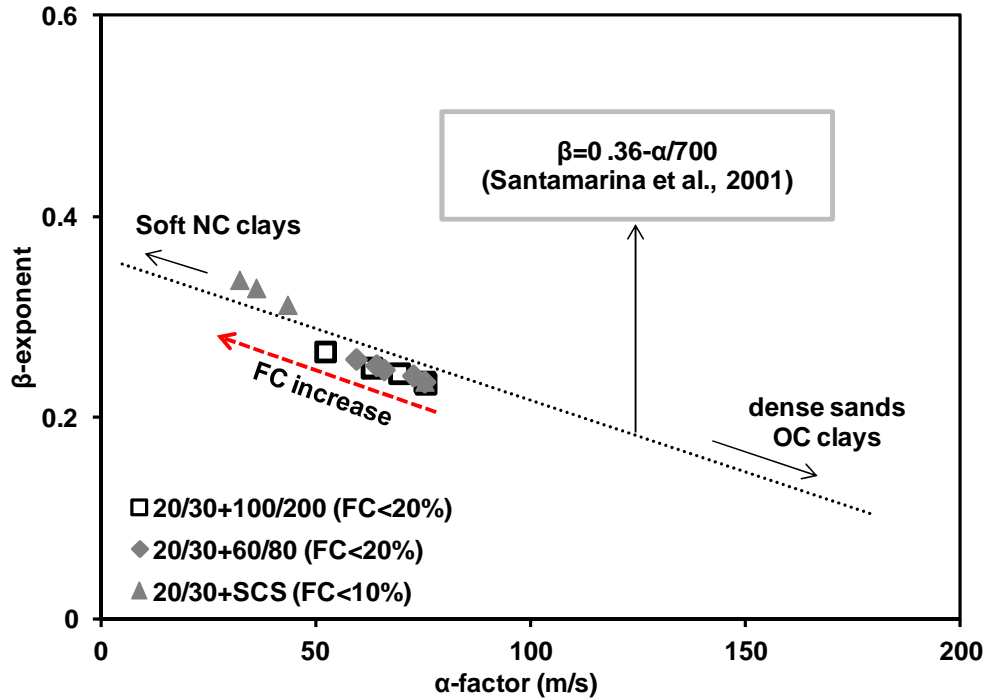


Figure 2.15. The relation of α - β for the tested binary mixtures (fines content < critical fines content): with increasing the fines content, the measured α -factor increased while the β -exponent decreased, indicating that the stiffness of the soil mixture decreased with the addition of fine particles.

2.5 Discussion

2.5.1 Effect of Packing Density

It is well accepted that the mechanical behavior of coarse grain soils are directly related to their relative density (Mitchell and Soga 2005), and dense soils with high relative density will have higher coordination number and higher strength or stiffness than soils with low relative density. However, the data gathered in this study demonstrated that the influence of relative density on the stiffness of binary mixtures is negligible when both conditions of fines content smaller than the critical fines

content and of the size ratio (d_s/D) of the binary mixtures being located between 0.414 and 0.155 is satisfied. When the difference in particle size between the large and the small grains allows smaller particles to be retained in the pore space of large particles it results in to less disruption the large-to-large particle contacts, as long as the soils are at low relative density. However, as the relative density is increased, the smaller particles were less likely to be retained in the pores of the large particles due to the decrease in pore space, resulting in a decrease in direct contacts between large particles (Figure 2.16). Consequently, at fines contents below critical, increasing the packing density did not contribute to increased interparticle coordination or increased stiffness; however, above the level of critical fines content, the stiffness of soils increases with an increase in packing density because the small particles began to act as the structural skeleton (Figure 2.8 and Figure 2.9). The fact that shear wave velocity increased with packing density in the cases where $d_s > 0.414 D_{50}$ or $d_s < 0.155 D_{50}$, also supported explanation (Figure 2.6 and Figure 2.12). In addition, the measured G_{max} of Ottawa sand with fines (Salgado et al. 2000) did not show a clear dependency of G_{max} on the tested void ratios. However, in terms of intermediate strain constrained modulus, tested mixture materials showed a dependency on relative density (data not shown in this paper), indicating that the small strain shear modulus or shear wave velocity was a constant fabric phenomenon representing a measure of current stiffness of contacts between particles; while compressibility was a measure of volume change due to the particle rearrangement (Santamarina et al. 2001; Shin and Santamarina 2013) indicating dense packing will experience low volume change with a change in confinement.

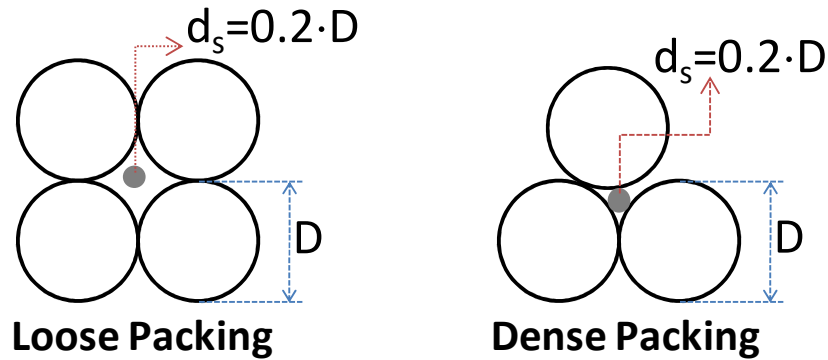


Figure 2.16. Retention of small particles according to packing ($sr=0.2$): small particles with the size of $0.155 D_{50} < d_s < 0.414 D_{50}$ can be retained into the pore space between large particles in the case of loose packing; however, they cannot be retained in the case of dense packing leading to greater interruption of direct contacts between large particles.

2.5.2 Effects of Fines Content and Size Ratio

Pinson et al. (1998) performed experiments using liquid bridge techniques and showed that, with an increase in fines content for binary mixtures, the contact between small particles and small particles and the contact between large particles and small particles increased, while the contact between large particles and large particles decreased. Thus, with an increase in fines content, the measured shear wave velocity decreased due to the decrease in interparticle contact or interparticle coordination between large particles at low fines content because large particles were the structural skeleton at low fines content ($FC < FC^*$).

Pinson et al. (1998) also noted that this change in contact modes between large and small particles was more apparent as the size ratio (d_s/D) decreased. In this aspect, a dramatic decrease in the stiffness of the mixture of ASTM 20/30 with Sil-Co-Sil R40 may be explained by comparing the mixtures of ASTM 20/30 with ASTM

100/200 (Figure 2.14 and Figure 2.15). The size ratios of ASTM 20/30 with ASTM 100/200 was 0.157, and that of ASTM 20/30 with SCS R40 was 0.014; therefore, ASTM 20/30 with SCS R40, which had much smaller size ratio than that of ASTM 20/30 with ASTM 100/200, had less developed active grain contacts between large grains at a given fines content, leading to a dramatic decrease in stiffness. Additionally, SCS R40 particles will have higher relevance of electrical force than other added materials due to their very small particle size. Consequently, the direct contact between large particles may be highly disrupted due to the coating (electrostatic attraction) of large particle surface with small SCS R40 particles. In addition, the mixture of ASTM 20/30 with ASTM 60/80 (size ratio of 0.282) had a somewhat greater stiffness than that of the mixture of ASTM 20/30 with ASTM 100/200 (size ratio of 0.157) (Figure 2.14 and Figure 2.15).

2.5.3 Intergranular Void Ratio

The shear wave velocity data were replotted to compare the stiffness between the unmixed soils and the binary mixtures of soils, where the open figures show the results of the binary mixtures, and the closed figures show the results of pure materials (stiffness of large and small grained soils) (Figure 2.17). The trend line between shear wave velocity and intergranular void ratio of the binary mixtures was essentially the same as the trend line between shear wave velocity and global void ratio of pure materials. Data from the literature that measured the shear wave velocities of a uniform Ottawa sand (mean grain size of 0.35) at void ratios ranging from $0.55 < e < 0.9$ were also included in Figure 2.17, according to the following relationship (Robertson et al. 1995):

$$V_s = (381 - 259 \cdot e) \cdot \left(\frac{\sigma'_0}{P_a} \right)^{0.26} \quad (2-14)$$

where, P_a : atmospheric pressure (100 kPa). Employing the concept of intergranular void ratio demonstrated that the shear wave velocity of the mixtures of ASTM 20/30 with ASTM 60/80 and ASTM 100/200 showed a very similar trend with that of uniform Ottawa sand, which was the function of the global void ratio.

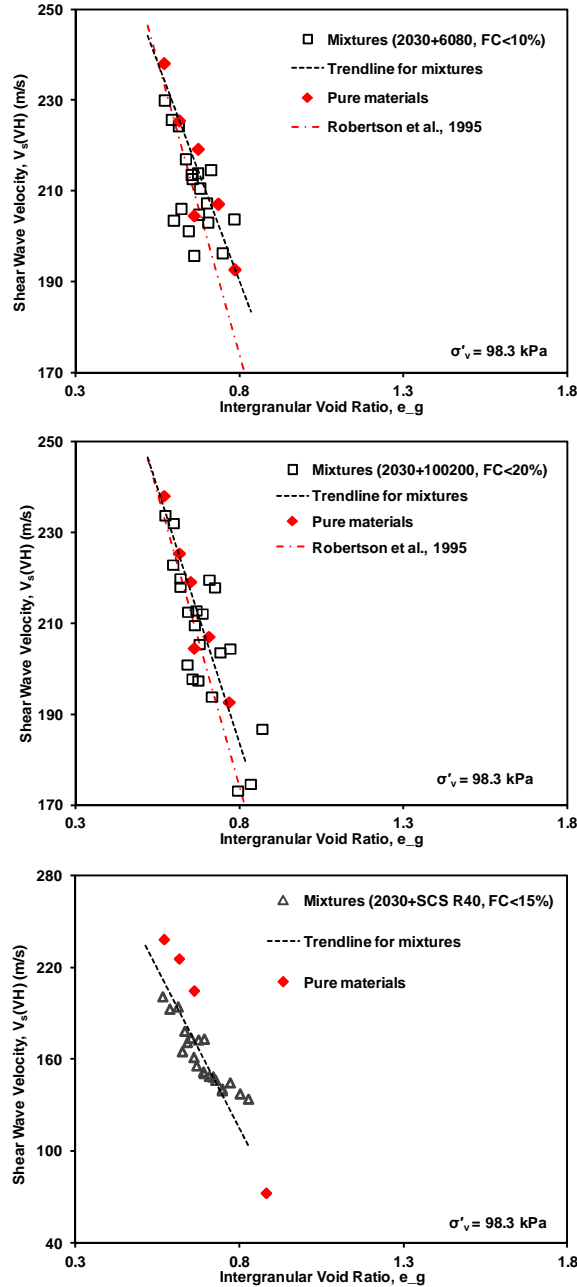


Figure 2.17. Comparison between the stiffness of unmixed soils with global void ratio and the stiffness of binary mixtures with intergranular void ratio at $\sigma'_v = 98.3$ kPa: for comparison, the result of Robertson et al. (1996) for Ottawa sand was also plotted above; closed figures = shear wave velocity of pure materials in terms of global void ratio; open figures = shear wave velocity of mixtures in terms of intergranular void ratio.

Examination of the data from the bender element test on binary mixtures of ASTM 20/30 with 60/80, 100/200, and SCS R40 demonstrated that as the fines content increased, there was an increase in the intergranular void ratio, but a decrease in the shear wave velocity. In addition, as the size ratio decreased (or size difference between particles increased), the relationship between the shear wave velocity and intergranular void ratio shifted to the left, indicating a smaller stiffness of soils for smaller size ratios at the same intergranular void ratio (Figure 2.18).

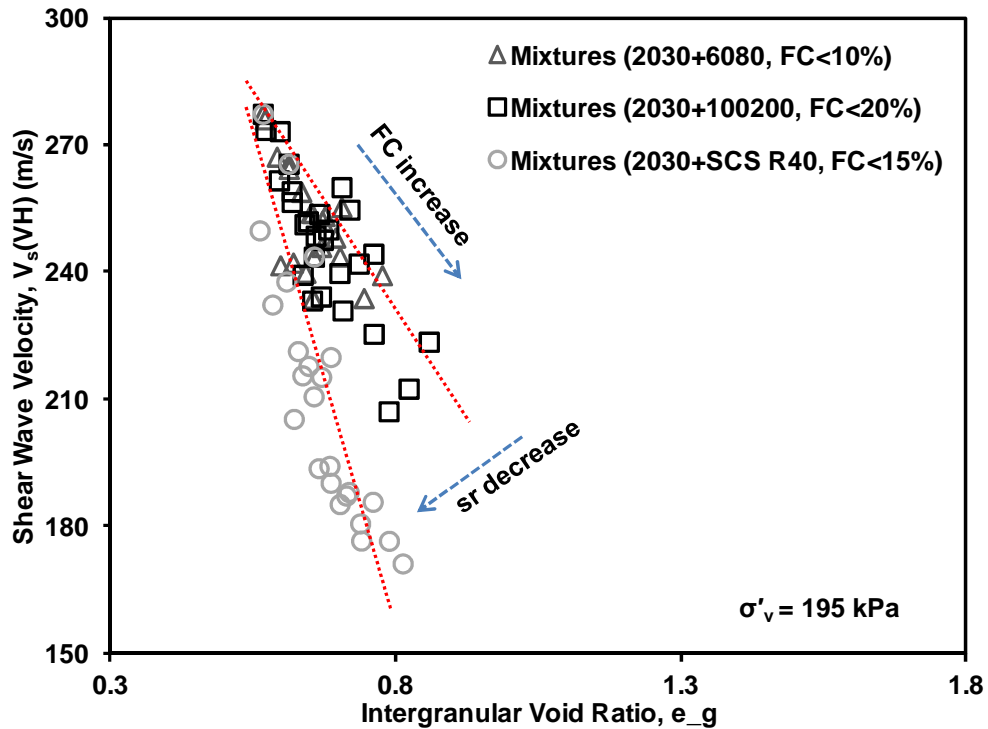


Figure 2.18. Effects of size ratio and fines content on shear wave velocity at $\sigma'_v = 195$ kPa: as the fines content increased, there was an increase in the intergranular void ratio, and as the size ratio decreased, the relationship between the normalized shear wave velocity and intergranular void ratio shifted to the left.

2.5.4 Critical Fines Content

The theoretical critical fines content, FC^* , of each binary mixture was determined using the extreme void ratios of each material, according to Equation (2-4) (Table 2-3). The critical fines content ranged from a low of approximately 15% to a high of approximately 32%, with the combination of the e_{min} of large grains with e_{max} of small grains always yielding the smallest critical fines content, as was anticipated. Comparison between the estimated critical fines contents with the current test results demonstrated that the slope of the α - β variations always change direction at approximately the calculated critical fines content (Figure 2.14). Additionally, the results of the normalized shear wave velocity of mixtures could be expressed as a single line until the fines content of mixtures was smaller than the critical values, with those critical values being similar to the calculated theoretical critical fines content. Therefore, it is believed that the theoretical critical fines content of binary mixtures was reasonably estimated by the previous equation.

Table 2-3. Calculated Critical Fines Content

ASTM 20/30	ASTM 60/80		ASTM 100/200		Sil-Co-Sil	
	e_{max}	e_{min}	e_{max}	e_{min}	e_{max}	e_{min}
e_{max}	0.280	0.319	0.283	0.322	0.209	0.312
e_{min}	0.208	0.241	0.211	0.243	0.152	0.234

Note: the values shown above were obtained by the combination of extreme void ratios of large particles (ASTM 20/30) with those of small particles (ASTM 60/80, ASTM 100/200 or SCS R40) by employing Equation (2-4) to estimate the possible ranges of critical fines content.

2.6 Summary

This chapter examined the dynamic properties of binary sand-sand and silt-sand mixtures with different particle size ratios. The variation of the measured shear wave velocity values for binary mixtures as a function of fines content, size ratios, and relative densities demonstrated the following:

1. Shear wave velocity decreased with increasing fines content due to the reduction in interparticle contacts or interparticle coordination between large grains at low fines content ($FC < FC^*$).
2. The reduction in stiffness of binary mixtures according to fines content was more pronounced as the size difference between small and large particles increased. This is because the direct contact between larger particles was more disrupted as the size ratio (d_s/D_{50}) decreased.
3. The shear wave velocity dependency on relative densities of mixtures varied as a function of the size ratio between the small and large particles. For the case where the size ratio ranged from 0.155 to 0.414, the shear wave velocity was not dependent on the relative density of the mixtures up to the critical fines content. This is attributable to the fact that pore size between the larger particles decreased as the packing density was increased.
4. Shear wave velocity of binary mixtures was effectively represented by the intergranular void ratio, reflecting the stiffness of the binary mixture was determined by the stiffness of contacts between large particles, which acted as the structural skeleton at low fines content ($FC < FC^*$).
5. The shear wave velocity, or stiffness dependency, of the test binary mixtures, was a function of the intergranular void ratio, and exhibited a trend similar to

that of the shear wave velocity of pure materials as a function of global void ratio.

CHAPTER 3 EFFECT OF OVERCONSOLIDATION RATIO ON DYNAMIC PROPERTIES OF BINARY MIXTURES OF SILICA PARTICLES

3.1 Introduction

Soils in the overconsolidated state have experienced greater state of stress in the past than is currently exerted. The past stress is known as the preconsolidation stress σ'_p , and is very important because it can be considered a yield point in the mechanical behavior of soils. Overconsolidated soils show very distinctive mechanical properties such as reduced compressibility, and increased strength and stiffness compared to that of normally consolidated soils. Multiple mechanisms can contribute to overconsolidation of a soil, including change in vertical stress, fluctuation of groundwater levels, desiccation, freeze-thaw, and chemical effects. Generally, the mechanisms of overconsolidation are complex, with more than one mechanism contributing to cause overconsolidation of soils (Chen and Mayne 1994; Jamiolkowski et al. 1985; Mitchell and Soga 2005).

Studies on the shear wave velocity (V_s) or maximum shear modulus (G_{max}) of normally consolidated binary soil mixtures are extensive and relatively well developed (Andrus and Stokoe 2000; Huang et al. 2004; Iwasaki and Tatsuoka 1977; Liu and Mitchell 2006; Randolph et al. 1994; Salgado et al. 2000). In general, the studies have shown that the shear wave velocity (or maximum shear modulus) of a soil decreased with increasing non-plastic fines content. Additionally, a significant amount of work has focused on the overconsolidation effect, or stress history effect,

on the shear wave velocity and stiffness of soils at small strains. Several studies have studied the impact of the overconsolidation ratio on the maximum shear modulus of soils, including sand and clay (Afifi and Richart 1973; Athanasopoulos 1994; Fam and Santamarina 1997; Hardin 1978; Hardin and Blandford 1989; Houlsby and Wroth 1991; Jamiolkowski et al. 1995; Tatsuoka et al. 1979; Viggiani and Atkinson 1995b). However, the stress-history-based studies of small strain stiffness on binary mixtures of particles, such as silty sands with varying size ratios and fines contents, are very limited, even though natural sand deposits typically consist of a mixture of sand particles with fines (Carraro et al. 2009; Georgiannou et al. 1990; Iwasaki and Tatsuoka 1977; Salgado et al. 2000; Thevanayagam et al. 2002; Yang et al. 2006).

Consequently, the present investigation studied the effect of fines content and particle size ratio on the maximum shear modulus of binary mixtures of silica particles, including sand-sand mixtures of two different sizes and silty sand mixtures containing a small amount of fines (~critical fines content). To evaluate the impact of these factors, a review of the theoretical aspects of binary mixtures was performed, along with an analysis of the factors influencing the overconsolidation ratio (OCR) exponent in the G_{\max} relationship. Finally, the results of an experimental investigation involving a total of eighty bender element tests on mixtures in a modified oedometer cell were analyzed within the theoretical framework.

3.2 Theoretical Framework

3.2.1 Critical Fines (Small Particles) Content

In binary mixtures, the fines (small particles) content can be defined as the ratio of the weight of fine particles to the weight of the total mixture:

$$FC = \frac{w_S}{w_L + w_S} \quad (3-1)$$

where, W_S : weight of small particles; W_L : weight of large particles. Additionally, the critical fines content can be defined as the fines content when the pore space between large grains are fully filled with smaller particles, but the contacts between large grains remain continuous (Lade et al. 1998). Therefore, the critical fines content can be expressed according to (Yang et al. 2006) (derivation of this equation can be found from Chapter 2):

$$FC^* = \frac{G_{sS} \cdot e_L}{G_{sL}(1 + e_S) + G_{sS} \cdot e_L} \quad (3-2)$$

where, FC^* = critical fines content; e_L is the void ratio of large particles, and e_S is the void ratio of small particles; G_{sL} : specific gravity of large particles; G_{sS} : specific gravity of small particles. Assuming the specific gravities of the particles in the mixture are the same, Equation (3-2) can be further simplified to:

$$FC^* \approx \frac{e_L}{1 + e_S + e_L} \quad (3-3)$$

As shown in Equation (3-3), the critical fines content of a binary mixture is determined by the void ratios of the matrices of the large grains and the small grains. It is notable that the void ratios of coarse grains reflect both the packing condition and physical characteristics of coarse grained particles. The void ratio will vary with soil type and fabric state, leading to a critical fines content of binary mixtures that is a function of soil type and packing condition.

3.2.2 Overconsolidation Ratio Exponent in Maximum Shear Modulus Relationship

The stiffness of a soil is primarily controlled by the applied effective stress according to (Hardin and Richart 1963; Houlsby and Wroth 1991; Jovicic and Coop 1997; Santamarina et al. 2001; Viggiani and Atkinson 1995b):

$$G_{\max} = A \cdot \left(\frac{\sigma'_0}{1kPa} \right)^n \quad (3-4)$$

where, G_{\max} = maximum shear modulus; σ'_0 = mean effective stress in kPa; $A = G_{\max}$ at 1 kPa = experimentally determined factor; n = experimentally determined stress exponent. The A-factor indicates the initial stiffness of the soil, reflecting the initial state of fabric and material properties. The n-exponent is controlled by the change in contact modes or coordination number between particles as a function of the loading process and reflects the dependency of the tested materials on applied stress. Stiffer (or less compressible) materials will have smaller n-exponents than soft materials with greater compressibility.

Considering a reasonable range of K_0 for soils, Equation (3-4) can be modified to (Robertson et al. 1995):

$$G_{\max} = A \cdot \left(\frac{\sigma'_0}{1kPa} \right)^n = A \cdot \left(\frac{(1+K_0) \cdot \sigma'_v}{2kPa} \right)^n \approx A' \cdot \left(\frac{\sigma'_v}{1kPa} \right)^n \quad (3-5)$$

which can be further modified to account for the effect of overconsolidation (Houlsby and Wroth 1991; Jovicic and Coop 1997; Viggiani and Atkinson 1995b):

$$G_{\max} = A' \cdot \left(\frac{\sigma'_v}{1kPa} \right)^n \cdot OCR^K \quad (3-6)$$

where $K = OCR$ exponent, primarily influenced by plasticity index (PI) (Seed et al. 1986). In this study, the vertical effective stress was employed, instead of mean

effective stress; therefore, the OCR function accounts not only for fabric change, but also for lateral stress locking during unloading.

The typical variation in G_{\max} as a function of effective vertical stress during loading and unloading demonstrates that, due to permanent fabric change and lateral stress locking during unloading, a higher maximum shear modulus (or smaller stress exponent) can be obtained during unloading than loading (Fam and Santamarina 1997) (Figure 3.1). Based on the geometry of Figure 3.1 and Equation (3-6), and similar to the stress history model for G_{\max} from Hryciw and Thomann (1993), the slope of the loading and unloading curves can be determined according to:

$$n_l = \tan \varphi = \frac{a + x}{b} \quad (3-7)$$

$$n_u = \tan \theta = \frac{a}{b} \quad (3-8)$$

where, n_l = stress exponent during loading; n_u = stress exponent during unloading.

Additionally:

$$x = \log \frac{G_{\max}(OC)}{G_{\max}(NC)} = K \cdot \log(OCR) \quad (3-9)$$

where, $G_{\max}(OC)$: G_{\max} of soils in the overconsolidated state; $G_{\max}(NC)$: G_{\max} of soils in the normally consolidated state.

Substituting (3-8) and (3-9) into Equation (3-7) yields:

$$n_l = n_u + \frac{K \cdot \log(OCR)}{b} \quad (3-10)$$

From the definition of OCR, b can be expressed:

$$b = \log(\sigma'_{\max}) - \log(\sigma'_i) = \log(OCR) \quad (3-11)$$

where, σ'_i : initial effective vertical stress; σ'_{\max} : maximum effective vertical stress.

Combining (3-10) and (3-11) will yield:

$$K = n_l - n_u \quad (3-12)$$

From Equation (3-12), it is clear that the difference between the stress exponents in loading and unloading is equivalent to the OCR exponent in Equation (3-6).

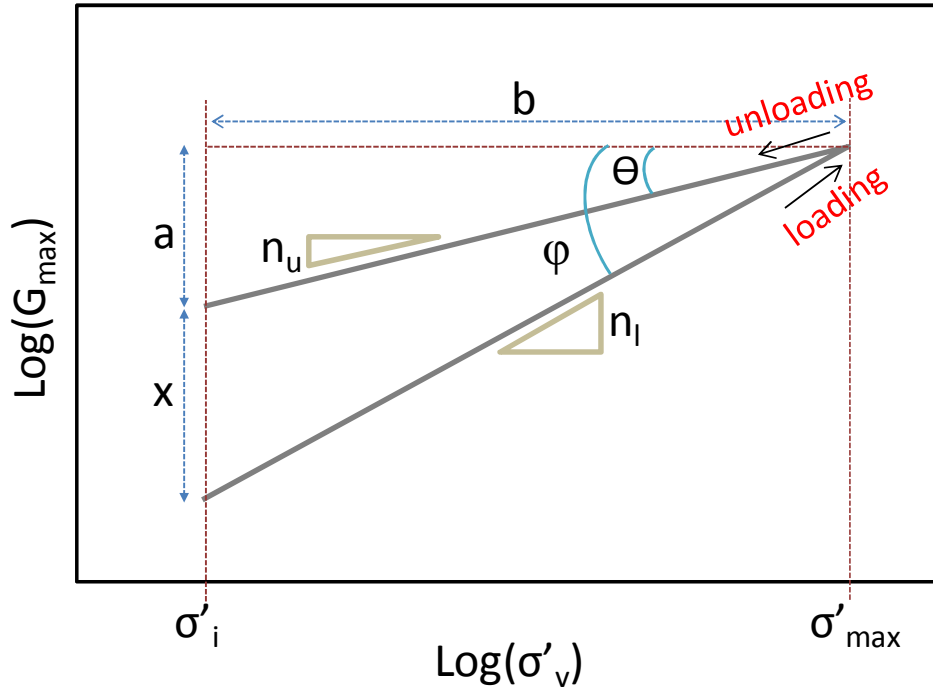


Figure 3.1. Typical variation of G_{\max} during loading and unloading for the model of OCR exponent estimation: σ'_i = initial effective vertical stress; σ'_{\max} = maximum effective vertical stress; n_u = stress exponent during unloading; n_l = stress exponent during loading.

3.2.3 Stress History and Stress Exponents during Loading and Unloading

Using the theoretically derived small strain stiffness estimating formula based on Hertz and Mindlin Contacts for a random packing of identical solid spherical particles, yields the following (Digby 1981; Duffaut et al. 2010):

$$G_{dry} = \frac{C_N \cdot (1-n)}{20 \cdot \pi \cdot R} \cdot (S_N + \frac{3}{2} \cdot S_T) \quad (3-13)$$

where, C_N = coordination number; n = porosity; R = radius of particles; S_N = normal stiffness; S_T = tangential stiffness. By introducing the normal and tangential stiffness of two elastic spheres in contact and from the relevant relationships of contact force with applied pressure and contact area with the radius of particles (Chang et al. 1991; Johnson 1985; Mindlin and Deresiewicz 1953), the small strain stiffness can be determined according to:

$$G_{dry} = \frac{3}{5} \frac{5-4\nu_g}{2-\nu_g} \cdot \left(\frac{C_N^2 \cdot (1-n)^2 \cdot G_g^2 \cdot \sigma_0}{18 \cdot \pi^2 \cdot (1-\nu_g)^2} \right)^{1/3} \quad (3-14)$$

where, ν_g and G_g = grain Poisson's ratio and grain shear modulus, respectively.

The theoretically derived stress exponent from in the G_{max} relationship equals 1/3; however, most previous experimental studies reported that a stress exponent equal to approximately 1/2. There have been several attempts to explain this discordance in stress exponents between theoretical derivation and experimental observation based on the characteristics of soils, such as plastic deformation due to the rearrangement of particles (Cascente and Santamarina 1996; Hryciw and Thomann 1993), and based on a separate theoretical derivation using cone-plane contacts, instead of Hertzian contacts (Goddard 1990). While it is likely that both mechanisms contribute to higher experimentally measured stress exponents, this study focuses on the deformation characteristics of soils and contact of particles based on the assumption of Hertzian contact, due to its relevance for the development of stress-history-based G_{max} for binary mixtures.

The deformation of an assemblage of granular materials can be divided into two components: the recoverable deformation caused by elastic deformation of the

individual particles and the irrecoverable, or plastic, deformation due to sliding or slip of particles relative to each other which results in permanent fabric change of the soil (El-Sohby and Andrawes 1972; Hardin and Blandford 1989). A significant portion of the permanent deformation occurs during initial loading, with a reduction in the magnitude of permanent deformation during unloading and reloading (El-Sohby and Andrawes 1972); therefore, it can be postulated that large parts of the deformation that occurs during unloading or reloading is elastic deformation, which is recoverable, and the plastic deformation will be minor. Consequently, the variation of stress exponents of different materials during unloading will be small, while stress exponents during loading will show a wide variation according to contact type, which is supported by experimental data that have demonstrated that stress exponents of coarse grain soils showed a wide range of values during loading (from 0.39 to 0.72), but ranged from from 0.35 to 0.42 during unloading (Hryciw and Thomann 1993). It follows that soils with higher stress exponents during loading may also exhibit higher stress history effects on the small strain stiffness when compared to soils that exhibit smaller stress exponents during loading as shown in Equation (3-12).

3.3 Experimental Program

3.3.1 Materials

ASTM 20/30 and ASTM 60/80 sands were selected as host materials for the binary mixtures and smaller particles were added according to the selected size ratios and fines content. In this study, the term large particles was used to indicate ASTM 20/30 sand or ASTM 60/80 sand and the added materials, such as ASTM 100/200 and Sil-Co-Sil R40, were referred to as small particles or fines for convenience, even

though the median grain size of ASTM 100/200 was greater than 0.075 mm. The specific gravity of the soils was determined according to ASTM D854, extreme void ratios were determined according to ASTM D4253 and ASTM D4254, and grain size distribution was determined according to ASTM D422 (Table 3-1 and Figure 3.2). All soils were used as received from U.S. Silica Company, and were composed of silicon dioxide (99.8%) and other trace materials (0.2%), such as iron oxide or aluminum oxide.

Table 3-1. Material Properties of Binary Mixtures

Properties	ASTM 20/30	ASTM 60/80	ASTM 100/200	Sil-Co-Sil R40
D_{50} (mm)	0.72	0.203	0.113	0.010
Specific Gravity	2.65	2.65	2.65	2.65
e_{\max}	0.742	0.912	0.879	1.81
e_{\min}	0.502	0.584	0.560	0.64

Note: D_{50} = median grain size; e_{\max} = maximum void ratio; e_{\min} = minimum void ratio

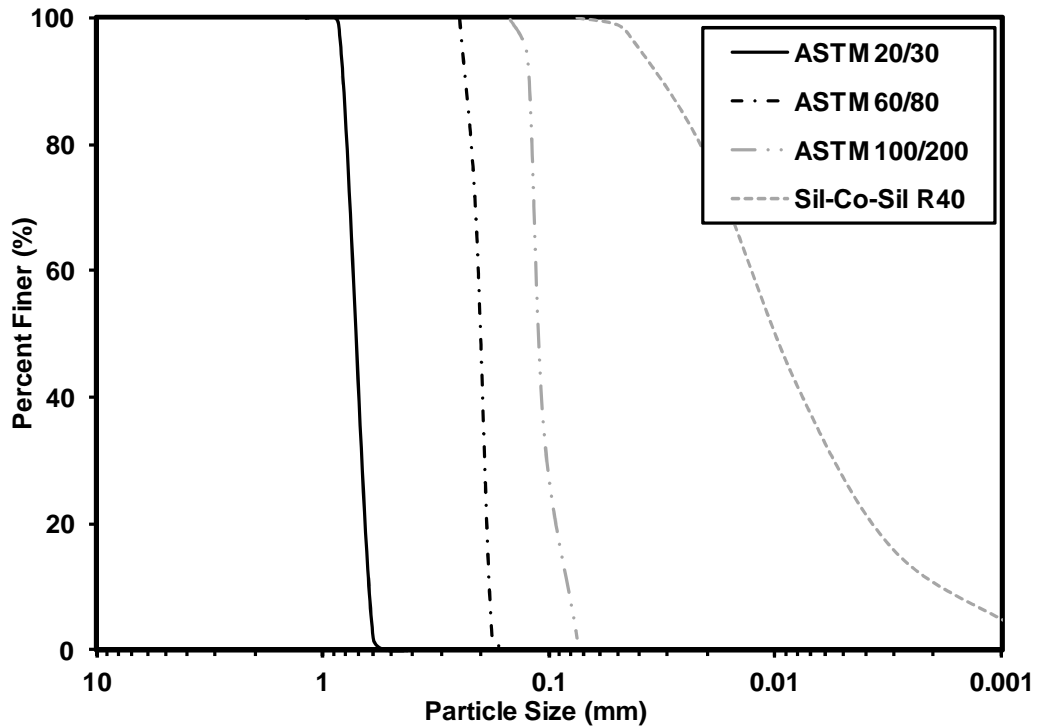


Figure 3.2. Grain size distribution of tested materials.

3.3.2 Test Equipment and Shear Wave Velocity Measurements

Shear wave velocity measurements of the soils were performed by employing a modified oedometer cell, with bender elements fitted in the top cap and bottom plate of the cell (Lee and Santamarina 2005). Each bender element was 10 mm in length, 7 mm in width, and 0.6 mm in thickness, and to ensure good coupling with soil particles, the extrusion length was selected as 4 mm. After preparing the test specimen in the cell, experiments were conducted in the K_0 condition using vertical stress ranging from 13.5 kPa to 388.6 kPa, and shear wave velocity was measured at the end of each loading/unloading step. A square wave with a frequency (f) = 20 Hz and amplitude = 10 V was generated by a function generator (33210A, Agilent) and was used as the input signal for the transmitter. The signal detected by the receiver bender element was filtered and amplified through a filter amplifier (3364, Krohn-Hite), and acquired

by a digital oscilloscope (DSO5014A, Agilent). To calculate the wave velocity, the tip-to-tip distance between the bender elements was used as the travel distance of waves (Fernandez 2000), with the travel distance was carefully selected as recommended in Lee and Santamarina (2005).

3.3.3 Sample Preparation and Testing Program

The dry funnel deposition method was chosen for preparation of the soil samples due to its ability to produce a wide range of relative densities of mixtures, and because the consistency of the resulting mixture has been verified by many researchers (Ishihara 1993; Lade and Yamamuro 1997; Yamamuro and Lade 1997). The initial relative densities of the tested mixtures ranged from 20 % to 80 %, and the maximum fines contents were selected based on the critical fines content of each mixture (Table 3-2). The test matrix was chosen with an emphasis on the contacts between large particles, where the size ratio defined in this study was the ratio of the median particle size of smaller particles (d_s) to the median particle size of large particles (D_{50}). A total of 80 bender element tests were performed to quantify the effects of size ratio, fines content, and overconsolidation ratio on the small strain stiffness of the binary mixtures.

Table 3-2. Test Matrix for Binary Mixtures

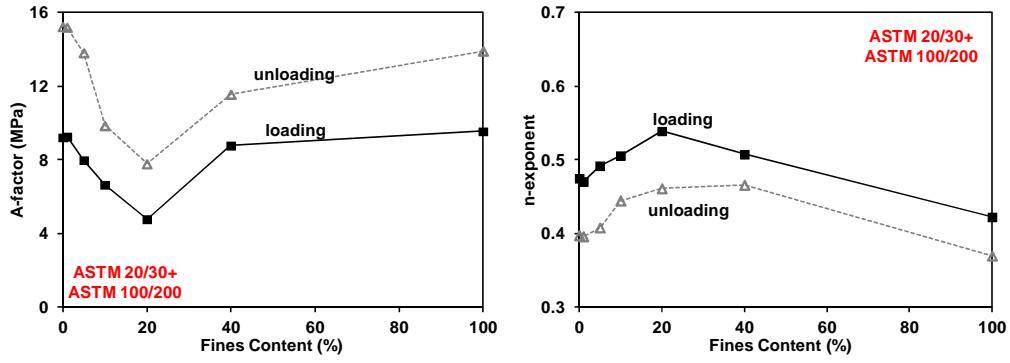
Host Material	ASTM 20/30	ASTM 20/30	ASTM 60/80
Added Material	ASTM 100/200	Sil-Co-Sil R40	Sil-Co-Sil R40
Size Ratio (d_s/D)	0.157	0.014	0.051
Initial Density	20 ~ 80 %	20 ~ 80 %	20 ~ 80 %
Fines Contents	1%	1%	1%
	5%	5%	5%
	10%	10%	10%
	20%	15%	15%
	40%	100%	100%
	100%	-	-

3.4 Results and Discussion

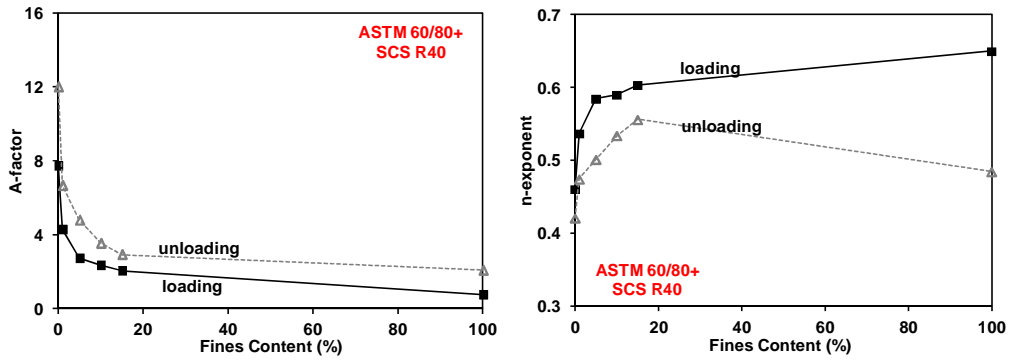
3.4.1 Small Strain Stiffness during Loading and Unloading

As the fines content was increased up to the level of the critical fines content, the mixtures tested in this study exhibited a decrease in the A-factor (G_{\max} at 1 kPa), but an increase in the n-exponent (experimentally determined stress exponent) in all cases during loading and unloading (Figure 3.3). Generally, as the stiffness of soils increased, the A-factor increased, but the n-exponent decreased (Santamarina et al. 2001), which reflected a decrease in the stiffness of soils with an increase in the non-plastic fines content, and is consistent with previous experimental observations (Andrus and Stokoe 2000; Huang et al. 2004; Iwasaki and Tatsuoka 1977; Liu and Mitchell 2006; Randolph et al. 1994; Salgado et al. 2000). In addition, a higher value of the A-factor and smaller value for the n-exponent can be obtained during unloading due to lateral stress locking and permanent fabric change, reflecting the greater

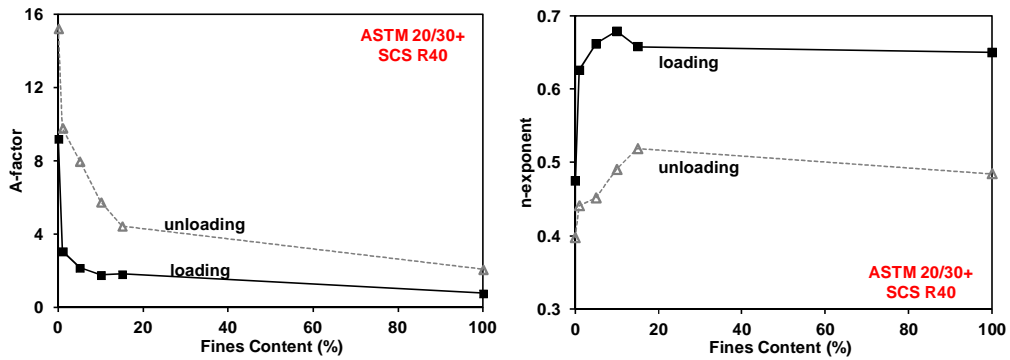
stiffness of soils during unloading than loading. In these experiments, both loading and unloading data indicated similar dependency of stiffness at small strains on the fines content. At low fines content ($FC < FC^*$), it can be postulated that smaller particles were retained in the pore space between large particles and did not contribute to the active grain contact force chain (applied stress was transferred through the contacts of large particles). Consequently, the influence of fines on the mechanical behavior of binary mixtures below the critical fines content was negligible (Carraro et al. 2003; Thevanayagam 1998; Thevanayagam et al. 2002; Yang et al. 2006). However, the stiffness of soils was determined by the nature of not only interparticle contacts, but also interparticle coordination number (Lee et al. 2007). Increasing the fines content yielded a decrease in both interparticle contacts and interparticle coordination number between the large particles, resulting in an A-factor that decreased with increasing fines content and a decrease in the stiffness of the soil mixture. When the fines content was larger than the critical fines content ($FC > FC^*$), the small particles acted as the structural skeleton, and the A-factors approached those of the added materials (100% fines).



(a) ASTM 20/30 with ASTM 100/200 (size ratio: 0.157)



(b) ASTM 60/80 with SCS R40 (size ratio: 0.051)



(c) ASTM 20/30 with SCS R40 (size ratio: 0.014)

Figure 3.3. A-n variations as size ratios and fines contents during loading and unloading: (a) ASTM 20/30 with ASTM 100/200 (size ratio: 0.157); (b) ASTM 60/80 with SCS R40 (size ratio: 0.051); (c) ASTM 20/30 with SCS R40 (size ratio: 0.014).

Examination of the trends in the n-exponent that reflected the stress dependency of the soil mixture, as fines content increased the binary mixtures experienced an increase in large particle-to-large particle coordination as the confining stress increased. Because the smaller particles were not in the primary load-carrying chain, they were easily excluded from the force chain, especially as the level of confining stress was increased, which led to better contacts between larger grains at high confining stress. Consequently, the n-exponent increased with increasing fines content, and exhibited a maximum at approximately the critical fines content. When the small particles acted as the load-carrying chain ($FC > FC^*$), n-exponents of each mixture approached those of the added materials (100% fines).

3.4.2 Effect of Size Ratio

In order to quantify the impact of the effect of size ratio on the stress-history-based G_{max} of different mixtures, a normalized G_{max} ratio was plotted as a function of size ratio (Figure 3.4, fines content = 5 %), according to:

$$normalized_G/G_{nc} = \frac{G/G_{nc}(mixture)}{G/G_{nc}(clean)} \quad (3-15)$$

where, a G_{max} ratio (G/G_{nc}) was defined as:

$$G/G_{nc} = \frac{G_{max}(OC)}{G_{max}(NC)} = \frac{A \cdot \left(\frac{\sigma'_v}{1kPa}\right)^n \cdot OCR^K}{A \cdot \left(\frac{\sigma'_v}{1kPa}\right)^n} \approx OCR^K \quad (3-16)$$

As the size ratio decreased (or size difference between large and small grains increased), the normalized G_{max} ratio increased, reflecting an increased influence of stress history. ASTM 20/30 - SCS R40, which had a much a smaller size ratio than the size ratios of other mixtures, will have less developed active grain contacts between large grains at low confinement, leading to a dramatic increase in the stress exponent

during loading process due to the greater increase in coordination number between large grains, when compared to that of mixtures with greater size ratios (Chapter 2). It has been demonstrated experimentally, using liquid bridge techniques, that as fines content is increased for binary mixtures, the number of small-to-small and large-to-small contacts increase, while the number of large-to-large contacts decrease, and the change in contact modes was more apparent as the size ratio (d_s/D) decreased (Pinson et al. 1998). In contrast, during unloading, the variation of the stress exponent for different materials was relatively small, due to the prevailing elastic deformation. Consequently, it follows from Equation (3-12), that the higher stress history effect may be closely related to higher stress exponent during loading. In summary, binary mixtures with smaller size ratios (or greater size differences between the particles) will experience a larger increase in their stress exponent during loading, which in turn leads to an increase in the OCR exponent. In addition, for the mixtures with size ratio greater than approximately 0.15, the normalized G_{max} ratio was close to one, indicating that the addition of smaller grains to clean sand had negligible effect on the alteration of the OCR exponent for clean sand. And it may be notable that stress history effect for clean sand is negligible (Fam and Santamarina 1997) leading to that stress history effect for mixture with size ratio greater than 0.155 will be minimal.

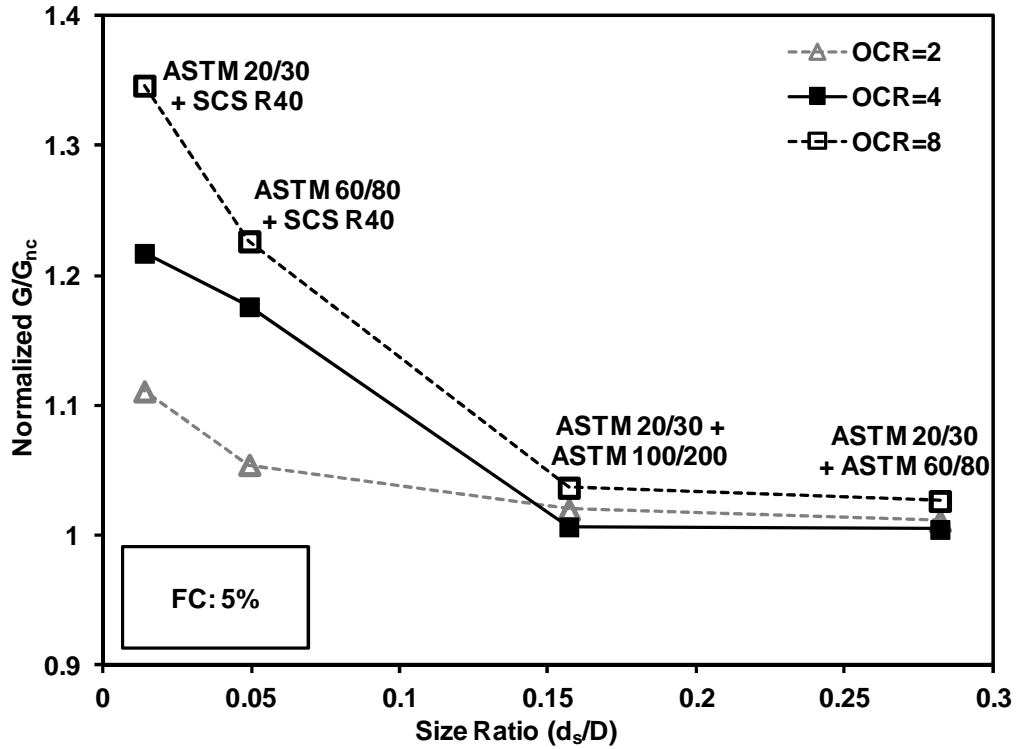


Figure 3.4. Normalized G_{max} ratio as a function of size ratio: normalized G_{max} ratio = Equation (3-15); d_s/D for ASTM 20/30 with ASTM 100/200 = 0.157; d_s/D for ASTM 60/80 with SCS R40 = 0.049; d_s/D for ASTM 20/30 with SCS R40 = 0.014. (For comparison, data from related investigation with tests on d_s/D for ASTM 20/30 with ASTM 60/80 = 0.282 are included above.)

3.4.3 Effect of Fines (Small Particles) Content

The data from the mixture of ASTM 20/30 – SCS R40 were analyzed to examine trends in the behavior during loading and unloading ($n_u - n_l$), as well as the G_{max} ratio (Equation (3-16)) as a function of fines content (Figure 3.5 and Figure 3.6). It can be observed from the Figure 3.5 and Figure 3.6 that the variations of $n_u - n_l$ and the G_{max} ratio according to fines content were very similar reflecting the relevance of Equation (3-12). Additionally, a higher G_{max} ratio can be obtained with an increase in

overconsolidation ratio (OCR) reflecting an increase in lateral stress locking with an increase in OCR (Mayne and Kulhawy 1982) (Figure 3.6). Most notably, it can also be observed that the maximum stress history effect was observed around the fines content of 5 %, which is smaller than critical fines content of the tested mixture.

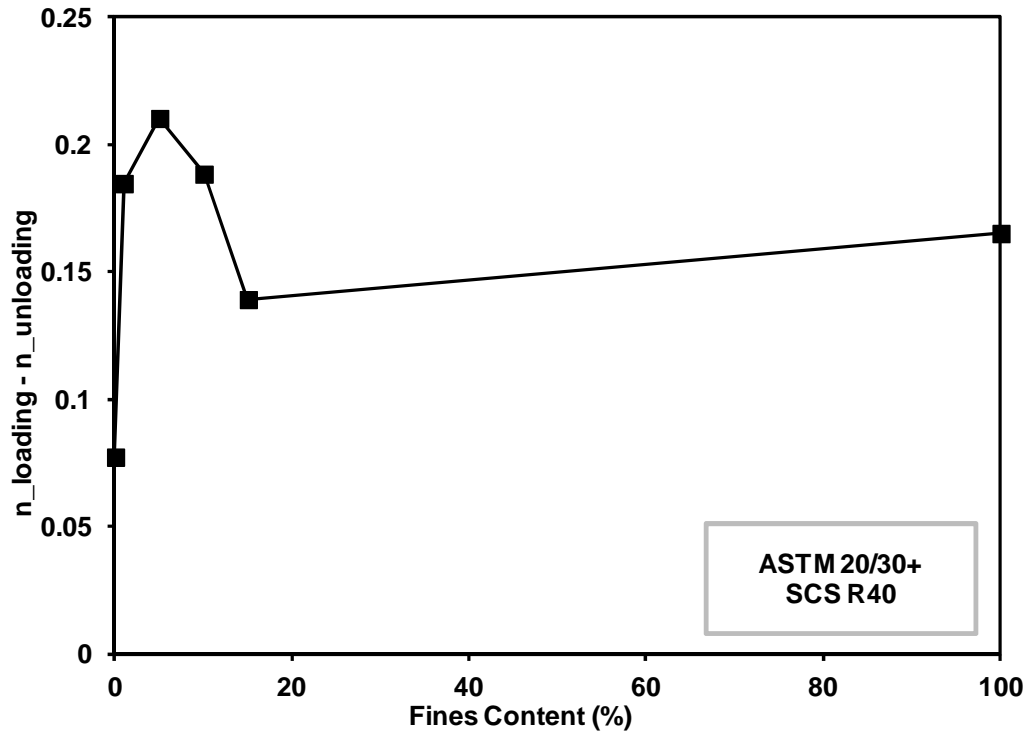


Figure 3.5. The variation of “ $n_l - n_u$ ” according to fines content: the mixture of ASTM 20/30 with SCS R40.

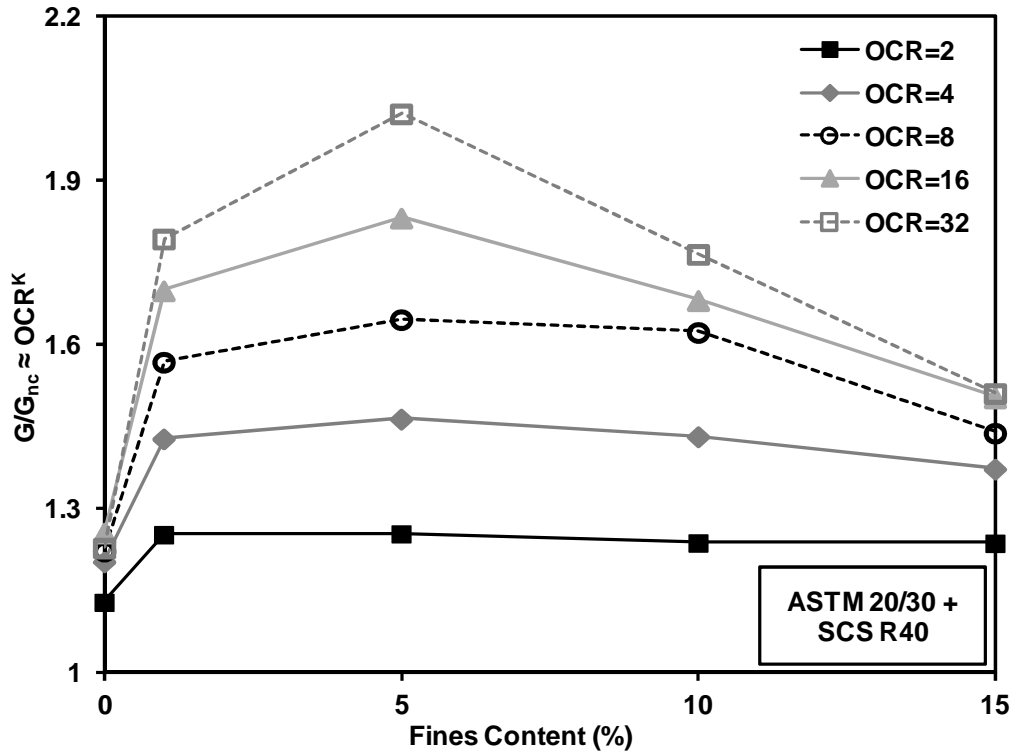


Figure 3.6. The variations of G_{max} ratio according to fines content: the mixture of ASTM 20/30 with SCS R40; G_{max} ratio = Equation (3-16).

To ensure that small particles (or fines) were confined within the pores between large particles regardless of packing density, the size ratio (d_s/D) maintained was less than 0.155 (Jang 2011; Santamarina et al. 2001). Under this framework, the larger grains controlled the primary deformation of mixtures, while the initial fabric of the small grain particles within the void space of the larger particles would be maintained under the condition of loose packing and low applied stress; however, as the applied stress or relative density was increased, deformation of the fabric of smaller particles increased, which resulted in a decrease in the void ratio within the fabric of the small grains. Thus, examination of the data demonstrated a distinguishing feature in the behavior of the mixtures: in cases where the void ratio of the host (or large grains) is kept constant, there is an increase in the critical fines

content of mixtures as the void ratio of the smaller grains is decreased (Table 3-3 and Equation (3-2)). It follows that the fabric of the small grains during unloading will be more densely packed than when loading; consequently, there will be a delay in the critical fines content during unloading when compared to that of loading. This phenomenon can also be observed in the experimental results of the n exponent versus fines content (Figure 3.3). The maximum value for the n exponent occurs at a higher fines content during unloading when compared to loading. Consequently, due to the shift in the critical fines content during unloading, the maximum stress history effect for binary mixtures will be occurred below the critical fines content of the mixtures since the OCR exponent in Equation (3-6) is equivalent to the difference between the stress exponents in loading and unloading. And this led to that the maximum stress history effect of the tested mixture (ASTM 20/30 with SCS R40) was observed at approximately a fines content of 5 %.

Table 3-3. Calculated Critical Fines (Small Particles) Content

ASTM 20/30	ASTM 100/200		Sil-Co-Sil R40	
	e_{max}	e_{min}	e_{max}	e_{min}
e_{max}	0.283	0.322	0.209	0.312
e_{min}	0.211	0.243	0.152	0.234
ASTM 60/80	Sil-Co-Sil R40			
	e_{max}	e_{min}		
e_{max}	0.245	0.357		
e_{min}	0.172	0.263		

Note: the values shown above were obtained by the combination of extreme void ratios of large particles (ASTM 20/30 or ASTM 60/80) with those of small particles (ASTM 100/200 or SCS R40) by employing Equation (3-3) to estimate the possible

ranges of critical fines content.

3.5 Summary

This chapter identified the stress-history-based small strain stiffness of binary mixtures of sand-sand particles and silty sands with a small volume fraction of fines. The following key observations were noted from the theoretical analysis and experimental investigation performed in this study:

1. Theoretical analysis demonstrated that the OCR exponent in the G_{\max} relationship could be expressed in terms of stress exponents during loading and unloading.
2. The stress exponent in the G_{\max} relationship during loading varied as a function of the size ratio and fines content of the mixture, reflecting change in interparticle contact or interparticle coordination between larger particles.
3. The stress exponent in the G_{\max} relationship during unloading was closer to the theoretically derived stress exponent $1/3$ than the exponent during loading, and showed smaller variation according to contact type than that of loading.
4. The effect of OCR on the small strain stiffness of binary mixtures increased with decrease in size ratio (or increase in size difference) because the stress exponents during loading increased with a decrease in size ratio. This phenomenon was due to the interparticle coordination between large grains; while, the variation of stress exponents during unloading of different mixtures was relatively small due to the prevalent elastic deformation
5. The maximum stress history effect of ASTM 20/30 with SCS R40 was observed at a fines content of approximately 5 %, which was smaller than

critical fines content of the mixture due to the delay in critical fines content during unloading compared to that of loading.

CHAPTER 4 SMALL TO INTERMEDIATE STRAIN PROPERTIES OF FLY ASH WITH VARIOUS CARBON AND BIOMASS CONTENTS

4.1 Introduction

Fly ash is the fine, lightweight residue, generated from the combustion of fuel sources such as coal and/or biomass. Fly ash represents the combusted component that rises with the flue gases during combustion. Traditionally, combustion of coal has been the most prevalent source of fly ash; however, more recently, biomass has received attention as a supplemental, renewable fuel source that provides no net increase in CO₂ (Baxter 2005; Sami et al. 2001). Therefore, the fraction of cofired fly ash from co-combusting coal with biomass has rapidly increased. Additionally, the percentage of high carbon content fly ash generated by the power industry has increased in recent years, due to the conversion to low NO_x and SO_x burners in power plants that leave a larger percentage of unburned carbon remaining in the ash (Hower et al. 1997).

As of 2010 in the U.S., over 67 million tons of fly ash were generated as a byproduct of coal combustion, with approximately 40% being beneficially reused and 60% typically land disposed in surface impoundments or landfills (ACAA 2011). While the largest portion of beneficial reuse for fly ash is as a supplement of cement and concrete, according to ASTM C618, fly ash with LOI (loss on ignition, or carbon contents) greater than 6 % or biomass coal cofired fly ash cannot be used as a supplemental material in concrete or cement. Fly ashes with high carbon content and biomass coal cofired fly ashes are generally landfilled unless another beneficial

application can be found.

Because the high organic carbon content in fly ash can negatively impact the chemistry of concrete, the use of fly ash in large volume projects such as filler in asphalt, flowable fill, and structural fill can provide alternative applications in cases where the fly ash is unsuitable for use in concrete (ACAA 2003). Since geotechnical projects generally require large quantities of material, they are attractive because they lead to reduction in disposal costs, as well as conservation of natural resources. The geotechnical characterization of fly ash, including strength and stiffness, is essential to the successful completion of large scale projects. Previous work to quantify the shear strength of compacted fly ash for geotechnical applications has demonstrated that the strength is comparable to that of sand (Kim and Prezzi 2008; Kim et al. 2005; Pandian 2004; Trivedi and Sud 2002). Additionally, fly ash has demonstrated high potential of liquefaction when disposed in surface impoundments (Jakka et al. 2010a; Jakka et al. 2010b). However, studies on the geotechnical properties of fly ashes with high carbon content or coal and biomass cofired fly ashes are limited, both in terms of static and dynamic properties. Consequently, the goal of this study was to quantify the small to intermediate strain geotechnical properties of fly ashes with varying contents of carbon and biomass particles.

4.2 Theoretical Aspects

In this study, fly ash was considered a binary mixture, consisting of two submatrices: a matrix of large particles, consisting of unburned or partially burned carbon particles, and a matrix of small particles, consisting of aluminosilicate glassy microspheres (e.g., cenospheres and plerospheres) (Figure 4.1). Simplification of the structure of fly ash was used to facilitate analysis using existing physical concepts of

binary mixtures.

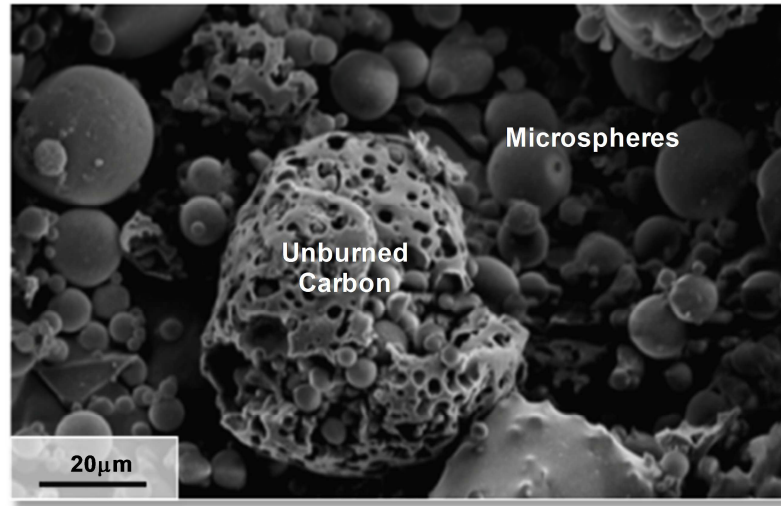


Figure 4.1. Typical SEM image for fly ash with unburned carbon.

4.2.1 Critical Fines Content / Critical Carbon Content

Taking fines content as the ratio of the weight of small particles to the weight of the total mixture results in a fines content (FC) that is equivalent to 1 – unburned carbon content or TOC. Combining the critical fines content (smallest void ratio of the mixture due to infilling of the pore space with smaller particles (Lade et al. 1998)), with the derivation from Chapter 2, results in the following:

$$FC^* = \frac{G_{sS} \cdot e_L}{G_{sL}(1 + e_S) + G_{sS} \cdot e_L} = 1 - TOC^* \quad (4-1)$$

where, e_S : void ratio of small particles (microspheres); e_L : void ratio of large particles (unburned carbons); G_{sL} : specific gravity of large particles; G_{sS} : specific gravity of small particles; FC^* : critical fines content; TOC^* : critical carbon content.

In cases where the specific gravities of particles are the same, Equation (4-1) can be simplified to:

$$FC^* = 1 - TOC^* \approx \frac{e_L}{1 + e_s + e_L} \quad (4-2)$$

In this study, Equation (4-1) was used, assuming different specific gravities for the particles in the mixture. The theoretical estimation of critical fines content (FC*) or critical carbon content (TOC*) of fly ash was obtained using the extreme void ratios of fly ash and carbon (Table 4-1), assuming a value of 1.8 for the specific gravity of unburned carbon particles, which were similar in nature to carbon black (Baltrus et al. 2001), and a specific gravity of 2.45 for fly ash (tested materials \approx 2.45, but generally ranged from 2 to 2.6, except in cases of high iron content). The variation of void ratio for unburned carbon particles, ranging from 1.6 ~ 3.5, was estimated from previous work that measured the variation of mass density for carbon black (Sanchez-Gonzalez et al. 2005), and the extreme void ratios of fly ash with low carbon content ranging from 0.5 to 1.7 (Charles-Cruz et al. 2008; Gandhi et al. 1999; Trivedi and Sud 2002). The combination of e_{\min} of small grains and e_{\max} of large grains yielded the largest number for critical fines content (or, the smallest critical carbon content) as anticipated: the maximum number will be obtained when the largest voids between large grains are filled with the smaller grains with the condition of their smallest voids. In cases where the content of unburned carbon particles is below 24 %, microspheres will be a structural skeleton, and the behavior of fly ash will be governed by the contacts between microspheres (Table 4-1).

Table 4-1. Calculated Critical Fines Content and Critical Carbon Content

Unburned Carbon	FC*		TOC*	
	Microspheres		Microspheres	
	e_{\max}	e_{\min}	e_{\max}	e_{\min}
e_{\max}	0.638	0.761	0.362	0.239
e_{\min}	0.442	0.588	0.558	0.412

Note: the values shown above were obtained by the combination of extreme void ratios of microspheres and unburned carbons by employing Equation (4-1) to estimate the possible ranges of critical fines content or critical carbon content.

4.2.2 Interfine Void Ratio

For binary mixtures that contain a large percentage of small particles, the global void ratio may not describe the behavior of soils because the small particles will be the active force chain while the large particles float within the small particle matrix and do not participate in the load carrying chain. Consequently, past work has introduced the concept of the interfine void ratio, instead of global void ratio, to describe the behaviors of mixed materials with high fines content ($FC > FC^*$) (Naeini and Baziar 2004; Thevanayagam 1998; Thevanayagam et al. 2002; Yang et al. 2006). In this concept of interfine void ratio, large particles are considered as zero volume since they cannot be retained into pore space of load-carrying skeleton, while, in the concept of intergranular void ratio, small particles, which are not a primary structural skeleton, are considered as void because they can be located between load-carrying large grains (Thevanayagam 1998) (Figure 4.2):

$$e_f = \frac{v_v}{v_s} = \frac{(v_s + v_L) \cdot e}{v_s} = \left(1 + \frac{v_L}{v_s}\right) \cdot e \quad (4-3)$$

where, V_v : volume of voids; V_s : volume of small particles; V_L : volume of large

particles; V_T : total volume; e : global void ratio. From Figure 4.2, the volume of large grains and small grains can be expressed in terms of weight as:

$$v_L = \frac{W_L}{G_{sL} \cdot \gamma_w} \quad (4-4)$$

$$v_S = \frac{W_S}{G_{sS} \cdot \gamma_w} \quad (4-5)$$

where, W_S : weight of small particles (microspheres); W_L : weight of large particles (unburned carbons). By substituting the definition of fines content ($FC = w_S / (w_L + w_S)$), (4-4) and (4-5) into Equation (4-3):

$$e_f = \left[1 + \left(\frac{1}{FC} - 1 \right) \cdot \frac{G_{sS}}{G_{sL}} \right] \cdot e = \left[1 + \left(\frac{1}{1-TOC} - 1 \right) \cdot \frac{G_{sS}}{G_{sL}} \right] \cdot e \quad (4-6)$$

If the specific gravities of mixtures are same, Equation (4-6) can be simplified to have the same form of Thevanayagam (1998):

$$e_f \approx \frac{e}{FC} = \frac{e}{1-TOC} \quad (4-7)$$

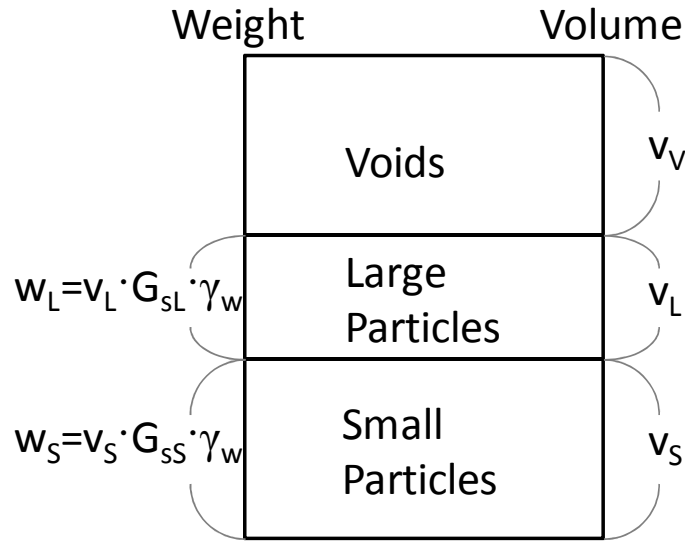


Figure 4.2. Phase diagram for fly ash with unburned carbon particles: large particles = unburned carbon particles; small particles = aluminosilicate microspheres.

4.3 Experimental Program

4.3.1 Materials

Seven different types of fly ash were obtained from four power plants throughout the southeastern United States: Georgia (CP1), Mississippi (CP2), and Alabama (CP3 and CP4). Typical material properties of the tested fly ash, including TOC, median grain size, specific surface, liquid limit, and specific gravity are given in Table 4-2 (Yeboah et al. (in preparation)). It is important to note that the specific gravity, or apparent specific gravity, of fly ash is impacted by its hollow structure, particle size, and iron content (Bouzoubaa et al. 1997; Kim et al. 2005; Pandian 2004; Paya et al. 1995; Tangpagasit et al. 2005), and is generally smaller than natural geomaterials, due to the retained air in the internal pore of the hollow microspheres. The fly ash samples tested in this study included ashes that resulted from the co-firing of coal and biomass, with the biomass wood contents indicated by weight (i.e. 4% co-

fire means that the fly ash was produced by co-firing 96% bituminous coal with 4% wood by weight.). The biomass wood materials include logging, paper mill, and sawmill waste. The resulting fly ashes had total organic carbon contents ranging from 1.1 to 9.6 %, resulting from initial unburned biomass contents ranging from 0 to 8.2 %, by weight.

Table 4-2. Material Properties

Sample ID	TOC (%)	D ₅₀	BET S _a	G _s	LL (%)	Type
		(μm)	N ₂ @ 77K (m ² /g)			
CP1	1.1	16.2	1.27	2.62	25.8	100% Coal
CP2-1	2.2	14	3.01	2.54	25.5	100% Coal
CP3-1	4.9	29.9	4.6	2.47	46.9	100% Coal
CP3-2	4.6	26.9	2.5	2.45	50	4% Co-fire
CP3-3	4.3	23.3	3.48	2.39	61.9	8.2% Co-fire
CP4-1	9.6	21.7	8.12	2.37	34.3	100% Coal
CP4-2	7.7	18.8	8.9	2.39	38.6	5.5% Co-fire

Note: CP = coal or cofired fly ash (class F fly ashes produced from bituminous coal);

D₅₀ = median grain size; S_a = specific surface; G_s = specific gravity; LL = liquid limit

Increases in the biomass wood content of the fly ash resulted in an increased liquid limit (Figure 4.3) under the assumption that initial combustion mixing ratio of coal and wood was preserved in the ratio of ashes derived from coal and wood. Increases in the liquid limit as a function of increased biomass content would indicate the presence of biomass derived particles composed of hydrophilic functional groups (Baxter 2005). The increased water demand has also been observed for coal biomass

cofired fly ash when mixing with cement (Wang et al. 2008). In contrast, there was no any specific relation identified between organic carbon contents of 100 % coal ashes and liquid limit under the tested carbon contents.

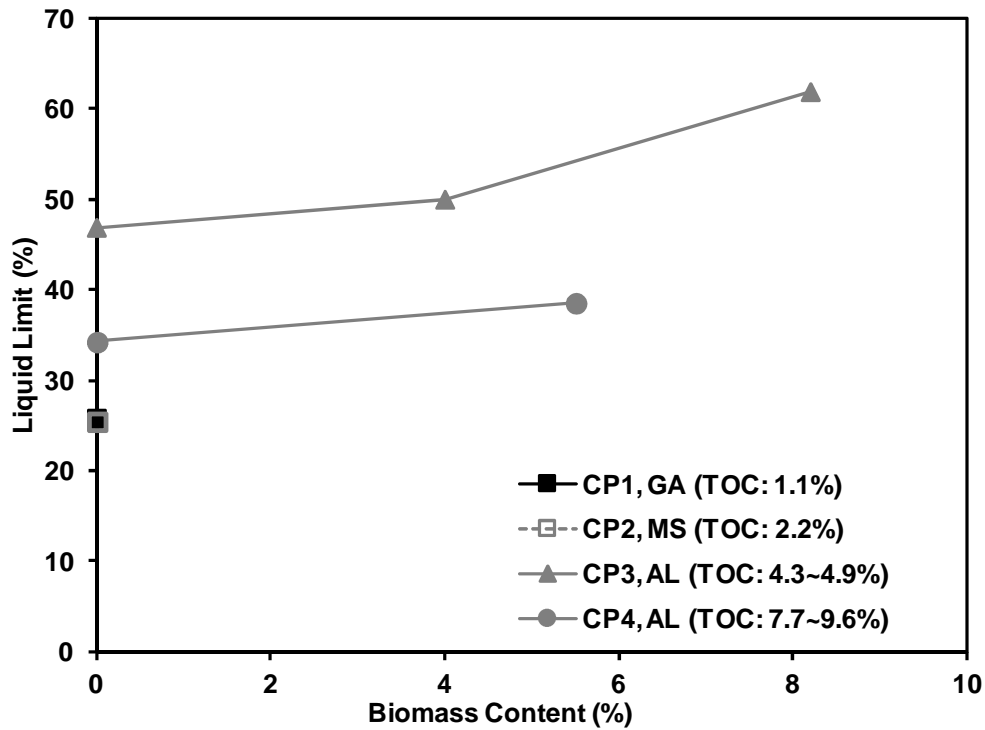


Figure 4.3. Liquid limit variation with biomass content, indicating the presence of hydrophilic functional group.

4.3.2 Test Equipment and Shear Wave Velocity Measurement

Bender elements were used to generate and detect shear waves ($V_s(VH)$ and $V_s(HH)$): parallel-type bender elements with dimensions of 10 mm in length, 7 mm in width, and 0.6 in thickness were used to minimize electromagnetic coupling, with two pairs of bender elements fitted inside a modified oedometer cell to detect the shear waves as a function of consolidation loading (Lee and Santamarina 2005)

(Figure 4.4). Prepared specimens were tested in K_0 conditions at vertical stresses ranging from 14.7 kPa to 427.3 kPa, and shear waves were measured during both consolidation loading and unloading processes. The generation of shear waves was made by the excitation of the transmitter with a square wave of a frequency (f) = 20 Hz, and amplitude = 10 V, as generated by a function generator (33210A, Agilent). The generated signal was detected by the receiver, which was connected to a filter amplifier (3364, Krohn-Hite), and the, filtered and amplified signal was collected using a digital oscilloscope (DSO5014A, Agilent). Shear wave velocity was determined from the simple equation between travel length and travel time (Equation 4-8), with the travel time (t) carefully chosen to consider the near field effect (Lee and Santamarina 2005; Sanchez-Salinero et al. 1986), and the tip-to-tip distance between two bender elements was selected as travel distance (L) (Fernandez 2000; Lee and Santamarina 2005; Viggiani and Atkinson 1995a):

$$V_s = \frac{L}{t} \tag{4-8}$$

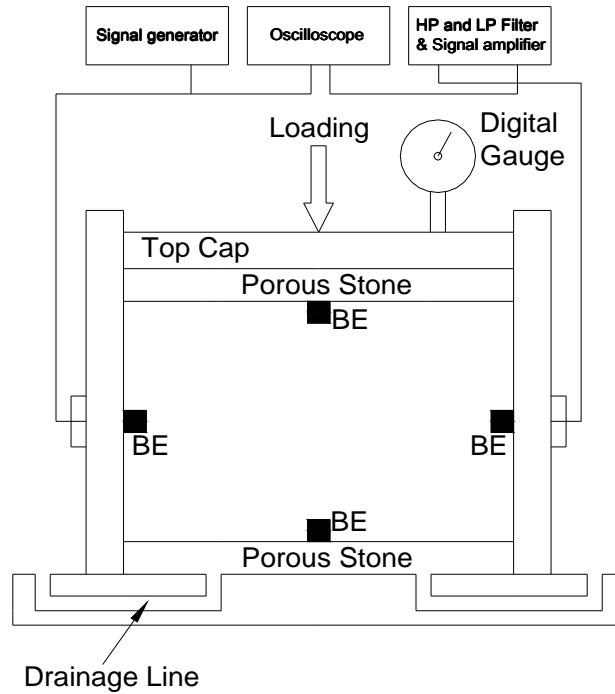


Figure 4.4. Setup for shear wave measurement, after the method of Lee and Santamarina (2005).

The wave velocity can be expressed as a function of the direction of wave propagation and particle motion, with stress terms that have two different directions (Equation (4-9)) (Roesler 1979; Santamarina et al. 2001; Yu and Richart 1984). Additionally, from the measured shear wave velocity, the maximum shear modulus can be calculated according to Equation (4-10). Consequently, by measuring shear wave velocity in different directions, the stiffness anisotropy of the soils can be evaluated. In this study, bender elements were installed in two different directions: vertically propagating and horizontally polarizing (VH), and horizontally propagating and polarizing (HH). Combining (4-9) and (4-10) yields stiffness as a function of the direction of wave propagation and particle motion:

$$V_s = \alpha \left(\frac{\sigma'_p + \sigma'_m}{2kPa} \right)^\beta \quad (4-9)$$

$$G_{\max} = \rho \cdot V_s^2 \quad (4-10)$$

$$G_{\max}(VH) = \Lambda_1 \left(\frac{\sigma'_v + \sigma'_h}{2kPa} \right)^{\xi_1} = \Lambda_1 \left(\frac{1+K_0}{2kPa} \cdot \sigma'_v \right)^{\xi_1} \quad (4-11)$$

$$G_{\max}(HH) = \Lambda_2 \left(\frac{\sigma'_h + \sigma'_h}{2kPa} \right)^{\xi_3} = \Lambda_2 \left(\frac{K_0}{1kPa} \cdot \sigma'_v \right)^{\xi_3} \quad (4-12)$$

where, ρ is mass density, σ'_p and σ'_m are the stresses of wave propagation and particle motion, respectively, σ'_v and σ'_h are the vertical and horizontal effective stresses, respectively, Λ is experimentally determined factor, which is same with the value of G_{\max} at 1 kPa, and ξ is an experimentally determined exponent.

4.3.3 Sample Preparation

In order to reduce the possibility of self-hardening due to the presence of CaO, all fly ash samples were washed with deionized water prior to testing to remove cementitious materials, and tests were conducted under both saturated and dry conditions. The test results for the dry specimens were used only for the evaluation of stiffness anisotropy, and the remaining test results were gathered under saturated conditions. Saturated fly ash specimens were prepared using a slurry method: dry fly ashes were mechanically mixed with pre-determined amount of water (typically 1.2~1.3 times LL) for 20 minutes, stored in a plastic bag for at least 24 hours for the proper hydration or saturation, and remixed for 20 minutes before specimen preparation. The dry specimens were air-rained into the oedometer cell, and moderately densified by symmetric vibration, to initial (dry) void ratios of CP1, CP4-1, and CP4-2 were 0.995, 1.266, and 1.306, respectively.

4.4 Test Results and Analysis

4.4.1 Effect of Carbon Content on G_{\max}

The test results from the fly ashes produced from firing of pure coal (100% coal) demonstrated that the maximum shear modulus (small strain stiffness) increased with an increase in vertical stress, due to the increase in both contact area and coordination number as anticipated, and decreased with an increase in carbon content (Figure 4.5). The fly ashes tested in this study contained large volumes of microspheres (small particles), and relatively small volumes of large, unburned carbon particles, with the mixture condition of $FC > FC^*$, or $TOC < TOC^*$; consequently, it can be assumed that the applied force was transferred through the contacts of microspheres. As the carbon content was increased, the interfine void ratio increased since larger carbon particles disrupted the direct contacts between small microspheres, and decreased the interparticle coordination number. Therefore, increasing TOC yielded a decrease of both interparticle contacts and interparticle coordination number between microspheres, resulting in a decrease in stiffness of fly ashes at a given global void ratio (Lee et al. 2007) until the mechanism shifted to carbon particles as the dominant applied load carrying skeleton ($TOC > TOC^*$). However, it is important to note that the interfine void ratio (or contacts between microspheres) is the function of not only carbon content but also global void ratio (Equation (4-6)), leading to the fact that the stiffness of fly ashes as a function of carbon content will be affected by both carbon content and global void ratio (or water content). Therefore, a decrease in small strain stiffness with an increase in carbon content will be only valid for a given void ratio. The combined effect of carbon

content and global void ratio may explain the negligible difference between G_{max} of CP3-1 and CP4-1: initial global void ratio of CP3-1 ($e_0=1.213$) was greater than that of CP4-1($e_0=1.091$) leading to almost identical interfine void ratio and similar small strain stiffness between those two since CP4-1 had higher carbon content.

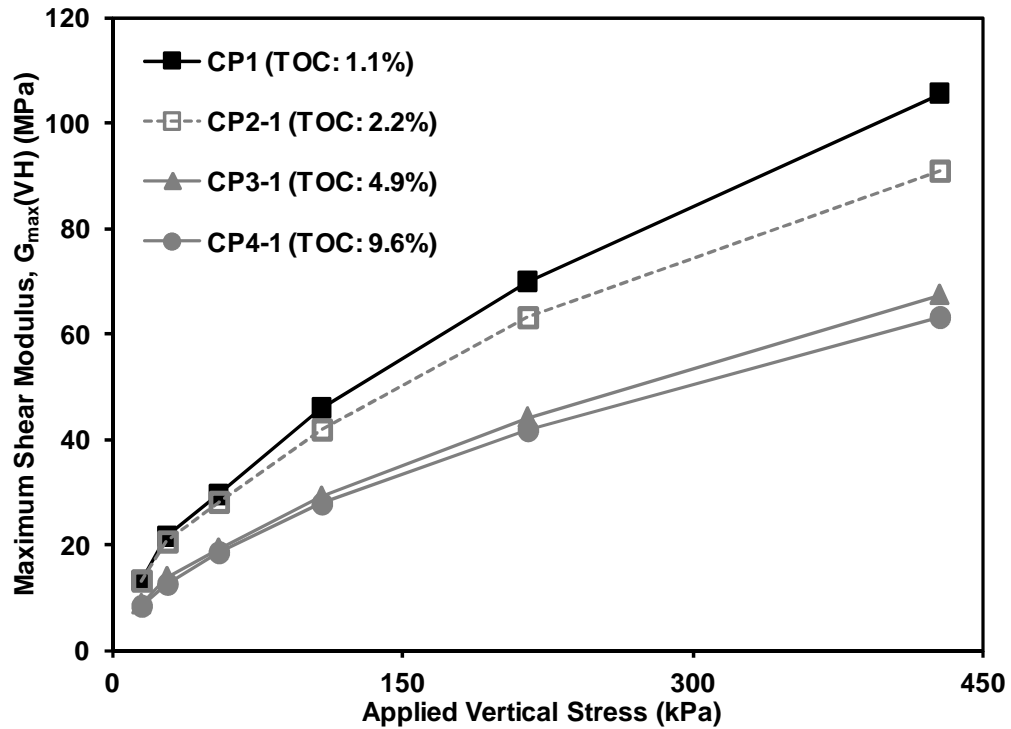
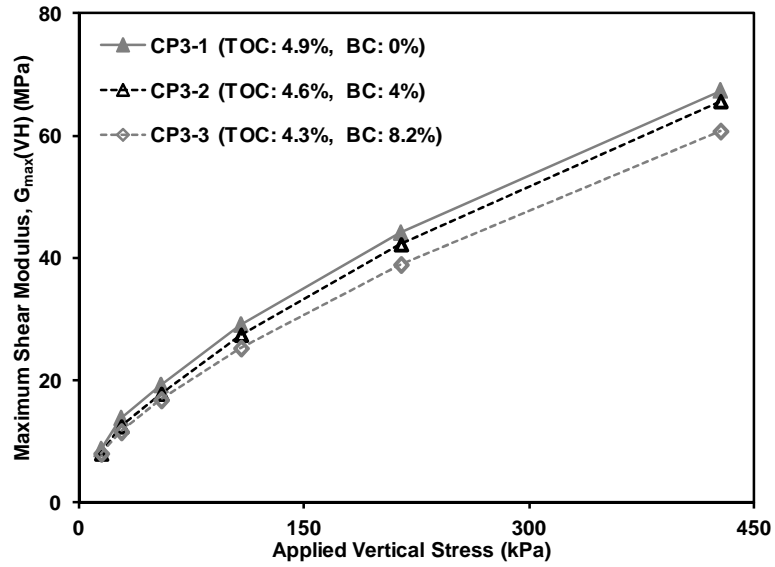


Figure 4.5. G_{max} dependency on carbon content for 100 % coal fired fly ashes: unburned carbon contents (TOC) = 1.1 ~ 9.6 %.

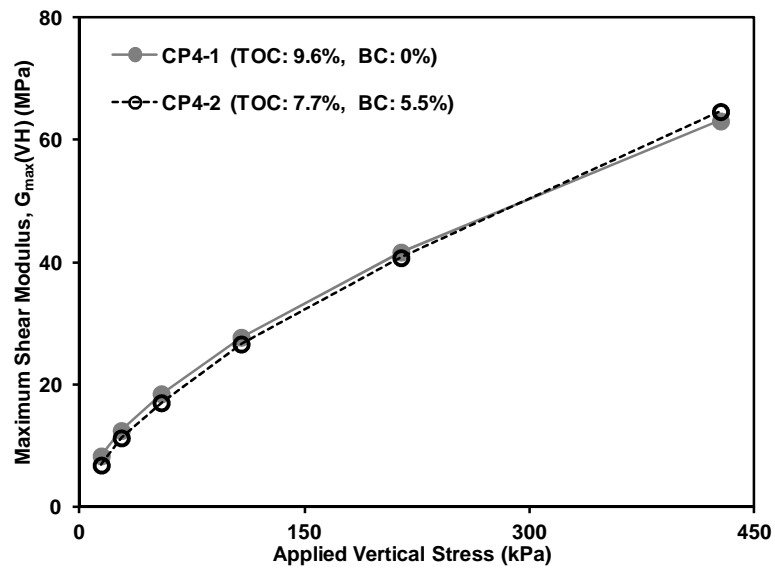
4.4.2 Effect of Biomass Content on G_{max}

Comparing pure coal and biomass cofired fly ashes produced in the same power plant demonstrated that the small strain stiffness of fly ash decreased as the initial content of the biomass was increased; that is, fly ash produced from the firing of pure coal resulted in a stiffer material when compared to fly ash that was produced

when biomass was cofired with coal (Figure 4.6). However, it can also be observed that the effect of biomass content on G_{\max} is minimal, and the small strain stiffness of fly ashes as a function of biomass content was comparable, regardless of the biomass contents (BC < 10% in this study). Additionally, for the cofired fly ash samples, the unburned carbon content of the fly ash decreased as the biomass content was increased. The samples tested in this study exhibited an increase in global void ratio as the biomass content was increased, which is believed to have resulted from an increased hydrophilicity of the particle surfaces due to the functional groups on the biomass derived ash particles. At the same time, the interfine (or, inter-microspheres) void ratio of the mixture will decrease with a decrease in carbon content, leading to limited change in overall net contacts between microspheres, which were the active force chain. Consequently, the comparable G_{\max} of fly ashes with various biomass contents (BC < 10%) can be observed. The reason for this contradictory trend between the carbon content and the biomass content is not clear; however, previous studies (Grammelis et al. 2006a; Wieck-Hansen et al. 2000) also observed similar trends when biomass contents were smaller than 20 % by weight.



(a) CP3 Samples



(b) CP4 Samples

Figure 4.6. G_{max} dependency on biomass content: (a) CP3 samples with biomass contents ranging from 0 to 8.2 %; (b) CP4 samples with biomass contents ranging from 0 to 5.5 %; BC = biomass content; TOC = unburned carbon content. Note that CP3 samples (CP3-1, 2 and 3) were produced in the same power plant, and CP4 samples (CP4-1 and 2) were produced in the same power plant.

4.4.3 G_{\max} in Terms of Interfine Void Ratio

Evaluation of the maximum shear modulus of fly ash as a function of interfine void ratio (Equation (4-6), Figure 4.7) indicated that the maximum shear modulus of different fly ashes could be expressed as a single function, regardless of carbon content or biomass content. Because the stiffness of soils is determined by the stiffness of interparticle contacts and fabric state (Lee et al. 2007; Mitchell and Soga 2005; Santamarina et al. 2001), which is represented by the nature of the interparticle contacts and interparticle coordination, it is clear that the alteration of the coordination and contact between spheres due to the carbon content can be captured using the concept of interfine void ratio (Figure 4.7). Additionally, higher stiffness of fly ash deposits can be obtained by reducing either global void ratio (or water content) or carbon content, because interfine void ratio is a function of both of those parameters.

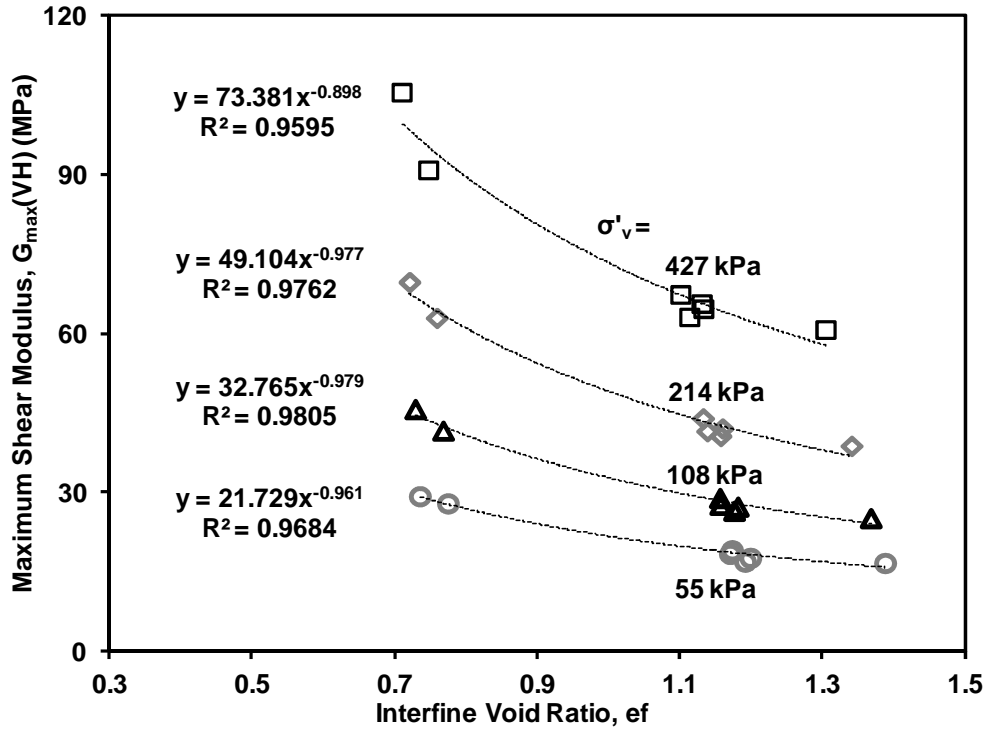


Figure 4.7. G_{\max} variation as a function of effective vertical stress and interfine void ratio: G_{\max} of different fly ashes can be expressed in terms of interfine void ratio regardless of fly ash fuel source.

4.4.4 Intermediate Strain Properties: Constrained Modulus or Compressibility

Test results of this study were evaluated in terms of the effect of initial mixing water content ($w = \text{weight of water} / \text{weight of dry fly ash}$) on the intermediate-strain constrained modulus of different fly ashes. Figure 4.8 shows the variation of volumetric (or vertical) strain of tested fly ashes according to the applied vertical stress: the variation of maximum vertical strain varied with fly ash type. Thus, constrained moduli of different fly ashes were plotted with their initial mixing water contents as shown in Figure 4.9. Most notably, it can be found that, regardless of fly ash type, the constrained moduli of different fly ashes were directly determined by their initial water content (or initial void ratio), which is consistent with previous

studies (Hardin 1987; Hryciw and Thomann 1993) reflecting soils with higher packing density or higher coordination number will have higher resistance to deformation or volume change. In addition, the constrained modulus increased with an increase in applied vertical stress as anticipated reflecting an increase in frictional resistance at interparticle contacts. Therefore, reducing the initial mixing water content will be the most efficient way to achieve higher constrained modulus or smaller compressibility of the fly ash deposits at a given applied stress.

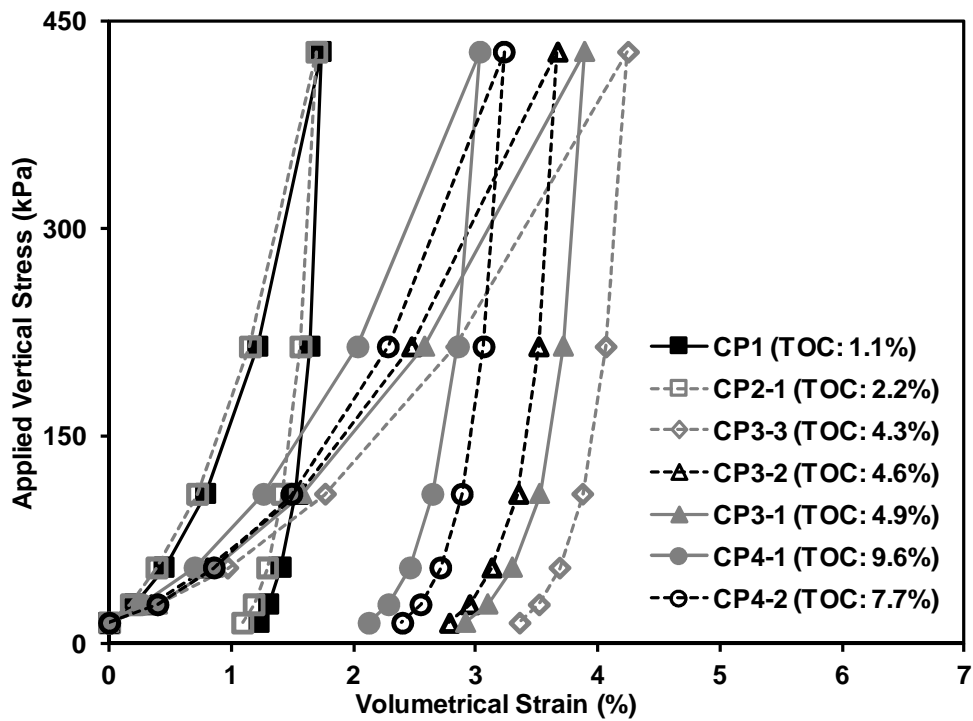


Figure 4.8. Variation of volumetric strain according to vertical stress: the variation of maximum vertical strain varied with fly ash type.

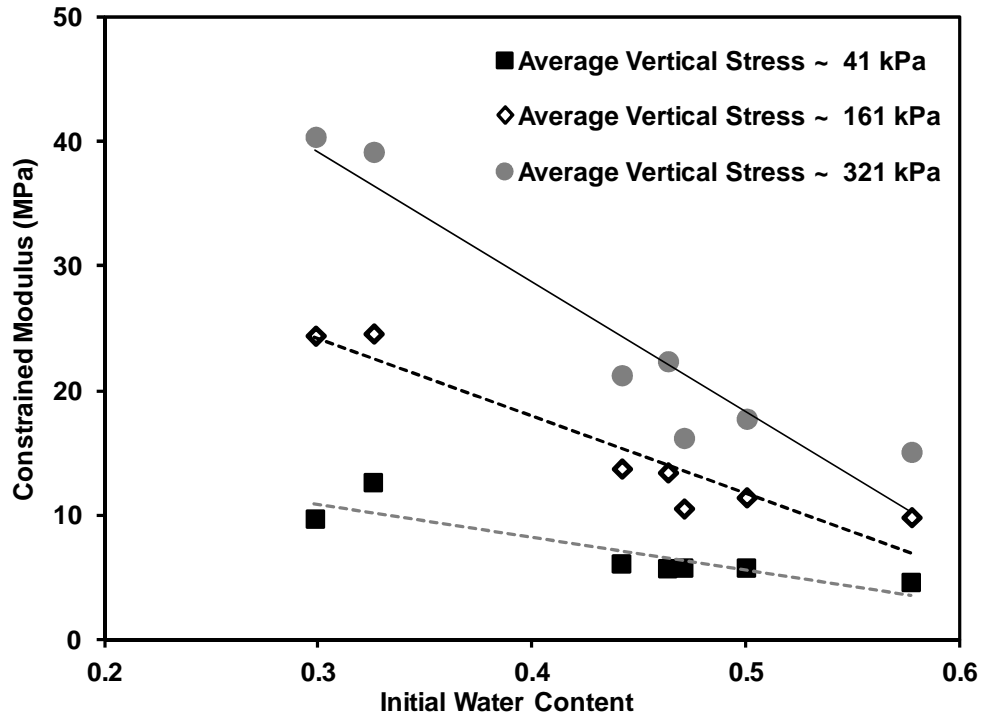


Figure 4.9. Variation of constrained modulus with initial water content: constrained modulus decreased with increasing initial mixing water content and applied stress reflecting an increase in mass density and frictional resistance.

4.4.5 Stiffness Anisotropy of Fly Ash

The ratio of $G_{\max}(\text{HH})$ to $G_{\max}(\text{VH})$ of the dry fly ashes tested as a function of loading in the vertical direction resulted in a ratio that was smaller than one (Figure 4.10), which reflected the prevalent stress-induced anisotropy of the tested fly ashes under K_0 conditions. These data were similar to the results of previous studies on normally consolidated coarse grains under K_0 conditions (Zeng and Ni 1999; Zeng and Ni 1998). For the soils satisfying conditions of stress-induced anisotropy, $G_{\max}(\text{VH})$ should be greater than $G_{\max}(\text{HH})$ under normally consolidated K_0 condition, because K_0 is typically smaller than 1 (Wang and Mok 2008). It is important to note

that there was no clear effect of carbon content on the alteration of stress-induced anisotropy, and the range of anisotropy ratio was very small, regardless of carbon content.

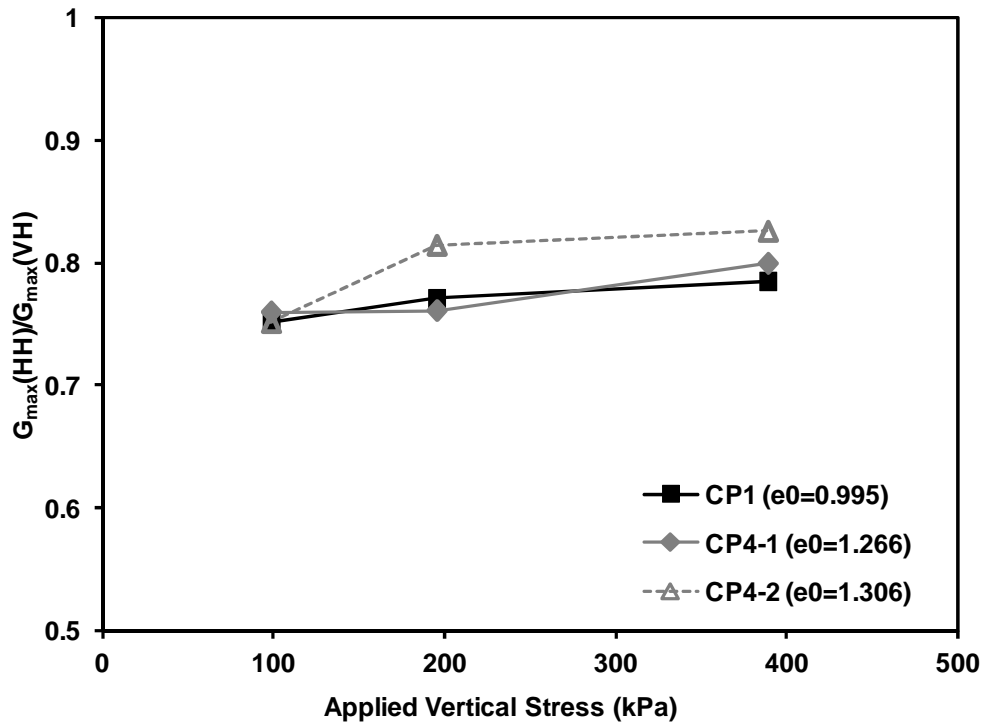


Figure 4.10. Stress-induced small strain stiffness anisotropy during loading: variation of $G_{\max}(\text{HH}) / G_{\max}(\text{VH})$ as a function of vertical stress. Note: $G_{\max}(\text{HH})$ (Equation (4-12)); $G_{\max}(\text{VH})$ (Equation (4-11)).

The inherent anisotropy can be evaluated under an isotropic stress state to isolate the effect of stress-induced anisotropy. In order to investigate the effect of inherent anisotropy indirectly, the fabric (or inherent) anisotropy factor A_F was defined in this study as the ratio of Λ_2 to Λ_1 (Equation (4-13)), which was derived by combining Equations (4-11) and (4-12) under the assumption that the stress exponents

ξ were same regardless of direction (Hardin and Blandford 1989). Additionally, the K_0 -coefficient during unloading was estimated from the relationship proposed by Mayne and Kulhawy (1982) (Equation (4-14)).

$$A_F = \frac{\Lambda_2}{\Lambda_1} = \frac{G_{\max}(HH)}{G_{\max}(VH) \left(\frac{2 \cdot K_0}{1 + K_0} \right)^\xi} \quad (4-13)$$

where, A_F = fabric (or inherent) anisotropy factor; K_0 = coefficient of lateral earth pressure at rest; ξ = stress exponent in G_{\max} formula.

$$K_0 = (1 - \sin \varphi) \cdot OCR^{\sin \varphi} \quad (4-14)$$

where, φ = friction angle; OCR = overconsolidation ratio. Furthermore, when the estimated “ $K_0 \approx 1$ ” due to the lateral stress locking during unloading, Equation (4-13) can be simplified to:

$$A_F = \frac{\Lambda_2}{\Lambda_1} = \frac{G_{\max}(HH)}{G_{\max}(VH)} \quad (4-15)$$

This allowed direct comparison between material constants Λ_1 and Λ_2 based on the measured maximum shear modulus. A_F is close to one for soils (sphere-shaped particles) with negligible inherent anisotropy, while, for soils that are composed of plate-shaped particles with strong inherent anisotropy, A_F is typically greater than one. The variation of the fabric anisotropy factor and K_0 -coefficient during unloading vertical effective stress ranges (50 ~ 100 kPa) showed that the fabric anisotropy factor was very close to one, when the estimated K_0 -coefficient was set equal to one (representing $A_F \approx 1$ at the condition of Equation (4-15)) (Figure 4.11). To estimate the K_0 -coefficient during unloading using Equation (4-14), the critical state friction of fly ash was assumed equal to 30 degrees (Kim et al. 2005), and A_F was calculated

using the estimated K_0 -coefficient (Equation (4-13)). These data showed that the tested fly ashes had negligible effects of inherent anisotropy, which can be attributed to the predominantly spherical shape of fly ash particles (Kutchko and Kim 2006; Matsunaga et al. 2002).

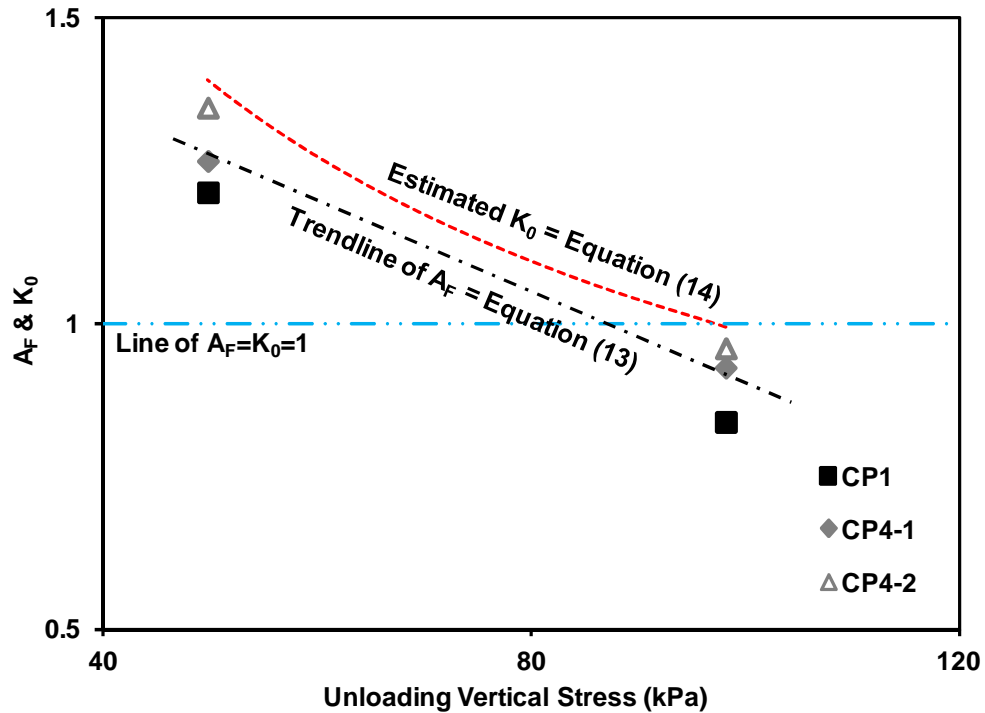


Figure 4.11. Inherent stiffness anisotropy at small strains obtained by plotting the variation of A_F and K_0 -coefficient according to unloading vertical stress: A_F (fabric anisotropy factor) = Equation (4-13); K_0 coefficient = Equation (4-14).

4.5 Summary

This chapter quantified the small to intermediate strain properties of fly ashes as a function of carbon and biomass contents. The following conclusions can be drawn:

1. With an increase in carbon and biomass contents, the small strain stiffness of fly ashes decreased due to a decrease in direct contacts between microspheres.
2. The stiffness of inter-microsphere contacts is affected by both carbon content and global void ratio.
3. The effect of biomass content on the alteration of small strain stiffness was limited due to the combined mechanisms of interaction: the global void ratio increased with an increase in biomass content; however, the interfine void ratio decreased with an increase in carbon content.
4. The alteration of the nature of the interparticle contacts or interparticle coordination number can be sufficiently captured by employing interfine void ratio instead of global void ratio.
5. Initial mixing water content governed the compressibility (or constrained modulus) of fly ashes.
6. Both small and intermediate strain properties were directly determined by void ratio (or water content) leading to beneficial reuse or stable disposal of fly ash that can be achieved by densification of fly ash or reduction of the initial mixing water content.
7. Fly ash particles showed strong stress-induced anisotropy; however, inherent anisotropy was negligible due to their spherical particle shape.

CHAPTER 5 IMPACT OF UNBURNED CARBON PARTICLES ON THE ELECTRICAL CONDUCTIVITY OF FLY ASH SLURRY

5.1 Introduction

Fly ash is the lightweight residue produced from the combustion of energy sources. Historically, combustion of coal has been the most prevalent source of fly ash, producing fly ashes that are generally low in carbon content. However, recent changes to the regulations governing power plants, as defined by the Clean Air Act, have necessitated conversion to low NO_x and SO_x burners during coal combustion, which when combined with the increase in co-combustion of coal and biomass as a fuel source to accommodate the Kyoto Protocol, has resulted in coal fired fly ash and biomass coal co-fired fly ashes with high carbon contents (Baxter 2005; Hower et al. 1997; Sami et al. 2001). This increase in organic content has resulted in a net decrease in the amount of fly ash that is suitable for beneficial reuse as a supplemental material in concrete or cement because ASTM C618 sets strict limits on organic content and fuel sources (ACAA 2011). Consequently, fly ashes with high carbon content or biomass coal co-fired fly ashes are generally either land disposed, or may be used in other construction materials (Hwang et al. 2002; Naik et al. 2006). Determination of accurate and reliable carbon content of fly ashes with relatively high unburned carbon content remains an important step in the beneficial reuse of fly ash.

Loss on ignition (LOI) is the most commonly accepted testing method to determine the unburned carbon content in fly ashes; however, it cannot be performed as a real time measurement. Consequently, several techniques for the on-line monitoring of carbon content such as microwave absorption, capacity measurement,

photoacoustic effect, infrared emission, and optical dispersion have been developed that can be performed during the combustion of fuel (Styszko-Grochowiak et al. 2004). In contrast, there is no proper method for determining the carbon content of fly ash after disposal, except LOI; however, it is important to note that using LOI for in-situ carbon content measurement is relatively time consuming and is limited due to difficulty in sampling and representativeness.

Recently, the stability issues associated with fly ash surface impoundments attracted attention due to the environmental and human health impacts that have resulted from spills during ash pond failures (Ruhl et al. 2009; Yeboah and Burns 2011). Among the several failures of ash ponds in the U.S., the TVA ash spill (Tennessee Valley Authority ash spill in Kingston, Tennessee in 2008) was the most significant. According to the final report from the TVA ash spill investigation team (AECOM 2009), the high water content (high void ratio of ashes) was one of the most critical factors contributing to the failure of the ash pond. In addition, it is well known that stress-strain relation of geomaterials is directly determined by state variables, with void ratio being one of the most important variables in determining the behaviors of materials such as compressibility, strength, and stiffness of the soil matrix. In cases where the estimated void ratio (or water content) of pond ash is very high, ground improvement to enhance the factor of safety of pond ash can be achieved by geotechnical methods such as blasting (Gandhi et al. 1999).

In this study, the electrical resistivity/conductivity method will be used for the estimation of void ratio because it is one of the most reliable, continuous, and precise methods for determining void ratio or water content of the particulate matrix. In mixtures of fly ash and unburned organic carbon particles, the method is particularly attractive because unburned carbon particles are electrically conductive, resulting in a

measured media conductivity that will be a function of carbon content. In this study, efforts were directed toward evaluating the electrical conductivity of fly ashes as a function of carbon content and void ratio by employing a four electrode resistivity probe.

5.2 Theoretical Aspects

5.2.1 Electrical Conductivity

The electronic transport phenomenon in a porous media can be modeled as three resistances in parallel, under the assumption that the orientation of particles is parallel to the applied electrical field (derivation of this equation can be found from Chapter 8):

$$\sigma_{mix} = \sigma_p \cdot (1-n) \cdot \left(\frac{L}{L_p}\right)^2 + \sigma_w \cdot \frac{n}{T^2} + \sigma_s \cdot \frac{1-n}{T^2} \cdot S_a \cdot G_s \cdot \rho_w \quad (5-1)$$

where, σ_{mix} , σ_p , and σ_w are the electrical conductivities of the media (or mixture), particles, and pore water, respectively (S/m); σ_s is the surface conductivity (S); S_a is specific surface (m^2/g); n : porosity; G_s : specific gravity; ρ_w : mass density of water; T : tortuosity; L : total length; L_p : length of flow path for particles. This relationship indicates that the measured (or mixed) media conductivity is the sum of particle conduction K_p (the first term), pore water conduction K_w (the second term), and surface conduction K_s (the last term).

In this study, fly ash was modeled as a binary mixture consisting of two subsets: the matrix of large particles (unburned carbon particles) and the matrix of small particles (aluminosilicate glassy microspheres, such as cenospheres and plerospheres) (Chapter 4). Consequently, the carbon contents TOC can be defined as

(Figure 5.1):

$$TOC = \frac{w_{CARBON}}{w_{MICROSPHERE} + w_{CARBON}} = \frac{v_{CARBON} \cdot G_{sCARBON}}{v_{MICROSPHERE} \cdot G_{sMICROSPHERE} + v_{CARBON} \cdot G_{sCARBON}} \quad (5-2)$$

where, w = weight; v = volume.

Additionally, the volume fraction of solid matrix can be defined as:

$$1 - n = \frac{v_{CARBON}}{v_T} + \frac{v_{MICROSPHERE}}{v_T} \quad (5-3)$$

Combination of the previous relationships results in a volume fraction of carbon particles that can be defined as:

$$\frac{v_{CARBON}}{v_T} = \frac{1 - n}{1 + \left(\frac{1}{TOC} - 1 \right) \cdot \frac{G_{sCARBON}}{G_{sMICROSPHERE}}} \quad (5-4)$$

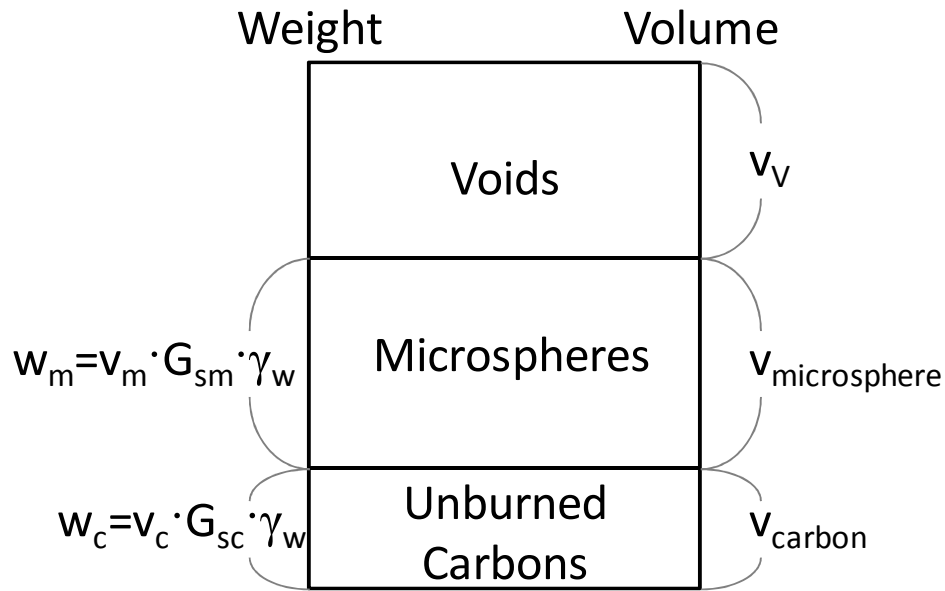


Figure 5.1. Phase diagram for fly ash with unburned carbon content.

Aluminosilicate glassy microspheres (cenospheres or plerospheres) are non-conducting materials, while, unburned carbon particles have high electrical

conductivity. Consequently, it was assumed that only the volume fraction of unburned carbon particles would contribute to the particle conduction of different fly ashes. Additionally, the mass contents of tested conductive unburned carbon particles (total organic carbon, TOC) was relatively small (i.e., TOC < 10%), so it was assumed that the carbon particles were dispersed and had limited direct contacts between them (Chapter 4), resulting in the use of a combined (or corrected) particle conductivity instead of the pure particle conductivity of carbon, according to the following:

$$\sigma_{mix} = \sigma_{cp} \cdot \frac{(1-n)}{\left(1 + \left(\frac{1}{TOC} - 1\right) \cdot \frac{G_{sCARBON}}{G_{sMICROSPHERE}}\right)} \cdot \left(\frac{L}{L_p}\right)^2 + \sigma_w \cdot \frac{n}{T^2} + \sigma_s \cdot \frac{1-n}{T^2} \cdot S_a \cdot G_s \cdot \rho_w \quad (5-5)$$

where, σ_{cp} = corrected particle conductivity in S/m.

5.2.2 Stress Dependency of Conductive Particles

Because soils are composed of particulate materials with variable contact points and contact area, the particle conduction (K_{cp} , first term in Equation (5-5)) is not a constant but will be affected by applied stress. The electric conduction of particulate materials will be determined by the conductivity (or, conduction) of the contacts between particles. According to the theory of electric contacts (Holm 1946), the contact resistance between two conductive spheres (or, the constriction resistance of the interface) can be expressed as (Figure 5.2):

$$r = \frac{\rho_1 + \rho_2}{4 \cdot a} \quad (5-6)$$

From the inverse relationship, the conductance is defined according to:

$$G = \frac{4 \cdot a}{\rho_1 + \rho_2} \quad (5-7)$$

where, r : resistance; G : conductance; ρ_1 and ρ_2 : resistivities of sphere 1 and 2 respectively; a : radius of the circular contact area of two spheres. Equations (5-6) and (5-7) clearly show that an increase in contact radius or area will result in an increase in electrical conductivity due to the increase in the volume of electric flow path (Slade 1999).

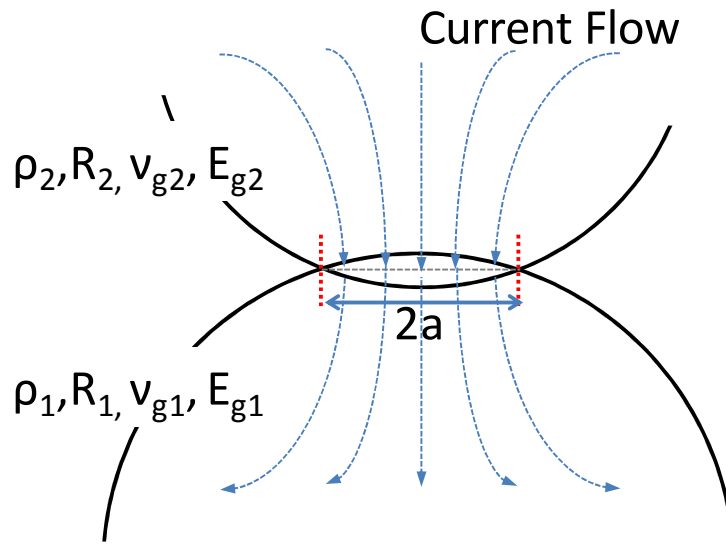


Figure 5.2. Schematic diagram of two electrically conductive spheres in contact: a = contact radius; E_g and ν_g = elastic properties of grains; R = radius of sphere; ρ = resistivity of sphere.

From the Hertzian contact, the contact radius between two spheres in contact in Equation (5-7) can be expressed as (Figure 5.2) (Johnson 1985):

$$a = \left(\frac{3 \cdot F_N \cdot R^*}{4 \cdot E^*} \right)^{1/3} \quad (5-8)$$

where, $\frac{1}{E^*} = \frac{1 - \nu_{g1}^2}{E_{g1}} + \frac{1 - \nu_{g2}^2}{E_{g2}}$ and $\frac{1}{R^*} = \frac{1}{R_1} + \frac{1}{R_2}$. In the case where two spheres

in contact have the same elastic properties (E_g and ν_g), and the same radius (R),

Equation (5-8) can be simplified to:

$$a = \left(\frac{3 \cdot F_N \cdot R \cdot (1 - \nu_g^2)}{4 \cdot E_g} \right)^{1/3} \quad (5-9)$$

where, F_N : normal force; R : radius of sphere; ν_g : Poisson's ratio of the material; E_g : elastic modulus of the material. Under the assumption of simple cubic (SC) packing, the normal force (F_N) can be expressed in terms of normal stress (Fernandez and Santamarina 2001):

$$F = 4 \cdot \sigma_N \cdot R^2 \quad (5-10)$$

where, σ_N : normal stress.

Combining (5-9) and (5-10) will yield:

$$a = \left(\frac{3 \cdot (1 - \nu_g^2)}{E_g} \right)^{1/3} \cdot R \cdot \sigma_N^{1/3} \quad (5-11)$$

Recalling Equation (5-7), in the case where the resistivities (ρ) of spheres in contact are the same, Equation (5-7) simplifies to:

$$G = \frac{2 \cdot a}{\rho} \quad (5-12)$$

Combining with the derivation based on the elastic deformation of two spheres in contact, and substituting (5-11) into (5-12) will yield:

$$G = \frac{2 \cdot a}{\rho} = \frac{2}{\rho} \cdot \left(\frac{3 \cdot (1 - \nu_g^2)}{E_g} \right)^{1/3} \cdot R \cdot \sigma_N^{1/3} \quad (5-13)$$

This relationship determines the conductance of two electrically conductive spheres in contact, and is a function of resistivity of the particle, elastic modulus, Poisson's ratio, radius of particle, and applied stress (proportional to the power of 1/3). It is interesting

to note that Holm (1967) determined that the conductance was proportional to the stress (or force) to the power of $1/3$ in the case of purely elastic deformation and $1/2$ in the case of purely plastic deformation.

5.3 Experimental Program

5.3.1 Materials

Seven fly ash samples were obtained from power plants in the southeastern United States (Georgia (CP1), Mississippi (CP2), and Alabama (CP3 and CP4)) and were tested in this study (Table 5-1). Detailed description of the physical and chemical characteristics of the tested materials is reported in Yeboah et al. (in preparation). The tested fly ashes had carbon contents (total organic carbon (TOC) or loss on ignition (LOI)) ranging from 1.1 to 9.6 % (TOC- $V_{CPH/CPN}$, SSM-5000A, Shimadzu Co. Kyoto, Japan). Biomass content, which represented the percentage of fuel source provided by biomass, ranged from 0 to 8.2 % by weight. Median grain size, which was measured by laser diffraction (Sympatec GmbH, Rodos T4.1) in air, showed a relatively narrow range, regardless of fly ash type. The specific gravity ranged from 2.37 to 2.62, with lower values resulting from the hollow shape of the fly ash particles (Bouzoubaa et al. 1997; Kim et al. 2005; Pandian 2004; Paya et al. 1995; Tangpagasit et al. 2005). The specific surface was measured by liquid nitrogen adsorption (Micromeritics, ASAP 2020), and the liquid limits were measured using the fall cone apparatus (Wykeham Farrance Engineering Ltd, Slough, England) (British Standard 1377).

Table 5-1. Material Properties

Sample ID	TOC (%)	LOI (%)	D ₅₀ (μm)	BET S _a N ₂ @ 77K	G _s	LL (%)	Type
CP1	1.1	1.4	16.2	1.27	2.62	25.8	100% Coal
CP2-1	2.2	3.1	14	3.01	2.54	25.5	100% Coal
CP3-1	4.9	5.8	29.9	4.6	2.47	46.9	100% Coal
CP3-2	4.6	5.5	26.9	2.5	2.45	50	4% Co-fire
CP3-3	4.3	5.2	23.3	3.48	2.39	61.9	8.2% Co-fire
CP4-1	9.6	8.9	21.7	8.12	2.37	34.3	100% Coal
CP4-2	7.7	7.4	18.8	8.9	2.39	38.6	5.5% Co-fire

Note: CP = coal or co-fired fly ash (class F fly ash produced from bituminous coal); D₅₀ = median grain size; S_a = specific surface (m²/g); G_s = specific gravity; LL = liquid limit

5.3.2 Test Equipment

In order to minimize the electrochemical effect on the tests (i.e. ion accumulation on electrode), a four electrode configuration was employed (Campanella and Weemees 1990; Kim et al. 2011a). A plane type 4 electrode resistivity probe was installed inside a modified oedometer cell constructed of PVC (Kim et al. 2011a) (Figure 5.3). In this configuration, the current flowed between the outer two electrodes and the electrical resistance was measured using the two inner electrodes using a LCR meter (Agilent, 4236B). The operating frequency of the LCR meter was selected as 100 kHz to prevent electrode polarization and resonance (Kim et al. 2011a; Kim et al. 2011b) and the input voltage was 1 V. The electrical resistance was converted to resistivity by employing the proper calibration factor (or geometrical

factor) (Equation (5-14)):

$$\rho = K \cdot R \quad (5-14)$$

where, ρ : resistivity in $\Omega \cdot m$; K: calibration (geometrical) factor in m; R: resistance in Ω . The factor K in Equation (5-14) can be determined using in either of two ways: the first is the indirect determination based on the geometry of electrodes (Reynolds 1997; Samouelian et al. 2005), and the other one is the direct determination via the calibration of probe with electrolyte solutions prepared at varying concentrations. Both methods were used in this study, and the measured calibration factors, determined using an aqueous electrolyte solution (NaNO_3) and the calculated geometrical factor based on spacing of electrodes, yielded very similar results (0.018 m).

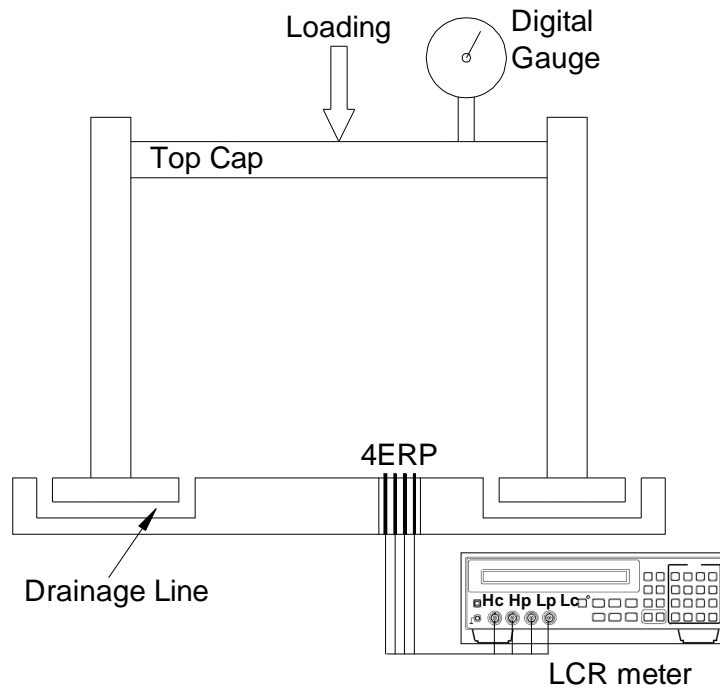


Figure 5.3. Setup for electrical resistivity/conductivity measurement after the method of Kim et al. (2011a).

5.3.3 Sample Preparation and Electrical Conductivity/Resistivity Measurements

All fly ash samples were washed with deionized water (Barnstead E-pure) before testing to control the pore water conductivity. Samples were washed until the conductivity of the supernatant was less than 0.01 S/m. Testing specimens were prepared by employing a slurry preparation method: fly ashes were mechanically mixed with pre-determined amount of water (typically 1.2~1.3 times LL) for 20 minutes. Those mixtures were stored in a plastic bag for at least 24 hours to allow for hydration. After remixing the pre-saturated fly ash slurries, test specimens were prepared in a PVC cell. Prepared samples were tested under K_0 conditions at vertical stresses ranging from 13.9 kPa to 443.6 kPa, with electrical resistivity/conductivity being measured at the end of each loading and unloading step. Tests were conducted

under three different pore water conductivities at 0.02 M, 0.1 M, and 0.5 M NaNO₃ in order to assess the impact of pore water conductivity on the measured media conductivity.

5.4 Test Results and Analysis

5.4.1 Electrical Conductivity as a Function of Void Ratio

The electrical conductivity of fly ash samples prepared at three levels of pore fluid conductivity demonstrated measured electrical conductivity of fly ash increased with an increase in carbon content (Figure 5.4). Note that the initial void ratio of different fly ash samples varied according to the measured liquid limit, and the change in void ratio (or densification of fly ash) was achieved using loading and unloading under vertical stress. In a notable deviation from most geomaterials, the variation of electrical conductivity as a function of void ratio did not follow Archie's equation, regardless of pore water conductivity, reflecting the relevance of particle conduction through unburned carbon particles (Figure 5.4 c). Most geomaterials are electrically non-conducting, resulting in a porous media conductivity that is primarily determined by pore water conduction and surface conduction of particles. Furthermore, if the specific surface area is not large (i.e., sand and gravel) or the salinity of pore water is high, the electrical conductivity of porous media will be controlled by the pore water conductivity, as shown by Archie's equation (Archie 1942). Consequently, if the soil deposit obeys Archie's equation, the electrical resistivity of soil will increase with a decrease in void ratio (or, the electrical conductivity of soil will decrease with a decrease in void ratio) due to the decrease in the number of channels available for electric conduction.

Additionally, the measured electrical conductivity obtained during loading and unloading did not match, which also supports the relevance of particle conduction since conductive particles are affected by applied stress due to the changes induced in the contact area and coordination number. Finally, with an increase in pore water conductivity, the measured conductivity increased, as was anticipated (Equation (5-5)).

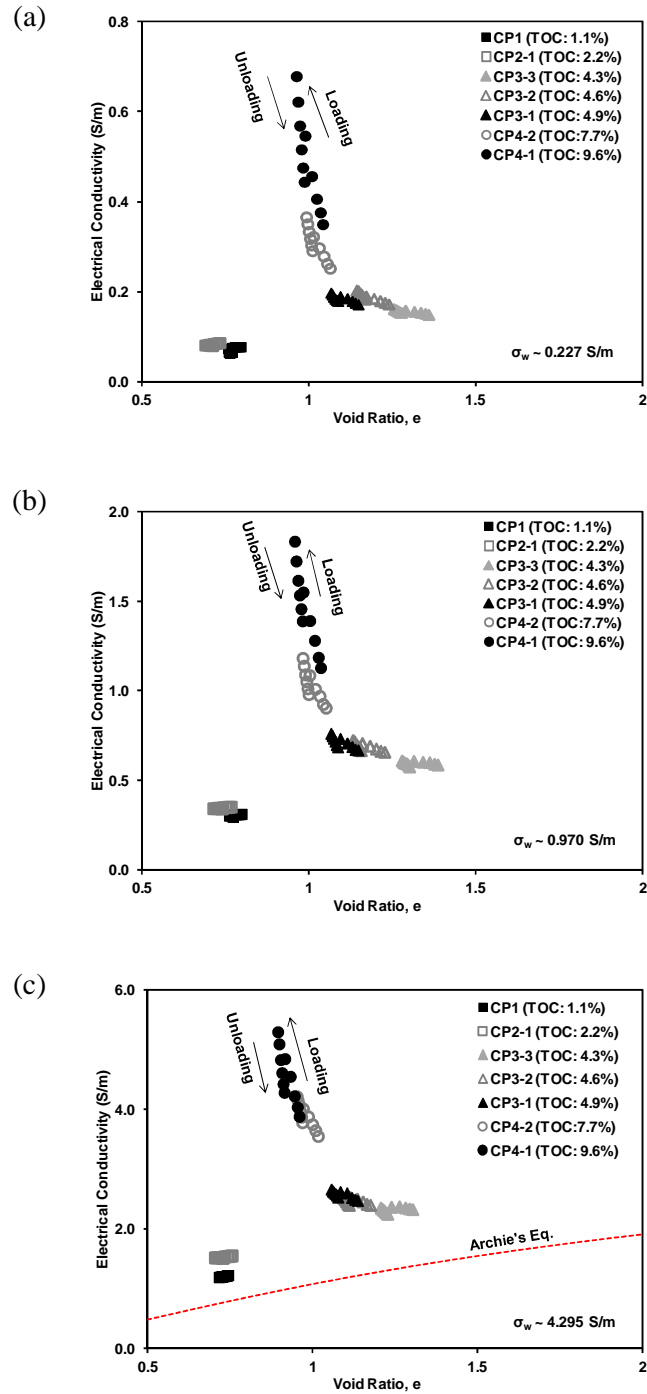


Figure 5.4. Electrical conductivity of tested fly ashes according to void ratio and applied stress: (a) $\sigma_w = 0.227$ S/m; (b) $\sigma_w = 0.970$ S/m; (c) $\sigma_w = 4.295$ S/m. Note that Archie's equation ($\sigma_{\text{mix}} = n^m \cdot \sigma_w$, m was assumed as 2) was plotted under the assumption of fully-saturated condition.

5.4.2 Carbon Particle Conduction

In this study, the role of surface conduction on the media conductivity was not considered, under the assumption that pore water conduction was much greater than surface conduction at high salinity, and the particle conduction was greater than the surface conduction at low salinity. Consequently, the contribution of surface conductivity on the conductivity of the porous media was neglected, and the carbon particle conduction was calculated from the measured mixed conductivity and the estimated pore water conduction as shown according to Equation (5-15):

$$\sigma_{cp} \cdot \frac{(1-n)}{\left(1 + \left(\frac{1}{TOC} - 1\right) \cdot \frac{G_{sCARBOM}}{G_{sMIRCOSPHERE}}\right)} \cdot \left(\frac{L}{L_p}\right)^2 = \sigma_{mix} - \sigma_w \cdot \frac{n}{T^2} \quad (5-15)$$

$$T = n^{-p} \quad (5-16)$$

The tortuosity in Equation (5-15) was estimated following the power law relation between tortuosity factor and porosity of the porous media as shown in Equation (5-16) (Boudreau 1996; Dias et al. 2006; Koponen et al. 1996; Matyka et al. 2008; Shen and Chen 2007), and the exponent “p” in (5-16) was assumed as 0.5 (Dias et al. 2006).

The carbon particle conduction as a function of the unburned carbon content of tested fly ashes (pore water conductivities of 0.970 and 4.295 S/m and applied vertical stress of 28 kPa) demonstrated that the carbon particle conduction increased almost linearly with an increase in carbon content (Figure 5.5). It is notable that the tested fly ashes were prepared under different initial water contents; consequently, in order to isolate the effect of pore water conduction and to highlight the variation of carbon particle conduction according to carbon content, the carbon particle

conduction calculated using Equation (5-15) was determined as a function of carbon content. The volume fraction of conducting carbon particles was directly determined from the carbon content (Equation (5-4)), and an increase in TOC (or with an increase in volume fraction of conducting particles) will produce an increase in the electrical conductivity of fly ash due to the decrease in spacing between conductive particles. Because the properties of unburned carbon particles in fly ash are very similar to the properties of carbon black (Baltrus et al. 2001), it is important to note that previous studies on the conductivity of carbon black also noted that the mass density of carbon black was one of the most important factors determining electrical conductivity/resistivity of the media. This is attributable to the fact that electron tunneling or jumping of electrons between particles can be more active with a decrease in the space between conducting particles (Marinho et al. 2012; Pantea et al. 2003; Sanchez-Gonzalez et al. 2005).

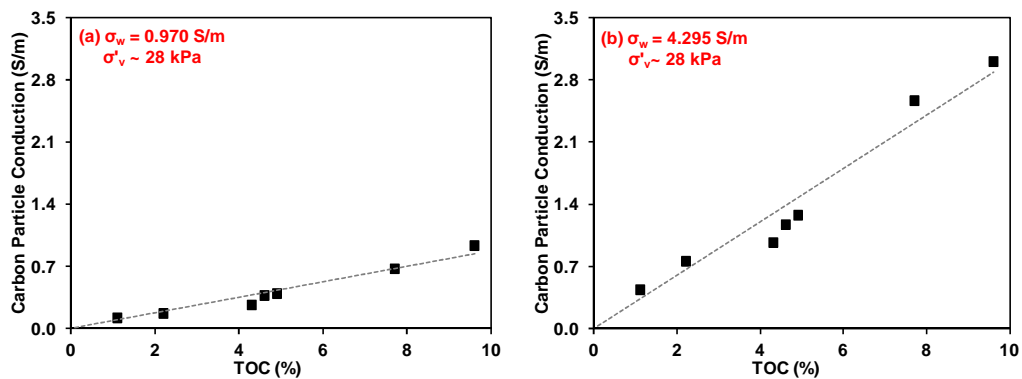


Figure 5.5. Carbon particle conduction according to carbon content: (a) $\sigma_w = 0.970$ S/m; (b) $\sigma_w = 4.295$ S/m; applied vertical effective stress: 28 kPa; carbon particle conduction = Equation (5-15).

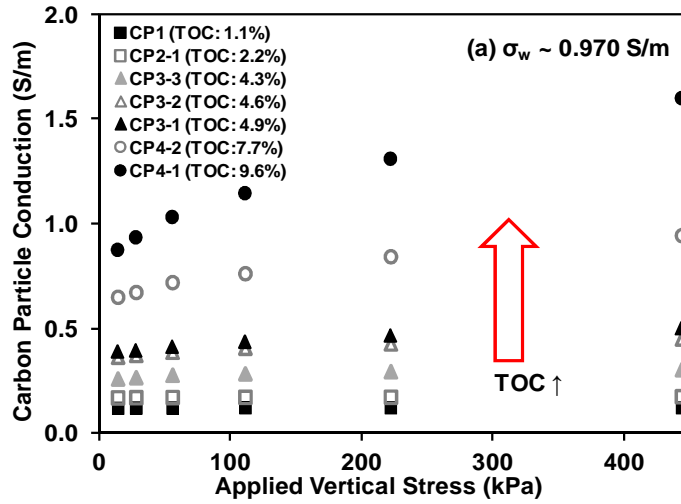
5.5 Discussion

5.5.1 Dependency of Carbon Particle Conduction on Stress

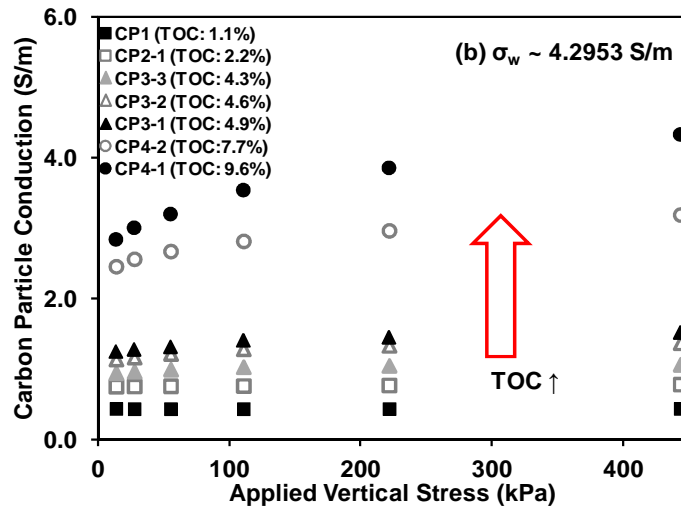
From the theory of electrical contacts, the measured conductivity of conductive materials in contact is stress-dependent; however, the maximum carbon content of tested fly ashes in this study was 9.6%. This resulted in a matrix of non-conducting aluminosilicate glassy microsphere particles that occupied the largest volume of the fly ash mixture. At this low percentage of carbon, it was difficult to make direct contact between the relatively small number of carbon particles, which resulted in a measureable, but limited effect of applied stress on the measured conductivity, especially in the case of very low carbon content fly ash samples (Figure 5.6). However, the observed dependency of carbon particle conduction on the applied stress increased with an increase in carbon content, and carbon particle conduction could be expressed as the power function of applied stress (Holm 1967)(Figure 5.6):

$$K_{cp} = \alpha \cdot \left(\frac{\sigma'_v}{1kPa} \right)^\beta \quad (5-17)$$

where, K_{cp} : corrected carbon particle conduction in S/m; α : experimentally determined factor in S/m; β : experimentally determined stress exponent reflecting stress-dependency of particle conduction (1/3 for purely elastic deformation and 1/2 for purely plastic deformation); σ'_v : vertical effective stress in kPa.



(a) $\sigma_w = 0.970$ S/m



(b) $\sigma_w = 4.295$ S/m

Figure 5.6. Dependency of carbon particle conduction on applied vertical stress: (a) $\sigma_w = 0.970$ S/m; (b) $\sigma_w = 4.295$ S/m.

Taking the stress exponent (β) of different fly ashes at pore water conductivity of 4.295 S/m showed that the stress exponent increased with an increase in carbon content (Figure 5.7). This can be explained by the development of direct

contacts between conducting carbon particles as the carbon content of the mixture is increased. Furthermore, it follows that the stress exponent would increase as the carbon content increases, to the mixture transition point at which unburned carbon particles would form the structural skeletal of fly ash. In this condition, the relatively larger carbon particles would make direct particle-to-particle contact and the smaller microspheres would be retained within the pore space of the carbon particles. This condition is described by the critical fines content (FC*) or critical carbon content (TOC*), and was previously estimated as ranging from 23.9 % to 55.8 % (TOC*), according to the packing density of the matrices of large and small particles (Chapter 4). At the packing volume where carbon particles develop direct contact between them ($TOC > TOC^*$), the increase in the stress exponent according to carbon content would be attenuated, and the stress exponent would approach that of electric conduction of conductive particles, ranging from $1/3$ to $1/2$.

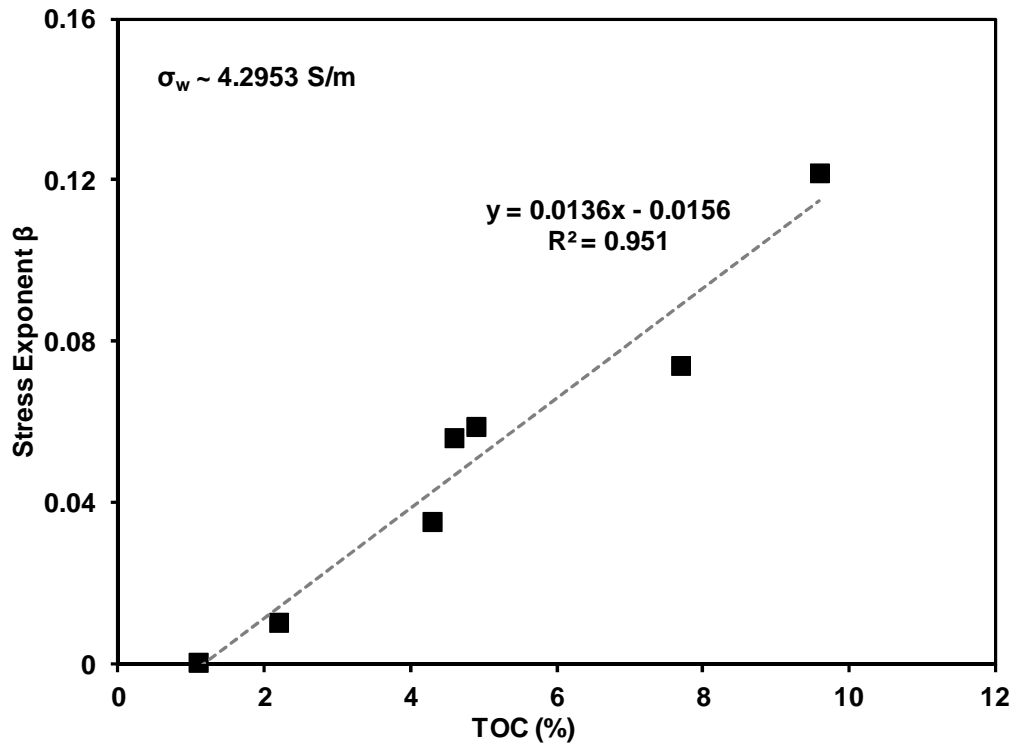


Figure 5.7. Stress dependency of different fly ashes according to carbon content: stress exponent reflects the dependency of carbon particle conduction on applied stress (Equation (5-17)).

5.5.2 Dependency of Carbon Particle Conduction on Pore Water Conductivity

It was reported that the major governing mechanism in the particle conduction of carbon black is electron tunneling between conductive particles (Jager et al. 2001; Sanchez-Gonzalez et al. 2005). Therefore, from the similar properties of unburned carbon particles with those of carbon black (Baltrus et al. 2001), the unburned carbon particle conduction may be mainly determined by electron tunneling between conductive unburned carbon particles. In addition, previous studies showed that electron tunneling is governed by the characteristics of pore water (Benjamin et al. 1997; Galperin et al. 2002); consequently, carbon particle conduction will be

mediated by the conductivity of pore water, which may affect the electron tunneling probability and acts as a barrier of electrical conduction between carbon particles. This explanation can be modeled as three modified resistances in parallel (i.e. particle resistance, pore water resistance, and surface resistance). Equation (5-1) was developed based on the three parallel resistances model, under the assumption of parallel geometry between the orientation of particles and the applied electrical field (Figure 5.8) (Klein and Santamarina 2003; Pfanckuch 1972):

$$\frac{1}{r_{mix}} = \frac{1}{r_p} + \frac{1}{r_w} + \frac{1}{r_s} \quad (5-18)$$

From the inverse relationship between resistance and conductance:

$$G_{mix} = G_p + G_w + G_s \quad (5-19)$$

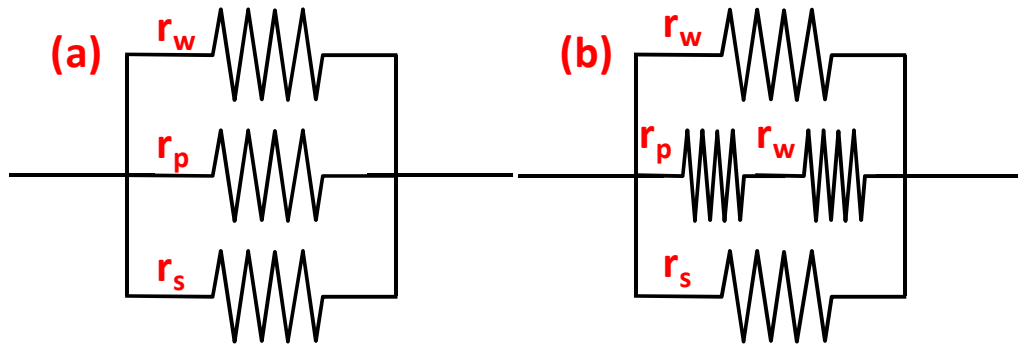


Figure 5.8. Three resistances in parallel: (a) general model; (b) modified model for carbon particles; r_w = pore water resistance; r_p = particle resistance; r_s = surface resistance.

However, electron tunneling is affected by the characteristics of pore water (i.e. pore water conductivity); thus, Equation (5-19) can be modified leading to (Figure 5.8):

$$\frac{1}{r_{mix}} = \frac{1}{r_p + r_w} + \frac{1}{r_w} + \frac{1}{r_s} \quad (5-20)$$

with the reciprocal of resistance equal to the conductance:

$$G_{mix} = G_{cp} + G_w + G_s \quad (5-21)$$

where, $G_{cp} = \frac{G_p \times G_w}{G_p + G_w}$ (corrected or combined particle conductance).

By comparing (5-19) and (5-21), it can be observed that the particle conductance term has been changed and it is affected by pore water conductance according to:

$$\lim_{G_w \rightarrow 0} \frac{G_p \times G_w}{G_p + G_w} = 0 \quad (5-22)$$

$$\lim_{G_w \rightarrow \infty} \frac{G_p \times G_w}{G_p + G_w} = G_p \quad (5-23)$$

This analysis demonstrated that the particle conductance (electron tunneling) of conductive particles in the saturated condition would be affected by both the pure conductance of particles and the pore water conductance. In cases where the conductivity of the pore water is very low, the overall particle conductance will be very small regardless of conductivity of particles, while, in cases where the pore water conductivity is extremely high, the overall particle conductance will approach that of pure particle conductance.

Examination of the impact of pore water conductivity on carbon particle conduction demonstrated that carbon particle conduction increased almost linearly with an increase in pore water conductivity, regardless of fly ash type or carbon content (Figure 5.9, plotted under applied vertical stress of 28 kPa). It is also notable that the relationship between the corrected particle conductance and pore water conductance (Equation (5-21)) also implied a linear relationship between particle

conductance and pore water conductance, except in the case where pore water conductance was very high. It also follows that fly ashes with high carbon content showed greater carbon particle conduction.

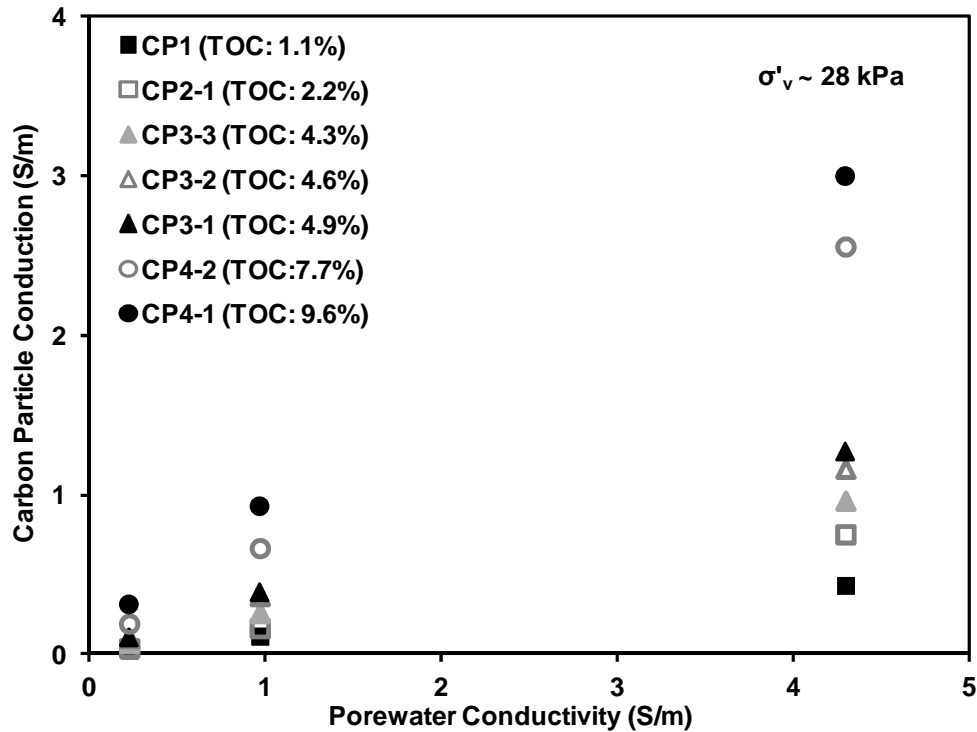


Figure 5.9. Dependency of carbon particle conduction on pore water conductivity: carbon particle conduction = Equation (5-15); applied vertical effective stress = 28 kPa.

5.5.3 Estimation of Carbon Particle Conduction by Regression Analysis

A regression analysis was performed using every possible factor that could impact the carbon particle conduction based on the theoretically derived electrical conductivity model and experimental results. The delicate interplay of those parameters, including carbon content, porosity, applied vertical stress, and pore water

conductivity, with the carbon particle conduction was evaluated with the help of regression software (R), result in the following conduction relationship ($R^2=0.985$):

$$K_{cp} = 0.0389 \cdot TOC^{0.9068} \cdot n^{-1.1006} \cdot \left(\frac{\sigma'_v}{1kPa} \right)^\beta \cdot \sigma_w^{0.8372} \cdot K_R^{0.1628} \quad (5-24)$$

where, $\beta = 0.0136 \cdot TOC - 0.0156$; TOC is in %; σ'_v is in kPa; σ_w is in S/m; K_R is reference conductivity (1 S/m); K_{cp} is in S/m. From the regression analysis, it is notable that the exponent of TOC in Equation (5-24) is close to one, similar to the TOC function in the theoretical model (Equation (5-15)), and the porosity function was comparable to the combined function of porosity and the ratio of total length to length of the particle path in Equation (5-15). In addition, as discussed above, the stress dependency of the unburned carbon particles in the dispersed state (TOC < TOC*) varied with carbon content, leading to a stress exponent in (5-24) that was a function of carbon content (Figure 5.7). Finally, the exponent of pore water conductivity was close to one, reflecting an almost linear relationship between corrected particle conduction and pore water conduction at low pore water conductivity, as was implicated in Equation (5-21).

In summary, under the assumption that the contribution of the surface conduction to media conductivity was small compared to that of particle conduction or pore water conduction, the porous media conductivity of fly ashes with various carbon contents can be expressed by combining carbon particle conduction (Equation (5-24)) and the pore water conduction:

$$\sigma_{mix} = \sigma_w \cdot n^m + 0.0389 \cdot TOC^{0.9068} \cdot n^{-1.1006} \cdot \left(\frac{\sigma'_v}{1kPa} \right)^\beta \cdot \sigma_w^{0.8372} \cdot K_R^{0.1628} \quad (5-25)$$

where, $m=2 \cdot p+1$ from Equations (5-15) and (5-16): the exponent “m” is a shape factor

or cementation factor from Archie's equation, and it generally ranged from 1.5 to 2.5, according to the shape of particles and pores (Glover et al. 1997; Salem and Chilingarian 1999). However, it is important to note that Equation (5-24) and (5-25) are only valid when $TOC < TOC^*$. In the case where unburned carbon particles have a continuous phase ($TOC > TOC^*$), the stress exponent will approach to that derived from theory, ranging from $1/3$ to $1/2$, regardless of carbon content. Finally, this study neglected the role of surface conduction, which means that the particle conduction (Equation (5-24) or (5-25)) may include the some portion of surface conduction at low salinity because the carbon particle conduction was calculated from the difference between the measured mixed conductivity and the estimated pore water conduction (Equation (5-15)).

5.6 Summary

This chapter examined the electrical properties of fly ashes as a function of carbon content and void ratio, and the role of unburned carbon particle conduction on the media conductivity was evaluated by a four electrode resistivity probe. The following key observations are drawn from this study:

1. With an increase in pore water conductivity, the measured media conductivity of the fly ashes increased, as was anticipated.
2. In a primary difference from fly ash microspheres, unburned carbon particles were electrically conductive. As carbon content increased, the measured electrical conductivity increased, regardless of pore water conductivity, due to the decrease in spacing between conductive particles.

3. With an increase in TOC, conductive carbon particles will be more dependent on applied stress due to the increased possibility of direct contacts between carbon particles. However, it can be postulated that carbon content dependency of stress exponent will be minimal when carbon particle become a structural skeleton ($TOC > TOC^*$).
4. The main mechanism of electric conduction of conductive unburned carbon particles was electron tunneling, resulting in carbon particle conduction that was impacted by both pure particle conduction, and pore water conduction.
5. Based on the electrical resistivity/conductivity measurement, a reasonable estimation of in-situ carbon content or void ratio of fly ashes can be achieved.
6. The effect of biomass content (percentage of biomass as fuel source) on electrical conductivity was not discussed in this study because the overall media conductivity was primarily governed by the unburned carbon content.

CHAPTER 6 THERMAL CONDUCTIVITY OF DRY FLY ASHES WITH VARIOUS CARBON AND BIOMASS CONTENTS

6.1 Introduction

More than 40% of the electricity generated in the United States is produced through the combustion of coal (EIA 2012), which results in the production of byproducts such as greenhouse gases and fly ash. Traditionally, fly ash was generated by the combustion of pure coal, resulting in low levels of unburned carbon content and levels of beneficial reuse of approximately 40 % in the United States (ACAA 2011). However, more recently, the level of unburned carbon in fly ash has increased as a result of stricter air emission standards and co-firing of biomass and coal (Baxter 2005; Hower et al. 1997; Sami et al. 2001). In the U.S., high carbon content makes the fly ash unusable by the cement and concrete industry, which is the biggest market for the reuse of fly ash (ASTM C618). As a result, the higher organic carbon content fly ashes are land disposed at a high rate, and the mechanical and chemical properties of fly ash are relatively well developed (Baxter 2005; Grammelis et al. 2006a; Grammelis et al. 2006b; Wang et al. 2008); however, the thermal properties of fly ash remain relatively unquantified. Therefore, this study assessed the thermal conductivity of ten different fly ashes as a function of carbon content and biomass content, and compared the behavior of fly ash with the thermal conductivity of natural geomaterials.

6.1.1 Thermal Conductivity

Because of their importance in many areas of engineering, soil science, and agriculture, the thermal properties of soils have been studied since the 1850s (Ochsner et al. 2001). The thermal conductivity, thermal diffusivity, and heat capacity are the three primary thermal properties that characterize a soil, with the thermal conductivity being the most important property for the soils in the steady state condition (Farouki 1981b). The thermal conductivity of a soil represents the soil's ability to conduct heat and governs the flow rate of heat through the soil. Recently, thermal conductivity of soils has attracted close attention because heat conduction thorough a soil is in engineering applications such as high rate of heat dissipation for buried high voltage electric cables or energy piles, or for thermally insulating facilities such as liquefied gas storage tanks founded on soils with low thermal conductivity (Abuel-Naga et al. 2009; Brandl 2006; Brandon and Mitchell 1989; Brandon et al. 1989; Farouki 1981b). These types of applications require thermal conductivity for the proper design of the subsurface facilities and for the prevention of thermal instability or thermally induced failure. In addition, thermal conductivity of soils determines the frost depth penetration in a soil, which is a key factor in the soil mechanics of frozen ground.

6.1.2 Thermal Conductivity Governing Factors

The thermal conductivity of natural soils is primarily controlled by mineralogy, porosity (or packing density), water content, saturation, testing temperature, applied stress, and pore water chemistry (Abu-Hamdeh and Reeder 2000; Brandon and Mitchell 1989; Cote and Konrad 2005; Farouki 1981a; Farouki 1981b; Johansen 1975; Lu et al. 2007; Mitchell and Soga 2005; Smith and Byers 1938; Yun and Santamarina 2008). Particle shape and particle gradation may affect the thermal conductivity of

soils; however, because those two factors determine the porosity of soils they are typically excluded from consideration (Cho et al. 2006; Mitchell and Soga 2005; Youd 1973; Yun and Santamarina 2008). In the case of dry soils, the thermal conductivity will be a primary function of mineralogy and porosity (or dry density) because heat transfer in dry soils is mainly conducted by heat conduction through contacts between particles (Yun and Santamarina 2008). Consequently, porosity (or dry density) which captures the quality of particle contacts, such as coordination number, will be a governing variable, while the thermal conductivity of minerals, which varies from 2 to 8 W/mK (Farouki 2004), is another important variable. For example, soils with high quartz content can show high thermal conductivity (Johansen 1975).

6.2 Experimental Program

6.2.1 Materials

Ten samples of fly ash were obtained from power plants in the southeastern United States (Georgia (CP1 and BP3), Mississippi (CP2), Alabama (CP3 and CP4), and Virginia (BP2)), with biomass contents ranging from 0 to 100 %, where 0 % biomass content indicated 100 % coal fired class F fly ash; 100 % biomass content represented 100 % biomass fired fly ash, with mixture of the two in the intermediate range. Additionally, one sample of granular activated carbon produced from bituminous coal was also selected for testing (Carbon Resources). Total organic carbon content (TOC) of 100% coal fired fly ash ranged from 1.1 to 32.6 % (TOC- $V_{CPH/CPN}$, SSM-5000A, Shimadzu Co. Kyoto, Japan). The apparent specific gravity (ASTM C188 with kerosene) showed smaller numbers than that of natural soils, with wide variation according to fly ash type (Table 6-1). Median grain size was

determined by laser diffraction (Sympatec GmbH, Rodos T4.1) in air and sieve analysis (ASTM D422), and specific surface was measured by liquid nitrogen adsorption (Micromeritics, ASAP 2020). Most samples were used as received after over-drying except HC1, which was a high carbon content sample that was prepared by electrostatic separation of the CP4-1 sample. Full sample details are given in Yeboah et al. (in preparation).

Table 6-1. Material Properties

Sample ID*	TOC (%)	D ₅₀	BET S _a	G _s	Type
		(μm)	N ₂ @ 77K (m ² /g)		
CP1	1.1	16.2	1.27	2.63	100% Coal
CP2-1	2.2	14	3.01	2.54	100% Coal
CP3-1	4.9	29.9	4.6	2.47	100% Coal
CP3-2	4.6	26.9	2.5	2.45	4% Co-fire
CP3-3	4.3	23.3	3.48	2.39	8.2% Co-fire
CP4-1	9.6	21.7	8.12	2.37	100% Coal
CP4-2	7.7	18.8	8.9	2.39	5.5% Co-fire
BP2-1	47.4	640	180	1.62	100% Biomass
BP3-1	80.5	1440	687	1.03	100% Biomass
HC1	32.6	60	24.77	2.28	100% Coal
AC	> 97	148	777	1.91	Activated Carbon

Note: CP = coal or co-fired fly ash (Class F fly ash produced from bituminous coal);

BP = biomass (logging, paper mill, and sawmill waste) fly ash; HC = high carbon fly

ash; AC = activated carbon

6.2.2 Thermal Conductivity Measurement

The thermal conductivity of dry fly ashes with various carbon and biomass contents was measured using the thermal needle probe method (Figure 6.1) (ASTM D5334-08). A stainless steel thermal needle probe (TC-18, East 30 Sensors) (60 mm in height and 1.27 mm in diameter) was inserted into the prepared specimens, and was also connected to data logger / power supply (CR3000 Micrologger, Campbell Scientific). Constant current was applied to the heater inside the probe to measure the temperature variation as a function of time. Test conditions consisted of heating and cooling periods of 100 seconds each, and the temperature rise (ΔT) after 100 seconds of heating period was maintained at 2 ~ 3 °C by adjusting the input voltage according to the variations in thermal conductivities of different materials (East30Sensors 2007). Thermal conductivity was determined according to the following relationship (ASTM D5334-08):

$$k_t = \frac{C \cdot Q}{4\pi \cdot S} \quad (6-1)$$

where, C: calibration factor; Q: power (W/m); S: slope obtained from regressing ΔT on $\ln(t)$. The calibration factor was obtained using 99% Glycerol (PTI Process Chemicals).

To prepare the specimens for testing, each material was rained into a stainless steel cell (diameter 73 mm and height 100 mm), followed by symmetrically vibration to achieve the desired testing density (ranging from loose to dense conditions) (Table 6-2). The bottom plate and top cap of the cell were made of styrene to minimize the effect of ambient temperature variation (Figure 6.1).

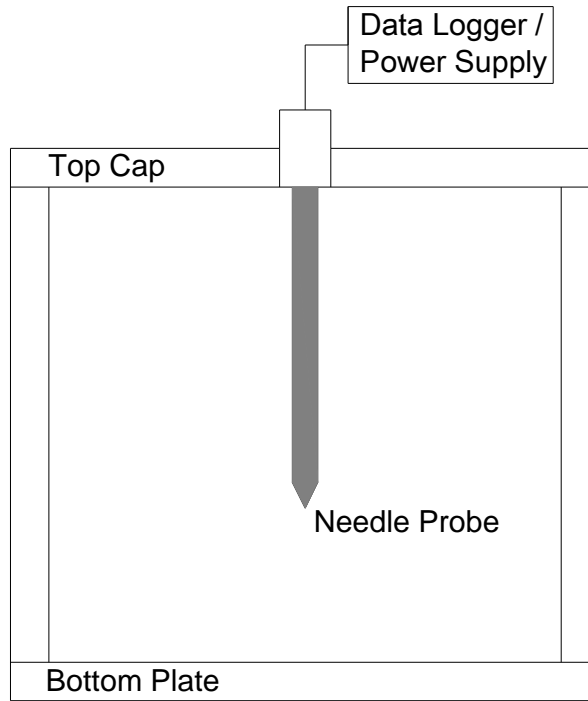


Figure 6.1 Setup for thermal conductivity measurement: thermal needle probe = 60 mm (height) and 1.27 mm (diameter); steel cell = 100 mm (height) and 73 mm (diameter).

Table 6-2. Test Matrix

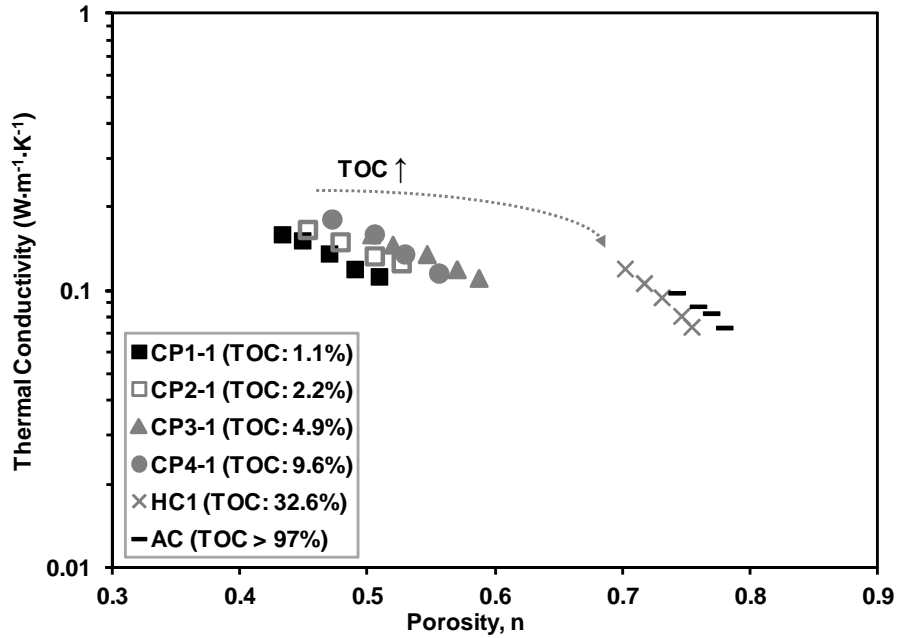
Type	CP1-1	CP2-1	CP3-1	CP3-2	CP3-3	CP4-1	CP4-2	HC1	AC	BP2-1	BP3-1
Dry Density, γ_d (g/cc)	1.29 ~1.49	1.20~ 1.39	1.02~ 1.23	1.00~ 1.20	0.90~ 1.10	1.05~ 1.25	1.00~ 1.20	0.58~ 0.68	0.42~ 0.49	0.18~ 0.23	0.08~ 0.13
Porosity (V_V/V_T) *	0.43~ 0.51	0.45~ 0.53	0.50~ 0.59	0.51~ 0.59	0.54~ 0.62	0.47~ 0.56	0.50~ 0.58	0.70~ 0.75	0.74~ 0.78	0.86~ 0.89	0.88~ 0.92

* V_V : volume of void space and V_T : total volume

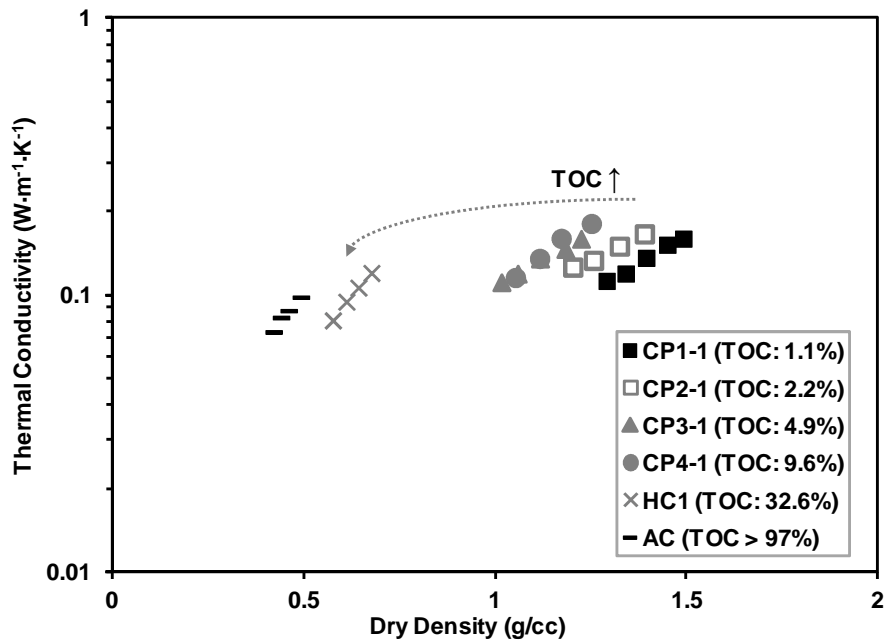
6.3 Results and Discussion

6.3.1 Effect of Carbon Content

Examination of the impact of total organic carbon on the thermal conductivity of fly ash demonstrated that even over a wide possible range of particle packing, the resultant thermal conductivities of fly ashes were very similar when the content of unburned carbon was low ($\text{TOC} < 10\%$) (Figure 6.2). Unburned carbon particles have a lower specific gravity than fly ash microspheres due to their organic carbon composition and very large internal pore space; consequently, as carbon content increased, the mixtures shifted to higher porosity (smaller dry density or higher void ratio), but thermal conductivities remained relatively constant at low carbon content. This reflected the higher thermal conductivity of unburned carbon particles when compared to aluminosilicate microspheres (cenospheres and plerospheres) because the smaller dry density (or higher porosity) resulted from a higher volume fraction of air, which has very low thermal conductivity ($\sim 0.024 \text{ W/mK}$). However, it is important to note that a further increase in carbon content may induce a decrease in thermal conductivity when unburned carbons occupy the dominant volume fraction, as opposed to microspheres, since this condition will result in a condition of both relatively constant particle/mineral conductivity and increasing of volumetric air content. In summary, the thermal conductivity of fly ashes according to carbon content remained relatively constant at low carbon content; however, with further increase in carbon content (i.e., $\text{TOC} > \text{critical carbon content}$, Chapter 4), the thermal conductivity will decrease with an increase in carbon content.



(a) Variation according to porosity

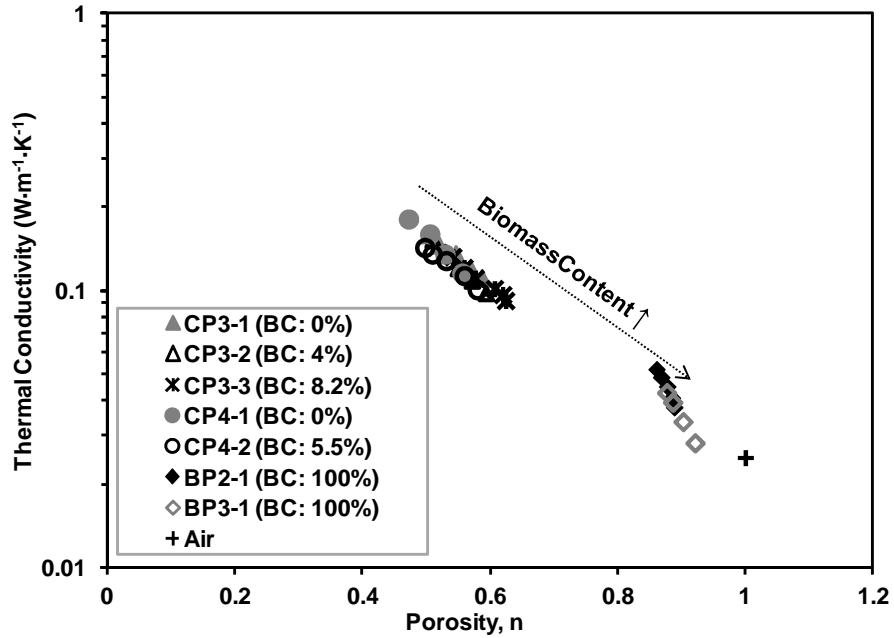


(b) Variation according to dry density

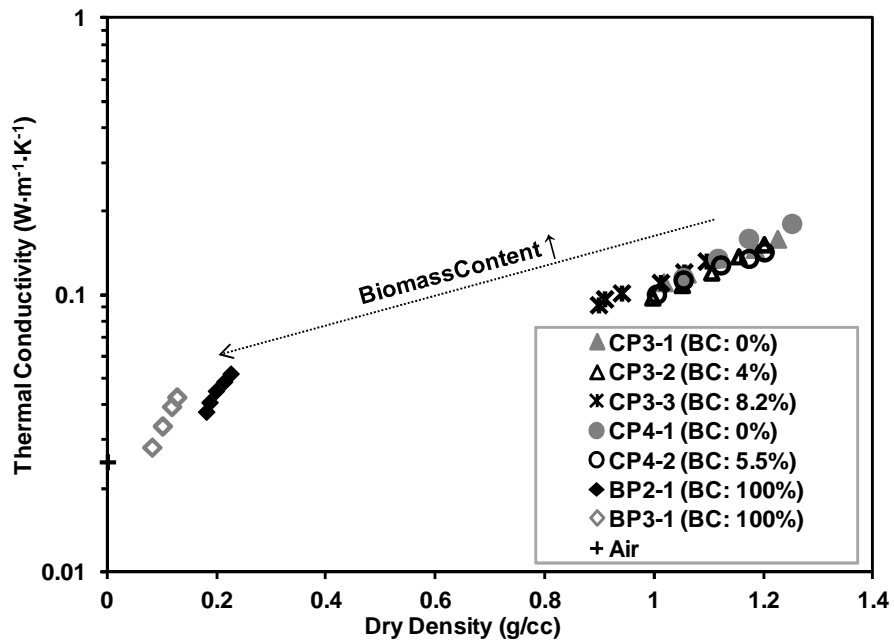
Figure 6.2. Effect of carbon content on thermal conductivity: (a) variation according to porosity; (b) variation according to dry density; TOC = unburned carbon content; thermal conductivity = Equation (6-1).

6.3.2 Effect of Biomass Content

An increase in the biomass content of fly ash increased the porosity of the samples, as a function of both the light weight and angular shape of the biomass fly ashes compared to coal fired fly ashes (Figure 6.3). The increased porosity resulted in a decrease in thermal conductivity as a result of the increased volumetric air content. Most notably, the thermal conductivities of 100% biomass fly ashes, BP2-1 and BP3-1, ranged from 0.028 to 0.052 W/mK according to their packing densities and biomass type, reflecting the possible application of biomass fly ash as thermally insulating materials, such as fireproof materials or materials to prevent frost action. This very low conductivity is indicative of the fact that the tested biomass fly ashes originated in part from the combustion of wood (thermal conductivity of dry wood = 0.079 ~ 0.17 W/mK) (USDA 2007). However, the dry density of 100 % biomass fly ashes was smaller than that of wood (typically, greater than 0.5 g/cc) (USDA 2007). Additionally, the variation of thermal conductivity of fly ashes as a function of biomass content may possibly be expressed as a single function, reflecting similar particle conductivities between coal and biomass fly ashes. Thus, the decrease in thermal conductivity with increasing of biomass content is attributed to an increase in volumetric air content.



(a) Variation according to porosity.



(b) Variation according to dry density.

Figure 6.3. Effect of biomass content on thermal conductivity: (a) variation according to porosity; (b) variation according to dry density; BC = biomass content.

6.3.3 Comparison with Thermal Conductivity of Dry Natural Soils

There are several theoretical models for describing thermal conductivity of soils, including the parallel model, series model, parallel-series model, geometric mean model, and the Hashin-Shtrikman boundaries model (detailed description of various models can be found from Farouki (1981b)). Among those models, it is known that the geometric mean model gives the most comparable conductivities to the experimental values determined for soils that were fully saturated. This indicates that the ratio of conductivities between soil particles and the material filling the pore space is smaller than 10 (Farouki 1981b; Johansen 1975). However, soils in the dry or unsaturated condition have very high conductivity ratios due to the very low thermal conductivity of air. As a result, there is difficulty quantifying the thermal conductivity of soils using theoretical models because these models yield considerable variation of thermal conductivity at a given porosity in case where the conductivity ratio is very high (Farouki 1981b; Johansen 1975). Consequently, the description of thermal conductivity of dry soils is typically based on empirical (or semi-empirical) models based on experimental results (Table 6-3).

Table 6-3. Empirical (Semi-empirical) Models for Thermal Conductivity of Dry Soils

Reference	Equation*	Note
Johansen (1975)	$k_t(dry) = \frac{0.135 \cdot \gamma_d + 64.7}{2700 - 0.947 \cdot \gamma_d} \pm 20\%$	Natural Soils γ_d in kg/m^3
Johansen (1975)	$k_t(dry) = 0.039 \cdot n^{-2.2} \pm 25\%$	Crushed Rocks
Gavriliev (2004)	$k_t(dry) = 0.025 + 0.238 \cdot \gamma_d - 0.193 \cdot \gamma_d^2 + 0.114 \cdot \gamma_d^3$	Mineral and Organic Soils γ_d in g/cc
Cote and Konrad (2005)	$k_t(dry) = \alpha \cdot 10^{-\beta \cdot n}$	$\alpha: 1.7$ & $\beta: 1.8$ (Crushed Rocks) $\alpha: 0.75$ & $\beta: 1.2$ (Natural Soils) $\alpha: 0.3$ & $\beta: 0.87$ (Organic Soils)
Lu et al.(2007)	$k_t(dry) = -0.56 \cdot n + 0.51$	$0.2 < n < 0.6$

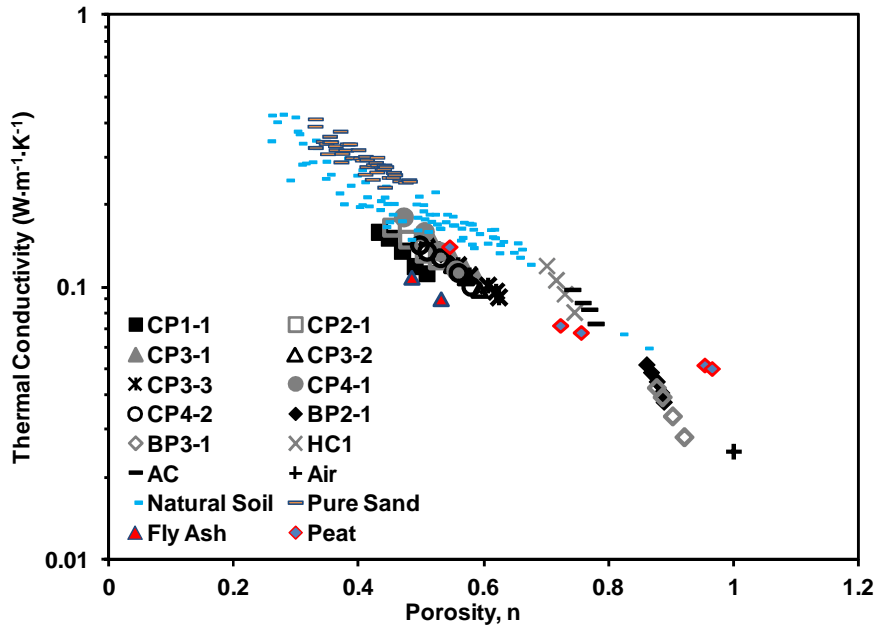
* $k_t(\text{dry})$: thermal conductivity of dry soil in W/mK ; γ_d : dry density; n : porosity

Comparing the thermal conductivity of tested materials with that of previous studies demonstrated that along the porosity, the thermal conductivities of dry fly ashes showed smaller values than those measured for dry natural soils (Figure 6.4). The apparent specific gravity of fly ash, which is impacted by its hollow shape, particle size, and iron content (Bouzoubaa et al. 1997; Kim et al. 2005; Pandian 2004; Paya et al. 1995; Tangpagasit et al. 2005), generally shows a smaller number (i.e., G_s : 2 ~ 2.6) than natural geomaterials, due to the retained air in the internal pore space of the hollow microspheres. Consequently, this retained air content cannot be evaluated through the concept of porosity, which resulted in smaller thermal conductivity of fly ashes compared to that of natural soils at a given porosity because the retained air in the internal pore space can act as a thermal conduction barrier. However, in terms of

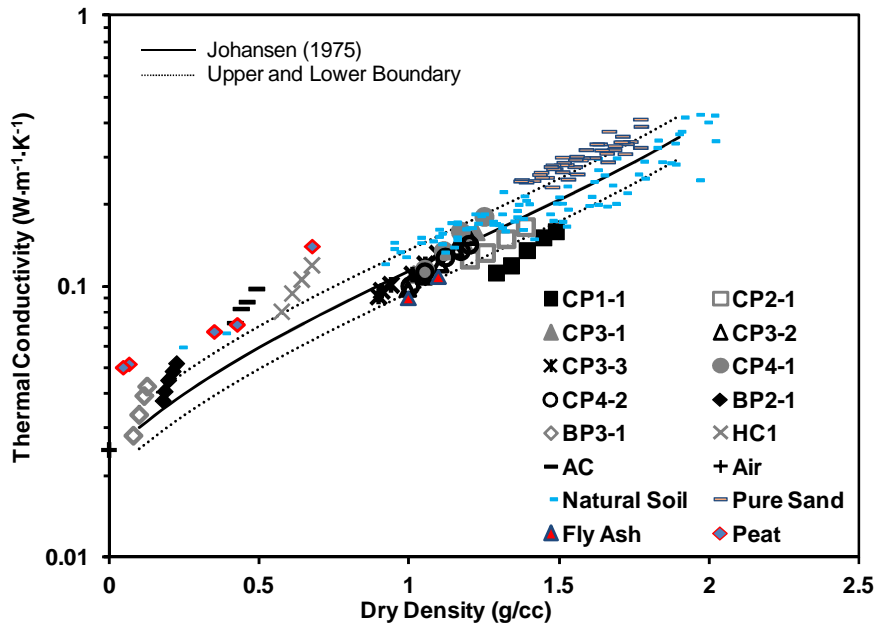
dry density, the variation of thermal conductivity of tested fly ashes showed very comparable results with the previous test results for natural soils and the empirical equation of Johansen for natural soils (Table 6-3 and Figure 6.4b). This good agreement suggested that the volumetric air content in fly ash specimens, including retained air in the internal pore, could be accurately evaluated by employing dry density because the chemical composition (or mineralogy) (i.e. aluminosilicate) of fly ashes is very similar to that of natural soils, resulting in similar particle (or mineral) conductivity, and the dry density is a function of not only porosity but also specific gravity (Equation (6-2)), resulting in the small value for specific gravity of fly ash that can include the effect of retained air:

$$\gamma_d = (1-n) \cdot G_s \cdot \gamma_w \quad (6-2)$$

where, n: porosity; G_s : specific gravity; γ_w : unit weight of water (1 g/cc at 4 °C). In summary, the thermal conductivity of dry fly ashes showed smaller conductivity when compared to that of natural soils in terms of porosity; however, in terms of dry density, thermal conductivities of fly ashes and natural soils were comparable.



(a) Variation according to porosity



(b) Variation according to dry density

Figure 6.4. Comparison with previous data (pure sand = Yun and Santamarina (2008); natural soil = Johansen (1975) & Smith and Byers (1938); peat = Smith and Byers (1938) & Gavriliev (2004); fly ash = Rao and Singh (1999); trend line = Johansen (1975)): (a) variation according to porosity; (b) variation according to dry density.

However, it is important to note that the fraction of soil or solid particles at a given volume is determined by porosity, not dry density, which makes evident the fact that fly ashes show thermally insulating properties when compared to natural soils. It is believed that this explains the trend observed by Demirboga and Gul (2003), which reported a decrease in thermal conductivity of concrete with an increase in fly ash contents. In addition, several previous studies (van de Lindt et al. 2008; Vilches et al. 2003; Yildirim et al. 1996) suggested the possibility of a composite of fly ash with waste materials such as titanium waste, polypropylene waste, and scrap tire fiber with fireproofing applications, such as fireproof doors and firewalls, thermally insulating building materials, and wood wall insulation supplements. These results also imply that utilization or landfilling of fly ash near the facilities that require high rates of heat dissipation should be done with caution to prevent thermal instability.

6.4 Summary

This chapter evaluated the thermal conductivities of fly ashes as a function of carbon and biomass contents to determine the effect of unburned carbon particles and biomass fired fly ash on the rate of heat transfer for fly ash. In addition, the obtained results were compared with the thermal conductivities of natural soils. The following key observations can be made:

1. The thermal conductivity of fly ashes according to carbon content does not vary significantly at low carbon contents; however, with further increases in carbon content (e.g., TOC > critical carbon content, Chapter 4), the thermal conductivity will decrease with an increase in carbon content.

2. With an increase in biomass content, the thermal conductivity of fly ashes

decreased, reflecting both similar mineral/particle conductivity of coal and biomass fly ashes and an increase in volumetric air content.

3. The thermal conductivity of fly ashes showed smaller values than that of natural soils when quantified in terms of porosity, due to the retained air in the internal pore space; however, in terms of dry density, both fly ashes and natural soils showed good agreement, reflecting the similar mineralogy of fly ash with natural soils.

4. The low thermal conductivity of fly ashes, especially biomass fly ashes, may suggest the possible application of fly ashes for thermally insulating purposes.

**CHAPTER 7 EFFECT OF COATING OF NANO-SIZED
PARTICLES ONTO SAND SURFACE: SMALL STRAIN
STIFFNESS OF IRON OXIDE COATED SANDS ACCORDING TO
IRON COATING DENSITY AND SAND PARTICLE SIZE**

7.1 Introduction

The presence of nano-sized particles on the surface of sand grains can dramatically alter the physical and chemical properties of the natural soils because the nano-sized particles (typically smaller than 100 nm) have large specific surface, and can exist at close to atomic or molecular dimensions, which can alter surface properties and interactions between particles or between particle and fluids (Dowling et al. 2004; Maurice 2009; Zhang 2007). In addition, the mechanical properties of soils may also be changed due to the presence of nano-sized particles because the contact modes between natural particles can be altered by the nano-sized particles. Interaction between silica grains can be altered when the silica surface is attached to nano-sized particles, such as iron oxides, due to electrostatic attraction or chemical reaction between the sand grains and the oxides. As a result, particle-to-particle interaction occurs through contacts between sand particle to sand particle, sand particle to nano-sized particle, or nano-sized particle to nano-sized particle. The contact mode will be a function of the coating density of the nano-sized particles onto the surface of substrate materials, the density of packing, and the confining stress on the soil.

Iron is the fourth most abundant element in the Earth's crust, which results in chemical weathering processes that cannot be separated from iron or iron oxide

formation (Cornell and Schwertmann 2003; Larrahondo 2011). Significant previous studies on the geotechnical properties of iron oxide coated soils having focused on the cementation effects of iron oxides, as they are often found as naturally occurring cementation agents that lead to the formation of aggregates and increases in strength and/or stiffness of soils (Cornell and Schwertmann 2003; Mitchell and Soga 2005; Zhang et al. 2004; Zhang et al. 2003).

The density of the surface coverage of nanoscale iron oxide particles is critical to the understanding of the behavior of iron oxide coated soils. Substrate particle size is the most critical factor determining iron oxide coating density, for both naturally occurring and lab-prepared iron oxide coated soils (Xu and Axe 2005). However, there is limited information on how the presence of iron oxide particles on a sand surface will change the contact mode and stiffness of a soil. This study examines the change in contact mode due to the presence of nano-sized particles that were chemically attached to a silica sand surface. Lab-prepared iron oxide coated sand particles were coated individually (i.e., without cementation) by a heterogeneous suspension reaction, and tests were performed on dry uncoated and coated sands to evaluate the effect of iron oxide coating on the alteration of contact modes and stiffness between particles. The iron coating density on the coated sand particles was controlled by changing the substrate sand particle size (ranging from 0.11 to 0.72 mm), with corresponding iron contents ranging from 0.13 to 6.35 mg_{Fe}/g_{sand}. The macro scale experimental results were analyzed using particle level contact behaviors (i.e. Hertz and Mindlin contacts) to gain a more fundamental understanding of change in a soil's natures due to iron oxide coating.

7.2 Review of Theoretically Derived Small Strain Stiffness

Soils are particulate materials, which means that the stiffness of soils is determined by the stiffness of the interparticle contact and the state of fabric (Lee et al. 2007; Mitchell and Soga 2005; Santamarina et al. 2001). The stiffness of the interparticle contact can be defined by the combination of normal and tangential stiffness of Hertz and Mindlin contact theories, both of which were derived based on two spheres in contact, with the state of fabric defined based on different packing models, coordination number, or void ratio. There have been many studies to express the maximum shear modulus based on contact stiffness and packing condition (Chang et al. 1991; Digby 1981; Petrakis and Dobry 1989; Santamarina and Cascante 1996; Santamarina et al. 2001). Among those formulas, this study will follow the case of random packing of spheres, based on the work of Hertz and Mindlin, due to the relevance of a covering wide range of soil fabrics (Chang et al. 1991; Digby 1981; Duffaut et al. 2010; Johnson 1985; Mindlin and Deresiewicz 1953).

7.2.1 Normal Stiffness

When two non-conforming spheres are brought into contact, a single contact point will be generated on initial contact. As the applied stress is increased, the two spheres will deform around the first contact point, with a contact radius (a) that is dependent on the applied stress (Figure 7.1). From the geometry of the figure and the analysis of Hertz (Johnson 1985), the following expression can be made:

$$u_{z_1} + u_{z_2} = \delta - (z_1 + z_2) \quad (7-1)$$

where, δ : interference (or remote displacement), u_z : normal displacement, and z can be expressed as follows based on the geometry of Figure 7.1:

$$z_1 = \frac{1}{2} \cdot \frac{1}{R_1} \cdot x^2 \quad (7-2)$$

$$z_2 = \frac{1}{2} \cdot \frac{1}{R_2} \cdot x^2 \quad (7-3)$$

Defining the gap function “h” as the sum of z_1 and z_2 results in:

$$h = z_1 + z_2 = \frac{1}{2} \cdot \frac{1}{R_1} \cdot x^2 + \frac{1}{2} \cdot \frac{1}{R_2} \cdot x^2 = \frac{1}{2} \cdot \frac{1}{R^*} \cdot x^2 \quad (7-4)$$

where, R^* : equivalent radius which can be defined as $1/R^* = 1/R_1 + 1/R_2$. The normal displacement for $x \leq a$ is given as (Johnson 1985):

$$u_{z1} = \frac{1 - \nu_{g1}^2}{E_{g1}} \cdot \frac{\pi \cdot \sigma_0}{4 \cdot a} (2 \cdot a^2 - x^2) \quad (7-5)$$

$$u_{z2} = \frac{1 - \nu_{g2}^2}{E_{g2}} \cdot \frac{\pi \cdot \sigma_0}{4 \cdot a} (2 \cdot a^2 - x^2) \quad (7-6)$$

where, E_g : grain (material) elastic modulus; and ν_g : grain (material) Poisson’s ratio.

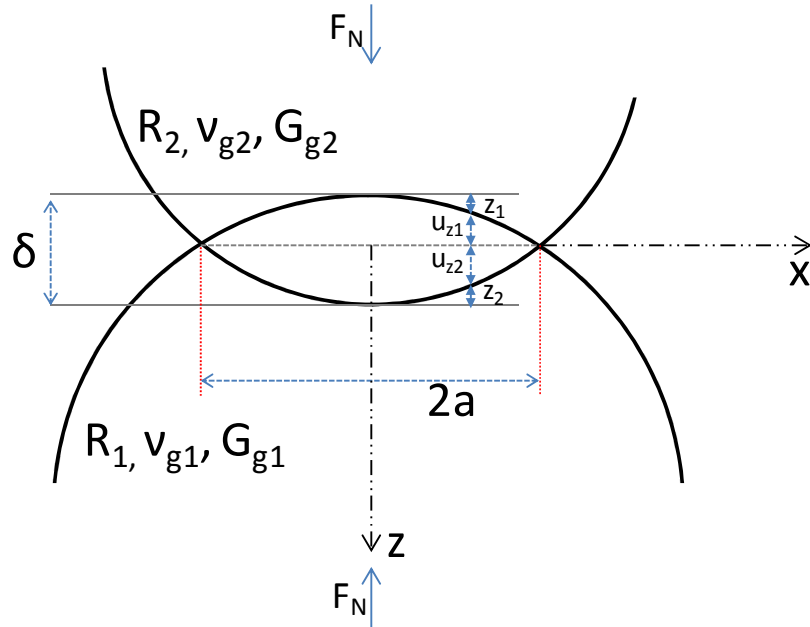


Figure 7.1. Two elastically dissimilar spheres in contact (Hertz contact).

Substitution of (7-4), (7-5), and (7-6) into (7-1) results in:

$$\frac{\pi \cdot \sigma_0}{4a \cdot E^*} (2 \cdot a^2 - x^2) = \delta - \frac{1}{2} \cdot \frac{1}{R^*} \cdot r^2 \quad (7-7)$$

where, σ_0 : peak normal stress; E^* : equivalent elastic modulus, which can be defined

as $\frac{1}{E^*} = \frac{1 - \nu_{g1}^2}{E_{g1}} + \frac{1 - \nu_{g2}^2}{E_{g2}}$. The peak normal stress (σ_0) can be found from the pressure distribution given by Hertz:

$$\sigma(x) = \sigma_0 \sqrt{1 - (x/a)^2} \quad (7-8)$$

From Equation (7-7), the contact radius (a) can be defined by taking derivative with respect to r:

$$a = \frac{\pi \cdot \sigma_0 \cdot R^*}{2 \cdot E^*} \quad (7-9)$$

From force equilibrium between normal force and normal stress:

$$F_N = \int_0^a \sigma(x) \cdot 2\pi \cdot x dx = \frac{2}{3} \sigma_0 \cdot \pi \cdot a^2 \quad (7-10)$$

where, F_N : normal force. By rearranging (7-10), the peak normal stress can be expressed in terms of normal force:

$$\sigma_0 = \frac{3 \cdot F_N}{2 \cdot \pi \cdot a^2} \quad (7-11)$$

Substitution of (7-9) into (7-7), combining with equation (7-11) yields:

$$\delta = \frac{\pi \cdot a \cdot \sigma_0}{2 \cdot E^*} = \frac{a^2}{R^*} = \left(\frac{9 \cdot F_N^2}{16 \cdot R^* \cdot E^{*2}} \right)^{1/3} \quad (7-12)$$

Consequently, the normal stiffness of two spheres in contact will be:

$$S_N = \frac{dF_N}{d\delta} = (6 \cdot R^* \cdot F_N \cdot E^{*2})^{1/3} \quad (7-13)$$

which can be rewritten as follows (Johnson 1985):

$$S_N = 2 \cdot a \cdot E^* = \frac{4 \cdot a}{\frac{1-\nu_{g1}}{G_{g1}} + \frac{1-\nu_{g2}}{G_{g1}}} \quad (7-14)$$

Mindlin and Deresiewicz (1953) defined the normal stiffness of one sphere:

$$S_N = \frac{4 \cdot G_g \cdot a}{1-\nu_g} \quad (7-15)$$

Theoretically derived shear modulus expressions have been derived based on the contact stiffness of one sphere. Equation (7-14) can be adjusted to consider the normal stiffness of only one sphere by taking a remote displacement as $0.5 \cdot \delta$ instead of δ under the assumption that deformation of two spheres is the same, which results in:

$$S_N = \frac{8 \cdot a}{\frac{1-\nu_{g1}}{G_{g1}} + \frac{1-\nu_{g2}}{G_{g1}}} \quad (7-16)$$

It is important to note that normal stiffness of particles in contact is determined by the combination of elastic properties of two contacting materials, and if two particles in contact are elastically inconsistent, Equation (7-15) may not be valid. In contrast, Equation (7-16) can be used in the case where two spheres in contact have different values for G_g and ν_g .

7.2.2 Tangential Stiffness

Hertzian contact theory assumed a frictionless contact, representing zero tangential force; however, the stress state of soil deposits is generally anisotropic, leading shear (or tangential) stress (or force). Additionally, even in the case where the stress state is isotropic, the lateral surface deformation of two elastically dissimilar

particles will differ, resulting in interfacial slip, without considering the effect of friction. Consequently, the effect of friction should be considered in the contact stiffness of particles. The effect of friction can be considered in two cases: one case is for two spheres without slip (or full stick), and the second case is for two spheres with partial slip. Following the work of Mindlin (Johnson 1985; Mindlin and Deresiewicz 1953), the shear stress can be modeled as a perturbation of the fully-sliding solution as follows (Figure 7.2):

$$\tau(x) = \mu \cdot \sigma(x) + \tau'(x) \quad (7-17)$$

where, $\tau'(x) = 0$ in slip zone ($c < x < a$); and μ : coefficient of friction. It is assumed in Equation (7-17) that the partial slip initiated from the edge of contact radius and the zone of slip increases inwardly with an increase in shear force (or stress). The resulting shear stress distribution is given as follows (Mindlin and Deresiewicz 1953):

$$\tau(x) = \mu \cdot \sigma(x) - \frac{c}{a} \cdot \sigma_0 \cdot \sqrt{1 - (x/c)^2} \quad (7-18)$$

where, $\sigma(x)$ is in Equation (7-8); σ_0 is in Equation (7-11). From force equilibrium between shear stress and shear force, the ratio of c/a can be obtained as:

$$\frac{c}{a} = \left(1 - \frac{F_T}{\mu \cdot F_N} \right)^{1/3} \quad (7-19)$$

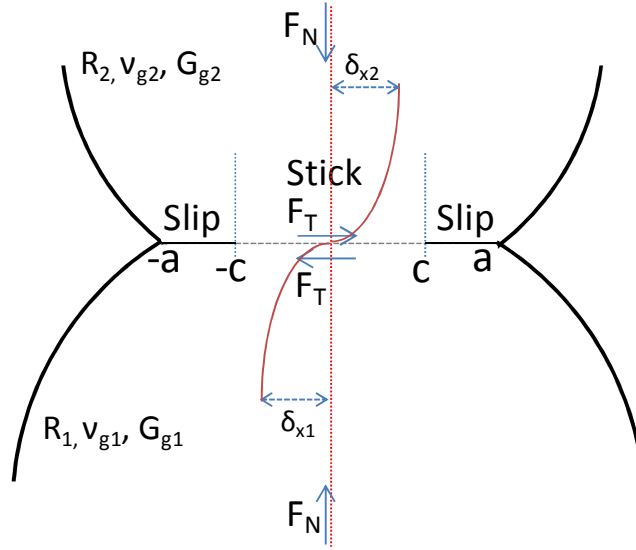


Figure 7.2. Profile of two spheres in contact under partial slip.

Following the derivation of Johnson (1985), the resultant tangential displacement of two spheres from the shear stress distribution of Equation (7-18) and Figure 7.2 is:

$$\delta_T = \delta_{x1} + \delta_{x2} = \frac{3 \cdot \mu \cdot F_N}{16 \cdot a} \cdot \left(\frac{2 - \nu_{g1}}{G_{g1}} + \frac{2 - \nu_{g2}}{G_{g2}} \right) \cdot \left(1 - \left(1 - \frac{F_T}{\mu \cdot F_N} \right)^{2/3} \right) \quad (7-20)$$

The tangential stiffness of two spheres in contact can be obtained from Equation (7-20) as follows:

$$S_T = \frac{dF_T}{d\delta_T} = \frac{8 \cdot a}{\frac{2 - \nu_{g1}}{G_{g1}} + \frac{2 - \nu_{g2}}{G_{g1}}} \cdot \left(1 - \frac{F_T}{\mu \cdot F_N} \right)^{1/3} \quad (7-21)$$

Under the assumption of no partial slip, Equation (7-21) becomes:

$$S_T = \frac{dF_T}{d\delta_T} = \frac{8 \cdot a}{\frac{2 - \nu_{g1}}{G_{g1}} + \frac{2 - \nu_{g2}}{G_{g1}}} \quad (7-22)$$

Mindlin and Deresiewicz (1953) defined the tangential stiffness of one sphere (not

two spheres) at the full stick condition:

$$S_T = \frac{8 \cdot G_g \cdot a}{2 - \nu_g} \quad (7-23)$$

In the same way with normal stiffness, Equation (7-22) can be adjusted to consider the tangential stiffness of one sphere as follows:

$$S_T = \frac{16 \cdot a}{\frac{2 - \nu_{g1}}{G_{g1}} + \frac{2 - \nu_{g2}}{G_{g1}}} \quad (7-24)$$

Being similar with the case of normal stiffness, in case particles in contact have different elastic properties, Equation (7-24) will be more suitable than Equation (7-23), and is the same with Equation (7-23) in the case where two spheres in contact have the same G_g and ν_g .

7.2.3 Theoretical Expression of Maximum Shear Modulus for Random Packing of Spheres

In order to develop more generalized formulas for use in this study, the isotropic pressure (P) was converted to confining force (F_N) between particles (Cascante and Santamarina 1996; Rothenburg and Bathurst 1989):

$$F_N = \frac{4 \cdot \pi \cdot R^2 \cdot P}{C_N \cdot (1 - n)} \quad (7-25)$$

where, C_N : coordination number; and n : porosity. Following the work of Digby (1981) for random packing of spheres, the shear modulus can be expressed as follows:

$$2G_{dry} = \frac{G_g \cdot C_N \cdot (1 - n)}{5 \cdot \pi \cdot R} \cdot \left(\frac{2 \cdot a}{1 - \nu_g} + \frac{6 \cdot c}{2 - \nu_g} \right) \quad (7-26)$$

where, G_{dry} : shear modulus of granular dry skeleton. The shear modulus (Equation (7-26)) can be expressed in terms of normal and tangential stiffness by combining (7-26) with (7-15) and (7-23) under the assumption of “ $c \approx a$ ” (Duffaut et al. 2010), resulting in:

$$G_{dry} = \frac{C_N \cdot (1-n)}{20 \cdot \pi \cdot R} \cdot \left(S_N + \frac{3}{2} \cdot S_T \right) \quad (7-27)$$

This experimental portion of this study was particularly focused on the change in contact behaviors, such as contact stiffness or contact modes, due to the presence of nano-sized particles; consequently, the theoretical shear modulus was expressed by employing normal and tangential stiffness of elastically dissimilar particles in contact (Equation (7-16) and (7-24)), leading to:

$$G_{dry} = \frac{2 \cdot C_N \cdot (1-n)}{5 \cdot \pi} \cdot \frac{a}{R} \cdot \left(\frac{1}{\frac{1-\nu_{g1}}{G_{g1}} + \frac{1-\nu_{g2}}{G_{g2}}} + \frac{3}{\frac{2-\nu_{g1}}{G_{g1}} + \frac{2-\nu_{g2}}{G_{g2}}} \right) \quad (7-28)$$

By combining (7-12) and (7-25), the ratio of “ a ” to “ R ” in Equation (7-28) can be expressed as:

$$\frac{a}{R} = \sqrt[3]{\frac{3}{2} \cdot \frac{\pi \cdot P}{E^* \cdot C_N \cdot (1-n)}} \quad (7-29)$$

Therefore, substitution of Equation (7-29) into (7-28) will yield:

$$G_{dry} = \frac{2}{5} \cdot \left(\frac{3 \cdot C_N^2 \cdot (1-n)^2 \cdot P}{4 \cdot \pi^2} \right)^{1/3} \cdot \left[\left(\frac{1-\nu_{g1}}{G_{g1}} + \frac{1-\nu_{g2}}{G_{g2}} \right)^{-2/3} + 3 \cdot \left(\frac{1-\nu_{g1}}{G_{g1}} + \frac{1-\nu_{g2}}{G_{g2}} \right)^{1/3} \cdot \left(\frac{2-\nu_{g1}}{G_{g1}} + \frac{2-\nu_{g2}}{G_{g2}} \right)^{-1} \right] \quad (7-30)$$

Finally, Equation (7-30) can be simplified for the case where two spheres in contact have same the G_g and ν_g . It is notable that this is the same formula as that of Chang et

al (1991) which describes the small strain stiffness of a statistically isotropic random packing:

$$G_{dry} = \frac{3}{5} \frac{5-4\nu}{2-\nu} \cdot \left(\frac{C_N^2 \cdot (1-n)^2 \cdot G_g^2 \cdot P}{18 \cdot \pi^2 \cdot (1-\nu)^2} \right)^{1/3} \quad (7-31)$$

In this study, the impact on the contact mode for interaction between particles were considered in three cases: 1) prevalent contacts between nano-sized particle and nano-sized particle, in the case where the spacing between adsorbed nano-sized particles onto sand surface is smaller than the diameter of nano-sized particle; 2) prevalent contacts between sand particle and nano-sized particle, in the case where the spacing between adsorbed nano-sized particles is smaller than the Hertz contact diameter of sand particles, but greater than the diameter of nano-sized particles; 3) prevalent contacts between sand particles and sand particles, in the case where the spacing between adsorbed nano-sized particles is greater than the Hertz contact diameter of sand particles (Figure 7.3). Based on these three scenarios, the theoretically estimated small strain stiffness (Equation (7-30)) was plotted, using the empirical relationship between coordination number and porosity ($C_N = \pi / n$) (Santamarina et al. 2001), with void ratio assumed = 0.7, with G_g of sand (quartz) and hematite as equal to 31.1 GPa and 88.35 GPa, respectively (Glasscock et al. 2008; Shustorovich and Shustorovich 2003; Yao et al. 2007), and ν_g of sand (quartz) and hematite equal to 0.17 and 0.33, respectively (Shustorovich and Shustorovich 2003; Yao et al. 2007) (Figure 7.3). Under this framework, the contacts between nano-sized particles (hematite particles) resulted in the highest small strain stiffness due to the greater elastic modulus of hematite when compared to that of quartz, and is also reflected in the high stiffness in the contacts between sand particles and nano-sized particles, when compared to sand-to-sand contacts. Consequently, the contact mode

between particles due to the presence of nano-sized particles will play an important role in the measured stiffness, which will vary according to the elastic properties of the particles and the coating density of the nano-sized particles on the sand substrate.

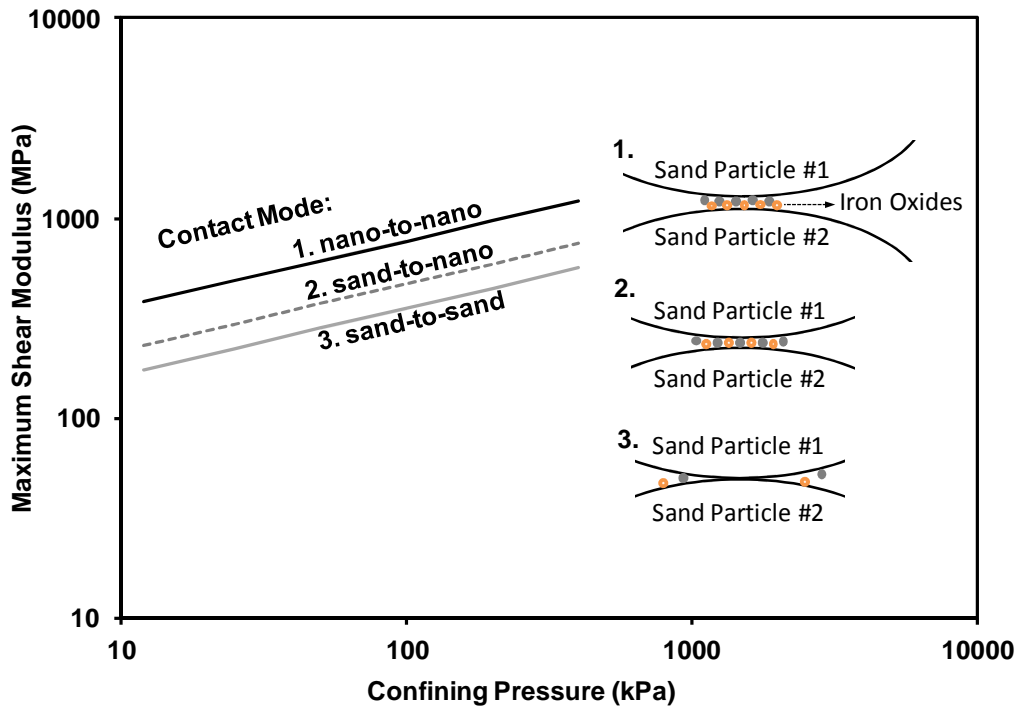


Figure 7.3. Theoretical G_{\max} estimation according to contact mode (contact model not to scale): (1) prevalent nano particle-to-nano particle contacts; (2) prevalent sand particle-to-nano particle contacts; (3) prevalent sand particle-to-sand particle contacts; $G_{\max} = \text{Equation (7-30)}$.

7.3 Experimental Program

7.3.1 Materials

Three silica sands (silicon dioxide > 99.8%), ASTM 20/30, ASTM graded, and ASTM 100/200 sands (U.S. Silica Company), were used as the sand, substrate and

two iron oxides, hematite and goethite, were used as the coating particles. Both hematite and goethite are prevalent in nature due to their high thermodynamic stability. The iron oxides were obtained from Sigma Aldrich Corporation and used as received. Additional chemicals, including NaNO_3 , HCl , H_2O_2 , NaHCO_3 , $\text{Na}_2\text{S}_2\text{O}_4$, $\text{C}_6\text{H}_5\text{Na}_3\text{O}_7$, HNO_3 , and NaCl were obtained from Sigma Aldrich Corporation and Fisher Scientific, and were used as received.

The heterogeneous suspension reaction method (Larraondo et al. 2011; Scheidegger et al. 1993) was used to sorb the iron oxides onto the sand surfaces in this study. A suspension of 40 mg iron oxide/1g sand was thoroughly mixed at pH 3 and ionic strength 0.01 M to prepare iron oxide coated sands (detailed description of preparation of iron oxide coated sand can be found from Larraondo et al. (2011)). The physical and chemical properties of the coated sands were measured, including: median grain size (ASTM D422), extreme void ratios of pure and iron oxide coated sands (ASTM D4253 and ASTM D4254); specific gravity (ASTM D854); and iron content (or iron oxide coating density) was measured by the DCB technique (Mehra and Jackson 1960) with analysis performed using ICP-OES (Optima 8000, PerkinElmer). Consistent with the previous result (Xu and Axe 2005), a decrease in iron content with an increase in substrate sand particle size was observed, reflecting a decrease in specific surface as the sand substrate diameter increased. In addition, due to the iron oxide adsorption onto the sand surface, an increase in specific gravity and a decrease in extreme void ratios were observed (Larraondo 2011). The changes in specific gravity and extreme void ratios were more apparent with an increase in iron content.

Table 7-1. Material Properties

Properties	ASTM 20/30			ASTM graded		ASTM 100/200*		
	Clean	Hem.	Goe.	Clean	Hem.	Clean	Hem.	Goe.
D ₅₀ (mm)	0.72	0.72	0.72	0.365	0.365	0.11	0.11	0.11
Specific Gravity	2.65	2.66	2.66	2.65	2.67	2.65	2.68	2.66
e _{max}	0.739	0.712	0.746	0.762	0.693	0.88	0.80	0.88
e _{min}	0.519	0.516	0.526	0.514	0.485	0.56	0.46	0.53
Iron Content (mg_Fe/g_sand)	-	0.43	0.13	-	1.22	-	6.35	0.62

Note: D₅₀ = median grain size; Clean = uncoated clean sand; Hem. = hematite coated sand; Goe. = Goethite coated sand; e_{max} = maximum void ratio; e_{min} = minimum void ratio; *: data from Larrahondo et al. (2011)

7.3.2 Test Equipment and Program

The shear wave velocity (V_s) was measured using bender element tests. One pair of bender elements was fitted on the top cap and bottom plate of modified oedometer cell to measure shear wave velocity as a function of consolidation load (Lee and Santamarina 2005). The shear wave generated by the source bender element, which was connected to a function generator (33210A, Agilent), with a square wave of frequency (f) 20 Hz, and amplitude 10 V, that traveled through the soil specimen. The signal was received by the receiver bender element, which was connected to a filter amplifier (3364, Krohn-Hite), which, in turn, was connected to a digital oscilloscope (DSO5014A, Agilent). A total of 1024 signals were stacked to reduce the uncorrelated noise. Travel time of the shear wave was carefully determined according to the recommendation of Lee and Santamarina (2005), and the tip-to-tip distance (the distance from the tip of the source bender to the tip of the receiver bender element)

was used as the travel distance (Fernandez 2000; Lee and Santamarina 2005). The shear wave velocity was determined from the measured travel distance (L) and travel time (t) as follows:

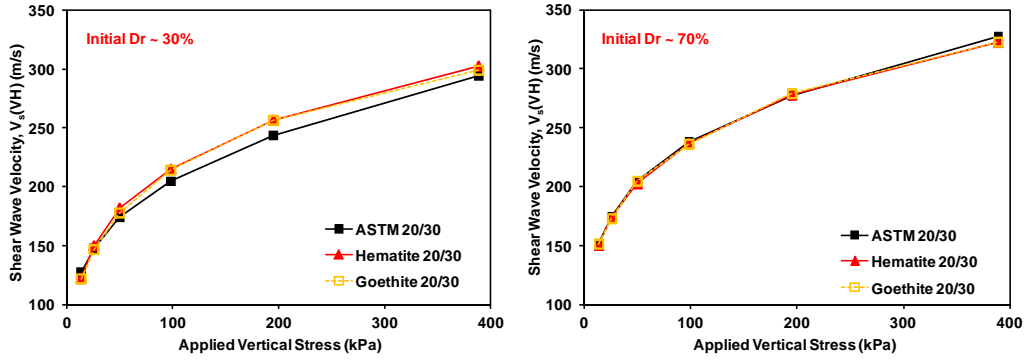
$$V_s = \frac{L}{t} \quad (7-32)$$

Testing specimens were prepared according to the given initial relative density, which ranged from 30 % to 80 %, by the air pluviation method. The initial targeted density was controlled by symmetric vibration. Tests were conducted in K_0 conditions using vertical stresses ranging from 13.5 kPa to 388.6 kPa, and shear wave propagation was measured at the end of each loading. All tests were performed in dry conditions.

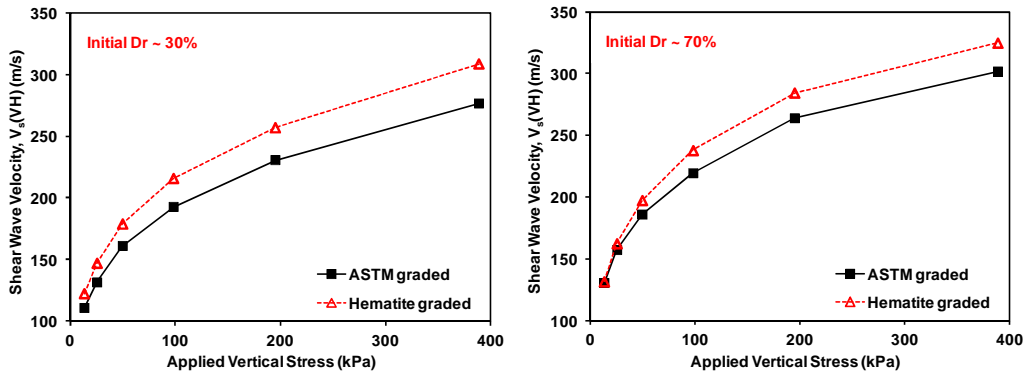
7.4 Results

The measured shear wave velocity ($V_s(VH)$, vertically propagating horizontally polarized wave velocity) showed that the measured shear wave velocity increased with an increase in applied stress and relative density, as anticipated (Figure 7.4). The stiffness or shear wave velocity of soils depends on the stiffness of interparticle contact and the state of fabric (Lee et al. 2007; Mitchell and Soga 2005; Santamarina et al. 2001). Therefore, with an increase in applied stress, which captures the alteration of the stiffness of interparticle contacts, and in relative density, which captures the change of fabric state, the shear wave velocity or the stiffness of soils will increase. It can also be observed that shear wave velocity of coated sands (both hematite and goethite coated sands) generally showed larger shear wave velocity than that of uncoated sands at a given packing density and applied stress. Additionally, the difference between wave velocities of coated and uncoated sands varied with applied stress and increased with an increase in coating density or with a decrease in substrate

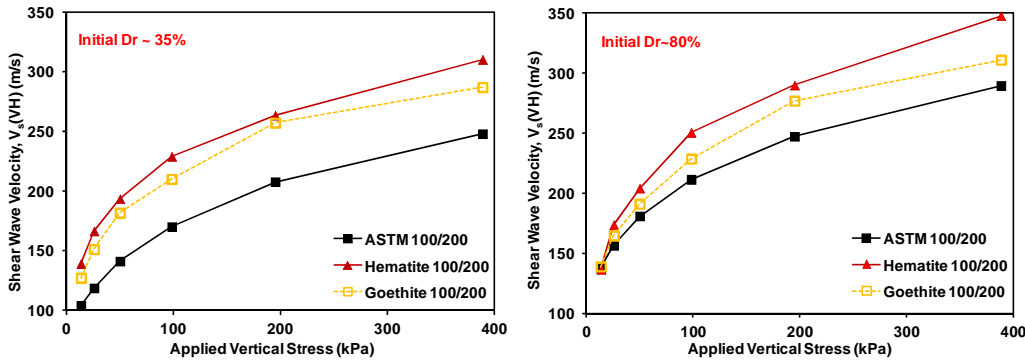
sand particle size. Most notably, the difference in wave velocities between iron oxide coated and uncoated sands was most pronounced in the case of loosely packed soils, when compared to that of densely packed soils. These measurements reflect the alteration in contact mode according to coating density of nano-sized particles, substrate sand particle size, applied stress as well as the packing density of the soil matrix.



(a) ASTM 20/30 sand



(b) ASTM graded sand



(c) ASTM 100/200 sand (data from Larrahondo et al. (2011))

Figure 7.4. Variation of shear wave velocity according to applied vertical stress: iron contents (mg_{Fe} / g_{sand}) for hematite coated 20/30 = 0.43; for goethite coated 20/30 = 0.13; hematite coated graded = 1.22; hematite coated 100/200 = 6.35; goethite coated 100/200 = 0.62.

7.5 Analysis and Discussion

7.5.1 Effect of Applied Stress and Packing Density on Contact Mode

The increase in applied stress will induce a deformation/settlement/fabric change of soils due to the rearrangement of soil particles, which is associated with sliding, slip, and rolling of particles under confinement (El-Sohby and Andrawes 1972; Hardin and Blandford 1989; Mitchell and Soga 2005). The measurement of shear wave velocity is a constant fabric phenomenon representing the stiffness of the current soil state; however, measuring shear wave velocity as a function of effective vertical stress under loading and unloading conditions captures the influence of the stiffness of current particle contacts, as well as the fabric changes (Cho et al. 2007; Santamarina et al. 2001). Consequently, monitoring of shear wave velocity with applied stress will give an implication of changes in contact mode due to the rearrangement of soil particles. Examination of the variation of shear wave velocity ratio (the ratio of shear wave velocity of hematite coated sands to shear wave velocity of uncoated sands) of tested soils as a function of applied stress under loose and dense conditions shows that the wave velocity ratio decreased with an increase in applied stress in the case of loose packing but increased with an increase in applied stress in the case of dense packing (Figure 7.5). Additionally, the ratio of shear wave velocity for loose packing was greater than that for dense packing; however, those ratios for loose and dense packings converged with confinement, reflecting initially different contact types that became more similar with an increase in applied stress. Finally, with a decrease in iron content (or increase in substrate sand particle size), the wave velocity ratio decreased, representing the reduced influence of nano-sized particles on the stiffness of the natural soil assemblage.

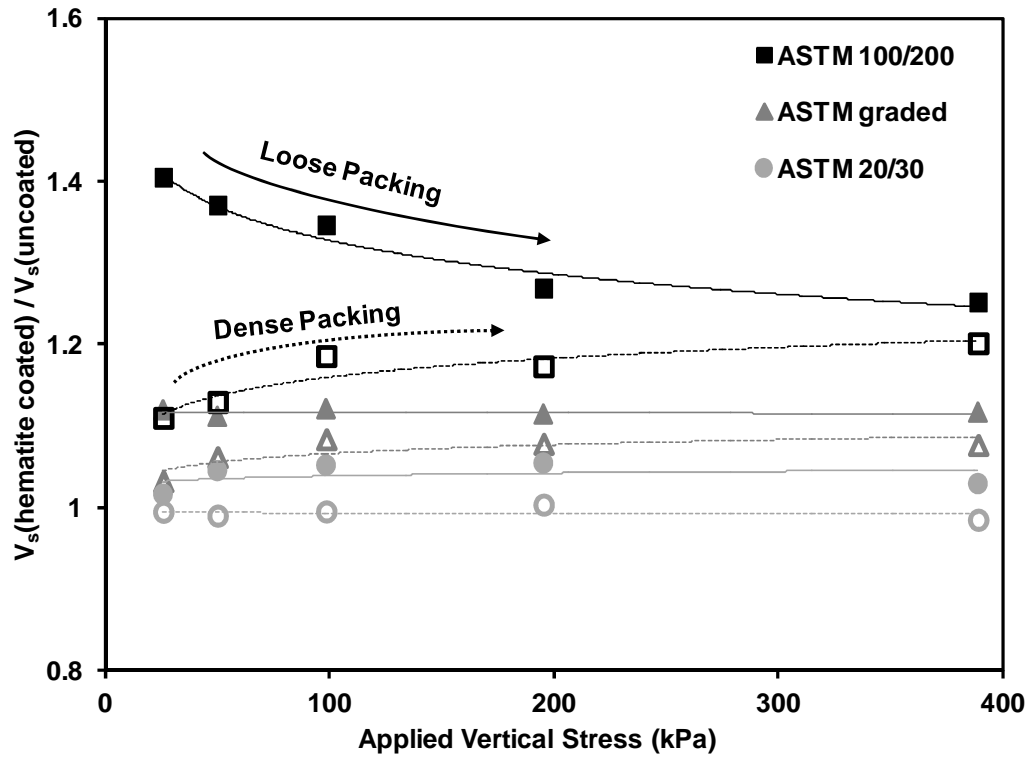


Figure 7.5. Variation of shear wave velocity ratio according to applied vertical stress: initial D_r of loose packing = 30~ 35 %; initial D_r of dense packing = 70~80 %; closed figures = loose packing; open figures = dense packing.

Nano-sized particles, like the iron oxides used in this study, attach on relatively smooth sand surfaces and act as protrusions. This results in high void ratios (or low relative densities) that can be achieved when the contacts are between protruding nano-sized particles, and occurs in the case of heavy coating density (i.e., high iron content), or when the contacts are between nano-sized particle and sand particle, which occurs in the case of low coating density (i.e., low iron content). However, with an increase in applied stress, the sand particles will be rearranged to have low energy potential, and the Hertzian contact area will be increased, all of which act to shift the contact mode from nano particle-to-nano particle contacts to nano particle-to-sand particle contacts or from nano particle-to-sand particle contacts

to nano particle-to-sand particle with the lower impact of the nano-sized particles' contacts, depending on coating density or iron content (Figure 7.6). This change in contact mode with increasing confinement may be attributed to a decrease in the wave velocity ratio according to applied stress (Figure 7.5) as shown in the theoretical G_{\max} estimation (Figure 7.3).

In contrast, to achieve high relative density (or low void ratio), the initial contacts between particles will be the contacts of sand particle-to-sand particle, in the case of low iron content, or the contacts of nano particle-to-sand particle, in the case of high iron content. However, for high relative density soils subjected to an increase in applied stress, there will be an increase in Hertzian contact area, leading to the change in contact modes from sand particle-to-sand particle to nano particle-to-sand particle or from nano particle-to-sand particle to nano particle-to-sand particle with the higher impact of the nano-sized particles' contacts, as a function of iron coating density (Figure 7.6). This shift in contact mode results in wave velocity ratios for densely packed specimens that increase with an increase in applied stress (Figure 7.5) and as predicted by theoretical analysis (Figure 7.3). Ultimately, the changes in contact mode of initially loose and dense packings with increasing applied stress will result in a similar contact mode at high confined stress (Figure 7.6), and correspondingly a similar wave velocity ratio as stress is increased (Figure 7.5).

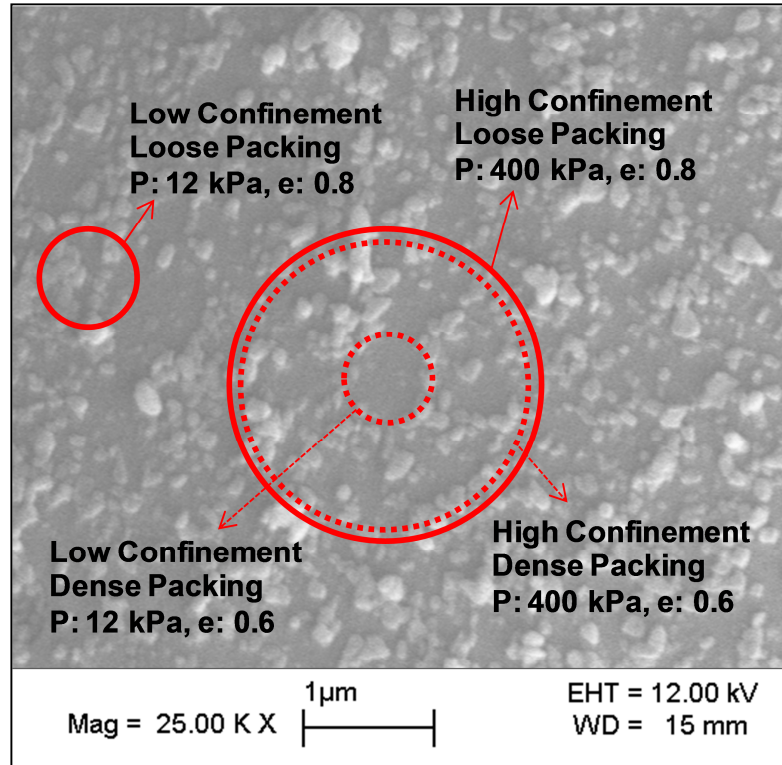


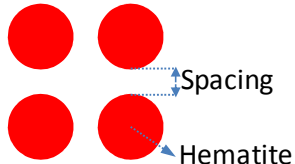
Figure 7.6. Hertzian contact area of ASTM 100/200: SEM = hematite coated 100/200 (size of hematite particle ≈ 140 nm); Hertz contact radius = Equation (7-29) at P (isotropic confining pressure) = 12 kPa (low confinement) and 400 kPa (high confinement) and e (void ratio) = 0.6 (dense packing) and 0.8 (loose packing).

7.5.2 Effects of Coating Density of Nano-sized Particles and Sand Particle Size on Contact Mode

Three cases of contact modes were considered in this study: 1) prevalent contacts between nano-sized particles; 2) prevalent contacts between sand particle and nano-sized particle; 3) prevalent contacts between sand particles. The contact mode varied depending on the size and spacing of nano-sized particles, as well as the Hertzian contact diameter of the sand particles. To assess the likelihood of these presumed contact modes due to the presence of nano-sized particles, the spacing between hematite nanoparticles and the Hertz contact diameter of the substrate sand

particles were calculated according to iron contents and sand particle size (Table 7-2). The spacing between nanoparticles was calculated under the assumption of uniform distribution of hematite nanoparticles with specific gravity = 5.26 and diameter of hematite particles = 140 nm (Schwertmann and Taylor 1989), and the Hertz contact diameter was calculated using Equation (7-29). With an increase in iron content, an increased number of hematite particles per square micron of sand surface and a decreased spacing between hematite particles was observed, as anticipated. Therefore, hematite 100/200 sand, with the highest iron coating density, had the smallest spacing between nanoparticles, leading to the development of prevalent nano particle-to-nano particle contacts, resulting in the highest measured shear wave velocity ratios (Figure 7.5).

Table 7-2. Theoretical Spacing between Hematite Nanoparticles

Type	Iron Content (mg_Fe / g_sand)	N / μm^2 *	Spacing (nm)	H (nm) at 1 kPa	Notation
ASTM 20/30	0.43	17	108	2250	 Diameter of hematite particle = 140 nm
ASTM graded	1.22	24	76	1142	
ASTM 100/200**	6.35	38	47	300	

Note: *= number of hematite particles per square micron of sand surface; **: data from Larrahondo et al. (2011); H = Hertzian contact diameter

The relative difference in the calculated spacing between hematite particles for sands with varying iron content was very small (47-108 nm), and did not correspond to the presumed contact modes and the measured shear wave velocity ratios for sands

with varying iron coating density (Figure 7.4 and Figure 7.5) (Table 7-2). Furthermore, the calculated spacings between nanoparticles for all tested soils were smaller than the diameter of hematite particles, indicating that all tested hematite coated sands had the prevalent contacts between nano-sized to nano-sized particles. However, the measured wave velocity ratios of hematite coated graded sand and hematite coated 20/30 sand were close to one, indicating that the prevalent contacts were the contacts of sand-to-sand or sand-to-nano particle. This indicated that the alteration in contact mode and stiffness cannot be solely explained by the spacing between nano-sized particles even in the case where the actual coating of iron oxides onto the substrate sand surface was not evenly distributed, but concentrated in pits and defects on the sand surface (Larrahondo et al. 2011; Scheidegger et al. 1993; Xu and Axe 2005), where the actual spacing between nano-sized particles would be greater than the calculated spacing (Figure 7.6 and Figure 7.7). Additionally, the spacing between hematite particles was much smaller than the area of Hertzian contact, resulting in contacts between sand particles and hematite particles (Figure 7.7). Consequently, the results that demonstrated essentially identical shear wave velocity for iron oxide coated 20/30 sand and uncoated clean sand cannot be fully explained solely by the presumed contact mode.

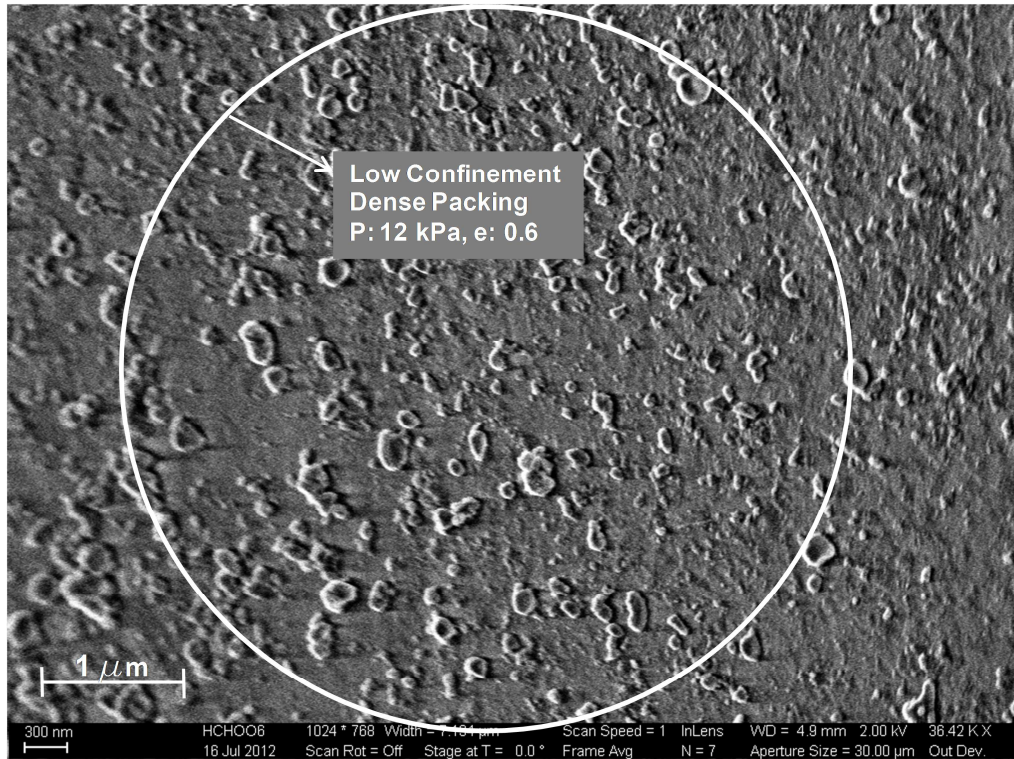


Figure 7.7. Hertzian contact area of ASTM 20/30: SEM = hematite coated 20/30 (size of hematite particle ≈ 140 nm); Hertz contact radius = Equation (29) at P (isotropic confining pressure) = 12 kPa (low confinement) and e (void ratio) = 0.6 (dense packing).

Comparison of the SEM image of hematite coated 20/30 sand to the SEM image of hematite coated 100/200 sand with the corresponding Hertzian contact areas illustrates a distinguishing feature in the ratio of the size of hematite particles to the diameter of Hertz contacts: there was a difference of almost one order of magnitude in the sand substrate particle sizes (Figure 7.6 and Figure 7.7). The change in the size ratios according to the size of substrate sand particle was accounted for using the concept of relative scales (i.e., relative roughness: size ratio of hematite particle to sand particle) for hematite 20/30, hematite graded, and hematite 100/200 sands. The calculated values for relative roughness were $1.94 \cdot 10^{-4}$ (hematite 20/30), $3.84 \cdot 10^{-4}$

(hematite graded), and $1.4 \cdot 10^{-3}$ (hematite 100/200). The surface of hematite coated 20/30 sand, with very low relative roughness, behaved as a smooth surface (Santamarina et al. 2001), with the protruded hematite particle exerting relatively little influence on the contact stiffness, resulting in the stiffness of soils that was primarily determined by the stiffness of the background sand particles (Figure 7.8). The resulting shear wave velocity of the iron oxide coated 20/30 sand was comparable to that of uncoated 20/30 sand (Figure 7.4). In contrast, hematite coated 100/200 sand, which had higher relative roughness compared to other iron oxide coated sands, resulted in a soil stiffness that was more closely related to the stiffness of protruded iron oxide nanoparticles (Figure 7.4 and Figure 7.8). And this explanation for the effect of relative roughness on the shear wave velocity can be further supported by previous experimental results of Cascante and Santamarina (1996) for clean steel spheres and Santamarina and Cascante (1998) for rusted steel spheres: the shear wave velocity of mildly rusted steel spheres, representing low relative roughness, was comparable with that of clean steel spheres; while, the shear wave velocity of highly rusted steel spheres, representing high relative roughness, showed very distinctive values compared to that of clean steel spheres. Additionally, it is also important to note that the shear wave velocity ratio is impacted by applied stress, packing density, and iron content, as well as relative roughness (Figure 7.8). In other words, the wave velocity ratio generally decreased with a decrease in relative roughness; however, the boundaries of shear wave velocity ratio were determined by the applied stress and packing density, and the maximum wave velocity ratio was closely related to the iron content (Figure 7.8).

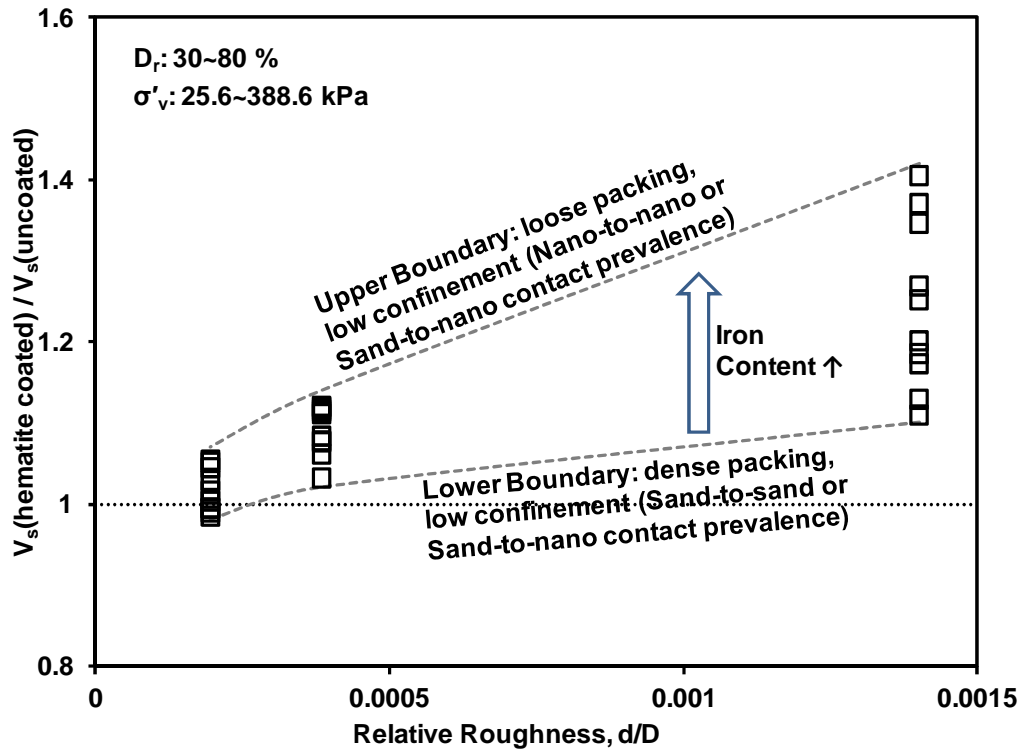


Figure 7.8. Variation of shear wave velocity ratio according to relative roughness: relative roughness = d/D ; d = diameter of hematite particles; D = diameter of substrate sand particles; initial relative density = 30 ~ 80 %; applied vertical stress = 25.6 ~ 388.6 kPa.

In contrast to hematite particles, goethite particles have a needle-like shape with dimensions of approximately 780 nm in length and 120 nm in diameter (Larrahondo et al. 2011), representing a much larger particle size than hematite, resulting in greater relative roughness when compared to hematite coated sands. Consequently, even though the iron coating density of goethite coated sands was smaller than that of hematite coated sands, the obtained shear wave velocities of goethite coated sands were comparable with those of hematite coated sands, due to the increased relevance of protruded iron oxide particles (Figure 7.4). In addition, the measured shear wave velocity of goethite coated sand was comparable to that of

uncoated sand, noted as the relative roughness decreased due to an increase in substrate sand particle size.

7.5.3 Comparison of Test Results with Theoretical G_{\max}

Using the measured shear wave velocity, the maximum shear modulus G_{\max} of soils was calculated as follows:

$$G_{\max} = \rho \cdot V_s^2 \quad (7-33)$$

where, ρ is mass density. Comparing the measured test results with theoretically determined values of the G_{\max} ratio (ratio of G_{\max} of coated sand to G_{\max} of uncoated sand) determined for nano particle-to-nano particle contact and sand particle-to-nano particle contact showed that the theoretical G_{\max} ratios acted as the boundaries for stiffness for coated soils, demonstrating insight into the alteration of contact modes according to iron oxide coating density, packing density, applied stress, and substrate sand particle size (Figure 7.9). For example, hematite coated 100/200 sand with loose packing and low confinement had a G_{\max} ratio that was very close to that of theoretical nano-to-nano contact (i.e., prevalent contact between nano-sized particles), while densely packed specimens with low applied stress showed ratios that were very close to that of theoretical sand particle-to-nano particle contacts (i.e., prevalent contacts between sand particles and nano-sized particles). In addition, with an increase in applied stress, the behavior of both specimens of initially loose and dense packings converged, representing intermediate contacts of nano particle-to-nano particle and sand particle-to-nano particle. Additionally, with a decrease in relative roughness or iron coating density (or increase in substrate sand particle size), the prevalent contact between particles shifted from nano-to-nano to nano-to-sand to

sand-to-sand, which resulted in densely packed hematite coated 20/30 sand showing almost identical stiffness to that of clean 20/30 sand.

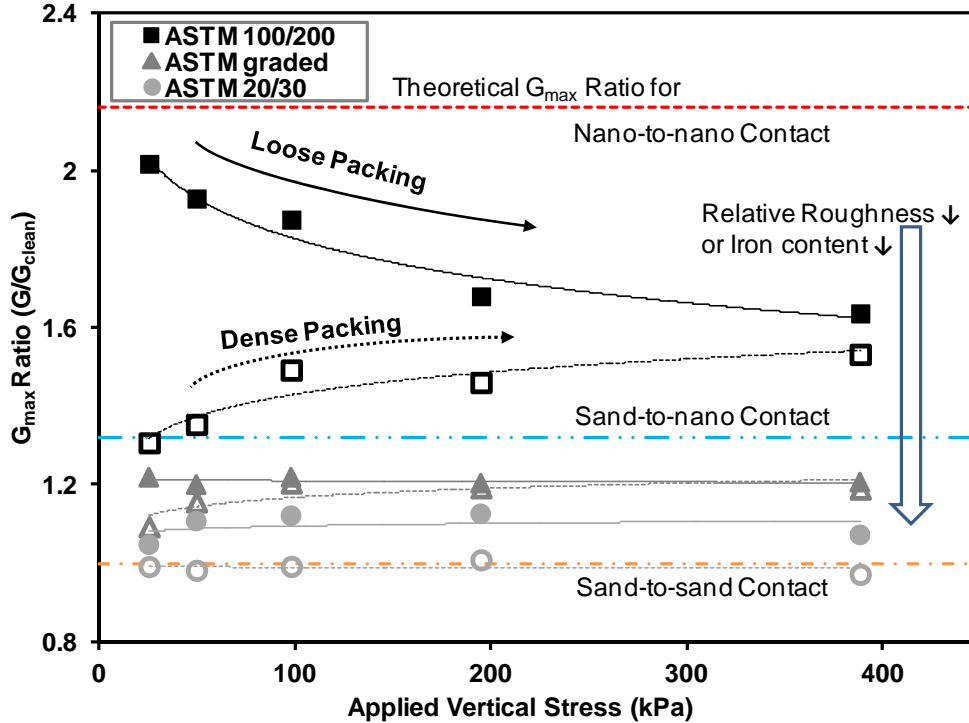


Figure 7.9. Comparison of measured G_{max} ratio with theoretical G_{max} ratio according to contact mode: G_{max} ratio = the ratio of G_{max} of hematite coated soil to G_{max} of uncoated soil; theoretical G_{max} ratio = Figure 7.3; closed figures = loose packing; open figures = dense packing.

7.6 Summary

This study presented the results of an analytical and experimental investigation designed to determine the impact of the presence of sorbed nano-sized iron oxide particles on the small strain stiffness of sands. The primary findings from this study demonstrated that:

1. The change in contact modes due to the presence of nano particles could be considered as three different contact cases, based on the spacing between nano-sized particle as well as the Hertzian contact diameter.
2. Contact between nano-sized hematite particles resulted in the highest theoretically calculated small strain stiffness, due to the greater elastic modulus of hematite compared to that of quartz.
3. Due to the differences in contact mode observed between particles according to initial relative density and applied stress, the shear wave velocity ratio (ratio of V_s of hematite coated sand to V_s of uncoated clean sand) decreased with an increase in applied stress in the case of loose packing; however, the ratio increased with an increase in applied stress in the case of dense packing. The ratios of shear wave velocities of loose and dense packings converged with increasing confinement, reflecting initially different contact types between loose and dense packings that became similar with an increase in applied stress.
4. With an increase in substrate sand particle size, the wave velocity ratio generally decreased due to the decrease in relative roughness. In this case, coated sands with very low relative roughness could be considered as smooth surfaces; however, the role of applied stress, packing density, and iron content on the stiffness of soils was still primary, even in the case low relative roughness.
5. The size of goethite particles was greater than that of hematite particles, which lead to greater relative roughness of goethite coated sands. Consequently, even though iron coating density of goethite coated sands was smaller than that of hematite coated sands, the obtained shear wave velocities of goethite coated

sands were comparable with those of hematite coated sands due to the increased relevance of protruded iron oxide particles.

6. Theoretical G_{\max} ratios (the ratio of G_{\max} of hematite coated sand to G_{\max} of uncoated sand) acted as the boundary of the stiffness for coated soils, yielding insight into the alteration of contact modes according to iron oxide coating density, packing density, applied stress, and substrate sand particle size.

CHAPTER 8 REVIEW OF ARCHIE'S EQUATION THROUGH THEORETICAL DERIVATION AND EXPERIMENTAL STUDY ON UNCOATED AND HEMATITE COATED SOILS

8.1 Introduction

Electrical resistivity ρ ($\Omega\cdot\text{m}$) is a measure of resistance of soil matrix against the flow electric current and is the reciprocal of electrical conductivity σ (S/m), which measures the ability of a soil matrix to carry electric current. Electrical resistivity/conductivity methods, which were developed in the early 1900s (Reynolds 1997), are currently one of the most widely used testing methods for subsurface exploration. Because the measurements are non-destructive, continuous, and precise, and demonstrate strong correlation with soil properties such as mineralogy, grain size distribution, void ratio, liquid limit, degree of saturation and water content, hydrologic properties (hydraulic conductivity and diffusive tortuosity), and geoenvironmental properties such as groundwater pollution monitoring, they are ideal for subsurface investigation (AbuHassanein et al. 1996; Archie 1942; Boudreau 1996; Campanella and Weemeees 1990; Fukue et al. 1999; Gorman and Kelly 1990; Pfannkuch 1972; Reynolds 1997; Samouelian et al. 2005; Shen and Chen 2007; Tiab and Donaldson 2004; Urish 1981).

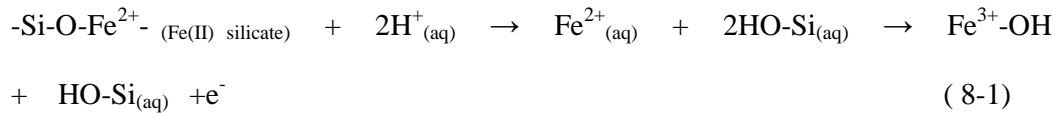
The most commonly invoked relationship for electrical conductivity (or resistivity) is based on the work of Archie (Archie 1942). Archie's equation is attractive due to its simplicity; however, it is a purely empirical equation, and may not be applicable for fine grained materials due to the lack of consideration for surface conduction. However, most coarse grained geomaterials such as sands, gravels, rocks,

and marine sediments obey Archie's equation, leading to the relevance of Archie's equation for the estimation of pore water conduction. However, the theoretical background for Archie's equation, and boundaries for the applicability of Archie's equation for various types of soils and water chemistry are not clear. Consequently, this study aimed at establishing a theoretically derived basis for the equation, and a robust electrical conductivity/resistivity formula a range of soils, including fine-grained soils. The suitability of the theoretical derivation of electrical conductivity was evaluated using electrical conductivity tests on uncoated soils, including clean Ottawa sands and Georgia kaolinite, and coated soils, including iron oxide (hematite) coated sands and kaolinite. Iron oxides were chosen for testing because iron oxides are abundant in nature (Cornell and Schwertmann 2003), but electrical measurements on iron coated soils are limited.

8.1.1 Chemical Weathering and Iron Oxide

Weathering, which is the process of breakdown of rocks, changes the properties of geomaterials, as the materials move toward a condition of higher thermodynamic stability (i.e. higher stability or lower energy potential) with their geochemical conditions. This weathering can be separated into mechanical (or physical) weathering and chemical weathering. Mechanical weathering represents the breakdown of rocks without chemical changes (e.g. unloading, thermal expansion and contraction, crystal growth, colloid plucking, and organic activity) (Mitchell and Soga 2005), while chemical weathering is the weathering of minerals by chemical reactions such as dissolution, hydrolysis, carbonation, and hydration (Maurice 2009). Generally, chemical weathering processes can be accelerated by mechanical weathering due to the increase in surface area exposed to chemical attack.

Because iron is the most fourth abundant element in Earth's crust, the process of chemical weathering cannot be separated from the role of iron or iron oxide formation (Larraondo 2011). In brief, the mechanism of iron oxide formation can be described as follows (Cornell and Schwertmann 2003; Larraondo et al. 2011):



Ferrous silicate, which is one of the most abundant iron bearing rock minerals, and Fe^{2+} cations in ferrous silicate can be displaced by electrostatic repulsion due to the attack of free protons in water. This process results in the release of the highly soluble Fe^{2+} cations. These highly soluble Fe^{2+} cations are very mobile in groundwater, but can be easily oxidized to form Fe^{3+} . The Fe(III) cation can be rapidly hydrolyzed, which results in the formation of iron oxides, often through nucleation and crystal growth on silicate or aluminosilicate surfaces (Schwertmann and Cornell 2000).

8.2 Theoretical Framework

8.2.1 Electrical Resistivity/Conductivity

The electronic transport phenomenon in a porous media can be modeled as three resistances in parallel, under the assumption that the orientation of particles is parallel to the applied electrical field (Klein and Santamarina 2003; Pfannkuch 1972). The first resistance is the electronic conduction via soil particles, the second resistance is the ionic conduction through the pore water, and the third resistance is the special form of ionic transport through particle-water interface, and can be described, along with conductance, according to:

$$\frac{1}{R_{mix}} = \frac{1}{R_p} + \frac{1}{R_w} + \frac{1}{R_s} \quad (8-2)$$

$$G_{mix} = G_p + G_w + G_s \quad (8-3)$$

Following the work of Pfannkuch (1972), the conductances in (8-3) can be expressed in terms of conductivities by considering the relevant geometry of Figure 8.1:

$$\left. \begin{aligned} G_{mix} &= \sigma_{mix} \cdot \frac{A}{L} \\ G_p &= \sigma_p \cdot \frac{A_p}{L_p} \\ G_w &= \sigma_w \cdot \frac{A_w}{L_e} \\ G_s &= \sigma_s \cdot \frac{A_w}{L_e} \cdot S_p \end{aligned} \right\} \quad (8-4)$$

where, σ_{mix} , σ_p , and σ_w are the electrical conductivities of the media, particles, and pore water, respectively in S/m; σ_s is the surface conductivity in S; S_p is specific internal surface.

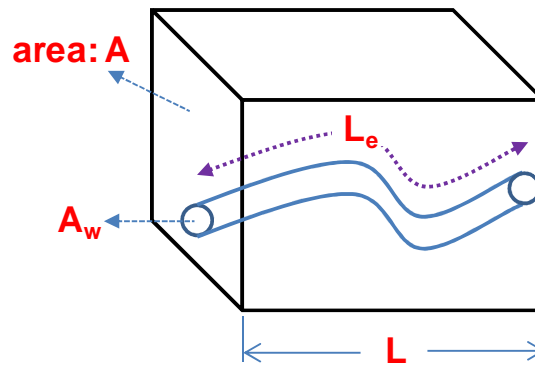


Figure 8.1. Model for electronic transport phenomena in a porous media: A = total area; A_w = area of water; L = total length; L_e = length of flow path for water.

Analysis of the geometry leads to the following relationships (Figure 8.1):

$$\frac{A \cdot L}{V_T} = \frac{A_w \cdot L_e}{V_w} = \frac{A_p \cdot L_p}{V_p} = 1 \quad (8-5)$$

The areas of the pore water and the particles can then be expressed in terms of porosity according to:

$$A_w = \frac{V_w}{V_T} \cdot \frac{A \cdot L}{L_e} = n \cdot \frac{A \cdot L}{L_e} \quad (8-6)$$

$$A_p = \frac{V_p}{V_T} \cdot \frac{A \cdot L}{L_p} = (1-n) \cdot \frac{A \cdot L}{L_p} \quad (8-7)$$

where, n: porosity; V_T : total volume; V_w : volume of water; V_p : volume of particles; A: total area; A_w : area of water; A_p : area of particles; L: total length; L_e : length of flow path for water; L_p : length of flow path for particles; and tortuosity can be defined as:

$$T = \frac{L_e}{L} \quad (8-8)$$

Combining Equations (8-4), (8-6), (8-7) and (8-8) into (8-3) and simplifying results in the following relationship for media conductivity:

$$\sigma_{mix} = \sigma_p \cdot (1-n) \cdot \left(\frac{L}{L_p} \right)^2 + \sigma_w \cdot \frac{n}{T^2} + \sigma_s \cdot S_p \cdot \frac{n}{T^2} \quad (8-9)$$

Note that Equation (8-9) was suggested by Pfannkuch (1972), and further analysis based on Equation (8-9) is performed in this study. The specific internal surface with respect to the pore volume of the sample in Equations (8-4) and (8-9) can be defined as solid volume-based specific surface as follows (Bear 1972; Urish 1981):

$$S_p = \frac{1-n}{n} \cdot S_v \quad (8-10)$$

Introducing the mass density of particles allows conversion of solid volume-based

specific surface in Equation (8-10) to mass-based specific surface according to:

$$S_v = \rho_p \cdot S_a = G_s \cdot \rho_w \cdot S_a \quad (8-11)$$

Substituting (8-10) and (8-11) to (8-9) will yield the electrical conductivity of a porous media:

$$\sigma_{mix} = \sigma_p \cdot (1-n) \cdot \left(\frac{L}{L_p} \right)^2 + \sigma_w \cdot \frac{n}{T^2} + \sigma_s \cdot \frac{1-n}{T^2} \cdot S_a \cdot G_s \cdot \rho_w \quad (8-12)$$

where, S_a is specific surface in m^2/g ; G_s : specific gravity; ρ_w : mass density of water. From Equation (8-12), it can be found that the mixed (or measured) conductivity of a porous media is the sum of particle conduction (the first term), pore water conduction (the second term), and surface conduction (the last term) under the assumption of fully saturated conditions. And particle conduction, pore water conduction, and surface conduction are functions of particle conductivity, pore water conductivity, and surface conductivity, respectively.

Most soil particles are electrically non-conducting materials; thus, it will be safe to neglect the role of particle conductivity on the total media conductivity. Thus, Equation (8-12) becomes:

$$\sigma_{mix} = \sigma_w \cdot \frac{n}{T^2} + \sigma_s \cdot \frac{1-n}{T^2} \cdot S_a \cdot G_s \cdot \rho_w \quad (8-13)$$

Finally, in the case where pore water has high salinity, leading to the condition where the conduction of pore water is much greater than that of particle-water interface, or in the case where the specific surface of a given soil is relatively small (i.e., sand and gravel deposits), the second term, surface conduction, in Equation (8-13) may be disregarded, leading to:

$$\sigma_{mix} = \sigma_w \cdot \frac{n}{T^2} \quad (8-14)$$

with the reciprocal of the conductivity is the resistivity:

$$\rho_{mix} = \rho_w \cdot T^2 \cdot n^{-1} \quad (8-15)$$

In addition, there have been several theoretical and experimental attempts to correlate the tortuosity factor with the porosity of a porous media (Boudreau 1996; Dias et al. 2006; Koponen et al. 1996; Matyka et al. 2008; Shen and Chen 2007). Assuming the following the power law relation between tortuosity factor and porosity:

$$T = n^{-p} \quad (8-16)$$

results in the following relationship for resistivity of Equation (8-15):

$$\rho_{mix} = \rho_w \cdot n^{-2p} \cdot n^{-1} = \rho_w \cdot n^{-(1+2p)} \quad (8-17)$$

Recalling the original Archie's Equation (Archie 1942) under fully saturated conditions:

$$\rho_{mix} = \rho_w \cdot n^{-m} \quad (8-18)$$

The relation between the theoretically derived Equation (8-17), which was developed by the conversion of tortuosity into porosity, and the most widely used empirical formula of Archie, Equation (8-18), is clear in case where the pore water conduction is dominant over the surface conduction. Klein and Santamarina (2003) suggested the simple conductivity model for the porous media based on infinitely long, parallel-shaped particles (Figure 8.2):

$$\sigma_{mix} = \frac{\sigma_p \cdot t_p + \sigma_w \cdot t_w + 2\sigma_s}{t_w + t_p} \quad (8-19)$$

From the relevant relation between particle thickness t_p and specific surface S_a , and estimated porosity from Figure 8.2, Equation (8-19) can be as follows (see details,

Klein and Santamarina (2003):

$$\sigma_{mix} = (1-n) \cdot \sigma_p + n \cdot \sigma_w + (1-n) \cdot \frac{\gamma_p}{g} \cdot \sigma_s \cdot S_a \quad (8-20)$$

Except for consideration of the tortuosity factor, it is surprising that (8-20) is exactly the same as (8-12) since Equation (8-20) was derived based on the assumption of infinitely long, parallel-shaped particles.



Figure 8.2. Simple conductivity model for a porous media: t_p = thickness of particle; t_w = thickness of water.

8.2.2 Surface Conductivity

Soil surfaces (or the soil-water interface) in natural aquatic environments have charges due to isomorphic substitution, proton association/dissociation, broken bonds, and excess ions accumulated near the surface. The net total charge density of a soil particle can be expressed (Maurice 2009; Sposito 2004) according to:

$$\rho_s = \rho_0 + \rho_H + \rho_{IP} + \rho_{OP} \quad (8-21)$$

When all charges are balanced, the net total charge density will be zero, resulting in the particle surface charge density ρ_p , which is the sum of ρ_0 and ρ_H . The particle surface charge density will be balanced by charges in the Stern and diffuse layers, resulting in:

$$\rho_p = \rho_0 + \rho_H = -\rho_{IP} - \rho_{OP} \quad (8-22)$$

where, ρ_s : total net charge density; ρ_0 : structural surface charge density due to

isomorphic substitution; ρ_H : proton surface charge density due to protonation/deprotonation; ρ_{IP} : surface charge density of inner part due to ions adsorbed at Stern layer; ρ_{OP} : surface charge density of outer part due to ions electrically attracted at diffuse layer. The charges at the soil particle-water interface will attract a higher density of counter ions near the surface (i.e. Stern layer and diffuse layer) than the ions in the bulk solution, leading to surface conduction (or surface conductivity), which is different from pore water conduction. Interest in surface conductivity has increased recently because it can reflect the electrokinetic properties of soil particles, such as abundance of counter ions, ion mobilities, and zeta potential (Lyklema and Minor 1998; Revil and Glover 1998). Older studies on surface conductivity attributed electronic transport phenomenon at the particle-water interface to ionic transport and electro-osmosis in the diffuse layer (Bikerman 1933; Bikerman 1935; Pfannkuch 1972); however, recent studies put the emphasis not only on the diffuse layer, but also on Stern layer to explain mineral surface conductivity (Leroy and Revil 2004; Lyklema and Minor 1998; Revil and Glover 1998; Urban et al. 1935). Following the work of Lyklema and Minor (1998), the surface conductivity can be expressed as:

$$\sigma_s = u_{IP} \rho_{IP} + u_{OP} \rho_{OP} + \frac{3 \cdot m}{z^2} u_{OP} \rho_{OP} \quad (8-23)$$

where, u_{IP} is ion mobility in the inner part; u_{OP} is ion mobility in the diffuse part; m is dimensionless parameter to consider the electro-osmosis in the diffuse part; z is the valency of excess ions (see details, Lyklema and Minor (1998)).

8.3 Experimental Program

8.3.1 Materials

ASTM 20/30 and ASTM 60/80 sands (U.S. Silica Company) were selected as the uncoated sands, and iron oxide (hematite) coated sands were prepared using these two sands as the substrate for the iron oxide adsorption. Georgia kaolinite (Dry Branch Kaolin Company) was used as the fine grained soil. The iron oxide (hematite) was obtained from Sigma Aldrich Corporation, and was used as received. All other chemicals (NaNO_3 , NaOH , HCl , H_2O_2 , NaHCO_3 , $\text{Na}_2\text{S}_2\text{O}_4$, $\text{C}_6\text{H}_5\text{Na}_3\text{O}_7$, HNO_3 , and NaCl) were obtained from Sigma Aldrich Corporation and Fisher Scientific, and were used as received. Deionized water (Barnstead E-pure) was used in all experiments.

The heterogeneous suspension reaction method of iron oxide coating preparation was adopted in this study, and iron oxide coated soils were prepared following the suggestions of those previous studies (Larrahondo et al. 2011; Nachtegaal and Sparks 2004; Scheidegger et al. 1993). All materials were digested in 3% H_2O_2 solution for 24 hours to remove organic matter on the soil particle surfaces, and iron oxide coated sands and clay were prepared under controlled pH and ionic strength. For sands, the suspension of 40mg hematite/1g sand was thoroughly mixed at pH 3 and ionic strength 0.01 M (Larrahondo et al. 2011; Scheidegger et al. 1993), and for clay, the suspension of 80 mg hematite/1g kaolinite was mixed at pH 7.5 and ionic strength 0.01 M (Nachtegaal and Sparks 2004).

Extreme void ratios of uncoated and iron oxide coated sands were determined according to ASTM D4253 and ASTM D4254, and the specific gravity was determined by ASTM D854. Liquid limit was determined by the fall cone method (British Standard 1377), and the specific surface was determined by the methylene blue method (Santamarina et al. 2002). Iron content was measured by the DCB

technique (Mehra and Jackson 1960) with analysis performed using inductively coupled plasma – optical emission spectrometry ICP-OES (Optima 8000, PerkinElmer). Properties of the tested materials are given in Table 8-1.

Table 8-1. Material Properties

Properties	ASTM 20/30	Hematite 20/30	ASTM 60/80	Hematite 60/80	Georgia Kaolinite	Hematite Kaolinite
G_s	2.650	2.662	2.649	2.663	2.600	2.762
e_{\max}	0.739	0.712	0.912	0.821	-	-
e_{\min}	0.519	0.516	0.584	0.557	-	-
LL (%)	-	-	-	-	45	50
S_a (m ² /g)	-	-	-	-	21.7	26.9
Iron Content (mg_Fe/g_soil)	-	0.431	-	1.771	-	43.3

Note: G_s = specific gravity; e_{\max} and e_{\min} = maximum and minimum void ratios respectively; LL = liquid limit; S_a = specific surface

8.3.2 Test Equipment and Electrical Resistivity Measurements

In order to measure the electrical resistivity/conductivity, a plane type four electrode resistivity probe was installed inside a modified oedometer cell which was made of PVC (Kim et al. 2011a) (Figure 8.3). The four electrode configuration was chosen in order to minimize the electrochemical effect by employing four electrodes, instead of two electrodes (Campanella and Weemeees 1990; Kim et al. 2011a). During the experiment, the current flowed from high current (Hc) to low current (Lc), and the potential difference (or resistance) was measured using the two inner electrodes. Consequently, the measured resistance (LCR meter, Agilent, 4236B) was converted to

resistivity by employing the proper calibration factor (or geometrical factor). The operating frequency of the LCR meter was selected as 100 kHz to prevent electrode polarization and electrical resonance (Kim et al. 2011a; Kim et al. 2011b) and input voltage was 1 V. In addition, for the easy installment and replacement of the resistivity probe into/from oedometer cell, 4 electrodes were housed in a nylon set screw by using epoxy resin.

The zeta potential of uncoated kaolinite and hematite coated kaolinite was measured using a ZetaPlus zeta potential analyzer (Brookhaven Instruments Corporation, Holtsville, NY, USA). Testing samples were prepared by mixing 0.6 grams of soils with 1000 mL of 0.01 M NaCl solution for 20 min. The zeta potential was measured as a function of pH, ranging from 2.5 to 10.

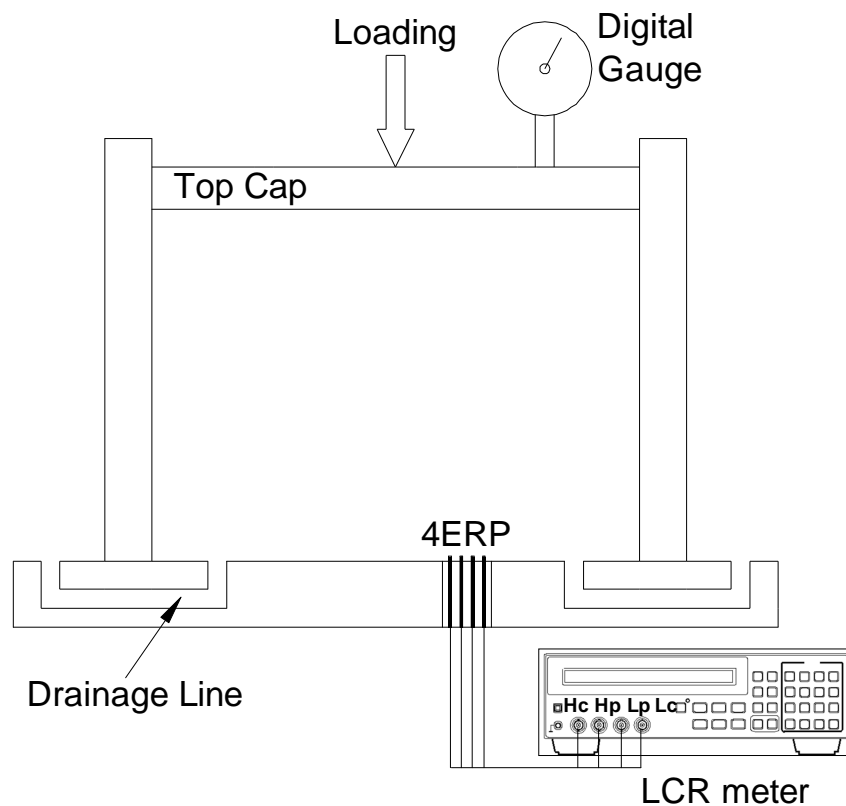


Figure 8.3. Setup for electrical conductivity/resistivity measurement after the method of Kim et al. (2011a)

8.3.2.1 Calibration of Probe

Electrical current flows through two outer electrodes (A and B) and the potential difference can be measured using two inner electrodes (M and N) (Figure 8.4). The measured electrical resistance converted from potential difference is related to electrical resistivity through geometric consideration as follows:

$$\rho = R \cdot K \quad (8-24)$$

The geometrical factor K in Equation (8-24) can be calculated from Ohm's law and hemispherical distribution of electrical equipotentials as follows (Reynolds 1997; Samouelian et al. 2005):

$$K = 2 \cdot \pi \cdot \left[\left(\frac{1}{AM} - \frac{1}{MB} \right) - \left(\frac{1}{AN} - \frac{1}{NB} \right) \right]^{-1} \quad (8-25)$$

When the spacing between electrodes is equidistant as "s" (i.e., AM=MN=NB=s), the arrangement of electrodes in Figure 8.4 is called a Wenner array, and Equation (8-25) can be simplified to:

$$K = 2 \cdot \pi \cdot s \quad (8-26)$$

where, s: distance between electrodes.

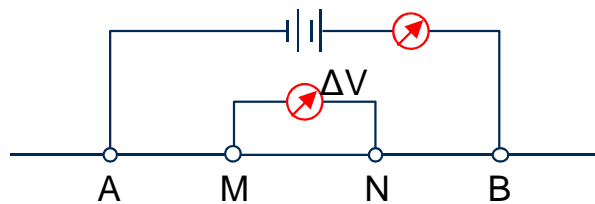


Figure 8.4. Typical arrangement of 4 electrodes: A and M = current electrodes; M and N = potential electrodes.

Figure 8.5 shows the result of calibration of the four electrode resistivity probe used in this study by comparing resistance measured by LCR meter with resistivity/conductivity measured by conductivity meter for various NaNO_3 solutions: electrical conductivity measurements of NaNO_3 solutions with various concentrations were obtained using a conductivity meter (Accumet Excel XL20) and temperature-compensated two-cell conductivity probe (Accumet). The measured calibration (or geometrical) factor was 0.018 m. Furthermore, the center-to-center distance between electrodes employed in this study was designed to equal 3 (± 0.1) mm, and by employing (8-26), the calculated geometrical factor was almost identical to the measured calibration factor.

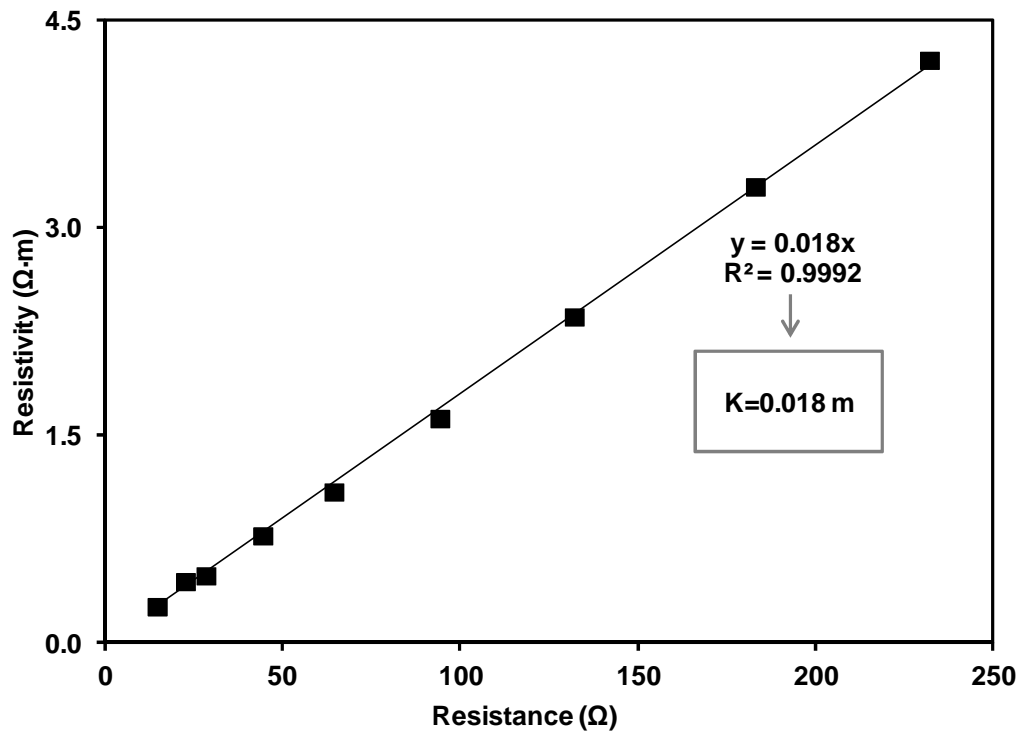


Figure 8.5. Calibration of resistivity probe with electrolytes: the slope K indicates the geometrical factor in Equation (8-24); resistance was measured by LCR meter; resistivity was measured by conductivity meter.

8.3.3 Sample Preparation and Testing Program

All tested samples were washed with deionized water (Barnstead E-pure) before the test until the conductivity of supernatant was below 0.001 S/m. For sands, prepared samples with initial relative densities ranging from 30 to 70 % were prepared by the water pluviation method to make sure fully saturated and homogeneous conditions (tested samples are well-sorted so that water pluviation-induced segregation of particles was minimal) and tested under K_0 conditions using vertical stresses ranging from 13.5 kPa to 400 kPa (Table 8-2). This allowed the measurement of electrical resistivity/conductivity as a function of consolidation loading and unloading processes. For the clays, samples were prepared in the slurry condition at 1.5 to 5 times the liquid limit in a solution with various NaNO_3 concentrations. All samples were mechanically mixed for 20 minutes. To obtain proper hydration or saturation, the mixtures were stored in a plastic bag for a minimum of 24 hours. Electrical conductivity measurements were conducted after remixing the mixtures in a plastic bag. Finally, to quantify the effect of pore water conduction on total medium conductivity, testing specimens were prepared under a range of pore water conductivities, ranging from $3.64 \cdot 10^{-2}$ to 4.14 S/m.

Table 8-2. Test Matrix

Type	Sand		Clay	
	Uncoated	Coated	Uncoated	Coated
	ASTM 2030 ASTM 6080	Hematite 2030 Hematite 6080	Georgia Kaolinite	Hematite Kaolinite
σ_w (S/m)	$6.65 \cdot 10^{-2} \sim$ 4.14	$6.65 \cdot 10^{-2} \sim$ 4.14	$3.64 \cdot 10^{-2} \sim$ 1.026	$3.64 \cdot 10^{-2} \sim$ 1.026
Initial D_r or w	30 ~ 70 %	30 ~ 70 %	1.5 ~ 5 LL	1.5 ~ 5 LL
σ'_v (kPa)	13.5 ~ 400	13.5 ~ 400	-	-

Note: σ_w = pore water conductivity; D_r = relative density; w = water content; σ'_v = applied vertical effective stress

8.4 Test Results and Analysis

8.4.1 Uncoated and Hematite Coated Ottawa Sands

Figure 8.6 indicates the variation of electrical conductivity/resistivity of hematite coated ASTM 60/80 and uncoated pure ASTM 60/80 sands as a function of porosity. Tests were performed at a relatively low pore water conductivity to emphasize the change in surface conduction due to the iron oxide coating on the sand surface. It can be observed that the electrical conductivity/resistivity of hematite coated and uncoated 60/80 sands showed very good agreement, leading to a negligible effect of iron oxide coating on the media (or mixed) conductivity. In addition, the measured conductivities of coated and uncoated sands were located on the same line during loading and unloading (data not shown), which revealed that there was no effect of applied stress on the electrical conductivity of hematite coated soils. This reflected the negligible particle conduction of iron oxide coated sands because electrically conductive particles would be impacted by the applied stress due to the

increase in contact area and coordination number (Holm 1967; Slade 1999). Consequently, the mixed conductivity of both uncoated and hematite coated Ottawa sands can be described by the sum of pore water conduction and surface conduction (Equation (8-13)). For analysis in terms of pore water conduction (Equation (8-14)), the measured conductivity (Figure 8.6) was plotted as a function of porosity, resulting in very similar pore water conduction between coated and uncoated sands at a given porosity. The similar pore water conduction was determined assuming similar values of tortuosity between the two soils; previous researchers have found similar values of hydraulic conductivity measured for of different iron oxide (hematite and goethite) coated and uncoated sands (Larrahondo 2011), which implied similar tortuosity for the soils. Thus, the comparable values determined for mixed conductivity and pore water conduction revealed that the change in surface conduction due to the adsorption of iron oxide onto the sand surface can be neglected.

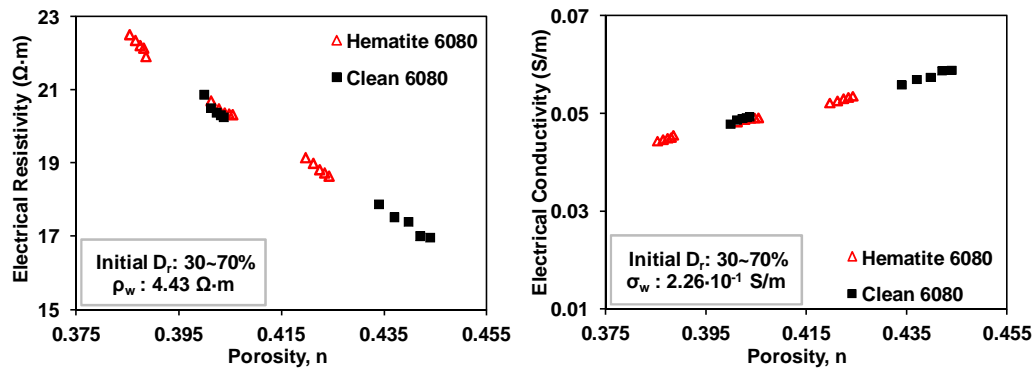


Figure 8.6. Electrical conductivity/resistivity variation of hematite coated and uncoated ASTM 60/80 sands according to porosity: pore water conductivity = 0.226 S/m; initial relative density = 30 ~ 70 %.

Figure 8.7 indicates the variation of the media conductivity of uncoated and hematite

coated ASTM 20/30 sands according to pore water conductivity under similar relative density of 30%. The hematite coated and uncoated ASTM 20/30 sands yielded similar extreme void ratios, because the preparation of samples under similar relative density resulted in a similar void ratio or porosity. The media conductivity of uncoated and hematite coated sands showed excellent agreement under similar relative density (or void ratio). Additionally, the relation between the mixed conductivity and pore water conductivity showed excellent linearity with an almost zero y-intercept, leading to a constant formation factor, the formation factor is the ratio of media conductivity to pore water conductivity, regardless of pore water conductivity. It is important to note that the formation factor of soils with high surface conduction, such as clays, will be variable according to pore water conductivity due to the change in the ratio of surface conductivity to pore water conductivity (Urish 1981). Therefore, from either zero y-intercept or constant formation factor and the variation of pore water conductivity (Figure 8.7), the contribution of surface conduction on the overall media conductivity was minimal, which resulted in the electrical conductivity (or resistivity) of hematite coated and uncoated Ottawa sands that will be governed by pore water conduction, indicating the relevance of Archie's equation.

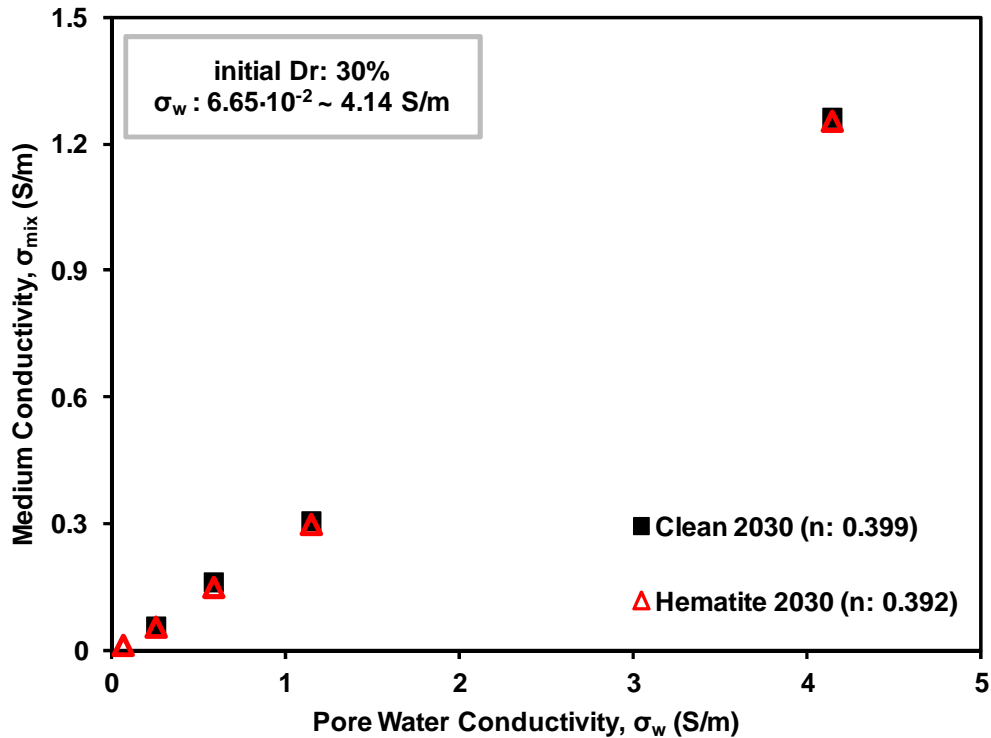


Figure 8.7. Conductivity of porous media according to pore water conductivity (hematite coated and uncoated ASTM 20/30 sands).

8.4.2 Uncoated and Iron Oxide Coated Kaolinites

8.4.2.1 Zeta Potential

The zeta potential represents the electrical potential at the shear plane (i.e., interface between the slipping plane and bulk fluid), is a measure of the energy of interaction between neighboring particles that gives insight into the surface charge of mineral surface (Bate and Burns 2010). The measured values of zeta potential showed comparable values with those of previous studies (Figure 8.8), where natural kaolinite ranged from 0 mV to -45 mV as a function of pore water chemistry (Smith and Narimatsu 1993; Williams and Williams 1978; Yukselen and Kaya 2003). The zeta potential of a soil mineral will vary with ionic strength and with pH due to the

protonation/deprotonation of mineral surface. Zeta potential of both uncoated and hematite coated kaolinite was measured over a pH range from 2.5 to 10, with the standard deviation of readings less than 0.5 mV. Most notably, it is clear from the data that there was no significant difference between measured zeta potential of uncoated pure kaolinite and hematite coated kaolinite, indicating similar surface charges for the clay specimens. Previous studies on zeta potential (ZP) or electrophoretic mobility (EM) measurement of iron oxide coated soils reported that ZP or EM was affected by iron content (iron oxide coating density) and iron oxide type (Cornell and Schwertmann 2003; Escudey and Galindo 1983; Osei and Singh 1999); however, at a relatively low iron content, the ZP (or EM) of iron oxide coated soils may be comparable to that of uncoated natural soils. With further increases in iron content, the variation of ZP (or EM) of iron oxide coated soils as a function of pH will be shifted to the right (i.e., higher isoelectric charge point (IEP) and less negative ZP at high pH (or higher positive ZP at low pH)) or approach to that of pure iron oxide due to the neutralizing effect of surface charge of natural soils with the adsorption of iron oxide onto mineral surface. In past studies, the EM of goethite coated kaolinite with coating density of 38 mg_Fe/g_kaolinite was comparable to that of uncoated kaolinite (Cornell and Schwertmann 2003), and so the tested hematite coated kaolinite (iron content of 43.3 mg_Fe/g_kaolinite) should have similar surface charge at the shear plane as that of uncoated kaolinite.

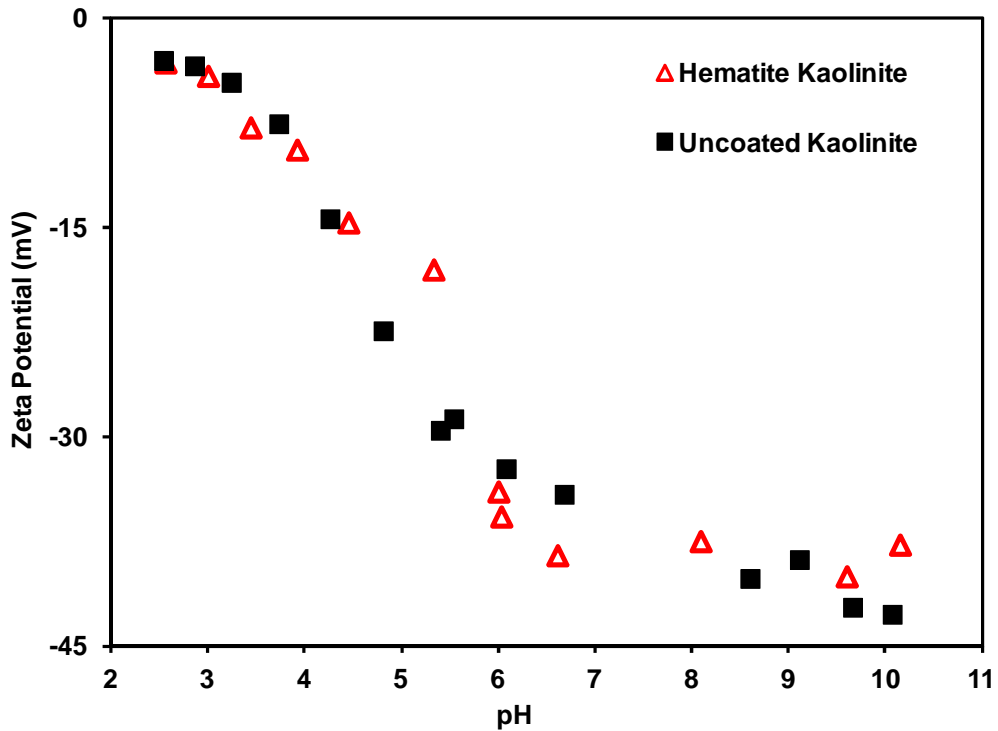


Figure 8.8. Zeta potential of hematite coated and uncoated kaolinite as a function of pH.

8.4.2.2 Electrical Conductivity/Resistivity

The variation of electrical conductivity and resistivity of uncoated and hematite coated kaolinites under pore water conductivity of $3.64 \cdot 10^{-2}$ S/m and 1.025 S/m demonstrated that the electrical conductivities of both uncoated and hematite coated kaolinites increased with a decrease in porosity in the case of very low pore water conductivity (Figure 8.9). However, the electrical conductivities of both soils decreased with a decrease in porosity in the case of high pore water conductivity, which is consistent with the previous observations of Klein and Santamarina (2003). Consequently, these observations reinforced both the importance of surface conduction in low salinity pore water (Equation (8-13)) and the insignificance of

surface conduction in high salinity pore water (Equation (8-14)). Most notably, the electrical conductivity of hematite coated kaolinite showed a higher value than that of uncoated kaolinite at low pore water conductivity; however, very similar conductivity or resistivity between coated and uncoated kaolinite was observed at high salinity. Consequently, the higher electrical conductivity of hematite-coated kaolinite compared to that of uncoated kaolinite can be attributed to the greater surface conduction of hematite coated kaolinite.

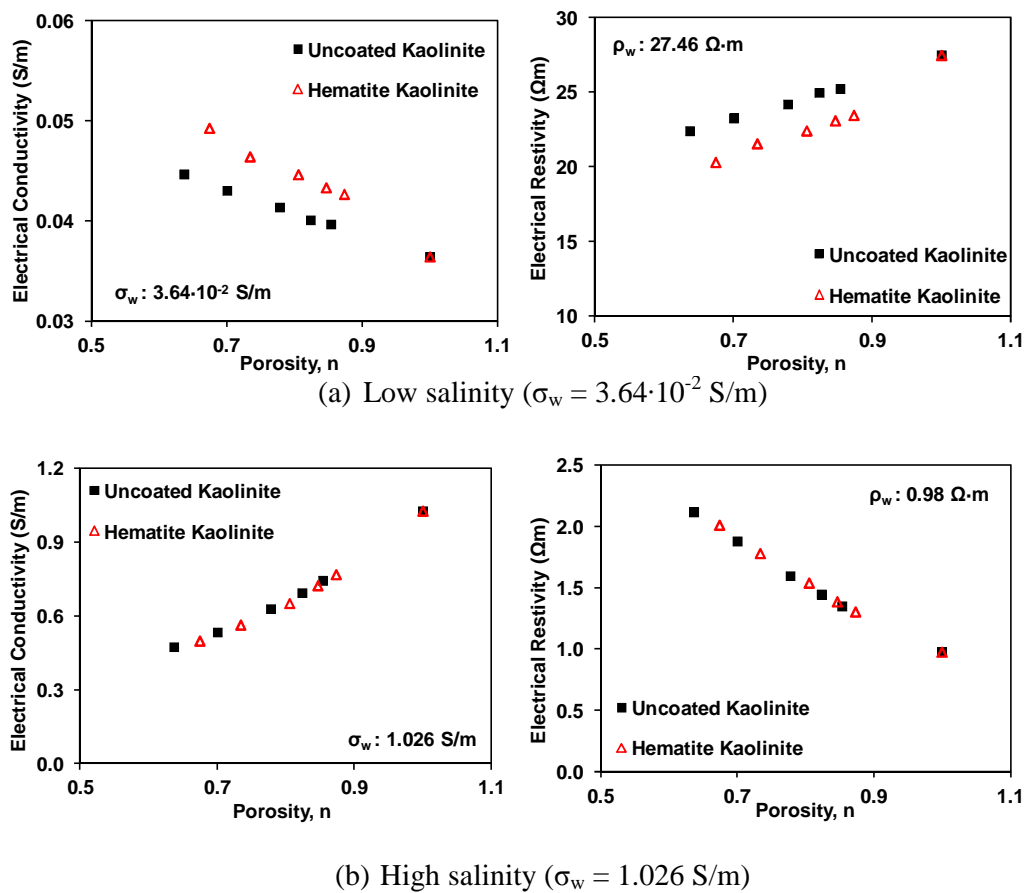


Figure 8.9. Electrical conductivity/resistivity variation of hematite coated and uncoated Kaolinites according to porosity: (a) pore water conductivity = $3.64 \cdot 10^{-2}$ S/m; (b) pore water conductivity = 1.026 S/m.

8.5 Discussion

8.5.1 Contribution of Surface Conduction to Conductivity of a Porous Media

8.5.1.1 Effect of Pore Water Conductivity and Specific Surface

For the spherical particles, the specific surface can be estimated based on uniformity coefficient, specific gravity, and median grain size as follows (Santamarina et al. 2001):

$$S_a = \frac{3 \cdot (C_u + 7)}{4 \cdot \rho_w \cdot G_s \cdot D_{50}} \quad (8-27)$$

Equation (8-27) will not be valid for platy particles such as clays; however, it can yield reasonable values for sands and gravels (Figure 8.10). Except for very fine grained sands, the specific surface of sand and gravel shows small values, typically smaller than $0.01 \text{ m}^2/\text{g}$.

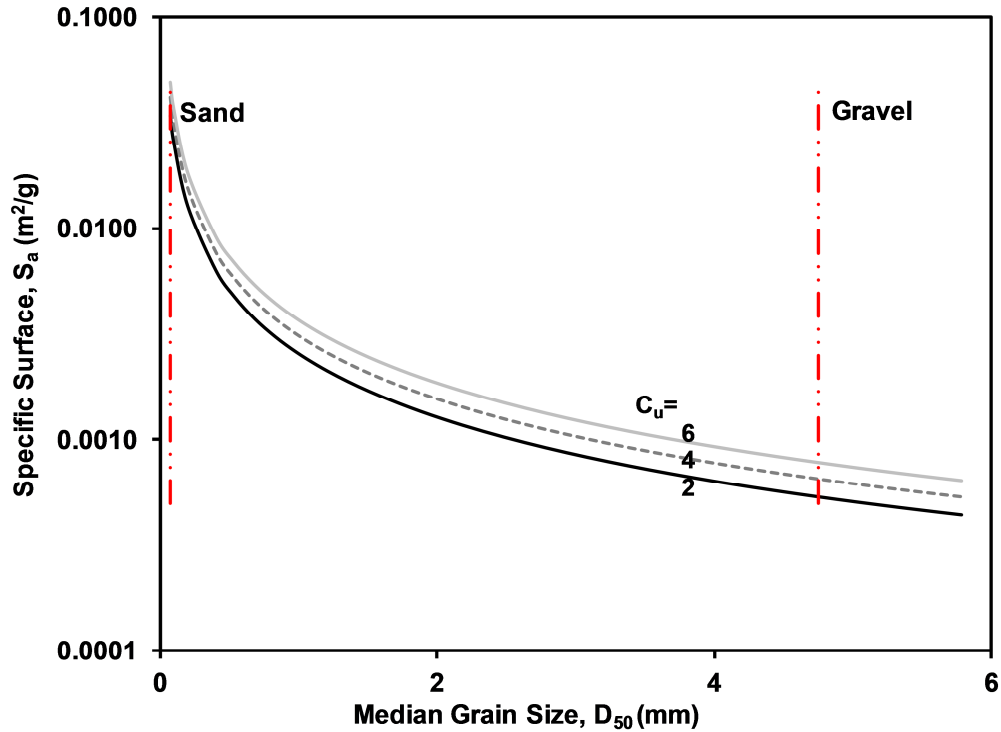


Figure 8.10. Estimated specific surface based on median grain size and uniformity coefficient: specific surface = Equation (8-27).

The mixed conductivity and pore water conduction were calculated using Equation (8-13) and (8-14), with specific gravity assumed equal to 2.65; surface conductivity in (8-13) was assumed equal to $8.9 \cdot 10^{-9}$ S/m for sand (or quartz) and $2.5 \cdot 10^{-9}$ S/m for clay (Revil and Glover 1998) (Figure 8.11). Because the mixed conductivity and pore water conduction were plotted together, similar numbers between those two represent the applicability of Archie's equation. At low salinity, the mixed conductivity was greater than pore water conduction, regardless of specific surface or soil type (i.e., very low pore water conductivity $\sigma_w < 1 \cdot 10^{-3}$ S/m) which indicated that surface conduction is the dominant mechanism of conductivity of soils at very low salinity. However, with an increase in pore water conductivity, the

relevance of surface conduction to the mixed conductivity of soils, especially sand and gravel sized materials, decreased. In addition, in the case where pore water conductivity or salinity was very high, such as sea water, the mixed (or measured) conductivity of porous media was almost identical to the pore water conduction representing the measured conductivity was effectively represented by pore water conduction, obeying Archie's equation. Only in the case where the specific surface of a soil was very high, such as montmorillonite, surface conductivity was not negligible.

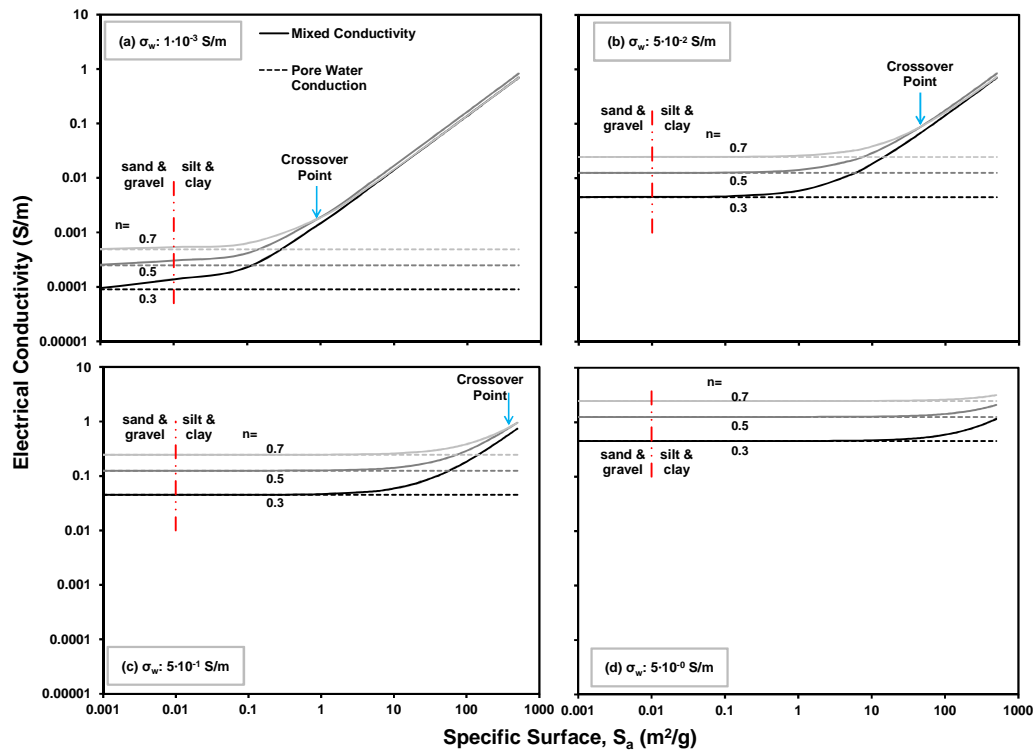


Figure 8.11. Comparison of mixed conductivity with pore water conduction under the various pore water conductivity and specific surface: (a) $\sigma_w = 1 \cdot 10^{-3}$ S/m; (b) $\sigma_w = 5 \cdot 10^{-2}$ S/m; (c) $\sigma_w = 5 \cdot 10^{-1}$ S/m; (d) $\sigma_w = 5$ S/m; mixed conductivity (solid line) = Equation (8-13); pore water conduction (dotted line) = Equation (8-14).

With an increase in porosity, the measured conductivity generally increased due to the increased flow path (number of channels for electric conduction) or due to the decrease in tortuosity for the soils (e.g. sands and gravels), with limited relevance of surface conduction. However, there was a cross-over point between electrical conductivities of $n=0.7$ and $n=0.5$ with an increase in specific surface, while electrical conductivity at $n=0.3$ showed the smallest values, indicating soils with higher relevance of surface conduction (e.g. silts and clays), they also showed a trend of increasing in electrical conductivity with a decrease in porosity (Figure 8.9a and Equation (8-13)). However, it is important to note that the smallest conductivity of $n=0.3$, regardless of specific surface also reflected that this behavior will be limited up to some critical porosity due to the large increase in tortuosity or due to the discontinuity of the pore water phase with a further decrease in porosity. This concept of critical porosity (or, water content), representing the maximum electrical conductivity at a certain porosity, is supported by the experimental observation of AbuHassanein et al. (1996). Finally, the importance of specific surface of mixed conductivity versus pore water conduction increased with an increase in porosity, indicating that the contribution of surface conduction to mixed conductivity will be greater for dense soils than loose soils, as anticipated from Equation (8-13) (Klein and Santamarina 2003).

8.5.1.2 Back-calculation of Surface Conductivity of Coated and Uncoated Kaolinite

The conductivity of the soil-water interface may be separated from the mixed conductivity in case where the pore water is ultra-pure deionized water (i.e., $\sigma_w \sim 5.5 \cdot 10^{-6}$ S/m). However, achieving this extremely low pore water conductivity is

difficult and surface conductivity also varies with pore water conductivity at extremely low values of conductivity (Mitchell and Soga 2005; Tiab and Donaldson 2004; Waxman and Smits 1968). Therefore, in this study, under the assumption that surface conductivity did not vary with electrolyte conductivity at a given pore water conductivity (e.g., salinity $> 10^{-3}$ M according to Revil and Glover (1998)), surface conductivity was back-calculated from the relationship between the mixed conductivity and pore water conduction, similar to the work of Waxman and Smits (1968). The surface conductivity is extrapolated from pore water conductivity and is taken as the y-intercept in Figure 8.12. Based on this concept, in Equation (8-13) where the conductivity of a porous media was equal to the sum of the pore water conduction and the mineral surface conduction, would be equivalent to Equation (8-28) when the measured conductivity was solely a function of surface conduction (in the where the case pore water conductivity approaches zero). Rearranging Equation (8-28), allowed the surface conductivity to be estimated as shown in Equation (8-29):

$$\sigma_{mix} = \sigma_s \cdot \frac{1-n}{T^2} \cdot S_a \cdot G_s \cdot \rho_w \quad (\text{when } \sigma_w \rightarrow 0) \quad (8-28)$$

$$\sigma_s = \frac{\sigma_{mix} \cdot T^2}{(1-n) \cdot S_a \cdot G_s \cdot \rho_w} \quad (8-29)$$

Calculating tortuosity according to Equation (8-16) with the exponent p assumed equal to 0.5 (Dias et al. 2006), resulted in back-calculated surface conductivities of hematite coated kaolinite and uncoated pure kaolinite of $2.09 \cdot 10^{-9}$ S and $2.15 \cdot 10^{-9}$ S, respectively. These comparable surface conductivities reflect no significant change in surface charge due to the hematite adsorption onto clay surface, which was consistent with the results of zeta potential measurements. Previous studies on the surface conductivity of kaolinite (Lorenz 1969) reported that surface

conductivity ranged from $1 \cdot 10^{-9}$ S to $2.8 \cdot 10^{-9}$ S as the absolute zeta potential of kaolinite increased from 17 mV to 40 mV (or with an increase in pH).

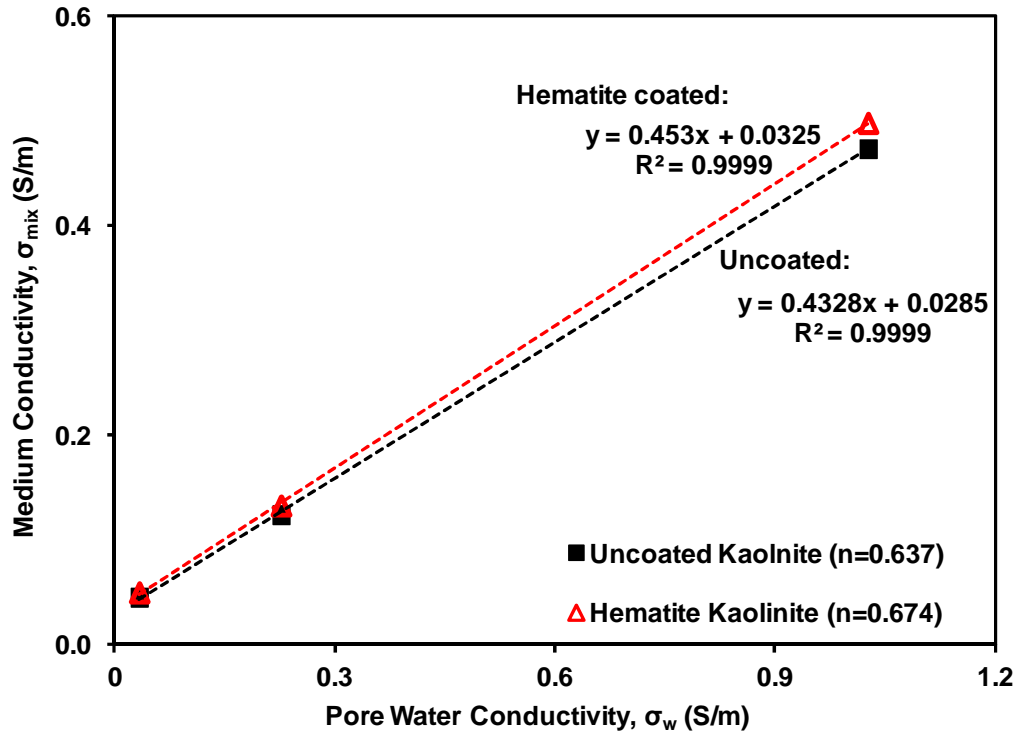


Figure 8.12. Back-calculation of surface conductivity from the relation between the mixed conductivity and pore water conductivity: surface conductivity = Equation (8-29) under the assumption of constant surface conductivity.

8.5.2 Effect of Iron Oxide Coating on Electrical Conductivity of Soils

It is known that hematite is a semiconductor (Maurice 2009; Mochizuki 1977) that is an excellent insulator at room temperature; however, it can be a conductor when temperature or pressure is extremely high or with the addition of impurities. Most iron oxides behave as semiconductors, with electrical conductivity that is very low ($\sigma \sim 10^{-7}$ S/m) at room temperature, except for magnetite which has metallic

properties (Cornell and Schwertmann 2003). For the iron oxides that behave as semiconductors, the contribution of particle conduction for most iron oxides on mixed conductivity will be negligible, as discussed previously. The test results demonstrated that electrical conductivity/resistivity of uncoated pure sands and hematite coated sands were quite similar under the tested salinity of electrolyte ($\sigma_w > 6.65 \cdot 10^{-2}$ S/m), indicating that the iron oxide coating on sand surface had negligible effect on the alteration of electrical conductivity of pure sand. However, it is important to note that, in this study, experiments on coated and uncoated sands were not performed at very low pore water conductivity, and, as mentioned above (Figure 8.11), the contribution of surface conduction to mixed conductivity is important at very low salinity. It is possible that there could be a change in measured conductivity at very low values of pore water conductivity, due to the iron oxide coating on sand surface.

The surface conduction is a function of surface conductivity, specific surface, porosity, and tortuosity (Equation (8-13)). Therefore, with other factors remaining constant, the increase in specific surface will result in an increase in surface conduction. Iron oxide adsorption onto a soil surface will increase the specific surface of natural soils (Cornell and Schwertmann 2003; Larrahondo et al. 2011; Sakurai et al. 1990; Scheidegger et al. 1993), which will in turn lead to an increase in surface conduction due to the presence of the iron oxide coating. However, it may also be important to recognize that the specific surface of sand or gravel is very small, even in the coated case, and the increase in specific surface due to the iron oxides coating on coarse grained materials, such as sand or gravel, is limited due to the limited increase in iron content as the substrate particle size gets larger (Xu and Axe 2005). Consequently, the change in electrical conductivity of tested sands due to the iron oxide coating was minimal, leading to measured conductivity/resistivity of both

hematite coated and uncoated sands that was represented by the Archie's equation under tested salinities.

In the case of clays, the measured electrical conductivity of iron oxide coated kaolinite was somewhat higher than that of pure kaolinite at low salinity, indicating that the adsorption of iron oxides onto clay particles altered the surface conduction of pure kaolinite (Figure 8.9). However, with a further increase in salinity, the electrical properties of hematite coated kaolinite and uncoated pure kaolinite showed excellent agreement because the surface conduction was overwhelmed by the pore water conduction at high salinity (Figure 8.11). The back-calculated surface conductivities of hematite coated kaolinite and uncoated pure kaolinite yielded very similar values, indicating that the effect of iron oxide coating on surface conductivity was negligible under the tested iron oxide coating density. Consequently, the increase in specific surface due to iron coating was responsible for the increase in surface conduction of hematite coated kaolinite. However, it is important to recognize that the characteristic of surface charge of coated particles according to pH could be changed if there was a further increase in iron content (iron oxide coating density). Compared to the PZC (points of zero charge) of kaolinite (approximately pH 3.5), the PZC of hematite was significantly higher (approximately pH 8), meaning that iron oxide coated soils can have a higher PZC than that of uncoated soils due to the neutralizing effect of the charge of substrate particles, which will result in a change in surface charge at a given pH (Cornell and Schwertmann 2003; Kosmulski et al. 2003; Maurice 2009; Sakurai et al. 1990). It is also important to note that an increase in PZC may yield smaller absolute surface conductivity near neutral pH because coated soils may have smaller surface charge density in the Stern and diffuse layers, when compared to uncoated soils due to the similarity between PZC and neutral pH (Santamarina et al. 2001).

Additionally, Sakurai et al. (1990) observed a decrease in cation exchange capacity (CEC) of iron oxide coated soils with an increase in iron content.

Consequently, it is hypothesized that the change in surface conduction of iron oxide coated soils may not be significant due to the offset mechanism between the increase in specific surface and the decrease in surface conductivity with an increase in iron oxide coating density. In summary, at low salinity, the electrical conductivity of the tested hematite coated kaolinite was greater than that of uncoated pure kaolinite due to the higher relevance of surface conduction (or due to the increase in specific surface); however, with an increase in salinity, electrical conductivity/resistivity of coated and uncoated kaolinites was comparable and effectively represented by Archie's equation.

8.6 Summary

This study investigated the theoretical foundation of Archie's equation, along with its suitability for application in fine grained soils and water chemistries. The work also developed a relationship for electrical conductivity that incorporated a soil's physical properties, as well. In addition, this study performed an experimental investigation to examine the electrical properties of uncoated and lab-prepared iron oxide (hematite) coated sands and clay, and the impact of adsorbed hematite on the electrical conductivity/resistivity was evaluated by the comparison of the electrical properties of coated soils with those of clean soils. The following key observations were drawn:

1. The electrical conductivity formula of soils was derived by employing the three parallel resistances model: the observed conductivity was the sum of the particle conduction, the surface conduction, and the pore fluid conduction.

2. At low salinity, the role of surface conduction cannot be neglected; however, with increase in salinity, the observed conductivity of a porous media will be primarily governed by the conductivity of pore water. In addition, with an increase in particle size (or decrease in specific surface), the contribution of surface conduction to mixed conductivity of a porous media will be insignificant, and Archie's equation will be applicable.
3. The observed conductivity/resistivity of iron oxide (hematite) coated and uncoated clean sands showed good agreement under the tested salinity; however, the electrical conductivity of iron oxide coated clay indicated a somewhat higher value than that of clean kaolinite at low salinity, due to the higher relevance of surface conduction.
4. The increased electrical conductivity of the tested hematite coated kaolinite at low salinity can be attributed to the increased specific surface due to the iron oxide adsorption onto the surface of clay particles, not to an increase in surface conductivity.

CHAPTER 9 CONCLUSIONS AND RECOMMENDATIONS

This dissertation explored the fundamental understanding of mixtures of soils with various physical and chemical properties such as binary mixtures, fly ashes, and iron oxide coated soils by wave based techniques (i.e. elastic shear wave measurements, electromagnetic wave measurements, and thermal wave measurements). Every experimental result was coupled with theoretical framework to gain in-depth understanding of physical and chemical characteristics of tested mixed materials. And the major lessons learned through this study are follows:

Elastic shear wave velocity (or, small strain stiffness) of mixed materials

- Soils are particulate materials leading to that the stiffness of soils is determined by the stiffness of interparticle contact and the state of fabric. And the stiffness of interparticle contact and the state of fabric can be represented by the nature of interparticle contact and interparticle coordination.
- The stiffness of mixed materials (e.g. binary mixtures such as silty sand and fly ash) is determined by the stiffness of active grain contacts. While particles, which do not participate in structural skeleton, can do the secondary work such as prevention of buckling, the stiffness (or, shear wave velocity) of soils is mainly governed by the stiffness of particles which carry applied load.
- Binary mixtures (sand-sand mixture and sand-silt mixture) with low fines content showed a decrease in shear wave velocity with increasing fines content due to the reduction in interparticle contacts or interparticle coordination between large grains.

- Shear wave velocity of binary mixtures was represented by the intergranular void ratio, reflecting the stiffness of the binary mixture of silica particles was determined by the stiffness of contact between large particles, which are structural skeleton.
- From theoretical framework, the OCR exponent in the G_{\max} formulation was equivalent to the difference between the stress exponents in loading and unloading.
- Due to the greater change in interparticle coordination number between large grains, binary mixtures of silica particles with smaller size ratio (or greater size difference) showed greater stress history effect.
- The maximum stress history effect of tested silty sand was observed around a fines content of 5 %, which was smaller than critical fines content of silty sand due to the delay in critical fines content during unloading, compared to that of loading.
- With an increase in carbon and biomass contents, the small strain stiffness of fly ashes decreased due to the decrease in direct contacts (i.e. interparticle coordination or interparticle contact) between microspheres. Additionally, the variation of maximum shear modulus of different fly ashes was effectively represented by the interfine void ratio, supporting the stiffness of mixture is determined by the stiffness of structural skeleton.
- Fly ash particles showed strong stress-induced anisotropy; however, inherent anisotropy was negligible due to their particle shape.
- The measurement of shear wave velocity is the constant fabric phenomenon representing the stiffness of current soil state; however, measuring shear wave velocity with loading/unloading process is affected by not only the stiffness of

current contacts but also the fabric changes. Consequently, monitoring of shear wave velocity with applied stress will give an implication of changes in contact mode due to the rearrangement of soil particles.

- The presence of nano-sized particles (e.g. iron oxides = hematite, goethite) can affect the contact mode between substrate sand particles. Additionally, due to the different change in contact mode between particles according to initial relative density and applied stress, the shear wave velocity ratio (the ratio of V_s of hematite coated sand to V_s of uncoated clean sand) decreased with an increase in applied stress in the case of loose packing; while, the ratio increased with an increase in applied stress in the case of dense packing. And those ratios of shear wave velocities of loose and dense packings were getting closer with confinement reflecting initially different contact types between loose and dense packings were getting similar with an increase in applied stress.
- With an increase in substrate sand particle size, the wave velocity ratio generally decreased due to the decrease in relative roughness reflecting that coated sands with very low relative roughness can be considered as the smooth surface.
- Theoretical G_{\max} ratios (the ratio of G_{\max} of hematite coated sand to G_{\max} of uncoated sand) acted as the boundary of the stiffness of coated soils leading to gaining the insight into the alteration of contact modes according to iron oxide coating density, packing density, applied stress, and substrate sand particle size.

Electrical conductivity (or, resistivity) of mixed materials

- The electrical conductivity formula of soils was derived by employing three parallel resistances model: the observed conductivity is the sum of the particle conduction, the surface conduction, and the pore fluid conduction. Additionally, most geomaterials are electrically non-conductive; thus, electrical conductivity of most geomaterials can be represented by the function of surface conduction and pore water conduction.
- At low salinity, the role of surface conduction cannot be neglected; however, with increase in salinity, the observed conductivity of a porous media will be mainly governed by the conductivity of pore water. In addition, with increase in particle size (or decrease in specific surface), the contribution of surface conduction to mixed conductivity of a porous media will be insignificant leading to the relevance of Archie's equation.
- The observed conductivity/resistivity of iron oxide (hematite) coated and uncoated clean sands showed a good agreement under the tested salinity; however, the electrical conductivity of iron oxide coated clay indicated a little higher value than that of clean kaolinite at low salinity due to the higher relevance of surface conduction. And this increased surface conduction of coated soil was attributed to the increase in specific surface.
- Electrically conductive particles are affected by applied stress due to the change in contact area and coordination number. And fly ash can be considered as the binary mixture consisting of the matrix of electrically conductive unburned carbon particles and the matrix of non-conductive microspheres. Therefore, with an increase in TOC, the measured electrical conductivity increased, and conductive carbon particles will be more

dependent on applied stress due to the increased possibility of direct contacts between carbon particles. However, it can be postulated that carbon content dependency of stress exponent will be minimal when carbon particle become a structural skeleton ($TOC > TOC^*$)

- The main mechanism of electric conduction of conductive unburned carbon particles was electron tunneling, resulting in carbon particle conduction that was impacted by both pure particle conduction, and pore water conduction.

Thermal conductivity of mixed materials

- Thermal conductivity of natural soils such as sand, silt, clay, and intermediate soils is mainly controlled by mineralogy, porosity (or packing density), water content, saturation, testing temperature, applied stress, and pore water chemistry. And especially, in the case of dry soils, the thermal conductivity will be the primary function of mineralogy and porosity (or dry density) since heat transfer in dry soils is mainly conducted by heat conduction through contacts between particles.
- Thermal conductivity of fly ashes decreased almost linearly with an increase in biomass content; while, the variation of thermal conductivity of fly ashes according to unburned carbon content was relatively small reflecting both increased volumetric air content and higher thermal conductivity of unburned carbons.
- Thermal conductivity of fly ashes showed smaller values than that of natural soils in terms of porosity due to the retained air in the internal pore space; however, in terms of dry density, both fly ashes and natural soils showed a good agreement reflecting similar mineralogy of fly ash with natural soils.

Future work / Recommendation

- The dynamic properties of binary mixtures of soil particles were analyzed according to size ratio, fines (small particles) content, and relative density since all materials used in this study were non-plastic silica particles. Therefore, studies on mixtures of sand particles with plastic fines such as clay can be recommended since plastic fines can give an additional interparticle force, which may result in different behavior compared to that of mixtures with non-plastic fines.
- Shear wave velocity and electrical conductivity measurements of fly ashes with unburned carbon particles were limited up around 10 % (by weight) of carbon contents in this study; thus, those measurements of fly ashes with carbon contents greater than 10 % will be an interesting study topic.
- The testing specimens for the electrical characterization of uncoated and hematite coated kaolinites were slurry condition. Therefore, the tests on preconsolidated clays with relatively low preconsolidation pressure will allow the information of electrical properties of uncoated and coated clays at low void ratio (or, porosity). In addition, it is known that, being different from other iron oxides, magnetite has metallic properties; therefore, electrical conductivity/resistivity measurements on magnetite coated soils may give an interesting result.
- Among the thermal properties of soils, only the thermal conductivities of dry fly ashes with various contents of carbon and biomass particles were measured in this study without applying any effective stress. Therefore, the characterization of additional thermal properties (i.e. thermal diffusivity,

specific heat) will give additional valuable information. Additionally, tests on thermal conductivity of saturated fly ashes will be also meaningful; however, in this case, tests should be done with caution to prevent convection-induced heat flow. Finally, since heat conduction is mainly occurred through the contact between particles, measurements of thermal properties of soils with loading/unloading steps will yield valuable results.

REFERENCES

- Abu-Hamdeh, N. H., and Reeder, R. C. (2000). "Soil thermal conductivity: Effects of density, moisture, salt concentration, and organic matter." *Soil Science Society of America Journal*, 64(4), 1285-1290.
- Abuel-Naga, H. M., Bergado, D. T., Bouazza, A., and Pender, M. J. (2009). "Thermal conductivity of soft Bangkok clay from laboratory and field measurements." *Engineering Geology*, 105(3-4), 211-219.
- AbuHassanein, Z. S., Benson, C. H., and Blotz, L. R. (1996). "Electrical resistivity of compacted clays." *Journal of Geotechnical Engineering-ASCE*, 122(5), 397-406.
- ACAA. (2003). "Fly Ash Facts for Highway Engineers." *FHWA-IF-03-019*, Federal Highway Administration / U.S. Department of Transportation.
- ACAA. (2011). "Ash at Work." Applications, Science and Sustainability of Coal Ash, Lester Publications, LLC, New York.
- AECOM. (2009). "Root cause analysis of TVA kingston dredge pond failure on December 22, 2008." Project No. 60095742; Volume I AECOM Technology Corporation, Access: 2012 10/11 url: <http://www.tva.com/kingston/rca/>.
- Afifi, S. E. A., and Richart, F. E. J. (1973). "Stress History Effects on Shear Modulus of Soils." *Soils and Foundations*, 13(1), 77-95.
- Andrus, R. D., and Stokoe, K. H. (2000). "Liquefaction Resistance of Soils from Shear-wave Velocity." *Journal of Geotechnical and Geoenvironmental Engineering*, 126(11), 1015-1025.
- Archie, G. E. (1942). "The electrical resistivity log as an aid in determining some reservoir characteristics." *Transactions of the American Institute of Mining and Metallurgical Engineers*, 146, 54-61.
- Athanasopoulos, G. A. (1994). "Preconsolidation Versus Aging Behavior of Kaolinite Clay - Closure." *Journal of Geotechnical Engineering-ASCE*, 120(9), 1645-1647.
- Baltrus, J. P., Wells, A. W., Fauth, D. J., Diehl, J. R., and White, C. M. (2001). "Characterization of carbon concentrates from coal-combustion fly ash." *Energy & Fuels*, 15(2), 455-462.
- Bate, B., and Burns, S. E. (2010). "Effect of total organic carbon content and structure on the electrokinetic behavior of organoclay suspensions." *Journal of Colloid and Interface Science*, 343(1), 58-64.
- Baxter, L. (2005). "Biomass-coal co-combustion: opportunity for affordable renewable energy." *Fuel*, 84(10), 1295-1302.
- Bear, J. (1972). *Dynamics of Fluids in Porous Media*, American Elsevier Pub. Co.
- Benjamin, I., Evans, D., and Nitzan, A. (1997). "Electron tunneling through water layers: Effect of layer structure and thickness." *Journal of Chemical Physics*, 106(16), 6647-6654.
- Benson, R. (2000). "An Overview of Geophysical and Non-destructive Methods for Characterization of Roads and Bridge." Use of Geophysical Methods in Construction, ASCE, Geotechnical Special Publication, 1-14.
- Bikerman, J. J. (1933). "Ionic theory of electroosmosis, the current flow and the surface conductivity." *Zeitschrift Fur Physikalische Chemie-Abteilung a-Chemische Thermodynamik Kinetik Elektrochemie Eigenschaftslehre*,

- 163(5/6), 378-394.
- Bikerman, J. J. (1935). "Scientific and technical collected essays - Surface conductivity and its significance." *Kolloid-Zeitschrift*, 72(1), 100-108.
- Boudreau, B. P. (1996). "The diffusive tortuosity of fine-grained unlithified sediments." *Geochimica Et Cosmochimica Acta*, 60(16), 3139-3142.
- Bouzoubaa, N., Zhang, M. H., Bilodeau, A., and Malhotra, V. M. (1997). "The effect of grinding on the physical properties of fly ashes and a Portland cement clinker." *Cement and Concrete Research*, 27(12), 1861-1874.
- Bowles, J. E. (1979). *Physical and geotechnical properties of soils.*, McGraw-Hill Book Company.
- Brandl, H. (2006). "Energy foundations and other thermo-active ground structures." *Geotechnique*, 56(2), 81-122.
- Brandon, T. L., and Mitchell, J. K. (1989). "Factors Influencing Thermal Resistivity of Sands." *Journal of Geotechnical Engineering-Asce*, 115(12), 1683-1698.
- Brandon, T. L., Mitchell, J. K., and Cameron, J. T. (1989). "Thermal-Instability in Buried Cable Backfills." *Journal of Geotechnical Engineering-Asce*, 115(1), 38-55.
- Campanella, R. G., and Weemee, I. (1990). "Development and Use of an Electrical-Resistivity Cone for Groundwater Contamination Studies." *Canadian Geotechnical Journal*, 27(5), 557-567.
- Carraro, J. A. H., Bandini, P., and Salgado, R. (2003). "Liquefaction resistance of clean and nonplastic silty sands based on cone penetration resistance." *Journal of Geotechnical and Geoenvironmental Engineering*, 129(11), 965-976.
- Carraro, J. A. H., Prezzi, M., and Salgado, R. (2009). "Shear Strength and Stiffness of Sands Containing Plastic or Nonplastic Fines." *Journal of Geotechnical and Geoenvironmental Engineering*, 135(9), 1167-1178.
- Cascante, G., and Santamarina, J. C. (1996). "Interparticle contact behavior and wave propagation." *Journal of Geotechnical Engineering-Asce*, 122(10), 831-839.
- Chang, C. S., Misra, A., and Sundaram, S. S. (1991). "Properties of granular packings under low amplitude cyclic loading." *Soil Dynamics and Earthquake Engineering*, 10(4), 201-211.
- Charles-Cruz, C., Cousens, T., and Stewart, D. "Compressibility and Creep Behaviour of Hydraulically Placed PFA and Mine Tailings Fills." *Proceedings of the 12th conference of the International Association for Computer Methods and Advances in Geomechanics*, India, 2269-2276.
- Chen, B. S., and Mayne, P. W. (1994). "Profiling the Overconsolidation Ratio of Clay by Piezocone Tests." *GIT-CEEEO-94-1*.
- Chien, L. K., Oh, Y. N., and Chang, C. H. (2002). "Effects of fines content on liquefaction strength and dynamic settlement of reclaimed soil." *Canadian Geotechnical Journal*, 39(1), 254-265.
- Cho, G. C., Dodds, J., and Santamarina, J. C. (2006). "Particle Shape Effects on Packing Density, Stiffness, and Strength: Natural and Crushed Sands." *Journal of Geotechnical and Geoenvironmental Engineering*, 132(5), 591-602.
- Cho, G. C., Dodds, J., and Santamarina, J. C. (2007). "Closure to "Particle shape effects on packing density, stiffness, and strength: Natural and crushed sands" by Gye-Chun Cho, Jake Dodds, and J. Carlos Santamarina." *Journal of Geotechnical and Geoenvironmental Engineering*, 133(11), 1474-1474.
- Cornell, R. M., and Schwertmann, U. (2003). *The iron oxides: structure, properties, reactions, occurrences and uses*, Wiley-VCH.
- Cote, J., and Konrad, J. M. (2005). "A generalized thermal conductivity model for

- soils and construction materials." *Canadian Geotechnical Journal*, 42(2), 443-458.
- DeAlba, P., Baldwin, K., Janoo, V., Roe, G., and Celikkol, B. (1984). "Elastic-Wave Velocities and Liquefaction Potential." *Geotech. Test. J*, 7(2), 77-87.
- Demirboga, R., and Gul, R. (2003). "The effects of expanded perlite aggregate, silica fume and fly ash on the thermal conductivity of lightweight concrete." *Cement and Concrete Research*, 33(5), 723-727.
- Dias, R., Teixeira, J. A., Mota, M., and Yelshin, A. (2006). "Tortuosity variation in a low density binary particulate bed." *Separation and Purification Technology*, 51(2), 180-184.
- Digby, P. J. (1981). "The Effective Elastic-Moduli of Porous Granular Rocks." *Journal of Applied Mechanics-Transactions of the ASME*, 48(4), 803-808.
- Dowling, A., Clift, R., Grobert, N., Hutton, D., Oliver, R., O'Neill, O., Pethica, J., Pidgeon, N., Porritt, J., Ryan, J., Seaton, A., Tendler, S., Welland, M., and Whatmore, R. (2004). "Nanoscience and nanotechnologies: opportunities and uncertainties." *London: The Royal Society & The Royal Academy of Engineering Report*.
- Duffaut, K., Landro, M., and Sollie, R. (2010). "Using Mindlin theory to model friction-dependent shear modulus in granular media." *Geophysics*, 75(3), E143-E152.
- East30Sensors. (2007). "Thermal Conductivity Sensor: User's Manual." <http://www.east30sensors.com/>.
- EIA. (2012). "Annual Energy Review 2011." U.S. Energy Information Administration <http://www.eia.gov/totalenergy/data/annual/pdf/aer.pdf>.
- El-Sohby, M. A., and Andrawes, K. Z. (1972). "Deformation Characteristics of Granular Materials Under Hydrostatic Compression." *Canadian Geotechnical Journal*, 9(4), 338-350.
- Escudey, M., and Galindo, G. (1983). "Effect of Iron-Oxide Coatings on Electrophoretic Mobility and Dispersion of Allophane." *Journal of Colloid and Interface Science*, 93(1), 78-83.
- Fam, M., and Santamarina, J. C. (1997). "A study of consolidation using mechanical and electromagnetic waves." *Geotechnique*, 47(2), 203-219.
- Farouki, O. T. (1981a). "The Thermal-Properties of Soils in Cold Regions." *Cold Regions Science and Technology*, 5(1), 67-75.
- Farouki, O. T. (1981b). "Thermal Properties of Soils." *CRREL Monograph 81-1*, US Army Corps of Engineers.
- Farouki, O. T. (2004). "Ground Thermal Properties." *Thermal Analysis, Construction, and Monitoring Methods for Frozen Ground*, David C. Esch, ed., ASCE, 259-276.
- Fernandez, A. L. (2000). "Tomographic imaging the state of stress," Georgia Institute of Technology, Atlanta.
- Fernandez, A. L., and Santamarina, J. C. (2001). "Effect of cementation on the small-strain parameters of sands." *Canadian Geotechnical Journal*, 38(1), 191-199.
- Fukue, M., Minato, T., Horibe, H., and Taya, N. (1999). "The micro-structures of clay given by resistivity measurements." *Engineering Geology*, 54(1-2), 43-53.
- Galperin, M., Nitzan, A., and Benjamin, I. (2002). "Numerical simulations of electron tunneling currents in water." *Journal of Physical Chemistry A*, 106(45), 10790-10796.
- Gandhi, S. R., Dey, A. K., and Selvam, S. (1999). "Densification of pond ash by blasting." *Journal of Geotechnical and Geoenvironmental Engineering*,

- 125(10), 889-899.
- Gavriliiev, R. I. (2004). "Thermal Properties of Soils and Surface Covers." *Thermal Analysis, Construction, and Monitoring Methods for Frozen Ground*, David C. Esch, ed., ASCE, 277-294.
- Georgiannou, V. N., Burland, J. B., and Hight, D. W. (1990). "The undrained behaviour of clayey sands in triaxial compression and extension." *Geotechnique*, 40(3), 431-449.
- Glasscock, J. A., Barnes, P. R. F., Plumb, I. C., Bendavid, A., and Martin, P. J. (2008). "Structural, optical and electrical properties of undoped polycrystalline hematite thin films produced using filtered arc deposition." *Thin Solid Films*, 516(8), 1716-1724.
- Glover, P. W. J., Gomez, J. B., Meredith, P. G., Hayashi, K., P. R. Sammonds, and Murrell, S. A. F. (1997). "Damage of saturated rocks undergoing triaxial deformation using complex electrical conductivity measurements: Experimental results." *Physics and Chemistry of the Earth*, 22(1-2), 57-61.
- Goddard, J. D. (1990). "Nonlinear Elasticity and Pressure-Dependent Wave Speeds in Granular Media." *Proceedings of the Royal Society of London Series a-Mathematical Physical and Engineering Sciences*, 430(1878), 105-131.
- Gorman, T., and Kelly, W. E. (1990). "Electrical Hydraulic-Properties of Unsaturated Ottawa Sands." *Journal of Hydrology*, 118(1-4), 1-18.
- Grammelis, P., Skodras, G., and Kakaras, E. (2006a). "Effects of biomass co-firing with coal on ash properties. Part I: Characterisation and PSD." *Fuel*, 85(16), 2310-2315.
- Grammelis, P., Skodras, G., Kakaras, E., Karangelos, D. J., Petropoulos, N. P., Anagnostakis, M. J., Hinis, E. P., and Simopoulos, S. E. (2006b). "Effects of biomass co-firing with coal on ash properties. Part II: Leaching, toxicity and radiological behaviour." *Fuel*, 85(16), 2316-2322.
- Hardin, B. "The nature of stress-strain behavior os soils." *Geotechnical Division Specialty Conference on Earthquakes Engineering & Soil Dynamics*, ASCE, Pasadena, CA, 3-90.
- Hardin, B. O. (1987). "1-D Strain in Normally Consolidated Cohesionless Soils." *Journal of Geotechnical Engineering-Asce*, 113(12), 1449-1467.
- Hardin, B. O., and Blandford, G. E. (1989). "Elasticity of Particulate Materials." *Journal of Geotechnical Engineering-Asce*, 115(6), 788-805.
- Hardin, B. O., and Richart, F. E. (1963). "Elastic Wave Velocities in Granular Soils." *Journal of Soil Mechanics and Foundation Division, ASCE*, 89(1), 33-65.
- Holm, R. (1946). *Electric Contacts*, H Geben.
- Holm, R. (1967). *Electric Contacts 4th Edition*, Springer-Verlag.
- Houlsby, G. T., and Wroth, C. P. (1991). "The variation of shear modulus of clay with pressure and overconsolidation ratio." *Soils Fdns*, 31(3), 138-143.
- Hower, J. C., Rathbone, R. F., Robl, T. L., Thomas, G. A., Haeberlin, B. O., and Trimble, A. S. (1997). "Case study of the conversion of tangential- and wall-fired units to low-NOx combustion: Impact on fly ash quality." *Waste Management*, 17(4), 219-229.
- Hryciw, R. D., and Thomann, T. G. (1993). "Stress-History Based Model for G(E) of Cohesionless Soils." *Journal of Geotechnical Engineering-Asce*, 119(7), 1073-1093.
- Huang, Y. T., Huang, A. B., Kuo, Y. C., and Tsai, M. D. (2004). "A laboratory study on the undrained strength of a silty sand from Central Western Taiwan." *Soil Dynamics and Earthquake Engineering*, 24(9-10), 733-743.

- Hwang, J. Y., Sun, X., and Li, Z. (2002). "Unburned carbon from fly ash for mercury adsorption: I. Separation and characterization of unburned carbon." *Journal of Minerals and Materials Characterization and Engineering*, 1(1), 39-60.
- Ishihara, K. (1993). "Liquefaction and Flow Failure during Earthquakes." *Geotechnique*, 43(3), 351-415.
- Iwasaki, T., and Tatsuoka, F. (1977). "Effects of grain size and grading on dynamic shear moduli of sands." *Soils and Foundations*, 17(3), 19-35.
- Jager, K. M., McQueen, D. H., Tchmutin, I. A., Ryvkina, N. G., and Kluppel, M. (2001). "Electron transport and ac electrical properties of carbon black polymer composites." *Journal of Physics D-Applied Physics*, 34(17), 2699-2707.
- Jakka, R. S., Datta, M., and Ramana, G. V. (2010a). "Liquefaction behaviour of loose and compacted pond ash." *Soil Dynamics and Earthquake Engineering*, 30(7), 580-590.
- Jakka, R. S., Ramana, G. V., and Datta, M. (2010b). "Shear Behaviour of Loose and Compacted Pond Ash." *Goetech Geol Eng*, 28(6), 763-778.
- Jamiolkowski, M., Ladd, C. C., Germaine, J. T., and Lancellotta, R. "New Developments in Field and Laboratory Testing of Soils." *PROCEEDINGS OF THE ELEVENTH INTERNATIONAL CONFERENCE ON SOIL MECHANICS AND FOUNDATION ENGINEERING*, San Francisco, 57-153.
- Jamiolkowski, M., Lancellotta, R., and Lo Presti, D. "Remarks on the stiffness at small strains of six Italian clays." *Proceedings of the 1st international symposium prefailure deformation characteristics of geomaterials*, 817-836.
- Jang, J. (2011). "Gas production from hydrate-bearing sediments," Georgia Institute of Technology, Atlanta.
- Johansen, O. (1975). "Thermal Conductivity of Soils." *CRREL Draft English Translation 637*, US Army Corps of Engineers.
- Johnson, K. L. (1985). *Contact Mechanics*, Cambridge University Press, 452.
- Jovicic, V., and Coop, M. R. (1997). "Stiffness of coarse-grained soils at small strains." *Geotechnique*, 47(3), 545-561.
- Kim, B., and Prezzi, M. (2008). "Evaluation of the mechanical properties of class-F fly ash." *Waste Management*, 28(3), 649-659.
- Kim, B., Prezzi, M., and Salgado, R. (2005). "Geotechnical properties of fly and bottom ash mixtures for use in highway embankments." *Journal of Geotechnical and Geoenvironmental Engineering*, 131(7), 914-924.
- Kim, J. H., Yoon, H. K., Cho, S. H., Kim, Y. S., and Lee, J. S. (2011a). "Four Electrode Resistivity Probe for Porosity Evaluation." *Geotechnical Testing Journal*, 34(6), 668-675.
- Kim, J. H., Yoon, H. K., and Lee, J. S. (2011b). "Void Ratio Estimation of Soft Soils Using Electrical Resistivity Cone Probe." *Journal of Geotechnical and Geoenvironmental Engineering*, 137(1), 86-93.
- Klein, K. A., and Santamarina, J. C. (2003). "Electrical conductivity in soils: Underlying phenomena." *J. Environ. Eng. Geophys*, 8(4), 263-273.
- Koponen, A., Kataja, M., and Timonen, J. (1996). "Tortuous flow in porous media." *Physical Review E*, 54(1), 406-410.
- Kosmulski, M., Maczka, E., Jartych, E., and Rosenholm, J. B. (2003). "Synthesis and characterization of goethite and goethite-hematite composite: experimental study and literature survey." *Advances in Colloid and Interface Science*, 103(1), 57-76.
- Kuerbis, R., and Vaid, Y. P. (1988). "Sand sample preparation—The slurry deposition

- method." *Soils and Foundations*, 28(4), 107-118.
- Kutchko, B. G., and Kim, A. G. (2006). "Fly ash characterization by SEM-EDS." *Fuel*, 85(17-18), 2537-2544.
- Lade, P. V., Liggio, C. D., and Yamamuro, J. A. (1998). "Effects of non-plastic fines on minimum and maximum void ratios of sand." *Geotechnical Testing Journal*, 21(4), 336-347.
- Lade, P. V., and Yamamuro, J. A. (1997). "Effects of nonplastic fines on static liquefaction of sands." *Canadian Geotechnical Journal*, 34(6), 918-928.
- Larrahondo, J. M. (2011). "Carbonate Diagenesis and Chemical Weathering in the Southeastern United States: Some Implications on Geotechnical Behavior," Georgia Institute of Technology, Atlanta.
- Larrahondo, J. M., Choo, H., and Burns, S. E. (2011). "Laboratory-prepared iron oxide coatings on sands: Submicron-scale small-strain stiffness." *Engineering Geology*, 121(1-2), 7-17.
- Lee, C., Truong, Q. H., Lee, W., and Lee, J. S. (2010). "Characteristics of Rubber-Sand Particle Mixtures according to Size Ratio." *Journal of Materials in Civil Engineering*, 22(4), 323-331.
- Lee, J. S., Dodds, J., and Santamarina, J. C. (2007). "Behavior of rigid-soft particle mixtures." *Journal of Materials in Civil Engineering*, 19(2), 179-184.
- Lee, J. S., and Santamarina, J. C. (2005). "Bender elements: Performance and signal interpretation." *Journal of Geotechnical and Geoenvironmental Engineering*, 131(9), 1063-1070.
- Leroy, P., and Revil, A. (2004). "A triple-layer model of the surface electrochemical properties of clay minerals." *Journal of Colloid and Interface Science*, 270(2), 371-380.
- Liu, N., and Mitchell, J. K. (2006). "Influence of nonplastic fines assessment on shear wave velocity-based of liquefaction." *Journal of Geotechnical and Geoenvironmental Engineering*, 132(8), 1091-1097.
- Lo Presti, D. C. F., Jamiolkowski, M., Pallara, O., Cavallaro, A., and Pedroni, S. (1997). "Shear modulus and damping of soils." *Geotechnique*, 47(Compendex), 603-617.
- Lorenz, P. B. (1969). "Surface Conductance and Electrokinetic Properties of Kaolinite Beds." *Clays and Clay Minerals*, 17(4), 223-&.
- Lu, S., Ren, T. S., Gong, Y. S., and Horton, R. (2007). "An improved model for predicting soil thermal conductivity from water content at room temperature." *Soil Science Society of America Journal*, 71(1), 8-14.
- Lyklema, J., and Minor, M. (1998). "On surface conduction and its role in electrokinetics." *Colloids and Surfaces a-Physicochemical and Engineering Aspects*, 140(1-3), 33-41.
- Marinho, B., Ghislandi, M., Tkalya, E., Koning, C. E., and de With, G. (2012). "Electrical conductivity of compacts of graphene, multi-wall carbon nanotubes, carbon black, and graphite powder." *Powder Technology*, 221, 351-358.
- Matsunaga, T., Kim, J. K., Hardcastle, S., and Rohatgi, P. K. (2002). "Crystallinity and selected properties of fly ash particles." *Materials Science and Engineering a-Structural Materials Properties Microstructure and Processing*, 325(1-2), 333-343.
- Matyka, M., Khalili, A., and Koza, Z. (2008). "Tortuosity-porosity relation in porous media flow." *Physical Review E*, 78(2).
- Maurice, P. A. (2009). *Environmental Surface and Interfaces from the Nanoscale to the Global Scale*, John Wiley & Sons.

- Mayne, P. W., and Kulhawy, F. H. (1982). "Ko-OCR Relationships in Soil." *Journal of the Geotechnical Engineering Division-ASCE*, 108(6), 851-872.
- McDowell, P. W., Barker, R. D., Butcher, A. P., Culshaw, M. G., Jackson, P. D., McCann, D. M., Skipp, B. O., Matthews, S. L., and Arthur, J. C. R. (2002). *Geophysics in Engineering Investigations (CIRIA)*, Construction Industry Research and Information Association, 252.
- Mehra, O. P., and Jackson, M. L. (1960). "Iron oxide removal from soils and clays by dithionite-citrate system buffered with sodium bicarbonate." *Clays and Clay Minerals*, 7th National Conference, 317-327.
- Mindlin, R. D., and Deresiewicz, H. (1953). "Elastic Spheres in Contact under Varying Oblique Forces." *Journal of Applied Mechanics-Transactions of the ASME*, 20(3), 327-344.
- Mitchell, J. K., and Soga, K. (2005). *Fundamentals of Soil Behavior*, John Wiley & Sons.
- Mochizuki, S. (1977). "Electrical conductivity of α -Fe₂O₃." *Physica Status Solidi A*, 41(2), 591-594.
- Nachtegaal, M., and Sparks, D. L. (2004). "Effect of iron oxide coatings on zinc sorption mechanisms at the clay-mineral/water interface." *Journal of Colloid and Interface Science*, 276(1), 13-23.
- Naeini, S. A., and Baziar, M. H. (2004). "Effect of fines content on steady-state strength of mixed and layered samples of a sand." *Soil Dynamics and Earthquake Engineering*, 24(3), 181-187.
- Naik, T. R., Kraus, R. N., Ramme, B. W., Chun, Y. M., and Kumar, R. (2006). "High-carbon fly ash in manufacturing conductive CLSM and concrete." *Journal of Materials in Civil Engineering*, 18(6), 743-746.
- Ochsner, T. E., Horton, R., and Ren, T. H. (2001). "A new perspective on soil thermal properties." *Soil Science Society of America Journal*, 65(6), 1641-1647.
- Osei, B. A., and Singh, B. (1999). "Electrophoretic mobility of some tropical soil clays: effect of iron oxides and organic matter." *Geoderma*, 93(3-4), 325-334.
- Pandian, N. S. (2004). "Fly ash characterization with reference to geotechnical applications." *Journal of Indian Institute of Science*, 84, 189-216.
- Pantea, D., Darmstadt, H., Kaliaguine, S., and Roy, C. (2003). "Electrical conductivity of conductive carbon blacks: influence of surface chemistry and topology." *Applied Surface Science*, 217(1-4), 181-193.
- Paya, J., Monzo, J., Borrachero, M. V., and Perismora, E. (1995). "Mechanical Treatment of Fly Ashes .1. Physicochemical Characterization of Ground Fly Ashes." *Cement and Concrete Research*, 25(7), 1469-1479.
- Petrakis, E., and Dobry, R. (1989). "Micromechanical Behavior and Modelling of Granular Soil." *AFOSR 89-1229*.
- Pfannkuch, H. O. (1972). "On the Correlation of Electrical Conductivity Properties of Porous Systems with Viscous Flow Transport Coefficients." *Developments in Soil Science*, 2, 42-54.
- Pinson, D., Zou, R. P., Yu, A. B., Zulli, P., and McCarthy, M. J. (1998). "Coordination number of binary mixtures of spheres." *Journal of Physics D-Applied Physics*, 31(4), 457-462.
- Polito, C. P., and Martin, J. R. (2001). "Effects of nonplastic fines on the liquefaction resistance of sands." *Journal of Geotechnical and Geoenvironmental Engineering*, 127(5), 408-415.
- Randolph, M. F., Dolwin, J., and Beck, R. (1994). "Design of Driven Piles in Sand." *Geotechnique*, 44(3), 427-448.

- Rao, M. V. B. B. G., and Singh, D. N. (1999). "A generalized relationship to estimate thermal resistivity of soils." *Canadian Geotechnical Journal*, 36(4), 767-773.
- Revil, A., and Glover, P. W. J. (1998). "Nature of surface electrical conductivity in natural sands, sandstones, and clays." *Geophysical Research Letters*, 25(5), 691-694.
- Reynolds, M. J. (1997). *An introduction to applied and environmental geophysics*, Wiley.
- Robertson, P. K., and Campanella, R. G. (1985). "Liquefaction Potential of Sands Using the Cpt." *Journal of Geotechnical Engineering-Asce*, 111(3), 384-403.
- Robertson, P. K., Sasitharan, S., Cunning, J. C., and Segoo, D. C. (1995). "Shear-Wave Velocity to Evaluate in-Situ State of Ottawa Sand." *Journal of Geotechnical Engineering-Asce*, 121(3), 262-273.
- Roesler, S. K. (1979). "Anisotropic Shear Modulus Due to Stress Anisotropy." *Journal of the Geotechnical Engineering Division-Asce*, 105(7), 871-880.
- Rothenburg, L., and Bathurst, R. J. (1989). "Analytical Study of Induced Anisotropy in Idealized Granular-Materials." *Geotechnique*, 39(4), 601-614.
- Ruhl, L., Vengosh, A., Dwyer, G. S., Hsu-Kim, H., Deonarine, A., Bergin, M., and Kravchenko, J. (2009). "Survey of the Potential Environmental and Health Impacts in the Immediate Aftermath of the Coal Ash Spill in Kingston, Tennessee." *Environmental Science & Technology*, 43(16), 6326-6333.
- Sakurai, K., Teshima, A., and Kyuma, K. (1990). "Changes in Zero-Point of Charge (Zpc), Specific Surface-Area (Ssa), and Cation-Exchange Capacity (Cec) of Kaolinite and Montmorillonite, and Strongly Weathered Soils Caused by Fe and Al Coatings." *Soil Science and Plant Nutrition*, 36(1), 73-81.
- Salem, H. S., and Chilingarian, G. V. (1999). "The cementation factor of Archie's equation for shaly sandstone reservoirs." *Journal of Petroleum Science and Engineering*, 23(2), 83-93.
- Salgado, R., Bandini, P., and Karim, A. (2000). "Shear strength and stiffness of silty sand." *Journal of Geotechnical and Geoenvironmental Engineering*, 126(5), 451-462.
- Sami, M., Annamalai, K., and Wooldridge, M. (2001). "Co-firing of coal and biomass fuel blends." *Progress in Energy and Combustion Science*, 27(2), 171-214.
- Samouelian, A., Cousin, I., Tabbagh, A., Bruand, A., and Richard, G. (2005). "Electrical resistivity survey in soil science: a review." *Soil & Tillage Research*, 83(2), 173-193.
- Sanchez-Gonzalez, J., Macias-Garcia, A., Alexandre-Franco, M. F., and Gomez-Serrano, V. (2005). "Electrical conductivity of carbon blacks under compression." *Carbon*, 43(4), 741-747.
- Sanchez-Salinerio, I., Rosset, J. M., and Stokoe, K. H. (1986). "Analytical studies of body wave propagation and attenuation." Texas.
- Santamarina, C., and Cascante, G. (1998). "Effect of surface roughness on wave propagation parameters." *Geotechnique*, 48(1), 129-136.
- Santamarina, J. C., and Cascante, G. (1996). "Stress anisotropy and wave propagation: A micromechanical view." *Canadian Geotechnical Journal*, 33(5), 770-782.
- Santamarina, J. C., Klein, K. A., and Fam, M. A. (2001). *Soils and waves : particulate materials behavior, characterization and process monitoring*, J. Wiley & Sons.
- Santamarina, J. C., Klein, K. A., Wang, Y. H., and Prencke, E. (2002). "Specific surface: determination and relevance." *Canadian Geotechnical Journal*, 39(1), 233-241.
- Scheidegger, A., Borkovec, M., and Sticher, H. (1993). "Coating of Silica Sand with

- Goethite - Preparation and Analytical Identification." *Geoderma*, 58(1-2), 43-65.
- Schwertmann, U., and Cornell, R. M. (2000). *Iron Oxides in the Laboratory: Preparation and Characterization*, WILEY-VC.
- Schwertmann, U., and Taylor, R. M. (1989). "Iron Oxides." Minerals in soil environments, J.B. Dixon and S. B. Weed, eds., SSSA, Madison WI, 379-438.
- Seed, H. B., Idriss, I. M., and Arango, I. (1983). "Evaluation of Liquefaction Potential Using Field Performance Data." *Journal of Geotechnical Engineering-Asce*, 109(3), 458-482.
- Seed, H. B., Wong, R. T., Idriss, I. M., and Tokimatsu, K. (1986). "Moduli and Damping Factors for Dynamic Analyses of Cohesionless Soils." *Journal of Geotechnical Engineering-Asce*, 112(11), 1016-1032.
- Shen, L., and Chen, Z. X. (2007). "Critical review of the impact of tortuosity on diffusion." *Chemical Engineering Science*, 62(14), 3748-3755.
- Shin, H., and Santamarina, J. C. (2013). "Role of Particle Angularity on the Mechanical Behavior of Granular Mixtures." *Journal of Geotechnical and Geoenvironmental Engineering*, 139(2), 353-355.
- Shustorovich, V., and Shustorovich, E. (2003). "Actual relationship between load and deflection for cellular ceramic substrates: effective moduli of substrates and materials." *Journal of the European Ceramic Society*, 23(10), 1715-1722.
- Slade, P. G. (1999). *Electrical Contacts Principles and Applications*, Markel Dekker Inc.
- Smith, R. W., and Narimatsu, Y. (1993). "Electrokinetic Behavior of Kaolinite in Surfactant Solutions as Measured by Both the Microelectrophoresis and Streaming Potential Methods." *Minerals Engineering*, 6(7), 753-763.
- Smith, W. O., and Byers, H. G. "The thermal conductivity of dry soils of certain of the great soil groups." *Soil Sci. Soc. Amer. Proc.*, 13-19.
- Sposito. (2004). *The Surface Chemistry of Natural Particles*, Oxford University Press, USA.
- Styszko-Grochowiak, K., Golas, J., Jankowski, H., and Kozinski, S. (2004). "Characterization of the coal fly ash for the purpose of improvement of industrial on-line measurement of unburned carbon content." *Fuel*, 83(13), 1847-1853.
- Tangpagasit, J., Cheerarot, R., Jaturapitakkul, C., and Kiattikomol, K. (2005). "Packing effect and pozzolanic reaction of fly ash in mortar." *Cement and Concrete Research*, 35(6), 1145-1151.
- Tatsuoka, F., Iwasaki, T., Fukushima, S., and Sudo, H. (1979). "Stress conditions and stress histories affecting shear modulus and damping of sand under cyclic loading " *Soils and Foundations*, 19(2), 29-43.
- Tatsuoka, F., and Shibuya, S. "Deformation characteristics of soils and rocks from field and laboratory tests " *Proc. of the 9th Asian Regional Conf. on SMFE Bangkok*, 101-170.
- Thevanayagam, S. (1998). "Effect of fines and confining stress on undrained shear strength of silty sands." *Journal of Geotechnical and Geoenvironmental Engineering*, 124(6), 479-491.
- Thevanayagam, S., Shenthan, T., Mohan, S., and Liang, J. (2002). "Undrained fragility of clean sands, silty sands, and sandy silts." *Journal of Geotechnical and Geoenvironmental Engineering*, 128(10), 849-859.
- Tiab, D., and Donaldson, E. C. (2004). *Petrophysics: Theory and Practice of Measuring Reservoir Rock and Fluid Transport Properties*, ELSEVIER,

- Gulf Professional Publishing.
- Trivedi, A., and Sud, V. K. (2002). "Grain characteristics and engineering properties of coal ash." *Granular Matter*, 4(3), 93-101.
- Urban, F., White, H. L., and Strassner, E. A. (1935). "Contribution to the theory of surface conductivity at solid-liquid interfaces." *Journal of Physical Chemistry*, 39(3), 311-330.
- Urish, D. W. (1981). "Electrical Resistivity-Hydraulic Conductivity Relationships in Glacial Outwash Aquifers." *Water Resources Research*, 17(5), 1401-1408.
- USDA. (2007). *The Encyclopedia of Wood*, U.S. Department of Agriculture, Skyhorse Publishing, 496.
- Vaid, Y. P., Fisher, J. M., Kuerbis, R. H., and Negussey, D. (1990). "Particle gradation and liquefaction." *Journal of Geotechnical Engineering*, 116(4), 698-703.
- Vallejo, L. E. (2001). "Interpretation of the limits in shear strength in binary granular mixtures." *Canadian Geotechnical Journal*, 38(5), 1097-1104.
- van de Lindt, J. W., Carraro, J. A. H., Heyliger, P. R., and Choi, C. (2008). "Application and feasibility of coal fly ash and scrap tire fiber as wood wall insulation supplements in residential buildings." *Resources Conservation and Recycling*, 52(10), 1235-1240.
- Viggiani, G., and Atkinson, J. H. (1995a). "Interpretation of bender element tests." *Geotechnique*, 45(1), 149-154.
- Viggiani, G., and Atkinson, J. H. (1995b). "Stiffness of fine-grained soil at very small strains." *Geotechnique*, 45(2), 249-265.
- Vilches, L. F., Fernandez-Pereira, C., del Valle, J. O., and Vale, J. (2003). "Recycling potential of coal fly ash and titanium waste as new fireproof products." *Chemical Engineering Journal*, 95(1-3), 155-161.
- Wang, S. Z., Miller, A., Llamazos, E., Fonseca, F., and Baxter, L. (2008). "Biomass fly ash in concrete: Mixture proportioning and mechanical properties." *Fuel*, 87(3), 365-371.
- Wang, Y. H., and Mok, C. M. B. (2008). "Mechanisms of small-strain shear-modulus anisotropy in soils." *Journal of Geotechnical and Geoenvironmental Engineering*, 134(10), 1516-1530.
- Waxman, M. H., and Smits, L. J. M. (1968). "Electrical Conductivities in Oil-Bearing Shaly Sands." *Society of Petroleum Engineers Journal*, 8(2), 107-&.
- Wieck-Hansen, K., Overgaard, P., and Larsen, O. H. (2000). "Cofiring coal and straw in a 150 MWe power boiler experiences." *Biomass & Bioenergy*, 19(6), 395-409.
- Williams, D. J. A., and Williams, K. P. (1978). "Electrophoresis and Zeta Potential of Kaolinite." *Journal of Colloid and Interface Science*, 65(1), 79-87.
- Xu, Y., and Axe, L. (2005). "Synthesis and characterization of iron oxide-coated silica and its effect on metal adsorption." *Journal of Colloid and Interface Science*, 282(1), 11-19.
- Yamamuro, J. A., and Lade, P. V. (1997). "Static liquefaction of very loose sands." *Canadian Geotechnical Journal*, 34(6), 905-917.
- Yamamuro, J. A., and Wood, F. M. (2004). "Effect of depositional method on the undrained behavior and microstructure of sand with silt." *Soil Dynamics and Earthquake Engineering*, 24(9-10), 751-760.
- Yang, S. L., Lacasse, S., and Sandven, R. F. (2006). "Determination of the transitional fines content of mixtures of sand and non-plastic fines." *Geotechnical Testing Journal*, 29(2), 102-107.

- Yao, H. Z., Ouyang, L. Z., and Ching, W. Y. (2007). "Ab initio calculation of elastic constants of ceramic crystals." *Journal of the American Ceramic Society*, 90(10), 3194-3204.
- Yeboah, N. N. N., and Burns, S. E. (2011). "Geological Disposal of Energy-Related Waste." *Ksce Journal of Civil Engineering*, 15(4), 697-705.
- Yeboah, N. N. N., Shearer, C., Burns, S. E., and Kurtis, K. E. (in preparation). "Characterization of high carbon content class F coal ash, coal and biomass co-fired ash, and pure biomass ash for productive reuse."
- Yildirim, M. S., Bicer, Y., and Yildiz, C. (1996). "Utilization of Fly Ash and Polypropylene Wastes in the Production of a New Porous Composite Material." *Journal of Porous Materials*, 3(3), 189-191.
- Youd, T. L. (1973). "Factors controlling maximum and minimum densities of sands." *ASTM Spec. Tech. Publ.*, 523, 98-112.
- Yu, P., and Richart, F. E. (1984). "Stress Ratio Effects on Shear Modulus of Dry Sands." *Journal of Geotechnical Engineering-Asce*, 110(3), 331-345.
- Yukselen, Y., and Kaya, A. (2003). "Zeta potential of kaolinite in the presence of alkali, alkaline earth and hydrolyzable metal ions." *Water Air and Soil Pollution*, 145(1), 155-168.
- Yun, T. S., and Santamarina, J. C. (2008). "Fundamental study of thermal conduction in dry soils." *Granular Matter*, 10(3), 197-207.
- Zeng, X., and Ni, B. (1999). "Stress-induced anisotropic G(max) of sands and its measurement." *Journal of Geotechnical and Geoenvironmental Engineering*, 125(9), 741-749.
- Zeng, X. W., and Ni, B. X. (1998). "Application of bender elements in measuring G(max) of sand under K-0 condition." *Geotechnical Testing Journal*, 21(3), 251-263.
- Zhang, G. "Soil Nanoparticles and Their Influence on Engineering Properties of Soils." *Geo-Denver 2007: New Peaks in Geotechnics*, Denver.
- Zhang, G., Germaine, J. T., Whittle, A. J., and Ladd, C. C. (2004). "Soil structure of a highly weathered old alluvium." *Geotechnique*, 54(7), 453-466.
- Zhang, G. P., Germaine, J. T., and Whittle, A. J. (2003). "Effects of Fe-oxides cementation on the deformation characteristics of a highly weathered old alluvium in San Juan, Puerto Rico." *Soils and Foundations*, 43(4), 119-130.

VITA

Hyunwook Choo was born in Korea in 1980. He earned Bachelors and Masters Degrees in Civil and Environmental Engineering from Korea University in 2006 and 2008, respectively. He worked as site development supervisor in Korea through 2008. He started pursuing graduate-level studies at Georgia Tech School of Civil and Environmental Engineering since 2009, and joined as a Graduate Research Assistant in the Geo-Environmental Engineering Group of Dr. Susan Burns. He is expected to complete his Ph.D. degree in August 2013.